RHEO-NMR OF COMPLEX FLUIDS UNDER STARTUP, STEADY STATE AND LARGE AMPLITUDE OSCILLATORY SHEAR

by

Jayesha S Jayaratne

A dissertation submitted in partial fulfillment
of the requirements for the degree

of

Doctor of Philosophy

in

Chemical Engineering

MONTANA STATE UNIVERSITY
Bozeman, Montana

December 2021

DEDICATION

To my loving mother Bhaddika, family, friends, Joe, Sarah, Jen, and all sweet puppies encountered. Thank you for all the lessons in life, the kind and caring moments shared and for all the smiles that made this journey a joyful and cherish-able one!

ACKNOWLEDGEMENTS

To the strongest woman and loving mother I am blessed to have in my life, Bhaddika Jayaratne, thank you for always being there for me. None of this would have been possible without your continued support.

I would like to acknowledge my chair Joseph Seymour and co-chair, Sarah Codd. Thank you for identifying my weaknesses and pushing me to make them my strengths. I would also like to thank my committee member, Jennifer Brown, for introducing me to the world of rheology and making me part of the MRM lab family.

I would like to thank William Hart and the entire rheology R&D team at Proctor & Gamble for bringing a new perspective and pace to our projects and for the continued funding for the rheo-NMR projects at MSU.

To Timothy Brox, thank you for the rheo-NMR equipment designs and for always being there to help fix issues with them. An acknowledgement to Petrik Galvosas for the valuable educational opportunity out at his MRM lab in Wellington, NZ is also due.

A special acknowledgement goes out to Scott Busse, the MSU MRM lab manager, for all the early morning interesting stories and continued smooth functioning of the spectrometers. All my lab mates, Matt Skuntz, Jeff, Rehab, Madison, Peng and Josie for the laughter and support throughout the years.

TABLE OF CONTENTS

TABLE OF CONTENTS CONTINUED

TABLE OF CONTENTS CONTINUED

TABLE OF CONTENTS CONTINUED

LIST OF TABLES

Table Page

LIST OF FIGURES

Figure Page

LIST OF FIGURES CONTINUED

Figure Page

LIST OF FIGURES CONTINUED

Figure Page

LIST OF FIGURES CONTINUED

Figure Page

ABSTRACT

Fluids are categorized as either simple or complex based on the intricacy of their structure and material response to deformation. Simple fluids composed of small molecules subject to deformation, readily flow with linear interaction dynamics with neighboring molecules. In contrast complex fluids like polymers, micelle solutions, colloidal gels and suspensions, composed of larger molecules or particulates alter the dynamics of individual constituents during deformation, requiring complicated constitutive models. Complex fluids are encountered daily, as they are found in consumer products such as food, pharmaceutical and personal care products. Knowing flow characteristics of these consumer products and their raw materials under industrially applicable deformations enables engineers to design efficient industrial processes and to formulate products to desired qualities. While classical rheology (the study of the flow and deformation of matter) techniques give good estimation of stress-strain bulk flow response, it fails to provide local flow information.

Proton nuclear magnetic resonance (1H-NMR) has been used to measure spatially and temporally resolved velocities of fluids subject to mechanical deformation. This research field is known as ‘Rheo-NMR’ and is a novel flow measuring technique in that it is non-invasive and able to quantify three-dimensional velocity fields even of opaque fluids. Velocity responses of complex fluids like worm-like micelle solutions, yield stress fluids and shear thinning fluids were studied under varied mechanisms of deformation and were compared to the responses of simple Newtonian fluids. How local velocities of the fluids change over time when a steady shear is applied suddenly, how the velocity fields are affected on applying large oscillatory shear deformations and how using different shearing geometries impacts the local flow response were explored. Using Rheo-NMR techniques, experimental protocols to study spatio-temporal velocity fields of complex fluids were developed and data analysis methods for quantifying such measurements were established.

CHAPTER ONE

INTRODUCTION

Pre-industrialization when no synthetic material was in existence, limited interest was paid to naturally occurring complex materials to categorize material used daily as either solid or liquids [1] [2]. With the onset of the industrial revolution alteration of materials for specific applications took on a new importance. This sparked the interest of scientists to study the 'simply' termed solids and liquids in depth, which by this point was not an adequate description of how complex materials behaved. The synthesis of new chemicals and desire to achieve materials with specific qualities using synthetic and natural materials paved the way for the study of material responses to subject deformations, today known in rheology as 'everything flows' [1].

Knowing material properties and classification of these complex materials or fluids via rheology is central to disciplines of physics, chemistry, engineering and mathematics. Its areas of application span to diverse industries, a dominant few being: food processing, cosmetics and personal care products, pharmaceuticals, oil and gas and construction [1, 3, 4]. These fields typically rely on drag flow rheometry where a fluid sample is suspended between one moving surface and a second stationary one. If a controlled strain is the chosen form of deformation applied on the fluids, the resulting stress response is calculated by measuring the amount of torque the 'bulk' of the fluid subjects on the moving surface. Rheology experiments can be divided into linear and non-linear regimes based on the degree of mechanical deformation applied to the sample. Linear rheology is a dynamic oscillatory shear experiment where the strain amplitude of the oscillatory motion is very small, hence termed small amplitude oscillatory shear

(SAOS) [5]. Here material responses like the storage and loss moduli (G' and G") can be found along with characteristic material relaxation times. Nonlinear rheology takes a steady shear approach or an oscillatory approach, both of which are substantially important in industrial applications. The steady shear approach relates information on the material properties, like viscosity and stress response to incremented shear rates. Dynamic nonlinear oscillatory shear experiments apply a strain amplitude that probes a material's nonlinear viscoelastic regime. The resulting stress responses to such large deformations show effects of structural modifications to the sample induced by the large strains and identified by the influence of higher order harmonics of the material moduli [5].

A limitation of rheology is that it relies on viscometric flow assumptions to provide relations between the macroscopic/bulk characteristics and the material functions over a wide range of flow regimes. The theory of viscometric flows works well for simple, small molecule Newtonian fluids, however fails in studying complex fluids that show flow heterogeneities stemming from hydrodynamic instabilities (worm-like micelle solutions) or transitions in behavioral response as in yield stress fluids [6]. Given the desire to study complex fluids, such as wormlike micelle solutions, shear thinning yield stress fluids and purely shear thinning fluids complementing the bulk flow responses of these materials with spatially resolved velocity profiles provides a more quantitative approach to the viscometric flow limitation. The velocity fields imaged using Rheo-NMR (rheo-nuclear magnetic resonance) techniques use a portable and magneto-safe rheometer capable of inducing mechanical shear on fluid samples in the imaging region of the NMR magnet. While NMR only has a few atomic nuclei it can study, as it is a technique that uses the magnetic dipole moment of unpaired protons in strong magnetic fields, it

provides significant benefits when used in dynamic fluid studies [7]. ^{1}H-NMR applied in the projects of this thesis used the unpaired proton of the hydrogen atom exclusively. ^{1}H being the highest signal generating NMR-sensitive atomic nuclei allows for a range of NMR velocimetry methods to be applied [8]. Complex fluids generally have a plethora of hydrogen atoms in their molecular structures facilitating use of 1H-MR. Combining rheology techniques with NMR velocimetry allows for non-invasive spatio-temporal study of fluids including those that are opaque.

In the current work, Rheo-NMR velocimetry was employed to measure velocity distributions of responses of complex fluids under steady state, start-up and oscillatory shear flows in a cylindrical Couette shear cell. Spatial distribution of velocity reflect local material responses not detected by bulk rheology measurements of torque to determining shear stress. Velocity distributions during a large amplitude oscillatory shear (LAOS) motion were measured by using advancements made to Rheo-NMR equipment [9]. The use of vane measurements to study yield stress materials is well established while the use of Rheo-NMR in studying yield stress materials has been established using a standard Couette shear cell [10-12]. New rheometry fractal vane geometries have been introduced in the recent years and with it a first time analysis of the fractal vane in place of the concentric cylinder cell in Rheo-NMR is introduced [13].

Outline

Chapter 2 introduces basic and advanced principles underlying the theory of nuclear magnetic resonance (NMR). The concepts of how the signal is acquired and imaging is performed in NMR is discussed with nuclear spin, precession, signal excitation and gradients.

Principles related to more advanced topics like spin relaxation and magnetic field flow imaging are also presented. Chapter 3 provides a brief overview on rheology. What rheology is, types of rheometry and frequently used geometries are detailed. Explanations of complex fluid behavior, systems of yield stress fluids and shear thinning fluids along with mathematical models used in describing them are included in this chapter. In Chapter 4, Rheo-NMR is applied to observe temporal fluctuations of shear banding phenomenon in a worm-like micelle solution for startup flow at a shear rate known to generate shear banding. Results of two different experimental protocols, one with and another without a pre-shear are analyzed [14]. Large amplitude oscillatory shear measured by Rheo-NMR is presented in Chapter 5. Novel 1D spatially resolved large amplitude oscillatory shear velocity profiles are measured for Newtonian fluids, yield stress fluids and shear thinning fluids. Given the novelty of the data, the analysis is approached in several ways to explore the information potentially available. The data represents the first detailed study by Rheo-NMR of transient material response in oscillatory flow and novel analysis methods explored. A novel geometry, the 12-arm fractal vane rotor, is studied using 1D and 2D velocity image data in Chapter 6 [13]. Here a Carbopol solution, a model simple yield stress fluid showing prominent wall slip when employing a concentric cylinder geometry, is used in comparing flow fields between the Couette shear cell and the fractal vane. Chapter 7 applies Rheo-NMR informing the start-up and steady state flows of several concentrations of oil-in-water emulsions. The data of the emulsions containing an aqueous phase of linear alkylbenzene sulfonate and a dispersed phase of hydrogenated castor oil are in the context of a critical shear rate flow model is undertaken [15].

References

1. Macosko, C.W., *Rheology : principles, measurements, and applications*. 1994, New York: New York : Wiley-VCH.

2. Callaghan, P.T., *Rheo-NMR: nuclear magnetic resonance and the rheology of complex fluids.* Reports on Progress in Physics, 1999. **62**(4): p. 599-670.

3. Chiara, F.F., et al., *Role of Rheology in Achieving Successful Concrete Performance.* Concrete International, 2017. **39**(6): p. 43.

4. Jarny, S., et al., *Rheological behavior of cement pastes from MRI velocimetry.* CEMENT CONCRETE RES, 2005. **35**(10): p. 1873-1881.

5. Hyun, K., et al., *A review of nonlinear oscillatory shear tests: Analysis and application of large amplitude oscillatory shear (LAOS).* Progress in Polymer Science, 2011. **36**(12): p. 1697-1753.

6. Coussot, P., *Rheometry of Pastes, Suspensions, and Granular Materials: Applications in Industry and Environment*. 2005, New York: Wiley.

7. Fukushima, E., *NUCLEAR MAGNETIC RESONANCE AS A TOOL TO STUDY FLOW.* ANNU REV FLUID MECH, 1999. **31**(1): p. 95-123.

8. Callaghan, P.T., *Principles of nuclear magnetic resonance microscopy*. 1993, Oxford: Oxford : Clarendon Press.

9. Brox, T.I., *New Methods for Studying Materials Under Shear with Nuclear Magnetic Resonance*, in *Physics*. 2016, Victoria University of Wellington.

10. Nguyen, Q.D. and D.V. Boger, *Characterization of yield stress fluids with concentric cylinder viscometers.* Rheologica acta, 1987. **26**(6): p. 508-515.

11. Barnes, H.A. and Q.D. Nguyen, *Rotating vane rheometry — a review.* Journal of Non-Newtonian Fluid Mechanics, 2001. **98**(1): p. 1-14.

12. Wassenius, H. and P.T. Callaghan, *NMR velocimetry studies of the steady-shear rheology of a concentrated hard-sphere colloidal system.* Eur. Phys. J. E, 2005. **18**(1): p. 69-84.

13. Owens, C.E., A.J. Hart, and G.H. McKinley, *Improved rheometry of yield stress fluids using bespoke fractal 3D printed vanes.* Journal of Rheology, 2020. **64**(3): p. 643-662.

14. Al-kaby, R.N., et al., *Rheo-NMR of transient and steady state shear banding under shear startup.* Journal of Rheology, 2018. **62**(5): p. 1125-1134.

15. M. Caggioni, V.T., and P. T. Spicer, *Variations of the Herschel–Bulkley exponent reflecting contributions of the viscous continuous phase to the shear rate-dependent stress of soft glassy materials.* Journal of Rheology, 2020. **64**(2): p. 413-422.

CHAPTER TWO

BASICS OF NUCLEAR MAGNETIC RESONANCE

Commonly referred to as magnetic resonance imaging (MRI) in the medical field, nuclear magnetic resonance (NMR) refers to the technique that allows for non-invasive chemical and biochemical analysis spectroscopy, material analysis (diffusion and solid state NMR) and velocimetry (rheo-NMR) [1-3]. This technique employs the magnetic properties of the atomic nuclei, specifically atomic nuclei that have non-zero magnetic moments. Thus atomic nuclei of the proton (^{1}H), fluorine (^{19}F), and isotopes of Nitrogen (^{14}N and ^{15}N) and an isotope of carbon (^{13}C) are able to be used in NMR as they have uneven atomic numbers and mass numbers resulting in a magnetic moment.

The starting point for the development of NMR was seen when the independent studies lead by E.M. Purcell [4] and F. Bloch [5], of two separate research groups succeeded in December 1945 and January 1946 observing the NMR phenomenon in solids and liquids. The pair then went onto share the Nobel Prize in Physics in 1952 for their discovery. Since then three additional Noble prizes have been awarded for the development of techniques in the field with the last being in 2003 to P.C. Lauterbur and P. Mansfield for the development of NMR imaging [6].

This chapter explores basic concepts, theories, terminology and principles involved in the NMR technique used for the projects described in this thesis. NMR is a technique that has come far since its origins in the 1940's and would have not been possible if not for those brilliant minds that contributed to its development.

Spin and Larmor Frequency

An atomic nucleus rotates about its axis at a quantifiable angular momentum, this can more simply be referred to as the spin of a nucleus. Since atomic nuclei are also positively charged, when rotating about their own axes, they behave like tiny electro magnets bearing a magnetic dipole moment. The magnetic dipole moment, μ, of an atomic nucleus is proportional to its angular momentum, L, the gyromagnetic ratio, γ, being the constant of proportionality:

$$\gamma = \frac{\mu}{L} \qquad \text{Eqn. 1}$$

The gyromagnetic ratio is a fixed quantity for a particular atomic nucleus ($\gamma = 2.75 \times 10^8 \frac{\text{rad}}{\text{s.T}}$ for protons).

When placed in an external magnetic field, B_o, these small electro magnets, atomic nuclei, begin to precess with an angular frequency governed by the strength of the external magnetic field and the magnetic dipole moment for the specific nuclei. The frequency at which precession occurs at is called the Larmor frequency, ω_o, shown in Eqn. 2 in units of rad/s:

$$\omega_o = \gamma B_o \qquad \text{Eqn. 2}$$

The α- spin state, also known as the spin up state, being the more preferred state, is a low energy spin state where the spins align parallel along the static magnetic field. β spin state, also known as spin down state, is a higher energy state where the spins align anti-parallel to the static magnetic field. The energy gap between the two spin states can be quantified by Plank's constant, $\hbar$, and the Larmor frequency.

A spin also bears a spin quantum number, I, which is a vector in that it has a magnitude and a direction. The magnitude is a fixed /definitive value for the nucleus in its ground state and may range through zero, half integers or integers (for a ^{1}H proton the spin magnitude of I= ½).

The spin quantum number will also possess a direction denoted by +/- when the nucleus is placed in an external magnetic field. Thus for a ^{1}H proton the magnetic dipole moment of the proton nuclei will spilt by aligning parallel or anti-parallel along the static magnetic field thus creating an I=+/- ½. This splitting is called the *Zeeman effect* where the total number of possible spin states = 2I+1 with the quantized energy differences between each state being ΔE [1] [7] [2]: This is basically the energy required for a spin up state to transition to the spin down state in a process called *spin flip*.

$$\Delta E = \hbar\omega_o = \hbar\gamma B_o \qquad \text{Eqn. 3}$$

Figure 1: The energy levels due to the Zeeman effect.

It must be noted that not one, but an ensemble of spins are present and distributed within the mentioned discrete energy states. The ratio between the spins population in the spin up state vs. the spin down state under thermal equilibrium can be determined by the Boltzmann distribution [1, 2, 8]:

$$N_-/N_+ = \exp\left(-\frac{\Delta E}{k_B T}\right) = \exp(-\frac{\hbar\gamma B_o}{k_B T}) \qquad \text{Eqn. 4}$$

where N_- denotes the population of spins (spin ensemble) in the lower energy (spin up) state, N_+ denotes the population of spins in the higher energy (spin down) state, k_B is the Boltzmann constant and T the thermodynamic temperature.

Net Magnetization

In considering a real sample, the number of spins present will be in the order of 10^{23} (Avogadro's constant). Hence instead of studying single spins, it is more appropriate to consider an ensemble average of spins. The magnetization resulting from all the excess spins in the spin up state over the spin down state gives rise to the net magnetization also known as the longitudinal magnetization at thermal equilibrium, denoted by **Mo**.

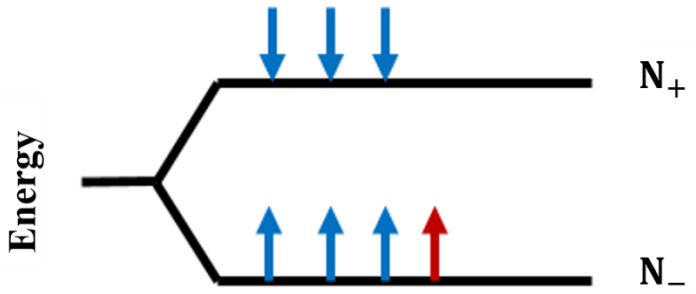

Figure 2: Spin excess is denoted by the red arrow pointing upwards that is in the lower energy state known as the spin up or α spin state. N_+ being the higher energy 'spin up' state and N_- being the low energy 'spin down' state.

It is important to realize that samples have spins that are randomly oriented unless placed in an external magnetic field in which case they bear no net magnetization since the randomly oriented magnetization vectors cancel each other out. Once placed in a magnetic field the aligning along and against the B_o field creates a net magnetization **Mo**.

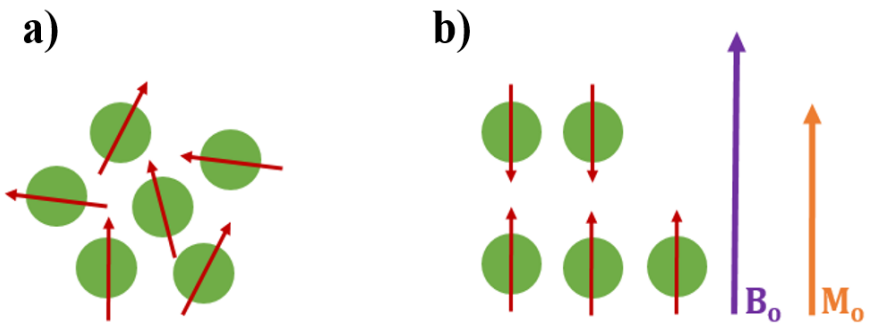

Figure 3: (a) Spins oriented randomly with a net magnetization canceling. (b) When placed in an external magnetic field, B_o, the orientation of the spins in spin up and spin down states enables for a net magnetization, M_o, to develop.

The Curie law also saw its origins using the concept of "spin", explaining how this equilibrium magnetization M_o (basically what translates to the NMR signal) is related to B_o:

$$M_o = N\frac{\gamma^2\hbar^2 I(I+1)}{3K_B T}B_o \qquad \text{Eqn. 5}$$

where N is the number of nuclei, $\hbar$, Plank's constant, K_B, Boltzmann constant and, I, the nuclear spin quantum number [2].

Excitation, Resonant Frequency and Relaxation

Excitation

The net magnetization, M_o, aligned along the z axis (with the B_o field) at thermal equilibrium can be manipulated as desired by applying yet another external magnetic field. The manipulation of the Mo is required as the effects of the B_o field dominate in the z-axis making the signal (M_o magnetization) undetectable. Perturbations of M_o from the longitudinal axis are hence referred to

as *excitations*. These excitations are created by applying an oscillating magnetic field, B_1, that is perpendicular to the B_o filed. The oscillating B_1 field uses radio frequency (RF) waves generated by an RF coil. The B_1 field with time can then be described by Eqn. 6 [1]:

$$B_1(t) = B_1 \cos(\omega_1 t)\, i - B_1 \sin(\omega_1 t)\, j \qquad \text{Eqn. 6}$$

where ω_1 is the frequency of the RF with B_1, the magnetic fiel created by the RF, i and j are unit vectors along x and y-axes. The frequency,ω_1, of the transverse field, is typically made to match the Larmor frequency of the sample to be detectable. The degree to which the magnetization is tipped can be controlled by the duration the B_1 field is applied for. It must be noted that maximum signal is observed when the magnetization vector is tipped 90^o from the z-axis on to the transverse plane. When an RF pulse excites spins what basically happens is an energy absorbance by the spins in the spin up state that then flip to the spin down state. When the magnetization is tipped 90^o from the z-axis, an equal number of spins in the spin up and spin down states will exist.

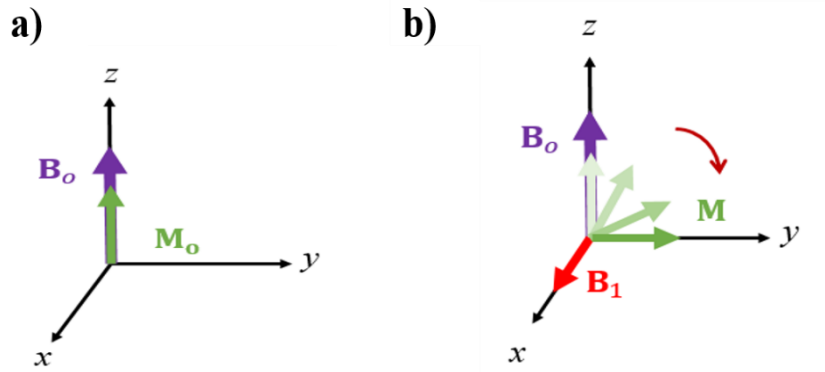

Figure 4: Effect of B_1 field on the magnetization vector. (a) Net magnetization at thermal equilibrium. (b) Net magnetization tipped $90^o$from the longitudinal axis onto the y-axis by applying a transverse B_1 field of appropriate strength, in the x-axis. The direction the magnetization orients is determined by the right hand rule.

When the magnetization is in the transverse plane, the spins keep precessing about B_o which in turn induces an oscillating current in the receiver coil, typically which is the same RF coil used for excitation. Due to in-homogeneities in the field this signal decays and is called the Free Induction Decay (FID). The amplitude of which is proportional to the magnetization and also depends on the *phase angle*.

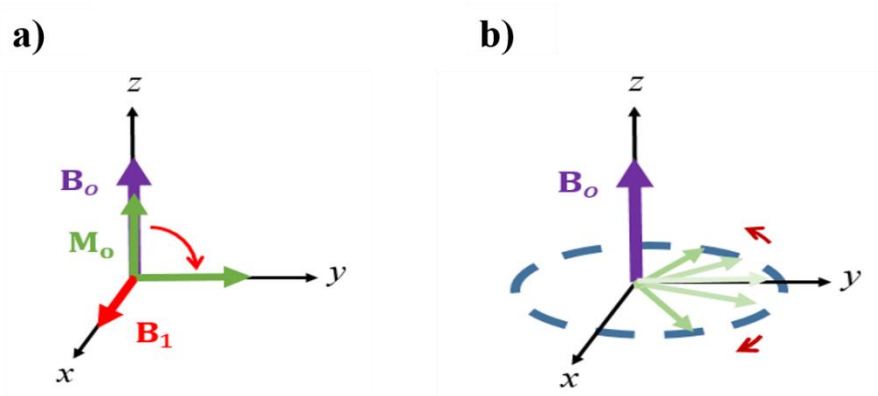

Figure 5: Visualization of dephasing of the magnetization.

All equations discussed thus far are based on a laboratory frame. The lab frame is as if being an outsider watching a biker throw a ball up and catch it while riding his/her bike. The observer sees the ball with a projectile motion. It is important to consider the rotating frame too if one is to simplify the equations. The rotating frame is as when the biker himself observes the ball go up and down in a linear motion. Projected onto NMR, the rotating frame gives the perspective of the oscillating B_1 field.

Resonant Frequency Field

It was previously mentioned that ω_1, is made to equal $\omega_o = \gamma B_o$ and this is said to be on-resonance (the static B_o field and oscillating B_1 field are not the same/not equal). The difference

between the two frequencies can be detected and is called the offset frequency, $\Delta\omega = \omega_o\text{-}\omega_1$. This can be used to find the difference between the longitudinal magnetic field and the transverse magnetic field by the RF coil,

$$\Delta B = B_o\text{-}B_1 = B_o\text{-}(\frac{\omega_1}{\gamma}) \qquad \text{Eqn. 7}$$

In the event that $\omega_1 = \omega_o$ there will be no net effect from the B_o field, and the magnetization in the transverse plane will be purely due to the magnetization by the spins. However if $\omega_1 < \omega_o$ the net magnetization will not tip all the way down to the desired tip angle due to the presence of an external magnetic field.

In the event that no offset frequency is present ($\Delta\omega = 0, \omega_o = \omega_1$), the time evolution of the net magnetization in the transverse plane, with a vantage point in the laboratory frame, can be depicted as in Eqn. 8.a, 8.b and 8.c [1]:

$$M_x = M_{o(t=0)} \sin(\omega_o t) \sin(\omega_1 t) \qquad \text{Eqn. 8.a}$$

$$M_y = M_{o(t=0)} \cos(\omega_o t) \sin(\omega_1 t) \qquad \text{Eqn. 8.b}$$

$$M_z = M_{o(t=0)} \cos(\omega_1 t) \qquad \text{Eqn. 8.c}$$

Relaxation

The net magnetization decays due to T_1 and T_2 relaxations.

T_1 Relaxation: This is also known as spin-lattice relaxation or longitudinal relaxation. Once a 90° pulse is applied, the longitudinal magnetization disappears with the absorbance of energy by lower level spins that equalizes spins in both spin-up and spin-down energy states [1]. In turn the magnetization orients in the transverse plane. However once the RF pulse is removed, an energy exchange between spins also between the surroundings (thermal reservoir) occurs

taking the magnetization back to thermal equilibrium. This results in the re-growth of the magnetization along the longitudinal direction which is termed T_1 relaxation time.
The longitudinal magnetization vector with time can then be represented by Eqn. 9.

$$M_z(t) = M_z(0) + M_o(1\text{-}e^{(-\frac{t}{T_1})}) \qquad \text{Eqn. 9}$$

T_2 Relaxation: Initially after a 90^opulse, the spins are all in coherence but after the pulse is removed, with time, begin to dephase, as shown in figure 5, leaving the transverse magnetization to decay. This dephasing is a result of spins experiencing the magnetic fields of their neighboring spins when in the transverse plane and also due to B_o field in-homogeneities. This is why the FID is decays. The technical terminology for this decay is T_2^* and is governed purely by the loss of phase coherence of spins.
T_2^* is the time taken for both a loss in phase coherence due to filed inhomogeneities also an exchange of energy between spins. The energy exchange between the spins is basically the same that happens during longitudinal relaxation that are seen to be irreversible and cause the decay of the transverse magnetization. Meanwhile, T_2, just refers to the loss of phase coherence due to energy exchange between spins.

To measure T_2 time Carr-Purcell-Meiboom-Gill (CPMG) pulse sequence is used (figure 7). Here an initial 90^o RF pulse is followed by a succession of 180^o pulses. The 90^o pulse is used to tip the magnetization to the transverse plane, a time τ is allowed to pass during which time spins will begin to dephase. A 180^o pulse is then applied that flips the direction of dephasing, in turn causing the spins to rephase back to coherence at a time τ after the 180^o pulse was applied at which point the signal called the echo is collected (figure 6 below shows a visualization of

how the refocusing of the dephased spins occur). Multiple 180^o pulses are applied to the sample with time 2τ apart and a single point at the center of each resulting echo is taken and fit to the equation [1]:

$$M_{x,y}(t) = M_{x,y}(0)e^{-t/T_2} \qquad \text{Eqn. 10}$$

where the $M_{x,y}(t)$ is the net transverse magnetization with time, $M_{x,y}(0)$ is the initial transverse magnetization when phase coherence was present and T_2 is the spin-spin relaxation time.

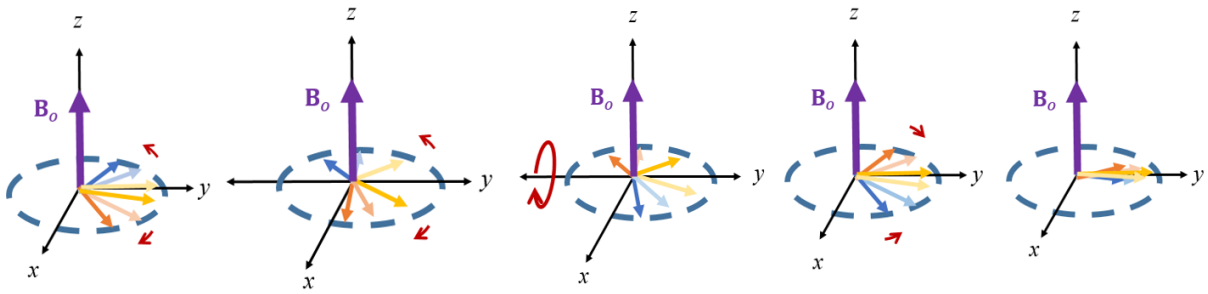

Figure 6: Visualization of the dephasing of the spins in the transverse plane followed by the flip of spins by a 180^o pulse in the transverse plane itself using a refocusing 180^o RF pulse and finally the spins refocusing to give maximum signal once again, impacted only by T_2 decay over 2τ.

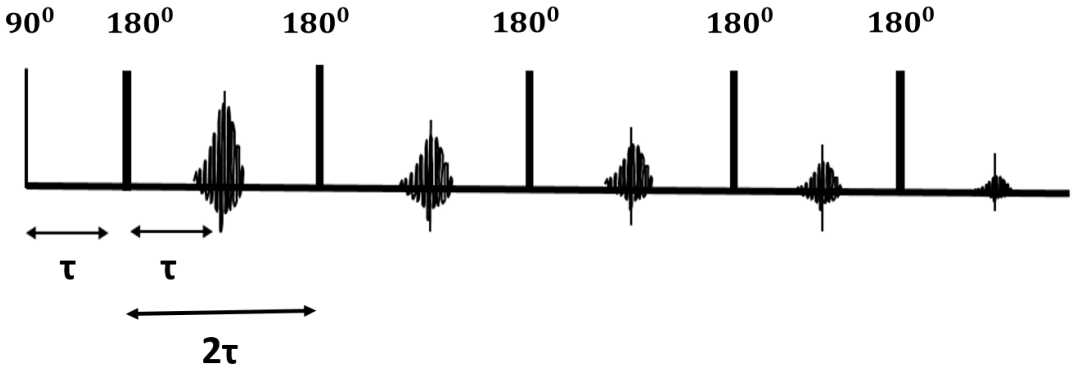

Figure 7: The CPMG pulse illustrated.

A Molecular Approach to Relaxation: $T_{2(solid)} < T_{2(liquid)}$ as liquids show rapid molecular tumbling, a process that describes the rate at which molecules move. With a higher tumbling rate the inter-nuclear dipolar interactions are averaged to zero. For solids, the motion of nuclei is restricted (the tumbling rate is slow) which facilitates the exchange of energy between spins via dipole coupling making $T_{2(solid)}$ time faster/shorter.

It is noteworthy that with the increase in molecular weight the tumbling slows, hence paving a pathway to more dipole interactions and a faster T_2 decay for large molecules. Note the correlation time τ_c is the rate at which tumbling occurs: $\tau_c = 1/t_{tumbling}$.

Spectral Density Functions: While the correlation function is a function of time, its Fourier transform gives a frequency domain function called the spectral density ($J_{(\omega)}$). This function basically describes the system's energy fluctuations based off of the system's molecular motions hence describing the magnetic field fluctuations that molecules experience (system energy based on time and frequencies of the molecular precessions) [1, 9].

For instance, if a low viscosity fluid/ liquid is considered, a broader range of molecular rotation times will exist owing to the higher random thermal effects of fluid molecules (compared to a more ordered system like a solid). The Fourier transform of this distribution will hence result in the entire spectrum of frequencies, $J_{(\omega)}$, covering the frequencies belonging to the broad range of random molecular rotation times (Figure 8).

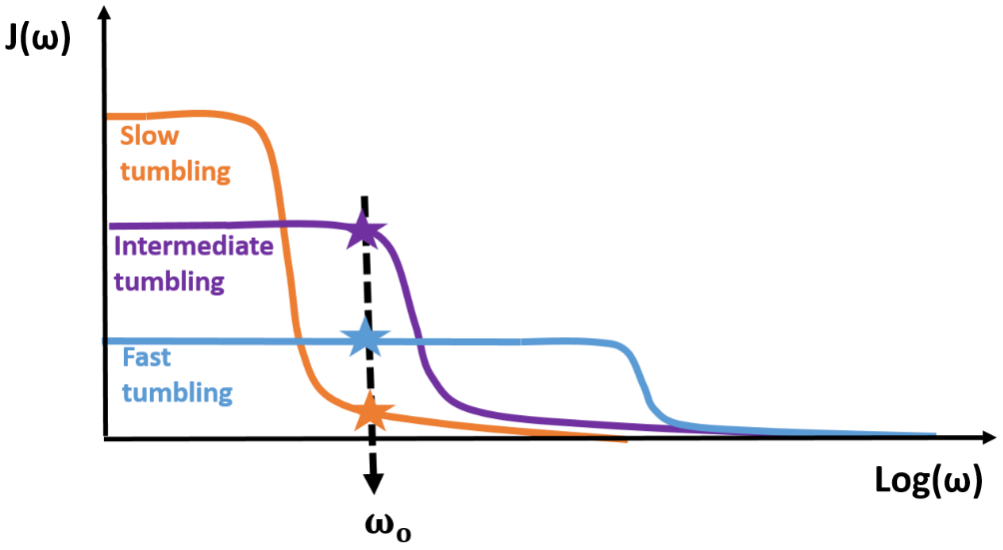

Figure 8: Spectral density function for slow, intermediate and fast motional regimes showing the distribution of the molecular tumbling rates ($\omega = 1/\tau_c$).

The spectral density, $J_{(\omega)}$, basically relates information on the probability of a particle to move at a certain frequency/range of frequencies and ties in information on dipole interactions molecules can make while showing these frequencies. Figure 8 explains how $J_{(\omega)}$ changes for fast tumbling, intermediate tumbling and slow tumbling materials assuming the total number of spins in the system is constant. In the figure, materials like Newtonian liquids and other low viscosity fluids that have faster tumbling molecules (short correlation times) are shown to achieve a wide spectrum of tumbling rates/frequencies. For T_1 relaxation to occur the rotational tumbling must be on resonance, if for example we say that this happens at the schematically represented 'ω_o' in figure 8, the spins tumbling at ω_o (blue star) will relax. If the fluid is now made thicker to achieve an intermediate viscosity or the previous liquid's temperature is decreased, less thermal motions owning to a decrease in the system's kinetic energy will be seen.

Meaning the spectrum of tumbling rates is narrower than before, but since we assume that the total spins in the system is constant, the proportion of spins tumbling at frequency ω_o becomes higher (purple star). Since more spins are rotating at ω_o, T_1 relaxation will be faster. However if we look at a slow tumbling material (long correlation times), without changing the total number of spins or by further decreasing the temperature of the initial liquid, the kinetic energy in the system is drawn closer to zero than the previous two cases resulting in the tumbling rate distribution to fall well below ω_o. Hence only a very small amount of molecules will end up rotating with a frequency, ω_o (orange star), taking a very long time to show T_1 relaxation (based on a macro scale).

T_1 and T_2 relaxations further can be related to the spectral density functions as shown in Eqn 11.a and 11.b:

$$\frac{1}{T_1} = \left(\frac{\mu_o}{4\pi}\right)^2 \gamma^4 \hbar^2 \frac{3}{2} I(I+1)\left[J^{(1)}(\omega_o) + J^{(2)}(2\omega_o)\right] \qquad \text{Eqn. 11.a}$$

$$\frac{1}{T_2} = \left(\frac{\mu_o}{4\pi}\right)^2 \gamma^4 \hbar^2 \frac{3}{2} I(I+1)\left[\frac{1}{4}J^{(0)}(0) + \frac{5}{2}J^{(1)}(\omega_o) + \frac{1}{4}J^{(2)}(2\omega_o)\right] \qquad \text{Eqn. 11.b}$$

Here we see that T_1 depends mainly on the two density functions $J^{(1)}(\omega_o)$ and $J^{(2)}(2\omega_o)$, where $J^{(1)}(\omega_o)$, the spectral density function that suggests the energy change resulting from a single spin flip , the spins bearing a tumbling rate equal to the Larmor frequency ω_o, while $J^{(2)}(2\omega_o)$, the spectral density function that suggests the energy change resulting from both spins of $2\omega_o$ frequency that flip to a new energy state. The exposure of T_2 to an additional spectral density function that is independent of any frequency, that is based on the single spin flips that occur

with no net energy state changes, $J^{(0)}(0)$, in addition to the Larmor frequency dependent $J^{(1)}(\omega_o)$ and $J^{(2)}(2\omega_o)$ compared to T_1, ensures that T_2 is always less than or equal to T_1. In order to inspect the T_1 and T_2 relaxation behaviors tied to molecular motions with respect to a fixed frequency ω_o, figure 9 can be considered. For a simple liquid with short correlation time ,τ_c, short lived dipolar coupling and a spectral density function covering a broad range of frequencies (not only ω_o),we can say that $\tau_c^{-1} \gg \omega_o$. As a result, $T_1 = T_2$ and both will be long. In the case of complex fluids or soft-condensed matter, both slow and fast motions are present, hence increasing the correlation time to a maximum of $\tau_c = 1/\omega_o$, at this point there is roughly only one spectral density function that will be at the ω_o frequency. Solids show very little to no molecular motion, hence possess long correlation times, $\tau_c^{-1} \ll \omega_o$, making $T_2 < T_1$.

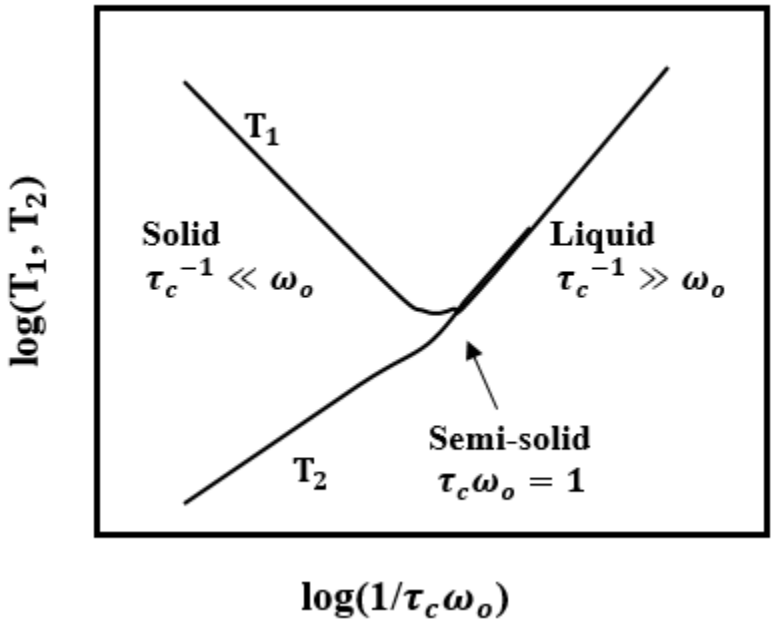

Figure 9: T_1 and T_2 relaxation as a function of the correlation time with a fixed ω_o.

Signal Detection, Phase Correction and Signal Averaging

Signal Detection

The precession of the non-equilibrium magnetization, M_o, is captured as a signal in NMR. An RF coil with its detection axis perpendicular to the z axis will have an electric current induced within it as the mentioned precessing **Mo** cuts through the coil. This is analogous to a moving permanent magnet within a coil inducing an electric current in that coil. Using a process known as heterodyning, the voltage produced post 90° RF pulse is measured against a selected reference signal and the difference of signal oscillates with both a phase and amplitude. Since the magnetization is what gives rise to this signal the projection of the net magnetization in the transverse plane can be shown as in Eqn. 12.a and 12.b. For clarity, we will assume the transverse magnetization starts out along the x-axis, with a maximum x component magnetization and a zero y component magnetization at t=0.

$$M_x = M_o(t = 0)\cos(\Delta\omega t) \qquad \text{Eqn. 12.a}$$

$$M_y = M_o(t = 0)\sin(\Delta\omega t) \qquad \text{Eqn. 12.b}$$

The components of the signal detected, S_x and S_y, being proportional to the magnetization components then become:

$$S_x(t) = S_o\cos(\Delta\omega t) \qquad \text{Eqn. 13.a}$$

$$S_y(t) = S_o\sin(\Delta\omega t) \qquad \text{Eqn. 13.b}$$

The heterodyne signal at the offset, $\Delta\omega$, which is a complex signal with a real part, S_x, and an imaginary part, S_y, is:

$$S(t) = S_x(t) + iS_y(t) = S_o\exp(i\Delta\omega t) \qquad \text{Eqn. 14}$$

This signal also undergoes effects of relaxation to form a decaying oscillation called the free induction decay (FID). Bringing us to Eqn. 15 [1] [7]:

$$S(t) = S_o \exp(i\Delta\omega t) \exp\left(-\frac{t}{T_2}\right) \quad \text{Eqn. 15}$$

The FID in the time domain is then Fourier transformed to the Frequency domain to obtain a spectrum. The real component in the time domain gets transformed to an absorption mode line, called the Lorentzian, whose frequency is at the offset frequency ($\Delta\omega/2\pi$) and full-width-half maximum (FWHM) is $1/\pi T_2$. The imaginary component in the time domain takes the form of a dispersion mode Lorentzian spectrum (shown in figure 10). In general, the mathematical formula of the Fourier transform of the signal will be as in Eqn. 16.

$$F\{S(t)\} = S(\omega) = \frac{1}{2\pi}\int_{-\infty}^{\infty} S(t)e^{-i\omega t}dt \quad \text{Eqn. 16}$$

In introducing Eqn. 12, it was assumed that once the magnetization was tipped to the transverse plane, the initial transverse magnetization was perfectly oriented along the x-axis. While this zero phase $\emptyset = 0$ start is the desired outcome, it is difficult to control the precise phase in the transverse plane that the RF pulse will tip the magnetization to. Instead the transverse magnetization may start with a phase shift between 0-360° from the positive x-axis, hence changing the expected absorption and dispersion spectra to be varied degrees of mixtures of the two in the frequency domain [10]. Mathematically when this phase shift, $\emptyset$, is included, the complex signal of Eqn. 15 becomes:

$$S(t) = S_o \exp(i\emptyset) \exp(i\Delta\omega t) \exp\left(-\frac{t}{T_2}\right) \quad \text{Eqn. 17}$$

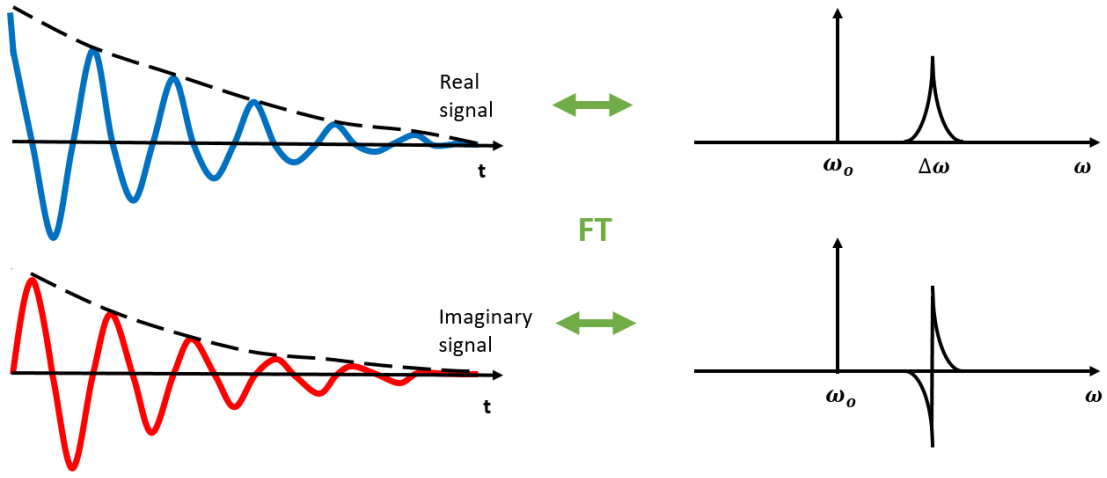

Figure 10: The NMR signal post excitation assuming the transverse magnetization starts along the positive x axis at time t=0. The respective Fourier transforms of the real and imaginary signals depicting an absorption spectrum and dispersion spectrum in the frequency domain.

Phase Correction/Phase Cycling

Before delving into the correction, a look into what the phase error is caused by is helpful. NMR imaging utilizes a repeated of RF pulses, both 90° and 180° pulses. These standard pulses also stimulate unwanted responses from a subset of spins that experience incorrect tip angles (unwanted coherences are created) [10, 11]. When the pulse sequences are repeated and averaged out in hope of a high signal to noise ratio, these unwanted coherences create accumulated errors. While spoiler/crusher gradients to dephase and spread out unwanted frequencies can be used, these gradients may also contribute in creating additional unwanted coherences or may not entirely rid of the unwanted coherences. The use of phase cycling enables to cancel unwanted coherent noise. Here, the phases of the relative pulses of each pulse sequence repetition is varied

so that the coherence is flipped to a different axis each time while the subset of spins receiving inexact excitations is cancelled out [12].

Signal Averaging

The signal thus acquired is also influenced by various forms of noise such as and not limited to: electrical noise, nonlinearity from signal amplifiers, thermal noise from RF coils and so on. '*Signal-to-noise ratio'* (SNR) expresses the relationship between the NMR signal and the contributing noise acquired. A higher SNR is desirable with the signal being higher than the noise [13]. While the SNR can be manipulated by changing the field of view (FOV), slice thickness, receiver bandwidth, magnetic field strength, image matrix etc., the most commonly used method is changing the number of acquisitions. This frequently used method in increasing the SNR acquires the same signal using multiple successive scans and adds them together. The reproducible NMR signal will add coherently, while the background noise adds randomly, leaving a signal that improves by the number of times the experiment was repeated (N). However since the noise also adds, with a scaling factor of the square root of N, the SNR ends up being proportional to the square root of N [1].

$$\mathrm{SNR} \propto \frac{\mathrm{N}}{\sqrt{\mathrm{N}}} = \mathrm{N}^{1/2} \qquad \text{Eqn. 18}$$

This method, while significantly enhancing SNR compared to other methods, comes at the cost of the total imaging time. It is also important to note that the SNR is also proportional to the product of the voxel volume and the square root of the total sampling time which is important in setting up FOV, image matrix and other SNR scaling methods mentioned before [14].

Gradients and Selective/Non-Selective Excitation

Gradients

In the presence of a longitudinal (z-direction) homogeneous magnetic field, all spins precess about the z-axis with the same frequency. This frequency called Larmor frequency, is a function of the external magnetic field strength (B_o) and the gyromagnetic ratio (γ). This same precession frequency is maintained even once the magnetization is tipped to the transverse plane throughout the entire region of the sample that is being excited.

However when a magnetic field 'gradient' is applied to the existing external field, B_o, an inhomogeneous field is created. This happens by linearly varying the magnetic field strength along the direction the gradient magnetization was applied at (x, y or z). Under a large magnetic field, where concomitant fields are negligible, the gradient can be described as:

$$G = \nabla B_o = \nabla B_z \qquad \text{Eqn. 19}$$

With the field strength dependent on position vector **r** is:

$$B_{tot} \sim B_o + r \cdot G \qquad \text{Eqn. 20}$$

As an example, if a gradient field in the x direction, G_x, is applied along with the external magnetic field B_{tot}will be:

$$G_x = \frac{\partial B_o}{\partial x} \qquad \text{Eqn. 21}$$

$$B_{tot} = B_o + x \cdot G_x \qquad \text{Eqn. 22}$$

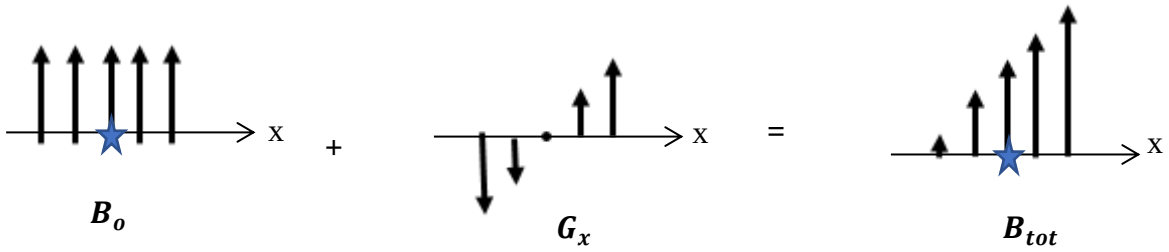

Figure 11: Adding a gradient along the x-axis to the main B_o magnetic field linearly varies the local magnetic field, B_{tot}.The star symbol depicts the isocenter of the B_o field.

While the gradients are added to the $B_o$field changing the local field strengths, at the isocenter (star depicted in figure 11) or the geometric center of the B_o field, the field strength remains as B_o, unchanged. Three parameters are adopted to measure the gradient performance: 1) the maximum gradient strength, 2) the rise time (time taken for the gradient to reach the allocated gradient strength) and 3) the slew rate (ratio of maximum gradient and rise time) [13].

Local Larmor Frequency: Since the magnetic field strength is different at different positions, this causes the Larmor frequency experienced by spins at different positions also to be different based on the location they are found at within the magnetic field gradient. The Larmor precession frequency (units of rads^{-1}) at each position **r** can then be described by Eqn. 22:

$$\omega_o(r) = \gamma B_o + r \cdot G \qquad \text{Eqn. 22}$$

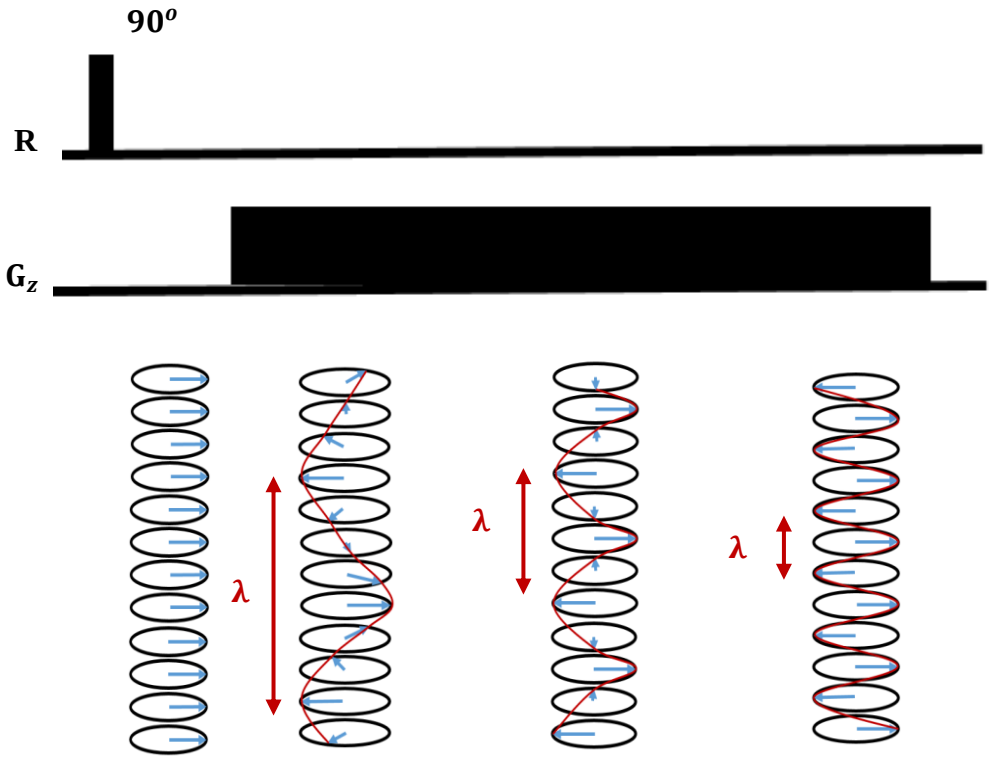

Figure 12: Phase evolution of spins along the z-axis when a gradient field is applied along the z-direction. Immediately after the 90ºRF pulse the spins are all in coherence, but when the gradient is applied, precession along the z-axis occurs at different frequencies, developing a helical variation in spin phase that gradually winds tighter as the time the gradient is applied increases.

Phase Evolution Due to Field Gradients

When the magnetization vector is tipped into the transverse plane, the angle it rotates due to precession is referred to as the phase angle. Immediately on being tipped to the transverse plane the magnetization vectors of all the spins are in phase. If no gradient is present, all spins will precess at the same Larmor frequency and under go T_2 relaxation. However on the introduction of a gradient, since spins attain position dependent local Larmor frequencies they

will precess at different frequencies. Hence the phase angle covered by spins belonging at position **r** will be different from the phase angle traversed by the spins at a location **r**+Δ**r**.
If a gradient field is applied along the z-axis as shown in figure 12, the precession frequencies being different along one line of spins in the z-axis causes a helical variation along the z-axis with a wavelength, λ. This helix winds tighter and tighter the longer the gradient is applied for with its wavelength getting shorter with time. The wavelength of the helix is inversely proportional to the gradient strength and time the gradient is applied for and can be described as:

$$\lambda = \frac{2\pi}{\gamma G t} \qquad \text{Eqn. 23}$$

The phase change between each set of spins along the z-axis is $\exp(ikz)$, where *k* is the *k*-space which is the reciprocal wave vector of λ (with units of rad/m):

$$k = \frac{2\pi}{\lambda} = \gamma G t \qquad \text{Eqn. 24}$$

Selective Excitation

Selective excitation requires both a gradient and a RF pulse applied simultaneously in order to excite spins within a desired region of the sample only. The principle behind it is that the gradient creates varying frequencies with position such that the spin precession frequency at one position is different from the precession frequency at another. When a shaped RF pulse contains only a specified frequency/range of frequencies (bandwidth of frequencies) only the spins bearing local Larmor frequencies that match the bandwidth frequencies contained in the RF pulse get excited.

Non-Selective vs. Selective Pulses

It is important to note that the bandwidth of frequencies that an RF pulse contains is primarily determined by the pulse duration. This is because time and frequency are inversely related by means of the Fourier transforms. The RF pulse bandwidth and RF pulse amplitude multiplied by its duration in the time domain are therefore related. If a broad bandwidth is desired the pulse duration must be made sufficiently short with a high time domain amplitude and vise-versa for a narrow bandwidth [1] [7].

Non selective (broadband) pulses also known as hard pulses in the time domain are narrow hat functions but are capable of exciting a large range of frequencies in the frequency domain as they transform into a sinc function with a broad bandwidth in the frequency domain (figure 13 (a)). As a result, going back to the relationship between bandwidth and time domain amplitude, it can be understood that a larger B_1 field strength is required for this process to achieve a higher amplitude for the narrow hat function in the time domain.

Selective (narrowband) pulses, also known as soft pulses, are often broad sinc functions in the time domain that are transformed to narrow hat functions in the frequency domain enabling the excitation of a narrow range of frequencies only (Figure 13 (b)). This pulse does not require a large B_1 field magnitude as the RF amplitude in the time domain is lower.

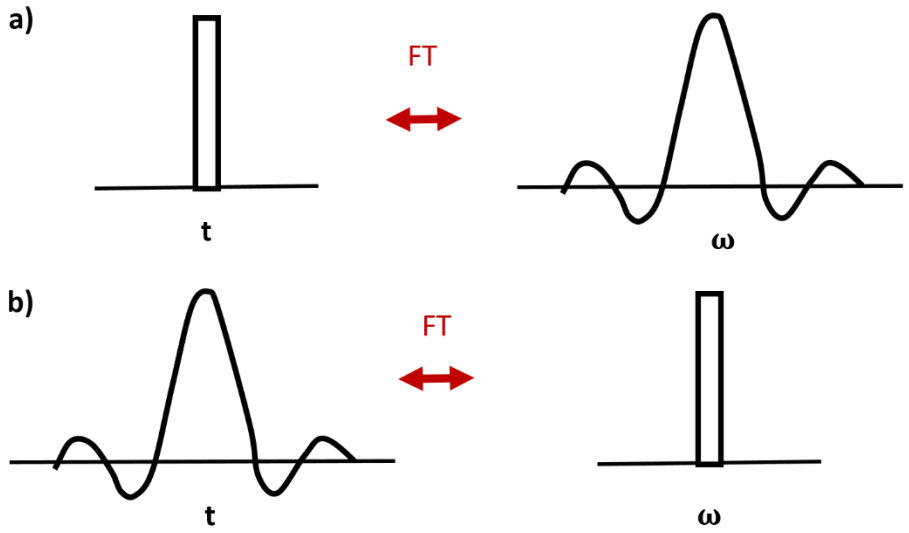

Figure 13: (a) A hard pulse in the time domain that results in a sinc function with a broad bandwidth of frequencies in the frequency domain. (b) A soft pulse in the time domain that results in a hat function with a narrow bandwidth of frequencies in the frequency domain.

Types of Echos

Spin Echo (SE)

Following a 90^o RF pulse spins dephase under T_2 relaxation effects, decreasing the transverse magnetization. If we then apply a 180^o RF refocusing pulse after a time τ, the direction of spin precession in the transverse plane can be reversed allowing the magnetization to refocus after a time 2τ creating an echo. This signal resulting from the refocusing of the transverse magnetization, by applying the 180° RF pulse either just once (as shown in figure 14) or multiple times, is referred to as a spin echo. SE sees an advantage in getting rid of artifacts arising from off resonance effects (magnetic field susceptibilities and field inhomogeneity) as the

180° RF pulse also seeks to refocus these off resonance effects unlike the GRE (discussed below) [14].

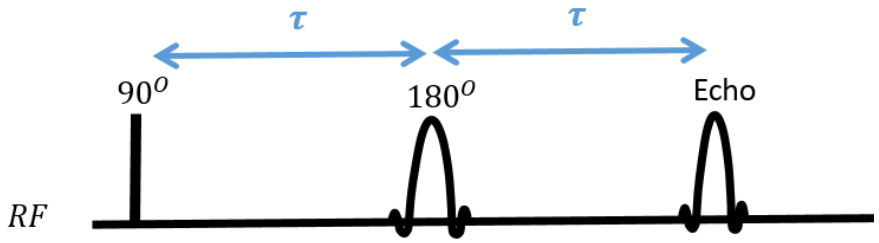

Figure 14: Schematic of a spin echo. A 90° RF pulse followed by a 180^{o} RF pulse after time τ forms a spin echo with the echo center forming after τ time.

Gradient Echo (GRE)

This class of pulse sequence is widely used for 3D volume imaging and in instances where fast acquisition speeds are required. Particularly seen used in cardio/vascular imaging or medical imaging that requires breath-holding, this type of sequence excludes the 180° refocusing RF pulse seen in the spin echo sequence. The echo condition is achieved by a gradient reversal on the frequency encoded axis [14]. As shown in Figure 15 this type of echo occurs when the effect of all gradients in the read direction (frequency encoding axis) is zero (this is when the echo condition: $\int_0^t g^*(t')dt' = 0$ occurs). The gradient echo forms at a point in time when k =0 [1].

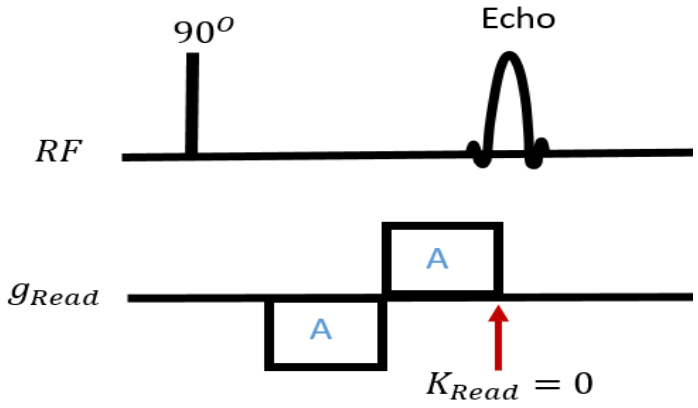

Figure 15: Schematic of a gradient echo. Read gradient of area A being applied after a 90° RF pulse preceded by a gradient of equal area, A, applied in the opposite direction will cause the echo center to line with *k*-space = 0. Transverse magnetization is not manipulated by 180°RF pulses.

Effective Gradient ($g^*_{(t)}$)

An effective gradient can be simply put as the gradient that the spins experience. It takes into account not only the directional changes of the gradient strength, but also the net gradient experienced when RF pulses are used. If only gradient echos are employed: $g^*(t) = g(t)$. In this event the echo condition will be met whenever the area under the effective gradients is zero, hence satisfying $\int_0^t g^*(t')dt' = 0$ (discussed next section).

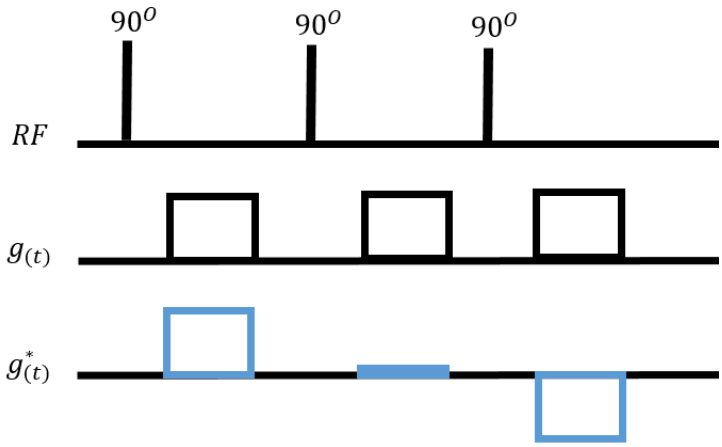

Figure 16: Schematic of how the effective gradient, $\mathbf{g}^*(t)$, varies with RF pulses applied.

Translational Motion and the Effects of Time Varying Gradients

In imaging, it is assumed that spins don't move hence that the local Larmor frequencies do not change. Most samples dealt with in the lab show some form of motion of spins, if not bulk motion then self-diffusion. When these spins, bearing local Larmor frequencies of their own, diffuse or move by convection, they carry their phases obtained from the initial location's local Larmor frequencies to a new position that bears a different local Larmor frequency. The echo affected by this process will depict a distribution of residual phase shifts, $\emptyset$.

This phase shift that a spin j in a spin sub ensemble experiences due to effective gradients g^* can be quantified as:

$$\emptyset_j(t) = \gamma \int_0^t g^*(t') \cdot r_j(t')\, dt' \qquad \text{Eqn. 25}$$

The transverse magnetization, $M_+(t)$, then being an ensemble average of the spins that show phase shift coupled with transverse relaxation effects:

$$M_+(t) = M_{+(0)} < \exp(i\emptyset_j) > \exp(-t/T_2) \qquad \text{Eqn. 26}$$

where $M_{+(0)}$ is the initial transverse magnetization detected when the spins are tipped to the transverse plane, $\emptyset_j$, the residual phase influencing the echo due to a spin's motion and T_2 being the relaxation time of the transverse magnetization. Since translational motion is encoded within the residual phase, $\emptyset_j$, it would be beneficial to be rid of the effects of T_2 relaxation on the echo amplitude. This can be done by assuming that relaxation is a uniform process associated with each spin rather than its spin position and to that end the concept of normalized spin echo amplitude is introduced.

The normalized spin echo amplitude, $E(t)$, is the transverse magnetization that bears phase information being normalized by the transverse magnetization without gradients applied [1].

$$E(t) = \frac{M_+(t)_{g^*(t)\neq 0}}{M_+(t)_{g^*(t)=0}} \qquad \text{Eqn. 27}$$

$E(t)$ provides information on translational motion free of relaxation effects and can be written in terms of an ensemble average of the spin contributions:

$$E(t) =< \exp(i\emptyset_j) > \qquad \text{Eqn. 28}$$

Going back to the phase shift that a spin of a spin sub ensemble experiences, shown in Eqn. 25, the path vector of the spin j $r_{j(t')}$ can be expanded using the Taylor series:

$$r_{j(t')} = r_o + \frac{dr_{j(t')}}{dt} t' + \frac{1}{2!}\frac{\partial^2 r_{j(t')}}{\partial t^2} t'^2 + \text{Higher order terms} \qquad \text{Eqn. 29}$$

r_o will be a constant that relates position information. The first derivative with respect to time can be seen as a constant velocity, v_o and the second derivative of the path vector with respect to time will be a constant acceleration a_o.

$$r_j(t') = r_o + v_o t' + \frac{a_o}{2!} t'^2 + \text{Higher order terms} \qquad \text{Eqn. 30}$$

Substituting the Taylor series definition of path vectors into Eqn. 25, the phase change of a spin can be re-written as:

$$\emptyset_j(t) = \gamma \left[r_o \int_0^t g^*(t')\, dt' + v_o \int_0^t g^*(t') \cdot t'\, dt' + \frac{1}{2} a_o \int_0^t g^*(t') \cdot t'^2\, dt' + \text{H. O. T.} \right]$$

$$= \gamma \left[r_o m_o + v_o m_1 + \frac{1}{2} a_o m_2 + \text{H. O. T.} \right] \qquad \text{Eqn. 31}$$

where $m_o = \int_0^t g^*(t')\, dt'$ is the zeroth moment that encodes for position. When an echo is formed $m_o = 0$, where one will be at the center of k-space(k=0), and hence also called the 'echo condition'. It must be understood that m_o is the area under the effective gradients, one example is when bipolar gradients of equal magnitudes are employed. On the other hand, $m_1 = \int_0^t g^*(t') \cdot t'\, dt'$, is the first moment that encodes for velocity.

If only velocity is to be measured, all other moments that encode for other parameters will have to be zero leaving the first momentum to be $m_1 = g\Delta\delta$. In order to achieve this, m_o, can be made zero by employing symmetric bipolar gradients while effects of m_2 and other higher order moments can be made negligible by employing short times scales Δ and δ. The second moment that encodes for acceleration, $m_2 = \int_0^t g^*(t') \cdot t'^2\, dt' = g\Delta\delta^2$, also requires for all other moments to be zero in order to measure the acceleration of the motion. As such, the

moments will continue with the n^{th} order moment being: $m_n = \int_0^t g^*(t') \cdot t'^n \, dt'$, however, higher order terms become increasingly noisier and are difficult to measure [2].

Bloch-Torrey Equations for Diffusion and Flow

Bloch-Torrey equations account for self-diffusion and average flow velocity by treating magnetization as a fluid. If this magnetization fluid is treated as a steady state flow a single spin's local time dependent position vector, $r_j(t)$ can be considered a position vector, r (can neglect time effects at steady state). The transport of magnetization can then be treated in an Eularian sense.

The Bloch equation for the x-axis transverse magnetization (laboratory frame) takes the form of Eqn. 32.

$$\frac{dM_x}{dt} = \gamma M_y \left(B_o - \frac{\omega}{\gamma} \right) - \frac{M_x}{T_2} \qquad \text{Eqn. 32}$$

Bloch-Torrey equations, on the other hand, explore the material derivative of the transverse magnetization which adds in an additional part to the Bloch equations. Here the conservation of magnetization (just as would be for momentum) is subject to Fick's law to relate the diffusion of spins. The transverse relaxation acting as the sink term. From this relation, the Bloch-Torrey equation for the above mentioned M_x becomes:

$$\frac{DM_x}{Dt} = \frac{dM_x}{dt} = \gamma M_y \left(B_o - \frac{\omega}{\gamma} \right) - \frac{M_x}{T_2} + \nabla \cdot D \cdot \nabla M_x - (V \cdot \nabla) M_x \qquad \text{Eqn. 33}$$

where D is the diffusion tensor, which for simplicity can be assumed to be isotropic, making it a scalar diffusion coefficient, *D*.

Coming back to the rotation frame, which is the frame NMR is concerned with most often, the Bloch-Torrey equation for the entire transverse magnetization can be considered by combining M_x and M_y ,$M_+ = M_x + iM_y$, to get Eqn. 34.

$$\frac{dM_+}{dt} = -i\gamma r \cdot g^*(t)M_+ - \frac{M_+}{T_2} + D\nabla^2 M_+ - (V \cdot \nabla)M_+ \qquad \text{Eqn. 34}$$

This transverse magnetization, M_+, will still be affected by both phase and relaxation effects as was shown in Eqn. 26. When considering the normalized echo amplitude, since the relaxation effects are nulled, M_+ will become a function of position vector, r,and time resulting in:

$$\frac{dM_+}{dt} = -i\gamma r \cdot g^*(t)M_+ + D\nabla^2 M_+ - (V \cdot \nabla)M_+ \qquad \text{Eqn. 35}$$

Taking the time derivative, neglecting the relaxation effects by assuming the final echo is normalized, $M_+(r,t)$ will be:

$$M_+(r,t) = A(t)\exp\left(-i\gamma r \int_0^t g^*(t')\,dt'\right) \qquad \text{Eqn. 36}$$

where $A(t)$ is a modulation factor. Under the echo condition($\int_0^t g^*(t')\,dt' = 0$), that is when $m_o = 0$, the modulation factor is equal to the normalized echo amplitude: $A(t) = E(t) = M_+(r,t)$ as the time-dependent exponential term reaches unity ($\exp(0) = 1$). Substituting Eqn. 36 in eqn.35, the modulation factor, $A(t)$, can be found.

$$A(t) = \exp\left(-D\gamma^2 \int_0^t \left(\int_0^{t'} g^*(t'')\,dt''\right)^2 dt'\right) \exp\left(i\gamma V \int_0^t \int_0^{t'} g^*(t'')\,dt''dt'\right)$$

Eqn. 37

Where the term $\int_0^t \left(\int_0^{t'} g^*(t'')\,dt''\right)^2 dt' = g^2\delta^2(\Delta - \frac{\delta}{3})$, while $\int_0^t \int_0^{t'} g^*(t'')\,dt''dt' = m_1 = -g\Delta\delta$.

Eqn. 37 can be used to determine the diffusion attenuation and average steady state velocity at the echo condition. However at any other time, besides the echo condition, the time dependent exponential term, $\exp(-i\gamma r \int_0^t g^*(t')\,dt')$**,** also known as the structure factor, exists and impacts the modulation factor's diffusion and average velocity results [1]. This becomes clearer on combining both Eqn. 35 and eqn. 36 to form:

$$M_+(r,t) = \exp\left(-D\gamma^2 \int_0^t \left(\int_0^{t'} g^*(t'')\,dt''\right)^2 dt'\right) \exp\left(i\gamma V \int_0^t \int_0^{t'} g^*(t'')\,dt''dt'\right) \exp(-i\gamma r \int_0^t g^*(t')\,dt') \quad \text{Eqn. 38}$$

Eqn. 38 simplifies to Eqn. 37 in the event of the echo condition being met, otherwise will influence the final signal.

Pulsed Gradient Spin Echo (PGSE) NMR and
Pulsed Gradient Stimulated Echo (PGStE) NMR

A single pulsed gradient spin echo (PGSE) sequence, schematically shown in Figure 17, consists of a 90^oRF pulse that tips spins to the transverse plane followed by a flow/phase encoding gradient, whose strength is denoted as $\boldsymbol{g}$ applied for a duration of δ. This gradient is employed to impart a phase on the spins. A refocusing 180^o RF pulse is then applied following a time τ after the initial 90^oRF pulse that reverses the precession direction of the spins. A second gradient of the same amplitude, g, and duration δ is then applied that will cancel the phase effects of the first gradient applied if no translational motion is present. In the presence of motion, however, a residual phase is imparted on the final spin echo after the second gradient

pulse. This PGSE sequence that employs spin echos, works well for samples that have long T_2 relaxation times, such as liquids and soft matter.

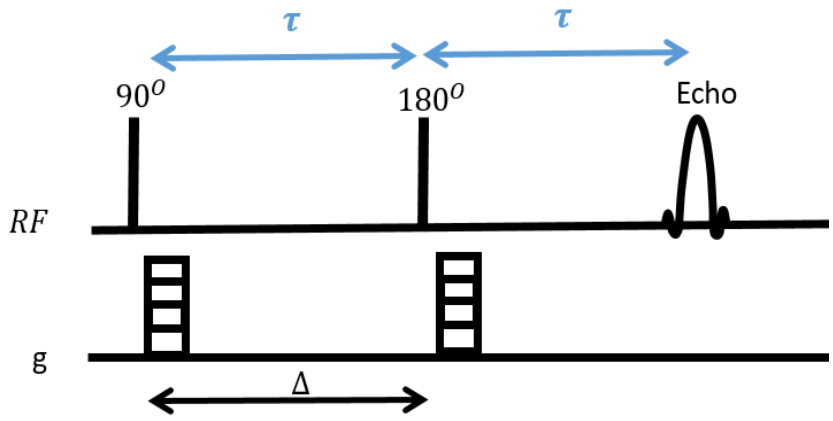

Figure 17: Schematic of a PGSE sequence using a spin echo.

A pulsed gradient stimulated echo (PGStE) sequence schematically depicted in Figure 18, is equivalent to a spin echo sequence from the perspective of motion-induced phase shifts, but is different in how the relaxation impacts the echo attenuation [1]. The PGStE sequence employs three 90^{o}RF pulses: the first tips the spins to the transverse plane; the second, applied after the first flow encoding gradient, tips it to the longitudinal plane; and a third 90^{o}RF pulse brings the spins back to the transverse plane. Hence this sequence takes advantage of the longitudinal magnetization relaxation, T_1, of a sample and short T_2 times, like solids and highly viscous fluids as this increases the time window transport can be observed over. PGStE allows observation times (Δ) as long as T_1 , as the rapid loss of phase coherence due to transverse relaxation can be avoided.

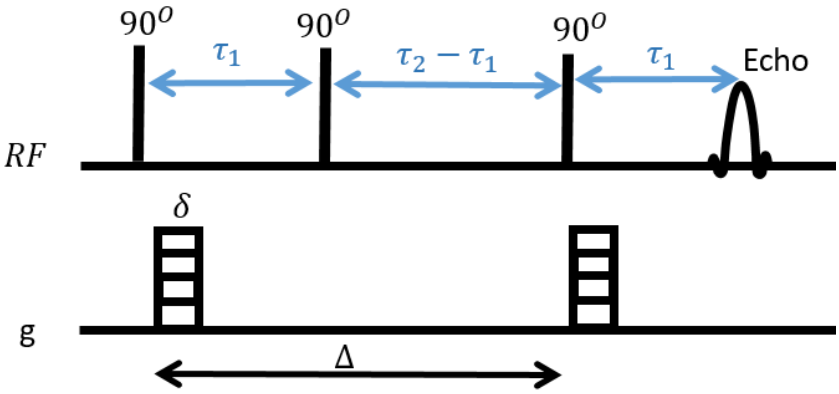

Figure 18: Schematic of a PGSE sequence using a stimulated echo commonly known as PGStE NMR.

Both PGSE and PGStE sequences will allow for the measurement of the mean square displacement if narrow gradient pulses are utilized. The observation time, Δ, determines the time taken for spins to migrate from the original position ***r***, to a postion ***r'*** after the said observation time, provided that there is spin motion. The average propagator, $\overline{P}(r|r',\Delta) = \overline{P}(R,\Delta)$, that describes the probability of displacement from position ***r*** to ***r'***, where ***R=r'-r***, during time Δ can be explained by Eqn. 39.

$$\overline{P}(R,\Delta) = \int \rho(r)\, P(r|r+R,\Delta)dr \qquad \text{Eqn. 39}$$

In other words the average propagator can be described as the product of the spin density, $\rho(r)$,at the initial position ***r*** and the conditional probability that a particle will displace by ***R*** during a time Δ and it is an ensemble average of all spins in the sample. The normalized spin echo is then shown by Eqn. 40.

$$E(q,\Delta) = \int \overline{P}(R,\Delta)\exp(i2\pi q \cdot R)\, dR \qquad \text{Eqn. 40}$$

The q seen in Eqn. 40 is the reciprocal space vector that describes the spin phase behavior given by:

$$q = \frac{\gamma \delta g}{2\pi} \qquad \text{Eqn. 41}$$

The average propagator for a normalized Gaussian distribution of displacement, such that is seen in Brownian motion, can be obtained by taking the Fourier transform of the normalized echo signal shown in Eqn. 40 will be:

$$\overline{P}(R, \Delta) = (4\pi Dt)^{-\frac{3}{2}} \exp\left(\frac{-|R|^2}{4Dt}\right) \qquad \text{Eqn. 42}$$

In the event that coherent bulk flow is also present, the propagator observed will be identical to that seen in Eqn. 42, but centered around a displacement Vt (the propagator for flow is just a delta function). Eqn. 42 can then be re-written as Eqn. 43.

$$\overline{P}(R, \Delta) = (4\pi Dt)^{-\frac{3}{2}} \exp\left(\frac{-|R-Vt|^2}{4Dt}\right) \qquad \text{Eqn. 43}$$

A graphical representation of the propagators with and without flow are shown in Figure 19.

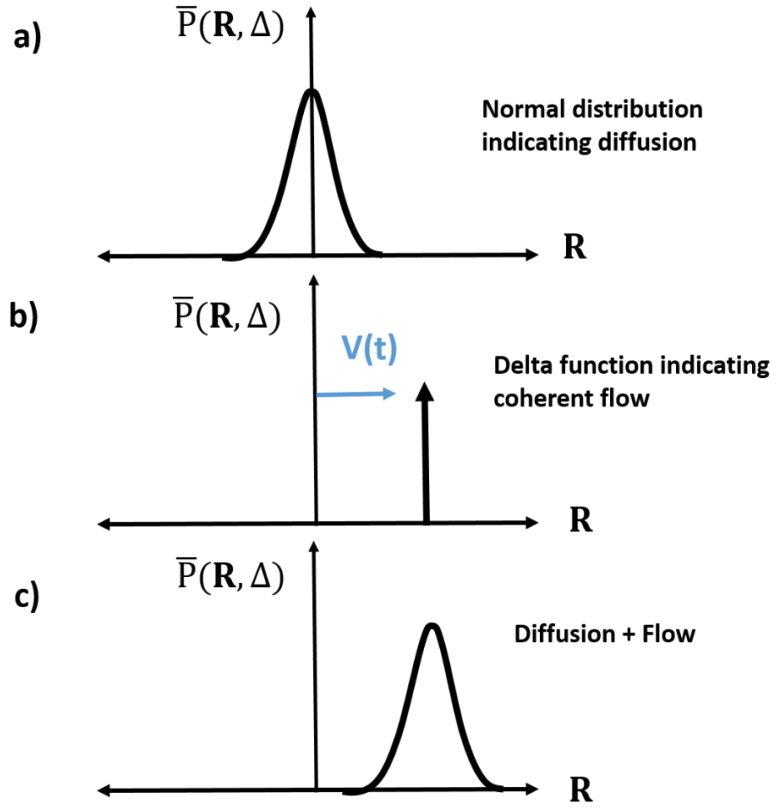

Figure 19: Schematic of propagator as a function of position vector, R. a) Propagator for diffusion. b)Propagator for flow. c) Propagator for both flow and diffusion.

Stejskal-Tanner Experiment

It was Stejskal and Tanner that introduced the propagator formalism in the limit of $\delta \rightarrow 0$. Either the PGSE or PGStE sequence can be used as the basis of the Stejskal-Tanner experiment.

The propagator for Brownian motion in one dimension is as shown in Eqn. 46 [1]:

$$\overline{P}(z,\Delta) = (4\pi Dt)^{-\frac{1}{2}} \exp\left(\frac{-|z|^2}{4Dt}\right) \qquad \text{Eqn. 44}$$

The resulting normalized echo attenuation due to diffusion shown by the well-known Stejskal-Tanner relation is:

$$E(g,\Delta) = \frac{S(g)}{S(0)} = \exp(-\gamma^2\delta^2 g^2 D\left(\Delta - \frac{\delta}{3}\right)) \qquad \text{Eqn. 45}$$

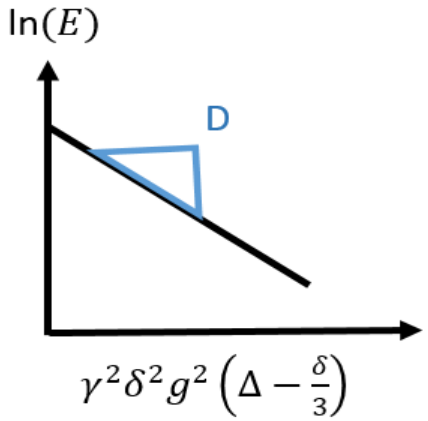

Figure 20: Stejskal-Tanner plot that can be used to find the diffusion coefficient, the slope of the plot.

which is a result of the ratio between the echo amplitude with a gradient vs. without a gradient. The $\frac{-\delta}{3}$ is a correction term added in to account the finiteness of the constant gradients being employed. Stejskal-Tanner plots show how the signal decays due to diffusion when the signal collected is plotted against $\gamma^2\delta^2 g^2\left(\Delta - \frac{\delta}{3}\right)$ as shown on Figure 20, the slope of which gives the diffusion coefficient, *D*.

When narrow gradient pulses are used, that is when $\Delta >> \delta$, the correction term, $\frac{-\delta}{3}$, is negligible. If coherent flow is also present the normalized echo signal will be affected by phase

shifts in addition to the attenuation due to diffusion. The phase shift is proportional to the amplitude of the coherent flow.

$$E(q,\Delta) = \exp\left(i2\pi q \cdot V\Delta - 4\pi^2\gamma^2\delta^2 g^2 D\left(\Delta - \frac{\delta}{3}\right)\right) = \exp\left(i2\pi q \cdot V\Delta - 4\pi^2 q^2 D\left(\Delta - \frac{\delta}{3}\right)\right)$$

Eqn. 46

Restricted Diffusion

In NMR the apparent diffusion coefficient, D_{app}, is a parameter related to the echo method used in measuring diffusion and hence is affected by the gradient strength and echo time, τ. Molecular self-diffusion, D_o, on the other hand is a stochastic process that depends on the particle itself and the liquid it is suspended in. In the case of unrestricted diffusion, where there are no boundaries that restrict the stochastic motion of particles, the mean squared displacement of particles sees a Gaussian distribution and under narrow pulsed gradients where the propagator formalism can be used, can be related using the Einstein definition. For a 3 dimensional case this would be mathematically represented as in Eqn. 47.

$$D_{eff}(t) = \frac{\langle (r' - r)^2 \rangle}{6t} = D_{app} \qquad \text{Eqn. 47}$$

where $D_{eff}(t)$ is the time dependent effective diffusion coefficient will be equal to the apparent diffusion coefficient D_{app}. Under the assumption of narrow gradient pulses and in the low q limit the PGSE NMR experiments allow the study of mean-squared displacement corresponding to the observation time, Δ. In the unrestricted case, D_{app} is equal to the self-diffusion coefficient, D_o. In the restricted case where either isolated pores or interconnected pores are concerned, the definition of D_{eff}, or D_{app} will change based on the time during which the displacement is

observed. This is because particles will begin to collide and bounce off the walls of the pores and effectively slow the observed transport in a given time. D_{eff} will hence be highly time dependent.

Interconnected Pores vs. Isolated Pores

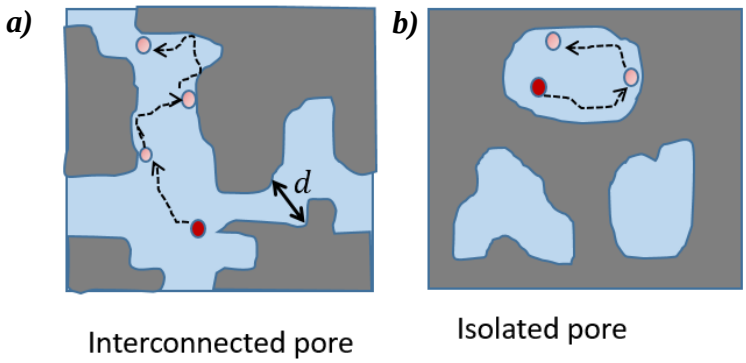

Figure 21: a) Schematic of an interconnected pore with, d, the pore diameter. b) Schematic of an isolated pore.

For interconnected pores: At short diffusion times most molecules will not yet have collided with the wall (unless they are right next to the wall) which leads to the effective diffusion coefficient measured being approximately the self-diffusion coefficient ($t \rightarrow 0$, $D_{eff} \approx D_o$). Under long times, $t \rightarrow \infty$, the particles will sample more of the pore space and are able to move into new pores too, however the collisions experienced with the walls will have increased too, decreasing D_{eff}.

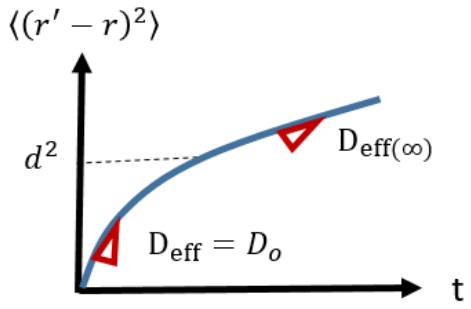

Figure 22: Time dependence of D_{eff} for an interconnected pore.

Figure 22 shows a plot of the mean squared displacement plot against time, the slope of which gives the effective diffusion coefficient. As can be seen, it shows how D_{eff} does not become zero with $t \rightarrow \infty$ as molecules can continue to diffuse through the interconnected pore space.

For Isolated Pores: Under the short diffusion time, the effective diffusion will once again be approximately the self-diffusion as most molecules will have not yet collided with the walls. As $t \rightarrow \infty$, since the molecular displacement will be confined within a single pore and cannot sample other pore spaces, the average mean square displacement will become zero as the collisions increase. Hence, $t \rightarrow \infty$, $D_{eff} \rightarrow 0$ as shown in Figure 23.

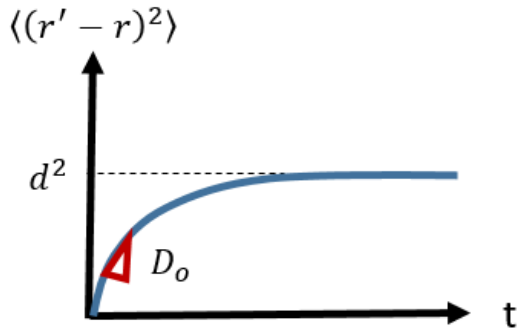

Figure 23: Time dependence of D_{eff} for an isolated pore.

Velocimetry

Velocimetry can be simply defined as the mapping of the local velocity fields in a fluid sample [2].Under steady state flow, velocity will be independent of time at a particular location. This means the spin density remains constant with time even though the velocity of the spin bearing molecules in a sample are changing over time. This allows the flow to be analyzed in the Eularian frame. The Eularian velocity field, V(r), is found by measuring the 'phase shift' of the signal.

Velocimetry sees a few physical constraints on being able to measure velocity accurately:

- The maximum velocity measurable is limited by the receiver coil length, l, since moving spins must be within the receiver coil over the observation timescale known as echo time (TE):

$$V_{max} \leq {}^{l}/_{TE}$$

- Minimum velocity measurable is limited by two factors:
    1) By the molecular self-diffusion, D, and the longest observation scale, which for the case of a stimulated echo will be T_1, and for a spin echo will be T_2:

       $V_{min} > \left(\frac{D}{T_1}\right)^{1/2}$ for a stimulated echo pulse sequence

       $V_{min} > \left(\frac{D}{T_2}\right)^{1/2}$ for a spin echo pulse sequence

    2) Hardware constraints: since lower velocity field measurements require larger gradient strength.

When bipolar gradients of equal duration and amplitude are used a zeroth moment ($m_o = 0$) can be achieved leaving first and higher order moments exposed. Using narrow pulse gradient PGSE NMR higher order moments can be neglected. The resulting first moment (m_1) will bear phase shift information at each pixel of a dynamic velocity image that can be used to find the mean flow rate at each pixel.

In dynamic imaging of velocity both k-space and q-space are involved as the echo is sampled as a function of *k*-space (position) and is phase encoded in *q*-space (displacement).

Three velocimetry methods exist:

1) Reference phase processing method
2) 2 q-step method
3) Fourier analysis method

Reference Phase Processing Method

This method applies two phase encoding q-gradients, one being $q = 0$ and the other $q = q_1$, with each producing two a separate complex signal $E(0, \Delta, r)$ and $E(q_1, \Delta, r)$ for the same pixel. The complex signal at a single pixel from a *q* step with a gradient ($q = q_1$) will be:

$$E(q_1, \Delta, r) = \rho(r) \exp(iq_1 V\Delta) \exp(-q^2 D\Delta) \qquad \text{Eqn. 48}$$

where $\exp(iq_1 V\Delta)$ term bears the oscillatory phase shift due to average flow and $\exp(-q^2 D\Delta)$ is the attenuation due to diffusion effects and $\rho(r)$is the spin density in each pixel at position vector, **r**.

The signal arising from a gradient of zero, will only bear spin density information of each pixel at r as no phase information will be imprinted with no PGSE gradients being applied. The resulting signal can be depicted as in Eqn. 49.

$$E(0, \Delta, r) = \rho(r) \exp(0) \exp(0) = \rho(r) \qquad \text{Eqn. 49}$$

The phase angle can hence be computed using the normalized complex signal:

$$\frac{E(q_1,\Delta,r)}{E(0,\Delta,r)} = A \exp(i\emptyset) \qquad \text{Eqn. 50}$$

Where $\emptyset = q_1 V\Delta$, from which the average velocity can be then calculated from, and $A \leq 1$ is the attenuation factor due to diffusive effects [1].

This method is flawed due to the use of a $q = 0$ step. Since no gradients are used in $q = 0$ step, the only other step of $q = q_1$, will require strong enough gradients to overcome the noise and obtain a SNR greater 10:1 in order to be able to confidently detect any phase shift information.

2 q-Step Method

This method is similar in that it employs 2 q-steps, however in this case the q-steps will be equal but opposite narrow PGSE gradient pairs.

The q-steps will be of magnitude:

$q_1 = \gamma\delta(-g_{max})$

$q_2 = \gamma\delta(+g_{max})$

The complex signal arising from each q-step at each pixel can then be broken down into its real and imaginary components from quadrature detection as shown in Figure 24 below.

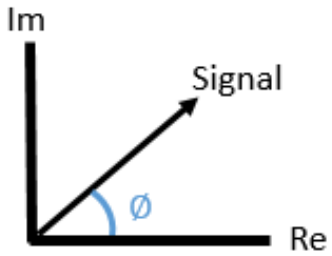

Figure 24: The complex signal can be broken into its real and imaginary components because of quadrature detection.

The angle,Ø, between the signal and the real part of the signal gives the phase shift, Ø, as shown in Eqn. 51.

$$\tan \emptyset = \frac{\text{Im}\,(S)}{\text{Re}(S)} \qquad \text{Eqn. 51}$$

Where Im (S) is the imaginary component of the signal and $\text{Re}(S)$ is the real component of the signal.

Measuring the phase shift of the first q-step, $\emptyset_1 = \tan^{-1}\left(\frac{\text{Im}(S_1)}{\text{Re}(S_1)}\right)$, and the phase shift arising from the second q-step, $\emptyset_2 = \tan^{-1}\left(\frac{\text{Im}(S_2)}{\text{Re}(S_2)}\right)$, the average velocity of the fluid can then be calculated by their difference as shown in the Eqn. 52 and 53 below.

$$\emptyset_2\text{-}\emptyset_1 = V\Delta(q_2\text{-}q_1) = \gamma V\Delta\delta((+g_{max})\text{-}(-g_{max})) \qquad \text{Eqn. 52}$$

$$\emptyset_2\text{-}\emptyset_1 = 2\gamma V\Delta\delta g_{max} \qquad \text{Eqn. 53}$$

Fourier Analysis Method

The q dimension will extend from *q*=0 to *q*=qmax with a series of images being collected with successively incremented gradients. The resulting q-step interval will then be as shown in Eqn. 54:

$$\Delta q = \frac{\gamma \delta g_{max}}{2\pi n_d} \qquad \text{Eqn. 54}$$

Where n_d is the number of gradient increments. Taking the Fourier transform of the resulting complex signal with respect to the k-space results in two sets of images: Real q-slice images and imaginary *q*-slice images. As one steps through each *q*-slice of each image, the PGSE gradient pulse intensity increases along with the accumulated phase angle.

These images can then be Fourier transformed with respect to the q-space dimension and will result in an average propagator, $\overline{P}(R, \Delta)$, at each pixel of the image. If the number of steps q-steps is small (4 or 8 steps) then this propagator will be Gaussian shaped and centered at a position k_v:

$$k_v = \frac{N\gamma \delta g_{max} V \Delta}{2\pi n_d} = \frac{N\emptyset}{2\pi} \qquad \text{Eqn. 55}$$

Taking the peak of the real component's propagator, k_v, the average velocity detected at each pixel can be found using Eqn. 55 shown above. The propagator derived by obtaining the Fourier transform with respect to the q-dimension of the imaginary set of images will relate information of the sign of the average velocity (the direction of flow).

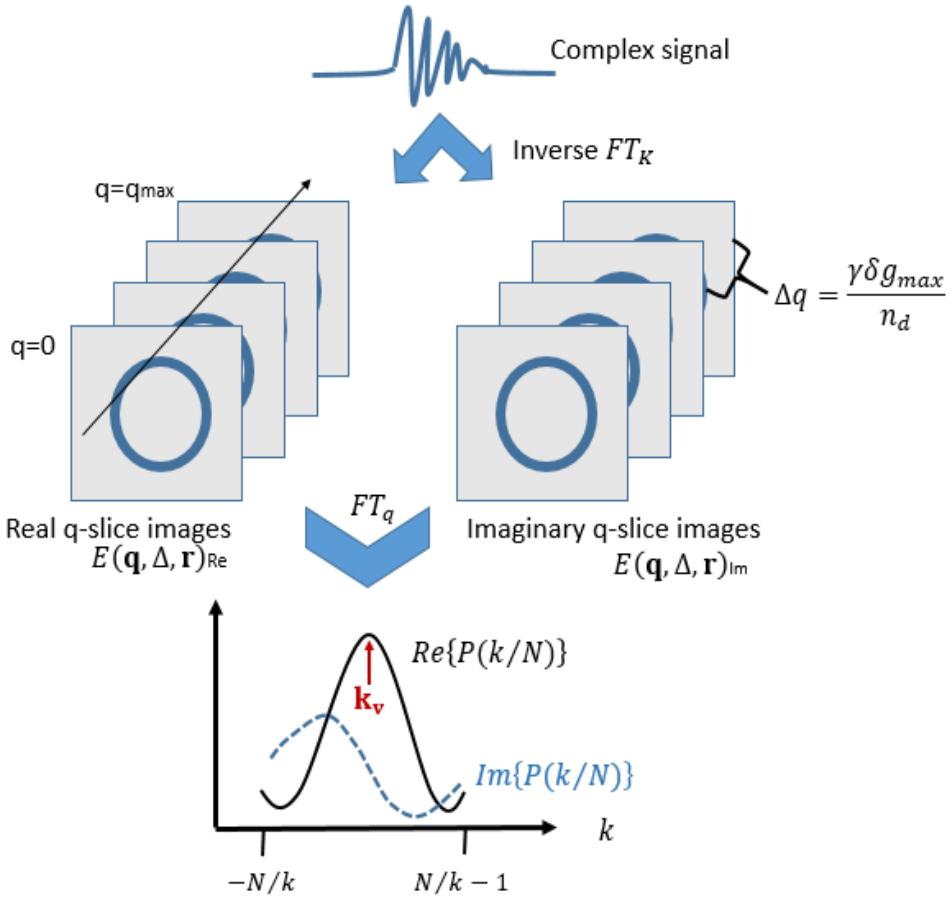

Figure 25: How dynamic NMR is processed using the Fourier analysis method.

Velocity Imaging

This thesis seeks to measure fluid velocities using the following basic PGSE pulse sequence with a few adjustments discussed within separate chapters.

An initial excitation tips the magnetization to the transverse plane allowing all the spins to align coherently and precess at $\sim\omega_o$ (if inhomogeneities are ignored). This excitation is followed by a *q* gradient (in addition to the imaging gradients) of magnitude g, and duration δ, causing the spins to wind up in the helical structure dependent on to the local Larmor frequencies

experienced and as was discussed in the PGSE pulse sequence section. Hence we can say that this first q-gradient imparts a phase to the spins. Once the first q-gradient is removed the spins will precess at position dependent frequencies. A 180° pulse is then employed to reverse the direction of the local precessions. Next a second phase is imparted on the spins by a second q-gradient equal in magnitude to the first, which now gets rid of the location dependent precession frequencies, hence unwinding the helix and creating an echo. If no translational motion (ignoring diffusion) was absent during Δ, the echo will see coherence. However if a translational motion is present during Δ, a residual phase shift, $\emptyset$, will be detected in the signal and can be translated to velocity be means of Eqn. 53. The process described is shown in Figure 26 while the residual phase shift, $\emptyset$, is described by Eqn. 56 below.

$$\emptyset = \gamma\delta\Delta g v \qquad \text{Eqn. 57}$$

where,

$$v = \frac{\emptyset}{\gamma\delta\Delta g} \qquad \text{Eqn. 56}$$

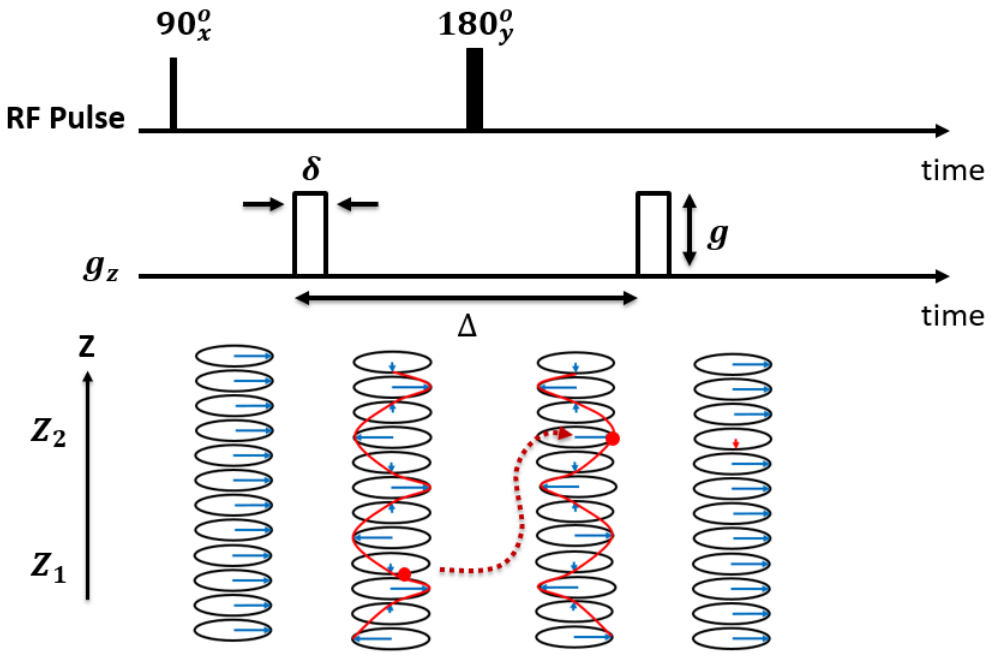

Figure 26: Motion encoded PGSE pulse sequence. The PGSE gradients of strength 'g' and duration δ being applied with an observation time Δ, during which time if translational motion is present it will create a residual phase shift in the final NMR signal.

References

1. Callaghan, P.T., *Translational Dynamics & Magnetic Resonance: Principles of Pulsed Gradient Spin Echo NMR*. 2011, New York: Oxford University Press.

2. Han, S.-l. and S. Stapf, *NMR imaging in chemical engineering*. 2006, Weinheim : [Chichester]: Weinheim : Wiley-VCH, Chichester : John Wiley, distributor.

3. Levitt, M.H., *Spin Dynamics*. 2013: Wiley.

4. Purcell, E.M., H.C. Torrey, and R.V. Pound, *Resonance Absorption by Nuclear Magnetic Moments in a Solid.* Physical review, 1946. **69**(1-2): p. 37-38.

5. Bloch, F., *NUCLEAR INDUCTION.* Physical Review, 1946. **70**(7-8): p. 460-474.

6. Günther, H., *NMR spectroscopy : basic principles, concepts and applications in chemistry*. 2013, Weinheim an der Bergstrasse, Germany : Wiley-VCH.

7. Callaghan, P.T., *Principles of nuclear magnetic resonance microscopy*. 1993, Oxford: Oxford : Clarendon Press.

8. Slichter, C.P., P. Fulde, and K. von Klitzing, *Principles of Magnetic Resonance*. Third Enlarged and Updated Edition. ed. Vol. 1. 1996, Berlin, Heidelberg: Berlin, Heidelberg: Springer Berlin / Heidelberg.

9. Vogt, S.J., *Nuclear magnetic resonance studies of biological and biogeochemical processes*, in *Engineering*. 2013, Montana State University.

10. Keeler, J., *Understanding NMR spectroscopy*. 2011: John Wiley & Sons.

11. Simkins, J.W., *Spatiotemporal mapping of oxygen in model porous media biofilms*, in *Chemical Engineering*. 2019, Montana State University.

12. Thrane, L.W., *Nuclear magnetic resonance studies to characterize phase transitions in porous systems*, in *Engineering*. 2018, Montana State University.

13. Weishaupt, D., *How does MRI work? An Introduction to the Physics and Function of Magnetic Resonance Imaging*, V.D. Koechli, B. Marincek, and V.D. Köchli, Editors. 2006, Berlin, Heidelberg : Springer Berlin Heidelberg : Imprint: Springer: Berlin: New York.

14. Bernstein, M.A., K.F. King, and X.J. Zhou, *Handbook of MRI Pulse Sequences*. 2004, San Diego: San Diego: Elsevier Science & Technology.

CHAPTER THREE

BASICS OF RHEOLOGY AND COMPLEX FLUIDS

Introduction

Rheology stems from the Greek word '*rheos',* meaning *to flow,* while the word *'logy'* meant *to study.* In essence, rheology is *the study of the deformation and flow of matter* [1]. Rheology, a term coined by Professor E. Bingham, was introduced in 1920 when a need for a new field to study materials showing "strange" flow behaviors arose with the advent of synthetic polymers in the chemical industry [2, 3]. This definition was then officially recognized with the establishment of the Society of Rheology in 1929 with their motto being a quote by Heraclitus, "πάντα ρεί" that translates to "everything flows" [4, 5]. Everything most certainly flows if the time of observation is long enough or if the material's relaxation is short enough, a belief owed to prophetess Deborah in the 'Book of Judges' who proclaimed "The mountains flowed before the Lord", a statement as explained by professor Reiner (one of the founders of modern rheology) that mountains flowed in the timescale fit for Gods, not humans [6-8]. The flow of materials is also influenced by the deformation force applied, direction of applied force and its duration, complexity of the material structure and a whole lot more, making its study relevant [4].

Rheology employs a wide variety of instruments called rheometers to measure material responses to deformations. The main two types of rheometers stem from the need to either measure a response to an extensional deformation, extensional rheometry, or the need to measure the response due to a shear deformation, shear driven rheometry [1-3]. Shear rheometry is

divided into two groups: *drag flow rheometry*, where the shear is analyzed between a moving boundary and a stationery surface and *pressure driven rheometry*, where the shear is generated as a result of a pressure difference within a closed channel [1-3, 5, 7]. Drag flow shear rheometers usually come in the form of strain controlled, where degree of deformation to the material is controlled, or stress controlled, wherein the applied torque on the material is controlled. The projects that concern this thesis used shear drag flow rheometry, combined with NMR techniques to measure the velocity field. Bulk rheology measurements (stress, % strain, small amplitude oscillatory shear and large amplitude oscillatory shear measurements) were also measured using an advanced form of drag flow rheometer capable of switching between strain and stress controlled modes. This chapter will explore what materials were studied, types of rheological tests that were employed and the governing constitutive equations.

Ideal Materials

Three hundred years back most materials may have appeared simple with the lack of studies. While today considered 'ideal' in description, for two whole centuries Hooke's law was thought to have satisfied all solids and Newton's law to have mollified all liquids. Today it is known that Hook's law describes an ideal solid behavior whilst the Newton's law of viscosity describes the ideal liquid behavior.

Hookean Solid

In 1678, Hooke noted that the force/weight, F, of a suspended mass on a "springy body" was directly proportional to its extension length, Δx *(*$F \alpha \Delta x$*)*. Today this relationship, used in describing a perfectly elastic solid like cross-linked rubber or a steel spring, is called the Hooke's

law with k the spring constant [1, 7, 9-11]. This ideally elastic body is basically formulated from the spring model as in Figure 1 a) below. Analogies to how it is used in rheology draw in from the simple linear relation between the tension, σ_s, strain, γ and a shear modulus (Young's modulus), G, being the proportionality constant (Eqn. 1). Hooke's law describes a perfect solid that will regain its original form once the stress subjected for an elastic deformation has been removed, so no dissipation of energy from the solid body is seen during the deformation [2].

$$\sigma_s = G\,\gamma \qquad \text{Eqn. 1}$$

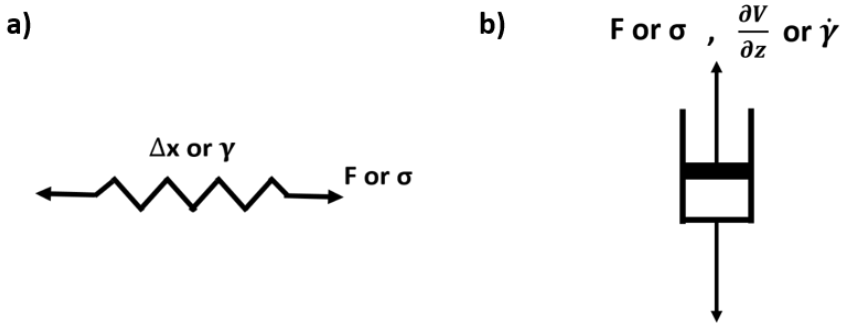

Figure 1: a) The spring model for an ideal elastic material b) The dashpot model for an ideal viscous fluid.

Newtonian Fluid

Shortly after the release of Hooke's elastic model, Newton found a linear relationship where he noted a constant material deformation rate, $\frac{\partial \gamma}{\partial t} = \dot{\gamma}$, on applying a constant stress, σ_d, scaled by a proportionality constant known as viscosity, η. Using a dashpot model, (Figure 1 b)) this can be described as the proportionality between the local forces, *F*, within the fluid changing as velocity gradient in position of the fluid layers changing, $\frac{\partial V}{\partial z}$, with proportionality constant, G [1, 2, 7, 9, 10].

$$\sigma_d = \eta\dot{\gamma} \qquad \text{Eqn. 2}$$

The Newtonian law describes a material that shows a complete release of its initial energy even after the stress that was responsible for creating the viscous deformation is removed. A Newtonian fluid can be described as [7]:

a) Constant viscosity with change in shear rate.

b) Constant viscosity over total time of applied sheared.

c) Stress of liquid immediately achieves zero state as the shear deformation is removed.

Viscoelasticity

A perfect elastic or perfect viscous deformation are very limited in considering real world fluids typically encountered. Instead, many materials will show a combination of both elastic and viscous effects each expressed at different degrees based on the material's internal structure. Real world materials depicting both ideal solid and ideal liquid behavior under deformation are called viscoelastic fluids. To find out how long to wait to observe the flow of a material, a non-dimensional number called the Deborah number, De, was introduced. De describes the relation between a material's relaxation time, λ_r, and the observation time, t, ($De = \frac{\lambda_r}{t}$). For a perfect solid the Deborah number would approach infinity, $De \to \infty$ while for an ideal liquid it would approach zero, $De \to 0$. The Deborah number for viscoelastic materials lie between 0 and ∞.

Figure 2: Corresponding material behavior based on Deborah number (De).

Linear Viscoelasticity

A viscoelastic material can be described as the linear combination of the spring and dashpot model either connected in series or in parallel as an electric circuit would be (Figure 3). These combinations that ca be thought of as fluids with different viscous and elastic properties are historically called the Maxwell fluid and Kelvin-Voigt solid respectively [1, 2, 5, 7, 9]. For a Maxwell model, the dashpot and spring are connected in series and the stress applied to the dash pot is equal to the tension of the spring (Eqn. 3) while the strains become additive (Eqn. 4) leaving a material shear rate as in Eqn. 5 (Figure 3 a)).

$$\sigma = \sigma_s = \sigma_d \qquad \text{Eqn. 3}$$

$$\gamma = \gamma_s + \gamma_d = \frac{\sigma}{G} + \int \frac{\sigma}{\eta} dt \qquad \text{Eqn. 4}$$

$$\dot{\gamma} = \frac{1}{G}\frac{d(\sigma)}{dt} + \frac{\sigma}{\eta} \qquad \text{Eqn. 5}$$

On considering the Kelvin-Voigt model, a parallel connection of the dashpot and spring is seen, where the stresses become additive (Eqn. 6) and the strains of the two individual components are equal (Eqn. 7) (Figure 3 b)).

$$\sigma = \sigma_s + \sigma_d \qquad \text{Eqn. 6}$$

$$\gamma = \gamma_s + \gamma_d \qquad \text{Eqn. 7}$$

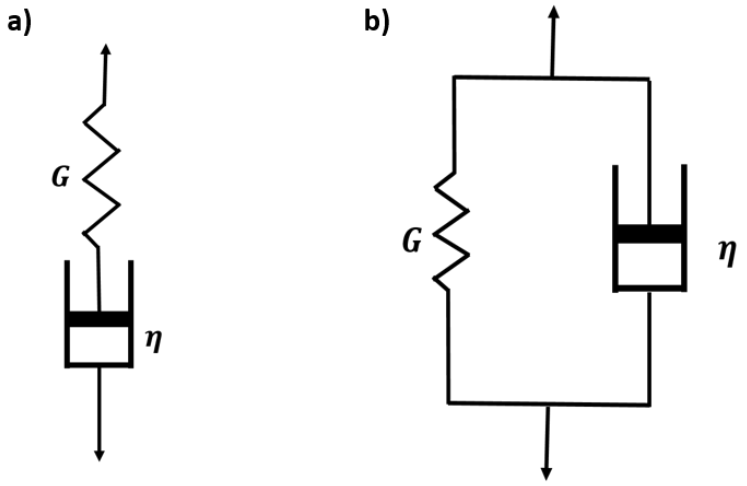

Figure 3: Schematic of the a) Maxwell model and b) Kelvin-Voigt model.

Complex, Non-Newtonian Fluids

The mentioned Newtonian assumption works well when the fluid/ materials we are dealing with are made of small molecules i.e. water, liquid argon etc., where the individual molecules do not alter the dynamics of the constituent molecules [12]. This can be attributed to the stress relaxation time, λ_r, (defined as relaxation time for De) that describes the time a material requires to deform under a suddenly applied stress. For a Newtonian fluid λ_r is related to its molecular self-diffusion time (both in the range $10^{-13} – 10^{-12}$ s), meaning that if one wanted to create a significant alteration to the dynamics of the constituents, an impractically high velocity deformation would have to be applied [12, 13]. Most fluid based consumer products however differ from this classical notion and show complex behaviors including, but not limited to, viscoelasticity. This section will introduce the behaviors of non-Newtonian complex fluids used in this thesis and introduce some of the models used in characterizing these fluids (Table 1).

A schematic of the nonlinear steady shear rheology flow curves of different types these fluids is shown in Figure 4.

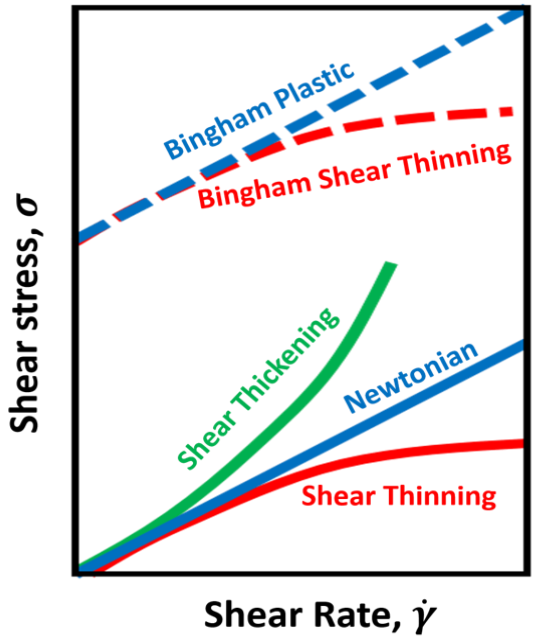

Figure 4: Schematic of flow curves representing the stress response of complex fluids to an increase of the applied shear rate.

Shear-Thinning Fluid

Shear thinning, unlike Newtonian behavior, describes the nature of a fluid whose viscosity decreases with increased shear rate or stress. The terms ‘temporary viscosity loss’ and ‘pseudoplasticity’ are also used interchangeably to describe the same behavior [7]. Many dispersions, polymer solutions and emulsions show this behavior with well-known examples being normal human blood and xanthan gum. Shear thinning fluids are used as viscosity modifiers (additives in hydraulic fluids, engine oils and transmission fluids) and in drug delivery applications and tissue engineering [14] [15]. At low enough shear rates shear thinning fluids

may exhibit a Newtonian plateau, characterized by a constant viscosity called the zero viscosity, η_0. At high shear rates, a second plateau can occur with a constant viscosity called the infinite shear viscosity, η_∞. Between the two limits, in the shear rate range where the Newtonian behavior is not captured, lies a region that is modeled by the Ostwald de Waele power law model (Table 1, Eqn. 9) [1] [16]. The Carreau model (Table 1 Eqn. 10) was introduced in order to model the shear thinning behaviors in the low and high shear rate limits. Another fluid that can be described using the power law model with a power law index greater than unity is a shear thickening fluid. As the name suggests the fluid becomes 'thicker' on increased applied stress, in that the fluid's viscosity increases. The focus will however remain on shear thinning fluid in this section as dilatant fluids are less commonly encountered in the practical world.

Mathematical model	Name of model	Comments
$\sigma = \eta\dot{\gamma}$ Eqn. 8	Newtonian liquid law	Used for fluids that show a linear relationship between the applied shear rate, $\dot{\gamma}$, and response stress, σ, where the viscosity, η, is always a constant.
$\sigma = K\dot{\gamma}^{n}$ Eqn. 9	Power law or Ostwald de Waele model	Used as a simple representation for fluids that show either shear thinning (n<1) or shear thickening (n>1) where the fitting parameters K and n are the flow consistency coefficient and the power law index respectively. Note: *K* changes as n changes, it is not a constant. If n=1, the fluid shows Newtonian behavior.
$\frac{\eta-\eta_\infty}{\eta_0-\eta_\infty} = \{1 + (\lambda\dot{\gamma})^2\}^{(n-1)/2}$ Eqn. 10	Carreau model	Used solely for shear thinning fluids and even takes into account the zero viscosity, η_0, and the infinite viscosity, η_∞ for the shear thinning fluid.
If $\sigma < \sigma_{yield}^{B}$ $\dot{\gamma} = 0$	Bingham plastic model	Adopted to describe an ideal yield stress fluid, the Bingham yield stress, σ_{yield}^{B}, and Bingham viscosity, η_B, are curve fitting

If $\sigma > \sigma_{yield}^{B}$ $\sigma = \sigma_{yield}^{B} + \eta_B \dot{\gamma}$ Eqn. 11		parameters whether or not the fluid possess a true yield stress.
If $\sigma < \sigma_{yield}^{H}$ $\dot{\gamma} = 0$ If $\sigma > \sigma_{yield}^{H}$ $\sigma = \sigma_{yield}^{H} + K\dot{\gamma}^{n}$ Eqn. 12	Herschel-Bulkley model	Used in describing real world yield stress fluids that also describes if the fluids show shear thinning behavior upon yielding. *K* and *n* are similar to that of Eqn. 9 and must be treated the same. σ_{yield}^{H} is the yield stress found from using the Herschel-Bulkley model.

Table 1: Fluid models.

Yield Stress Fluid

The ideal yield stress fluid behave as an elastic solid until a stress of a finite, critical value referred to as the 'yield stress', σ_y, is surpassed. When the applied stress exceeds the yield stress, the material begins to flow, behaving as a Newtonian liquid, with a plastic viscosity, η_B. This definition established by the British standards in 1975 takes an approach of the Bingham model, where paint was described as a yield stress fluid in 1916 by E. Bingham using the ideal Bingham model (Table 1 Eqn. 11) [16]. The two models, Ostwald de Waele power law model and Bingham model, provide very similar outcomes with parameter variations, making them interchangeable (for an example drawn using yogurt, refer to page 92 of Macosko, 1994) [1]. A

more accurate interpretation of the yield stress behavior was hence introduced by Herschel and Bulkley in 1926 (Table 1 Eqn. 12) where post overcoming the yield stress, the material may behave as a shear thinning fluid. Even today, the existence of a 'true' solid behavior at stresses below a yield stress being is debated in rheology with some authors suggesting that the solid regime should in fact be named a 'highly viscous' regime while others suggesting it is a true solid regime[16, 17].

Many daily encountered fluids like food, cosmetics, emulsions, pastes polymer gels and foams, clays and many more show this behavior [18]. The origins of the yield stress of each fluid varies. For example the yield stress of foods like mayonnaise and ice-cream are the result of droplets and air bubbles (emulsion and foam) while the yield stress in mustard is created from its suspension/pasty internal structure [19]. Furthermore, the origins of the yield stress nature can be classified based on the fluid's microstructure: i) jammed structures showing repulsive interactions (glasses) ii) networked structures showing attractive interactions (gels) iii) combination of the two. Suspensions of polymer micro gel particles (i.e. carbopol swollen micro gel particles), foams (i.e. Gillete shaving foam), suspensions of hard non Brownian granular particles and oil-in-water emulsions (i.e. mineral oil- in-water emulsions) form the repulsive jamming microstructure [20-22]. Jammed glasses showing a repulsive interaction will exhibit a yield stress as the jammed particles push against each other and yielding to flow only once the structures rearrange to slide past each other (Figure 5). Network based yield stress fluids on the other hand show a yield stress as the attraction based microstructures resist being pulled part during deformation and only begin to flow once the recoverable attractions are broken (Figure 4). Particle gels (i.e. Bentonite and Laponite colloidal clays) and other polymer solutions whose

crosslinks can re-form post shear breakage constitute as examples for this type of yield stress fluid [20]. Nevertheless a feature of yield stress fluids under flow deformation is wall slip making them a very hard to study category of fluids using rheology alone. For instance, an aqueous foam when sheared will form a lubricating layer at the smooth boundaries of the geometry used leaving part of the foam less sheared than expected. Gelled colloidal systems also show the wall slip phenomena due to the same mentioned reason [19]. This wall slip that occurs for yield stress fluids has a big impact on the flow behavior of the fluid deeming rheologists to believe that there may be a 'true' solid like regime for the fluid at stresses lower than the assumed yield stress of the fluid, when in fact, the fluid is just showing plug flow [17].

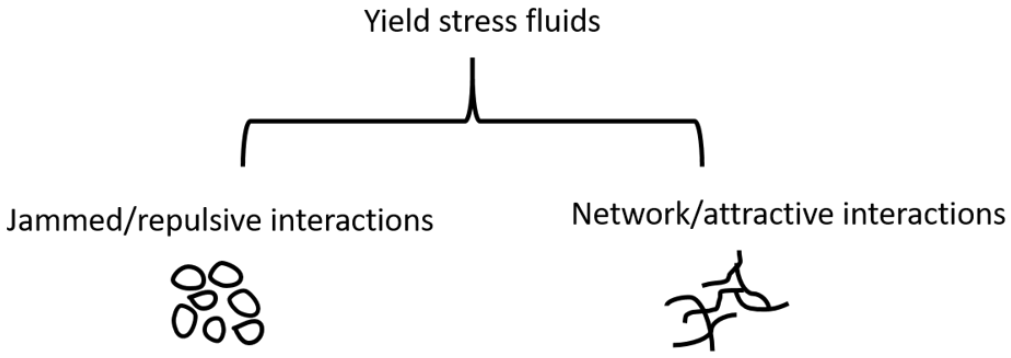

Figure 5: Schematic of the microstructural differences between two types of yield stress fluids.

The yield stress of a material can be determined using flow tests. The use of flow curves and modeling fitting enables to find the dynamic yield stress, the minimum stress required to maintain flow. While flow tests in rheology such as stress growth and stress ramp tests are used to directly determining the static yield stress, stress needed in initiating the flow, of the fluid

[23]. These tests are discussed in detail in the steady shear rheology section below. Determining the yield stress is important in industrial applications. The force required to pump yield stress consumer products into packaging containers and through pipelines can be determined when the yield stress is known [24].

Carbopol: This is one of the prominent model fluids used in rheology, industry and this thesis to describe yield stress fluids depicting a Herschel-Bulkley model behavior. Carbopols refer to a family of poly acrylic aci d polymers that are cross-linked with allyl sucroses introduced in the 1950's as thickeners. They are widely used in the cosmetics, pharmaceutical industries and are found in powder form in dry state. They produce a murky acidic dispersion in water that when neutralized employing a base like sodium hydroxide (NaOH) or triethanolamine (TAE) to a pH of 7, form an aqueous clear gel (hair gel), the choice of base having had no impact on the rheological properties [25] [21]. This is because on neutralization, the polymers that are cross linked partially uncoil and on ionization and absorb and retain water to form irreversible swollen sponges that may extend to 10 times the original polymer powder particle diameter. This is then referred to as the micro gel that shows a jammed structure who's degree of jamming is dependent on the type and strength of the crosslinks found in the original polymers [21, 22].

Steady Shear Rheology and Oscillatory Rheology

Steady Shear Rheology

Steady shear rheology, or non-linear rheology, measures the stress or shear rate response from the fluid to an applied unidirectional shear rate or stress, respectively. The resulting data is called a 'flow curve' or a 'rheogram' and is used to obtain material properties such as the

material's viscosity and the material's stress/shear rate responses (Figure 4). While a flow curve is a basic test in steady shear rheology, other tests that apply a constant strain rate or constant stress can be used in determining the time taken to reach steady state (start-up tests). Steady shear tests can also be used to determine a material's yield stress as mentioned in the yield stress material section. For a consumer product, a flow curve with a fitting model of Herschel-Bulkley model provides the stress corresponding to the initial sign of flow as a reasonable dynamic yield stress [23]. A stress growth test where the stress build-up over time is measured for a constantly increasing applied strain also falls in this category of rheology tests. Here the shear rate is kept constant and the material elastic elements begin to stretch in the shear field with the increasing strain till a critical strain is met. At this point a peak in the shear stress with time characterizes the structural breakdown of the material, this stress value being the static yield stress [23]. Conversely a stress ramp test, where the strain rate is monitored over time for a constantly increasing applied stress, can also be used as a quick and easy method in determining the yield stress. Here the viscosity increases as the material undergoes elastic deformation, peaking at the viscosity corresponding to the static yield stress where the material's structure would have broken down [23]. Shown in Figure 6 is a schematic of the flow tests used in determining yield stresses.

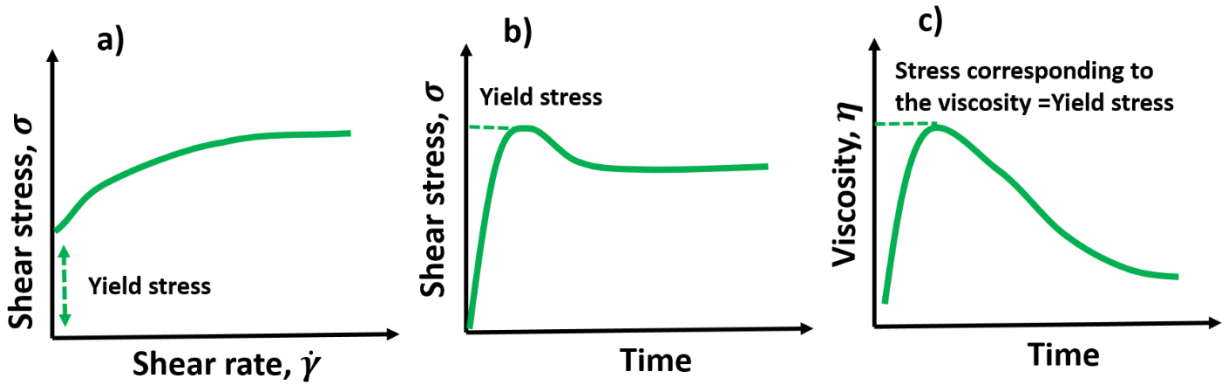

Figure 6: Schematic of yield stress measurement flow tests. a) Flow curve where Herschel Bulkley fit is used to determine the dynamic yield stress, b) stress growth curve showing a direct measurement of the static yield stress and c) viscosity vs time curve for a stress ramp test at a fixed shear rate.

Small Amplitude Oscillatory Shear (SAOS)

Small amplitude oscillatory rheology, or linear rheology, subjects materials to a sinusoidal deformation and measures the resulting stress response [26]. As the name suggests, SAOS applies a very 'small' back and forth, sinusoidal deformation that varies harmonically in time, $\gamma_{(t)}$, (Eqn. 8) to a degree that enables the material to respond with a perfectly sinusoidal stress response, $\sigma_{(t)}$, (Eqn. 9) hence coining the term 'linear rheology'[1, 7]. SAOS tests are used to measure material properties in the linear viscoelastic regime and since the deformations are not large, the material is left undamaged [27].

$$\gamma_{(t)} = \gamma_o \sin(\omega_1 t) \qquad \text{Eqn. 13}$$

$$\sigma_{(t)} = G^{'}\gamma_o \sin(\omega_1 t) + G^{''}\gamma_o \cos(\omega_1 t) \qquad \text{Eqn. 14}$$

Where, γ_o is the strain amplitude, ω_1 is the fundamental frequency of the periodic motion, and G' and G'' are the storage and loss modulis of the material respectively. Under such small deformations, Hookean solids show purely elastic responses where the stress is always proportional to the strain and is independent of the strain rate [28] . Hence there is a phase angle $\delta = 0°$ between stress and strain sinusoidal response curves. On the other ideal spectrum are Newtonian fluids that show purely viscous responses where the fluid's stress response is proportional to the rate of strain (rate of deformation) but independent of the strain alone. Hence there is a phase angle $\delta = 90^0$ between stress and strain sinusoidal response curves. Viscoelastic fluids exhibit viscous and elastic responses with the phase angle between the stress and strain sinusoidal curves being $0^0 < \delta < 90^0$ (Figure 7) [10].

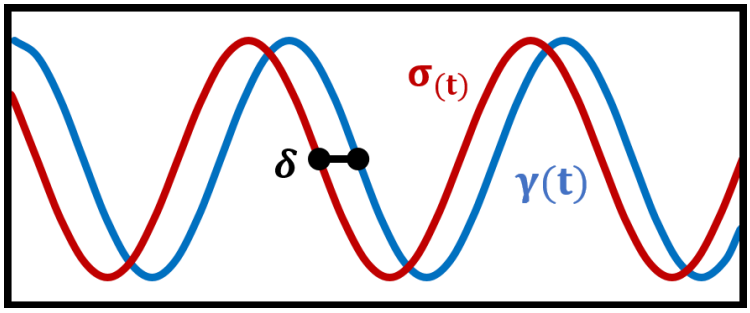

Figure 7: Schematic of an applied sinusoidal strain, $\gamma_{(t)}$, with a stress response, $\sigma_{(t)}$, that is also perfectly sinusoidal. When no phase difference is present, $\delta=0^0$, the material is considered a Hookean solid. When the phase difference is $\delta =90^0$, the material is considered to be a Newtonian liquid. When the phase difference between the stress response and applied strain is in between, $0^0 < \delta<90^0$, it is a complex fluid exhibiting both viscous and elastic properties.

In the linear regime G' and G'' are independent of the applied strain and depend only on the applied frequency. The storage modulus, G', defines how much energy is restored post

deformation and hence relates how solid-like a material is. The loss modulus, G'', relates how much energy the material lost in viscous dissipation and corresponds to how liquid-like the material is. The two can then be related to the phase lag as $\tan(\delta) = \frac{G''}{G'}$ and tied into Eqn. 9 with an introduction of a complex number called the complex modulus, G* (see Figure 8 for clarity).

$$G^* = G' + iG'' \qquad \text{Eqn. 15}$$

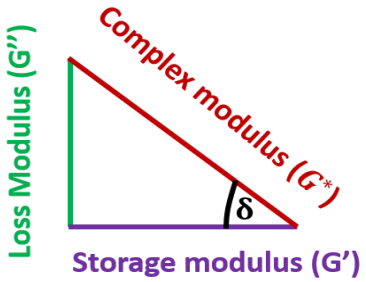

Figure 8: Relationship of the complex modulus to the storage and loss modulus.

Large Amplitude Oscillatory Shear (LAOS)

LAOS tests are important because large and rapid oscillatory shear is used in industry, provoking the raw materials and products to be in the non-linear regime. For example in the manufacture of ketchup, the tomato puree is mixed with vinegar sugar, salt, and other ingredients in large vats that use nonlinear oscillatory shear to produce a homogeneous mixture. Scientists then conduct shear rate experiments using tilted surfaces to ensure that the viscosity of the fluid is on par, such that it will not form blobs or disperse in odd directions than in the intended direction once squeezed out of the bottle. This desired texture is achieved provided that the

ingredients were mixed well at the correct oscillatory shear rates within the large vats. This thesis therefore studied the velocity responses due to LAOS.

When the amplitude of the periodic deformation is increased into the non-linear regime of a material, the stress response from the material will no longer be perfectly sinusoidal (Figure 9). This is because the material gets permanently deformed at high applied strain amplitudes, showing irreversible changes in the structure of the material [26, 27]. G' and G'' are also no longer strain independent and are influenced by higher order odd harmonics. The resulting response stress wave form is no longer sinusoidal, bearing nonlinear viscoelastic moduli that are both strain and harmonic dependent, $G'_n(\gamma_o)$ and $G''_n(\gamma_o)$, making it difficult to analytically quantify the moduli. It must be noted that the new material moduli have an ambiguous physical definition to that of the linear viscoelastic moduli (G' and G'') discussed previously. That is to say that while G' and G'' fully describe the linear viscoelastic mechanical material responses, they do not describe the storage and loss of the system in the nonlinear viscoelastic regime [29]. However this amplitude dependent leading order (fundamental frequency, where n=1), G' and G'', still can be used in the nonlinear regime to deduce plenty of information. Based off the of the behaviors of the leading order moduli at a higher dependent strains ($G'_1(\gamma_o)$ and $G''_1(\gamma_o)$) under LAOS, four groups of fluids have been identified [26, 27, 29]:

1) Strain thinning: observed in systems where entanglements occur but with weak molecular interactions. Here, polymer chains that are entangled in the SAOS regime will disentangle with the increased strains at LAOS and align with the flow field i.e. polymer solutions and melts.

2) Strain hardening: observed in systems with complex and strong microstructures where the deformations result in the formation of more elaborate structures. Here, polymer chains resist the alignment with flow as the strain is increased, forming shear-induced networks i.e. poly(vinyl alcohol)/sodium borate solutions.
3) Weak strain overshoot: systems with stable molecular structures at rest that are capable of creating shear induced structures under moderate shear. The structures are however destroyed and re-oriented parallel to the flow once a critical strain is exceeded i.e. long side chain bearing polymer solutions like xanthan gum.
4) Strong overshoot: this behavior is similar to the weak overshoot except that the forces of the shear induced structures are stronger than before i.e. micellar systems and colloidal aggregate gels.

For further details, the reader is directed to studies by Kyu Hyun *et. al.* [26, 29].

For LAOS, the applied sinusoidal strain takes the form of Eqn. 13, only with a higher strain amplitude, γ_o, the stress response can be represented as a Fourier series as shown in Eqn. 16 [26, 30]:

$$\sigma_{(t)} = \gamma_o \sum_{n,odd} G_n^{'}(\omega, \gamma_o)\sin(n\omega t) + G_n^{''}(\omega, \gamma_o)\cos(n\omega t) \qquad \text{Eqn. 16}$$

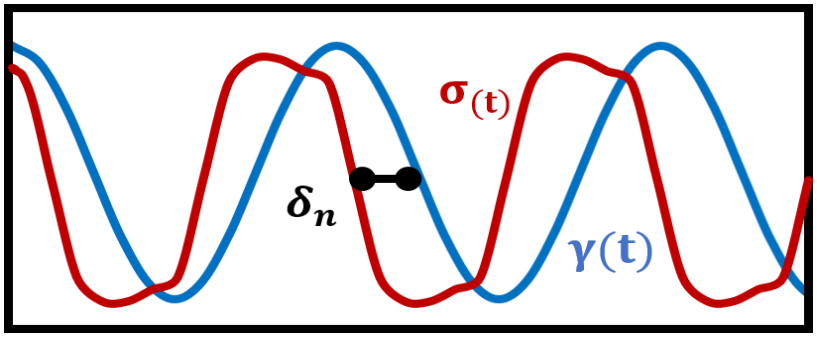

Figure 9: Applied sinusoidal large amplitude oscillatory strain and the response distorted sinusoidal strain amplitude and higher order harmonic dependent stress response (LAOS).

While linear viscoelasticity provides an understanding between the microstructure and rheological behavior of complex fluids, LAOS allows for the sub-characterizations of fluids. In other words, data from LAOS tests can distinguish among categories of fluids bearing similar micro- and nano- or molecular structures. For instance, LAOS is able to distinguish between branched or un-branched polymers [26].

LAOS tests are analyzed employing Fourier transforms or Lissajous curves (proper term being Lissajous-Bowditch curves). Previous studies conducted with Fourier transform analysis (FT analysis) of LAOS flow has shown the contribution of higher order odd harmonic components to the fundamental stress components, $G_1^{'}(\gamma_o)$ and $G_1^{''}(\gamma_o)$. The contributions from even harmonics to the stress have been attributed to wall slip, combined effects of inertia elasticity and shear thinning, geometry misalignments and yield stress [26, 31-34]. Lissajous figures are however a more popular choice as they present all the raw data compactly over FT analysis. Lissajous plots refer to closed loop plots of the measured stress wave function plotted against the applied strain or strain rate wave function. When the oscillatory stress in time, $\sigma(t)$,

is plotted as a function of the strain in time, $\gamma(t)$,the resulting 2D curve is termed 'elastic Lissajous curve'. If $\sigma(t)$, is plotted as a function of the strain rate in time, $\dot{\gamma}(t)$, it is termed 'viscous Lissajous curve'. An elastic material response will appear as a straight line for elastic Lissajous curves while appearing as a circle in the viscous Lissajous curve (Figure 10 a)). Contrary to this a pure Newtonian fluid will appear as a circle in the elastic Lissajous curve while as a line in the viscous Lissajous curves (Figure 10 b)). Viscoelastic material response in the linear (SAOS) regime will appear as a perfect ellipse on both forms of Lissajous figures. As the response is shifted to a nonlinear LAOS regime, the elliptic viscoelastic response will begin to show distortions [35].

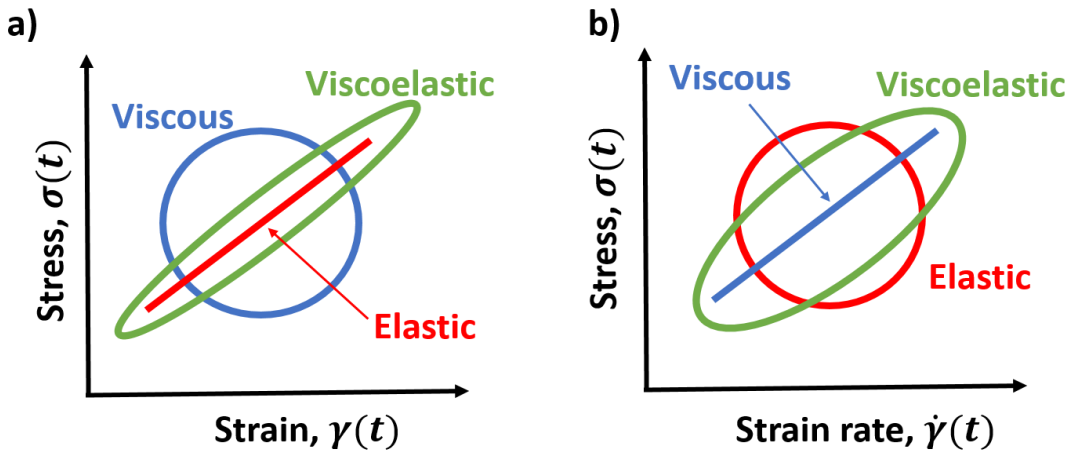

Figure 10: Schematic of an a) elastic Lissajous-Bowditch curve and a b) viscous Lissajous-Bowditch curve. The responses depicted are for the linear regime.

Rotational Drag Flow Rheometers

In this thesis work, drag flow rheometers were used. Rheometers utilize well-defined ideal geometries including parallel plates, cone and plates and concentric cylinders with small fluid gaps where the strain and/or stress are constant for Newtonian fluids. For these geometries

then, the response of a complex fluid to a deformation does not depend upon the geometry and is a reflection of the fluid material properties. While most of the rheological experiments in this thesis use a cone-and –plate geometry, the concentric cylinder geometry will also be discussed as it is the geometry used with the rheo-NMR rheometer. A concentric cylinder geometry was also used infrequently in rheology measurements for low viscosity fluids. The ARG2 rheometer and the portable rheo-NMR rheometer, are both in essence drag flow rheometers only with different responses being probed. The typical rheometer acquires torque responses from the bulk of the fluid while the rheo-NMR driveshaft probes local velocity responses. There are two rheo-NMR rheometers available in the lab, one capable of measuring the bulk torque responses, to steady applied shear, simultaneously with velocity data from NMR methods. The second rheo-NMR rheometer is capable of shearing suspended samples with both steady shear and oscillatory shear while acquiring NMR velocity data, however is incapable of measuring torque. For projects in this thesis the second rheo-NMR rheometer was used.

Concentric Cylinder/ Couette Shear Cell

The concentric cylinder was the first geometry created for a rotational drag rheometer. It is comprised of two cylinders, one that rotates (rotor) and another that is stationery (stator), between which the sample that is been sheared is suspended in (in some cases both cylinders may rotate). It was first designed by M. Couette in 1890 for a strain controlled rheometer and had an outer rotating cup. The concentric cylinder geometries used in this thesis however have an inner rotating cylinder (inner rotor), r_i, and an outer stationery cylinder (outer stator), r_o, between which the sample is sheared within. The geometry employed with the rheo-NMR rheometer was a concentric cylinder geometry. One of the projects included a fractal vane

geometry as an interchangeable geometry for the concentric cylinder while keeping the physics of the two geometries the same. The mathematical description of the concentric cylinder will hence be discussed in detail in this section.

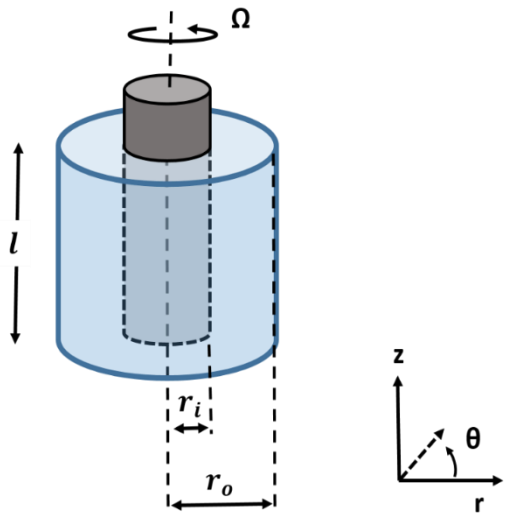

Figure 11: Schematic of a concentric cylinder geometry for the purpose of modeling the Rheo-NMR shear cell.

The equations of motion for a Newtonian fluid in cylindrical coordinates found in [36] can be solved for the concentric cylinder geometry, for an ideal situation, with the following assumptions:

1) Steady state, laminar flow: $\frac{dv_\theta}{dt} = 0$

2) Unidirectional flow in the azimuthal direction: $v_\theta = v_\theta(r)$

3) No secondary flow or edge effects: $v_r = v_z = 0$

4) Symmetry/fully developed flow in θ, $\frac{d}{d\theta} = 0$

Keeping in mind that the divergence is zero ($\Delta \cdot v = 0$) for an incompressible fluid, and that the hydrostatic pressure is a function of r and z due to centrifugal forces and gravity ($P = P(r, z)$), the equations of motion narrow down to the following components:

r-component: $-\rho \frac{v_\theta{}^2}{r} = -\frac{dP}{dr}$ Eqn. 17.a

θ-component: $0 = \frac{d(r^2 \tau_{r\theta})}{dr}$ Eqn. 17.b

z-component: $0 = -\frac{dP}{dz} + \rho g_z$ Eqn. 17.c

Note: Normal stresses of τ_{rr} and $\tau_{\theta\theta}$ become equal to zero due to assumptions 3) and 4) being made for an incompressible fluid.

Since our interest lies on finding the velocity, stress and shear rates of the flow, the r-component and z-component can be neglected and our focus can be tuned to the shear stress tensor, $\tau_{\theta r}$.

$$\tau_{\theta r} = \eta \left[r \frac{d(v_\theta / r)}{dr} + \frac{1}{r} \frac{dv_r}{d\theta} \right] = \eta \left[r \frac{d(v_\theta / r)}{dr} \right] \quad \text{Eqn. 18}$$

This stress tensor is now the total stress, $\sigma_{r\theta}$:

$$\sigma_{\theta r} = \eta \left[r \frac{d(v_\theta / r)}{dr} \right] = \eta \dot{\gamma} \quad \text{Eqn. 19}$$

Where the shear rate, $\dot{\gamma}(r)$ is a function of the radial position, r:

$$\dot{\gamma}(r) = \left[r \frac{d(v_\theta / r)}{dr} \right] = \left[\frac{dv_\theta}{dr} - \frac{v_\theta}{r} \right] \quad \text{Eqn. 20}$$

Solving Eqn. 17.b for the velocity profile and plugging in the boundary conditions shown, the velocity profile for a Newtonian fluid will be as in Eqn. 21:

1) At $r = r_i$, $v_\theta = \Omega r_i$

2) At $r= r_o$, $v_\theta = 0$

$$v_\theta = \frac{\Omega r_i^2 r}{r_o^2 - r_i^2}\left(\frac{r_o^2}{r^2} - 1\right) \qquad \text{Eqn. 21}$$

The stress calculatioun takes into account the measured torque, *M*. Based on the Lever rule, the torque is equal to the force and perpendicular distance from the axis of rotation: *M=F x d*. For the case of the inner rotation cylinder, *d*=r_i, and the force F=$\sigma_{\theta r}$x Area of inner cylinder (A_i). For a cylinder the area will be: $A_i = 2\pi r_i l$. Leaving the measured torque, M, to be:

$$M = \sigma_{\theta r}(2\pi r_i l) r_i = \sigma_{\theta r} 2\pi r_i^2 l \qquad \text{Eqn. 22}$$

The concentric cylinder geometry has a stress dependent on the radial position across the fluid gap, where the stress measurement at the inner cylinder is calculated as:

$$\sigma_{\theta r} = \frac{M}{2\pi r_i^2 l} \qquad \text{Eqn. 23}$$

The narrow gap assumption assumes a constant shear rate across the fluid gap. Typically for narrow gap geometry the curvature effects will be negligible hence, $\kappa = r_i/r_o$ will be a value $\kappa \geq 0.99$. When the curvature effects are negligible, a simplification of the calculation can be made by assuming that $r_i \approx r_o \approx \bar{r}$, ($\bar{r}$, the mean radius $\bar{r} = \frac{r_i + r_o}{2}$). Allowing the simplification of the position dependent shear rate in Eqn. 20 to obtain a radially independent shear rate that is constant throughout the fluid gap under this narrow gap assumption:

$$\dot{\gamma} = \frac{\Omega r_i}{r_o - r_i} \qquad \text{Eqn. 24}$$

The curvature for the geometry used in rheo-NMR studies in this work was $\kappa = 0.89$, classified in the limit of a fairly narrow gap ($0.5 < \kappa < 0.99$). However, the narrow gap assumption was proven justified in NMR experiments conducted by Kuczera *et al*. Here, a new curvature parameter, $q = (r_o\text{-}r_i)/r_i$, was introduced. The study found that in the limit of $q \ll 1$, deviations from a linear velocity profile were at most 2% with respect to the rotor wall velocity [37, 38]. Wherein the curvature parameter for the used concentric cylinder geometry in the rheo-NMR set up was $q = 0.125$, complying with the expected NMR velocimetry narrow gap assumption.

Cone and Plate Geometry

The cone-and-plate was introduced in 1934 by Mooney and Ewart [1, 39]. As the schematic in Figure 12 shows, this geometry consists of a lower stationery plate and an upper rotating cone. The upper rotating cone has a small cone angle, $\beta = 2^o$ (measured in radians for calculations), and is truncated to 54 μm at the tip. A very small (β <6° or 0.1 *rad*) cone angle means the shear rate and shear stress are considered constant throughout the fluid [1, 2]. The downside to having a small cone angle however is that the data can have errors due to misalignments and small eccentricities. Rheometers today combat this issue by a process known as rotational mapping prior to the start of an experiment where the geometry related errors are negated from the acquired data.

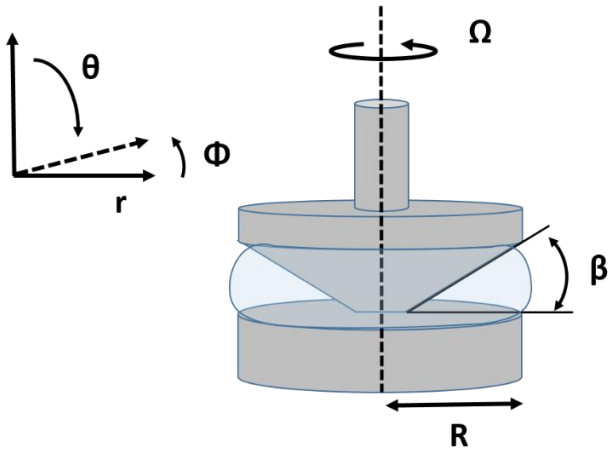

Figure 12: Schematic of a cone and plate geometry.

Conservation momentum equations for the cone and plate can be solved as was shown for the concentric cylinder geometry. The following quantification of the physics of the system are applied for the solution. Where under a small angle approximation (β <0.1 *rad*), assuming a steady laminar unidirectional and isothermal flow for a Newtonian fluid, the stress, $\sigma_{\phi\theta}$, calculated from the measured torque, M, for the cone and plate is [1]:

$$\sigma_{\phi\theta} = \frac{3M}{2\pi R^3} \qquad \text{Eqn. 25}$$

Where *R* is the radius of the cone-an-plate geometry. Followed by a shear rate defined as:

$$\dot{\gamma} \approx \frac{\Omega}{\beta} \qquad \text{Eqn. 26}$$

As can be seen from Eqn. 25 and 26, the shear stress and shear rate are independent of positon across the gap for the cone and plate geometry. The stress being proportional to the measured torque and the shear rate being purely dependent on the angular velocity, Ω (*rad/s*), and β(*rad*).

This equation has been effectively proven to provide accurate shear rate readings with an error of only 0.7% even at the highest small angle approximation ($\beta = 0.1$ rad) [40].

Functionality of the Rheo-NMR Magneto-Safe Portable Rheometer Motor

Three functional versions of the rheoNMR portable rheometer, also called drive shaft, is found at the MSU MRM lab that. A drive shaft that is capable of both oscillatory and steady shear flow (no torque measurements possible which was employed in most of the experiments in this thesis. A second rheometer capable of only steady unidirectional flow that has upgraded hardware that minimizes user errors in geometry attachments. Also a third advanced rheo-NMR rheometer capable of applying steady unidirectional deformation to a sample while also acquiring the torque responses of the fluids. Each rheometer is equipped with a concentric cylinder geometry of an inner rotor made of PEEK of radius 8mm and an outer stationary stator cup made of borosilicate of radius 9mm.

The rheometer capable of both oscillatory and steady flow, assembled in 2015, was used for three of the four projects in this thesis, hence will be discussed in detail. It is one of the only drive shafts that exists capable of subjecting an oscillatory motion on a sample suspended in the concentric cylinder shear cell in rheo-NMR. The main hardware components of this rheometer are: 1) the user computer, 2) the raspberry pi, 3) the ‘shield’ comprising the i) Aurdrino due and the ii)SAM3X printed circuit board (PCB), 4) the ST-23 stepper motor [41] with an 4)optical encoder and an 5) EvoDrive controller. Once all the wires have been connected, the user interacts with a guii on the computer. The commands input by the user are sent to a raspberry pi that contains an SD card bearing the operating system that runs the drive shaft’s motor. The raspberry pi processes the user’s commands and converts it to a readable form for the Aurdiuno

due mounted on top of the driveshaft next to the motor. Commands are sent via serial connection of RS485 (involves a communication method via long wire connections where data transfer is slow, however is less noisy and enables feedback loops) from the raspberry pi to the Arduino due. The Aurduino due together with the PCB reads software from the raspberry pi, processes it, converts the RS485 and sends the command via a UART connection (fast form of communication with higher noise possibility) to the Evo-Drive found on the motor.

The rheometer is equipped with a step motor that is a brushless DC motor capable of moving in 200 discrete points (1.8° discrete motions) requiring 2.8A of a winding current to complete [41]. This creates 200 discontinuities at each revolusion, hindering the resolution of the continuous motion. A micro stepping technique where the winding current output (the 2.8A current of each stepper motor step) is further stepped/discretized has been used to increase this resolution, however adding a risk. The risk being the possibility of skipping a micro step. To avoid this, the motor has a built in optical encoder that provides a feedback loop to the EvoDrive as to where in the assigned motion the rotor currently is at based on the step it previously made (its position vector). The EvoDrive controller applies corrections for any missed micro steps as required (this may contribute to a poor resolution of the flow between the two micro steps). Since a back and forth communication between the encoder and the EvoDrive is maintained, the time the EvoDrive has to come up with a correction is half the time for the resolution of the micro stepping. The step size for the servomotor is 2048 position vectors/revolution (0.176° steps). Leaving the EvoDrive only the time taken for the rotor to rotate 0.088° to assign the next velocity vector or make corrections to micro stepping errors (example time calculation shown below).

For the oscillatory motion concerned in this thesis for the strain amplitudes used with a period of 32 seconds, the resolution from the servo-stepper motor is 32,000 ms/ 2048 points = 15.6 ms/position vector point. Giving the optical encoder 15.6ms to send and recieve pulses for the assigned periodic motion. The accuracy of the position vector being guaranteed by the velocity commands sent out by the EvoDrive takes 7.8 ms. This may result in slight velocity offsets, if the modulation of the winding current is missed in a single or few micro steps (i.e. for the above example it would be offset by 7.8ms each time). It must be noted that the entire servo motor package was offered by Evarobotics in 2015, the references above are for the new company, Motion Control Products that sell the motors separately as Eva Robotics has discontinued the production of equipping the stepper motors with optical encoders and an EvoDrive since 2016.

The exclusively steady unidirectional shearing rheo-NMR rheometer, assembled in 2018, was designed with attachment pieces to reduce user errors from attaching the rotor improperly. This device was equipped with push in rotor attachments in place of the screw on attachments found in the previously discussed model. The motor of this model is able to appl steady shear in both the clockwise and anti-clockwise directions however only once the motor has been stopped between the flow reversals. It must be noted that this model does not support a continued oscillatory motion. This drawback is attributed to the change in communication style between the user interface and the shield. This communication form was integrated by T.I. Brox, in efforts to produce a faster communication mechanism (also to prevent injury to the raspberry pi and the shell which were exposed to people dropping the small units etc.) [10]. The chosen form of

communication then being UART made it possible to have all the commanding hardware together in a box. This rheometer was used in the project in chapter 4.

References

1. Macosko, C.W., *Rheology : principles, measurements, and applications*. 1994, New York: New York : Wiley-VCH.

2. Chhabra, R.P., Richardson, J.F. , *Non-Newtonian Flow in the Process Industries: Fundamentals and Engineering Applications*. 1999: Butterworth-Heinemann. 436.

3. Coussot, P., *Rheometry of Pastes, Suspensions, and Granular Materials: Applications in Industry and Environment.* JCT coatingstech, 2005. **4**(1): p. 306.

4. Janmey, P.A. and M. Schliwa, *Rheology.* CURR BIOL, 2008. **18**(15): p. R639-R641.

5. Astarita, G., G. Marrucci, and L. Nicolais, *Rheology: Principles*. 2013, New York, NY: New York, NY: Springer.

6. Poole, R.J., *The Deborah and Weissenberg numbers.* The British Society of Rheology, 2012. **2**(53): p. 32-39.

7. Barnes, H.A., Hutton, J.F., and Walters, K., *An Introduction to Rheology*. 1989: Elsevier :, Distributors for the U.S. and Canada, Elsevier Science Pub. Co. 201.

8. Astarita, G., *Rheology Volume 1: Principles*, G. Marrucci and L. Nicolais, Editors. 1980, New York, NY : Springer US : Imprint: Springer.

9. Franck, A., *Viscoelastic and dynamic mechanical testing* AN004-TA Instruments.

10. Brox, T.I., *New Methods for Studying Materials Under Shear with Nuclear Magnetic Resonance*, in *Physics*. 2016, Victoria University of Wellington.

11. Spagnolie, S.E., *Complex Fluids in Biological Systems Experiment, Theory, and Computation*. 2015, New York, NY : Springer New York : Imprint: Springer.

12. Morozov, A. and S.E. Spagnolie, *Introduction to Complex Fluids*, in *Complex Fluids in Biological Systems: Experiment, Theory, and Computation*, S.E. Spagnolie, Editor. 2015, Springer New York: New York, NY. p. 3-52.

13. Dreisbach, D., *Statistical Theory of Liquids (Fisher, I. Z.).* J. Chem. Educ, 1966. **43**(10): p. A912.

14. Marx, N., et al., *Shear Thinning and Hydrodynamic Friction of Viscosity Modifier-Containing Oils. Part I: Shear Thinning Behaviour.* Tribol Lett, 2018. **66**(3): p. 1-14.

15. Guvendiren, M., Lu, H.D. and Burdick, J.A., *Shear-thinning hydrogels for biomedical applications.* Soft Matter, 2012. **8**.

16. Barnes, H.A. and K. Walters, *The yield stress myth?* Rheologica acta, 1985. **24**(4): p. 323-326.

17. Coussot, P., *Yield stress fluid flows: A review of experimental data.* J NON-NEWTON FLUID, 2014. **211**: p. 31-49.

18. Alexandrou, A.N., N. Constantinou, and G. Georgiou, *Shear rejuvenation, aging and shear banding in yield stress fluids.* J NON-NEWTON FLUID, 2009. **158**(1): p. 6-17.

19. Larson, R.G., *The structure and rheology of complex fluids*. 1999, New York: New York: Oxford University Press.

20. Nelson, A.Z., *Rheology and Design of Yield-Stress Fluids*. 2018, ProQuest Dissertations Publishing.

21. R. Varges, P., et al., *Rheological Characterization of Carbopol® Dispersions in Water and in Water/Glycerol Solutions.* Fluids (Basel), 2019. **4**(1): p. 3.

22. Piau, J.M., *Carbopol gels: Elastoviscoplastic and slippery glasses made of individual swollen sponges Meso- and macroscopic properties, constitutive equations and scaling laws.* J NON-NEWTON FLUID, 2007. **144**(1): p. 1-29.

23. Malvern Instruments Limited, S.p., *Understanding Yield Stress Measurements.* White paper, 2012.

24. Franck, A., *Understanding Rheology of Structured Fluids.* AAN016-TA Instruments.

25. Barry, B.W., Meyer, M.C., *The rheological properties of carbopol gels I. Continuous shear and creep properties of carbopol gels.* Int. J. Pharm. **2**(1): p. 1-25.

26. Hyun, K., et al., *A review of nonlinear oscillatory shear tests: Analysis and application of large amplitude oscillatory shear (LAOS).* Progress in Polymer Science, 2011. **36**(12): p. 1697-1753.

27. Ptaszek, P., *Chapter 5 - Large Amplitude Oscillatory Shear (LAOS) Measurement and Fourier-Transform Rheology: Application to Food*, in *Advances in Food Rheology and Its Applications*, J. Ahmed, P. Ptaszek, and S. Basu, Editors. 2017, Woodhead Publishing. p. 87-123.

28. Ferry, J.D.a.H.S.M., *Viscoelastic Properties of Polymers.* Journal of The Electrochemical Society, 1961. **108**(7).

29. Hyun, K., et al., *Large amplitude oscillatory shear as a way to classify the complex fluids.* J NON-NEWTON FLUID, 2002. **107**(1): p. 51-65.

30. Nettesheim, F. and S.A. Rogers, *The unification of disparate rheological measures in oscillatory shearing.* PHYS FLUIDS, 2019. **31**(7): p. 73107.

31. Dodge, J.S., *OSCILLATORY SHEAR OF NONLINEAR FLUIDS*. 1969, ProQuest Dissertations Publishing.

32. Nam, J.G., et al., *Prediction of normal stresses under large amplitude oscillatory shear flow*. J NON-NEWTON FLUID, 2008. **150**(1): p. 1-10.

33. Carotenuto, C., M. Grosso, and P.L. Maffettone, *Fourier Transform Rheology of Dilute Immiscible Polymer Blends: A Novel Procedure To Probe Blend Morphology.* MACROMOLECULES, 2008. **41**(12): p. 4492-4500.

34. Mas, R. and A. Magnin, *Experimental validation of steady shear and dynamic viscosity relation for yield stress fluids.* Rheol Acta, 1997. **36**(1): p. 49-55.

35. Ewoldt, R.H., et al., *Large amplitude oscillatory shear of pseudoplastic and elastoviscoplastic materials.* Rheol Acta, 2010. **49**(2): p. 191-212.

36. Bird, R.B., *Transport phenomena*. 2nd ed.. ed, ed. W.E. Stewart and E.N. Lightfoot. 2002, New York: New York : J. Wiley.

37. Kuczera, S. and P. Galvosas, *Advances and artefact suppression in RARE-velocimetry for flow with curved streamlines.* J MAGN RESON, 2015. **259**: p. 135-145.

38. Brox, T., et al., *Observations of the influence of Taylor-Couette geometry on the onset of shear-banding in surfactant wormlike micelles.* Journal of Rheology, 2016. **60**(5): p. 973-982.

39. Mooney, M. and R.H. Ewart, *The Conicylindrical Viscometer.* Physics (New York. 1931), 1934. **5**(11): p. 350-354.

40. Adams, N. and A.S. Lodge, *Rheological Properties of Concentrated Polymer Solutions II. A Cone-And-Plate and Parallel-Plate Pressure Distribution Apparatus for Determining Normal Stress Differences in Steady Shear Flow.* Phil. Trans. R. Soc. Lond. A, 1964. **256**(1068): p. 149-184.

41. Products, M.C. *NEMA 23 High Torque Stepper Motors Hybrid Stepper Motor*. 2021; Available from: https://www.motioncontrolproducts.com/electric-motors/stepper-motors/hybrid-stepper-motors/nema-23-high-torque-stepper-motors/.

CHAPTER FOUR

RHEO-NMR OF TRANSENT AND STEADY STATE SHEAR BANDING UNDER SHEAR STARTUP

Contribution of Authors and Co-Authors

Manuscript in Chapter 4

Author: Rehab N. Al-Kaby

Contributions: Wrote manuscript. Helped in designing the experiment. Prepared samples, collected, and analyzed Rheo-NMR data.

Co-Author: Jayesha S. Jayaratne

Contributions: Prepared samples. Collected and analyzed Rheology measurements.

Co-Author: Timothy I. Brox

Contributions: Rheo-NMR equipment designer. Provided feedback and comments on the manuscript.

Co-Author: Sarah L. Codd

Contributions: Helped conceive and designed the experiment. Discussed and helped with data interpretation. Provide feedback and comments on the manuscript.

Co-Author: Joseph D. Seymour

Contributions: Helped conceive and implement study design. Discussed the data and provide feedback on the manuscript.

Co-Author: Jennifer R. Brown

Contributions: Helped conceive and designed the experiment configuration. Secured funding. Discussed and helped with data interpretation. Provide feedback and comments on the manuscript.

Manuscript Information

Rehab N. Al-Kaby, Jayesha S. Jayaratne, Timothy I. Brox, Sarah L. Codd, Joseph D. Seymour, Jennifer R. Brown

Journal of Rheology

Status of Manuscript:
___ Prepared for submission to a peer-reviewed journal
___ Officially submitted to a peer-reviewed journal
___ Accepted by a peer-reviewed journal
_X_ Published in a peer-reviewed journal

The Society of Rheology, Inc.

62(5), 1125–1134 September/October (2018)

RHEO-NMR OF TRANSENT AND STEADY STATE SHEAR BANDING

Abstract

In this work shear band formation following shear startup as a function of flow protocol are investigated in the wormlike micelles (WLMs) system of 6 wt. % cetylpyridinium chloride (CPCl) and sodium salicylate (NaSal) in 0.5 M NaCl brine in a Couette Rheo-NMR shear cell. 1D velocity profiles across the 1 mm fluid gap are recorded every 1 s after shear startup using Rheo-NMR velocimetry and used to evaluate shear banding characteristics, including the shear rates in the low and high shear band, the interface position and the apparent wall slip. The velocity, and therefore the shear banding characteristics, exhibit large temporal fluctuations following an abrupt start-up to 12 s^{-1} due to apparent slip at the inner rotating wall and the presence of flow instabilities. Characteristic time scales were used to characterize the transition of the flow from transient to steady state and the Fourier transform of time autocorrelation functions was used to quantify fluctuation frequencies. Shear start-up experiments were performed for flow protocols with and without pre-shear. Pre-shear resulted in different magnitudes of the timescales and a shift in the frequencies of the fluctuation of all shear banding characteristics.

Introduction

In an aqueous solution and under certain conditions, surfactant molecules can self-assemble into the semi flexible, elongated, and rod-shaped aggregates called wormlike micelles (WLMs) [1, 2]. At high enough concentrations, they form a viscoelastic entangled network similar to polymers but with an ability to dissociate and recombine dynamically [3]. In 1991, Rehage and

Hoffmann [2] pointed out that some of those systems obey a robust Maxwellian viscoelastic model; *i.e.*, in contrast to polymer solutions that exhibit a wide range of relaxation times, they have a single relaxation time λ_R at small deformations [4]. This unique mechanical response time is predicted based on the reptation-reaction kinetics model in the fast-breaking regime, where the breaking and reformation events are faster than reptation [5]. Hence, the breakage and reptation relaxation mechanisms are characterized by the time scales of λ_{break} and λ_{rep}, respectively and the relaxation time is of the order $\sqrt{\lambda_{break}\lambda_{rep}}$ [6]. Due to the simple viscoelastic behavior of WLM systems and the fact that they are relatively easy to prepare and not generally susceptible to aging or degradation, they have become of significant interest for wide studies using different experimental techniques [7-9].

The nonlinear rheological behavior of WLMs is highly complex. When subjected to shear stresses, semi dilute and concentrated wormlike micelle solutions can exhibit an unusual mechanical response where the flow organizes into two macroscopic bands with distinct viscosities and local shear rates along the velocity gradient direction [10, 11]. This nonlinear transition is called shear banding and associated with the existence of a stress plateau in the steady state flow curve that occurs between two critical shear rates [12, 13]. Below the first critical shear rate $\dot{\gamma}_l$ and beyond the second critical shear rate $\dot{\gamma}_h$ the flow is homogeneous and the shear stress increases monotonically with the shear rate. Between the two critical shear rates, the flow becomes heterogeneous, forming shear bands, and stress stays nearly constant or varies slightly depending on the curvature of the flow geometry [14]. This plateau stress is independent of the flow history [15, 16]. When wall slip is negligible, the shear banded flow is usually assumed to follow a simple lever rule $\dot{\gamma}_a = \alpha\dot{\gamma}_h + (1-\alpha)\dot{\gamma}_l$, where $\dot{\gamma}_a$ is the applied shear rate,

$\dot{\gamma}_h$ is the shear rate in the high shear band, $\dot{\gamma}_l$ is the shear rate in the low shear band and α is the proportion of the fluid gap occupied by the high shear rate, or the interface position. The high and low shear rates, $\dot{\gamma}_h$ and $\dot{\gamma}_l$, correspond to the start and end of the stress plateau in the flow curve.

This nonlinear transition is widely observed in different complex fluids where applied shear changes the internal molecular microstructure and induces shear banding [17-19], including polymer solutions [20, 21], foams [22, 23], emulsions [24], colloidal glasses [25, 26], as well as in granular materials [27, 28]. Shear banding is thought to occur mainly due to the coupling of the microstructure and the flow field [29]. There is a rich literature that focuses on the shear-banding flow of wormlike micelles and their dynamics are well documented [30, 31] with experimental techniques like nuclear magnetic resonance NMR [32-34], particle image velocimetry PIV [14, 35], and ultrasonic velocimetry USV [36, 37]. Numerous early studies showed an interplay between wall slip and the shear banded flow in 1D velocity profiles [38-40]. Later experimental studies reported the existence of temporal fluctuations in the velocity [41-44]. Most recently, 2D flow visualizations revealed that the shear banded flow is hydro dynamically unstable, resulting in development of secondary flows [45-47]. In the stress plateau, the instability manifests initially as vortices in the high shear band [48] that cause undulations in the interface position along the vorticial direction and at higher shear rates, the occurrence of turbulent bursts [49]. Periodic or chaotic fluctuations observed previously in the velocity with 1D measurements could be attributed to the 3D nature of the flow field. Shear banded flow therefore involves not only temporal dynamics, but also a spatial heterogeneity.

As many of the applications using WLM solutions occur under time dependent conditions, such as startup or in complex geometries, work has been devoted to studying shear banding under time dependent flow protocols. For example, in shear startup is where an applied shear rate is imposed at a constant rate for all times $t > 0$ [50, 51], while in a strain ramp, the sample is sheared until a desired strain amplitude is reached [52-54]. A step stress protocol is performed by applying a constant stress for a certain amount of time [14, 55].

In this work, we use Rheo-NMR to obtain 1D velocity profiles across the fluid gap of a concentric cylinder shear cell as a function of time following shear startup at an applied shear rate within the stress plateau. We analyze the evolution of the shear banded flow from transient to steady state and the impact of pre-shear on the fluid response following the shear startup.

Materials and Methods

Sample Preparation

The wormlike micelle system investigated in this work is a 6 wt. % cetylpyridinium chloride (CPCl) and sodium salicylate (NaSal) solution with a molar ratio [NaSal]/[CPCl] = 0.5 in 0.5 M NaCl-brine. Furthermore, 0.2 % $GdCl_3$ was added to reduce the ^1H NMR relaxation time to facilitate faster acquisition of NMR velocity profiles. The rheological measurements show that the addition of 0.2 % $GdCl_3$ had no noticeable influence on the mechanical behavior of the sample. All the materials were purchased from Sigma-Aldrich. The sample was prepared by mixing all components for 120 min at a temperature of 45 ˚C. The samples were then stored at 30 ˚C in a container preventing ambient light exposure conditions for at least 1 month before the experiments. This system has been extensively studied and is well-known to form elongated wormlike micelles [15].

Rheometry

The linear and nonlinear rheological measurements were performed using a TA instruments AR-G2 rheometer equipped with a steel cone-and-plate geometry with a 60 mm diameter and a 2˚ angle. Experiments were run at 25˚C and under a controlled strain. The linear viscoelastic measurement is shown in Figure 1, exhibiting a single mode Maxwellian behavior with characteristic relaxation time λ_R = 0.436 s and plateau modulus G_o = 100 Pa.

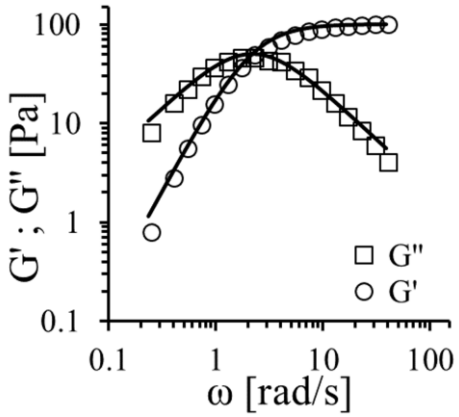

Figure 1: Storage and loss moduli as a function of frequency at a fixed 5% strain for 6 wt. % CPCl/NaSal in 0.5 M NaCl-brine. The data measured at T=25 °C using a cone-and-plate geometry. The solid lines are fits to the Maxwell model with λ_R = 0.436 s and G_o = 100 Pa.

This sample exhibits shear banding in the stress plateau region of the steady-state flow curve and a transient stress overshoot under shear startup within a few seconds [14, 56]. Figure 2 (a) and (b) show the nonlinear rheology of 6% CPCl/NaSal under the steady state and transient conditions respectively. The steady flow curve (Figure 2a) exhibits a stress plateau that extends from $\dot{\gamma}_l \approx 2.6$ s^{-1} to $\dot{\gamma}_h \approx 24$ s^{-1}. The values of $\dot{\gamma}_l$ and $\dot{\gamma}_h$ were found by the same means as in Salmon *et al.* [40] and are in good agreement with those reported in the literature [46]. Figure 2b depicts the transient shear stress response after shear startup to $\dot{\gamma}$ = 12 s^{-1}. The shear stress

exhibits a significant overshoot (culminates up to 90 Pa) within a time less than 2 s, followed by a decrease until the steady-state value is obtained. However, a slow increase in stress just prior to steady state is observed, see inset Figure 2b. This dynamic feature is known as a "stress undershoot" and has been shown to appear in some cases after a critical shear rate [57]. To the best of our knowledge, the small undershoot has only been highlighted by Berret *et al.* [15] on different CPCl/NaSal/brine samples and by Lerouge and coworkers[58] on the wormlike micelle solution formed by the surfactant cetyltrimethylammonium bromide (CTAB).

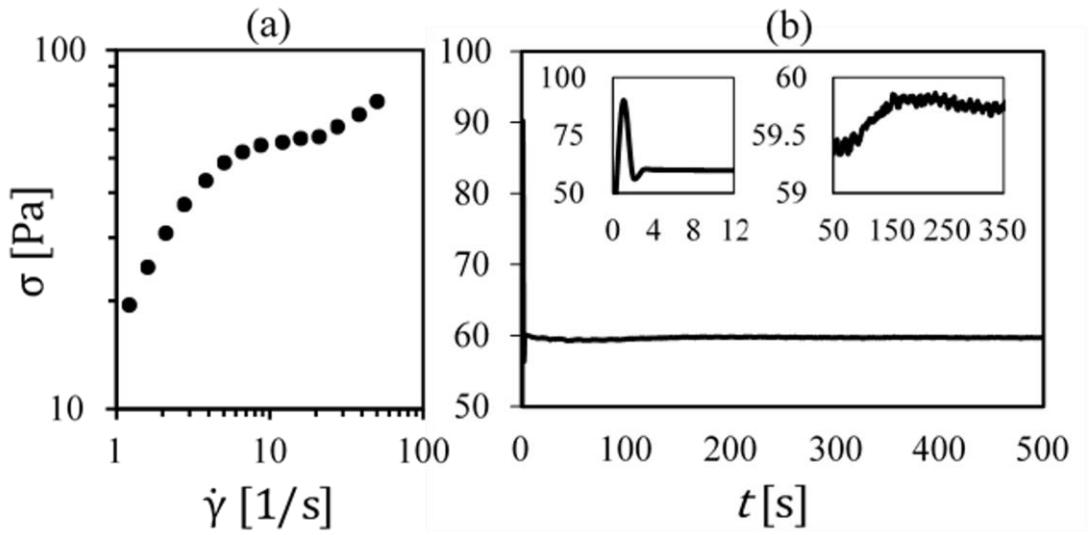

Figure 2. Bulk rheometry for 6% CPCl/NaSal wormlike micelle solution. (a) Stress vs applied shear rate exhibiting the stress plateau characteristic of shear banding that extends from $\dot{\gamma}_l \approx 2.6$ s^{-1} to $\dot{\gamma}_h \approx 24$ s^{-1} and (b) Stress as a function of time following *shear startup* to 12 s^{-1}. A large initial stress overshoot occurs in the first two seconds following *shear startup* and a small stress undershoot is observed at later times, as shown in the insets.

Rheo-NMR

Rheo-NMR experiments were performed in a Rheo-NMR Couette cell comprised of a glass stator and a polyether ether ketone (PEEK) rotor with a roughened cross hatched surface. The

outer and inner radii of the shear cell were R_o = 9 and R_i = 8 mm, respectively, resulting in a fluid gap of 1 mm and a radius ratio ($\kappa = R_i / R_o$) of 0.89. All Rheo-NMR measurements are carried out at T = 22˚C, above the Krafft temperature of 21.5˚C. A Thermo Electron Corporation (Merline M25) recirculating chiller was used to control the temperature and a thermocouple interred inside the NMR probe at the base of the resonator coil and bottom of the Rheo-NMR shear cell was used to measure the temperature by converting the sensor signal to a digital temperature reading.

A Bruker AVANCE 300 spectrometer equipped with a Micro-2.5 gradient system (maximum Gradient: 1.5 T/m 60A) and a 25 mm birdcage resonator coil, along with Bruker Topspin software, was used to acquire all Rheo-NMR data. The data analysis was performed using Prospa (Magritek, Wellington NZ) software. Pulsed gradient spin echo (PGSE) motion encoding was employed [59] with double slice selection and 1D image acquisition as depicted in Figure 3 [60]. All experiments had rf pulse durations of 52 μs for the 90^0 excitation pulse and 104 μs for the two 180^0 refocusing pulses, echo time TE = 55 ms and repetition time TR = 217 ms. 1D velocity profiles were acquired across the fluid gap (velocity gradient direction; x-axis) with spatial resolution of 59 μm (FOV = 30 mm and 512 points). The imaging region (Figure 3b) is a slab consisting of a 10 mm thick slice selected along the vorticity direction (z-axis) and a 1 mm thick slice along the velocity direction (y-axis). Velocity was measured in the direction of flow (y-axis) with displacement observation time Δ = 11 ms, magnetic field gradient pulse duration δ = 1 ms and two flow encoding gradient steps.

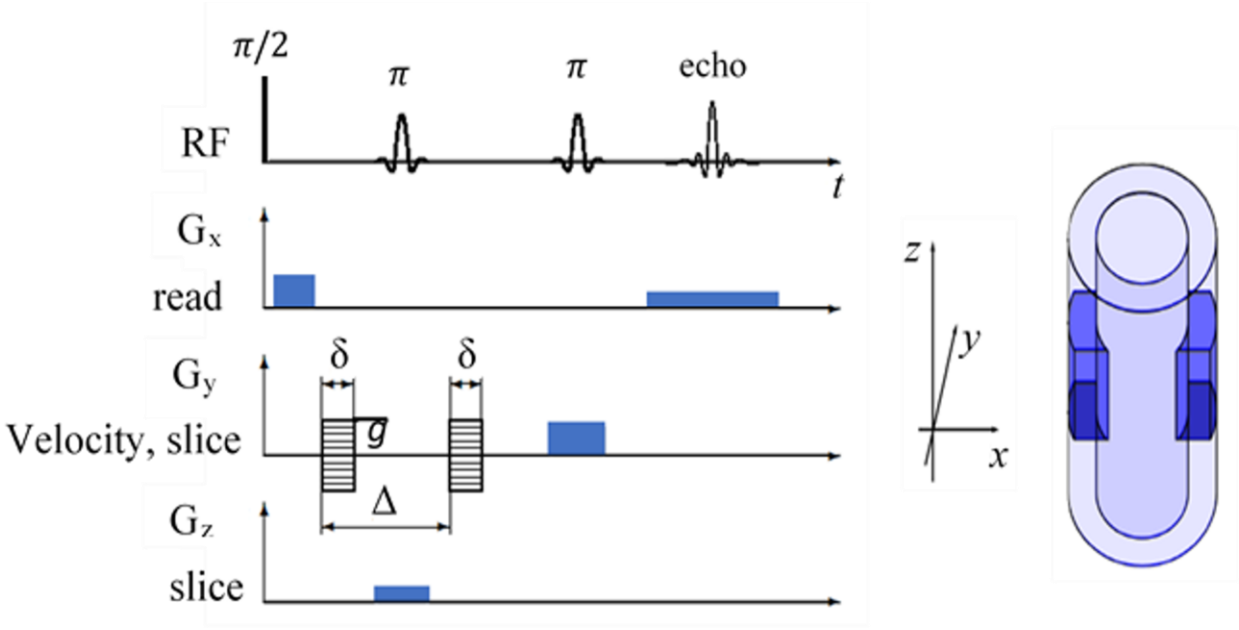

Figure 3: (a) Timing diagram for collecting a 1D velocity image across the fluid gap of the Couette cell using PGSE motion encoding with double slice selection. A 10 mm thick slice was selected along the vorticity direction (z-axis) and a 1 mm thick slice along the velocity direction (y-axis) in order to acquire data from the imaging region shown in the shaded section of the Couette schematic (b). The 1D image was acquired across the fluid gap in the velocity gradient direction (x-axis) with spatial resolution of 59 μm/pixel. Velocity was measured in the direction of flow (y-axis) with displacement observation time Δ = 11 ms and δ = 1 ms.

Experimental Protocols

In this work, we compare results from two different experimental protocols:

- Protocol 1 (no pre-shear): between each shear startup experiment, the sample was at rest for a wait time t_w = 300 min, in order to allow the system to return to an isotropic equilibrium state.

- Protocol 2 (with pre-shear): prior to each shear startup experiment, a pre-shear of 10 s^{-1} was applied for 1 min, followed by 2 min of rest. This protocol has been used previously in the literature in an attempt to ensure homogenization [55].

Results

In order to correlate the bulk mechanical stress response with the shear banding flow behavior of 6% CPCl/NaSal 1D velocity profiles are acquired across the fluid gap of a Rheo-NMR concentric cylinder Couette geometry under shear startup conditions. Figure 4a shows a representative shear startup experiment where 1D velocity profiles were acquired with a time resolution of 1 s following shear startup at 12 s^{-1}. There are fluctuations in the velocity with time due at least partially to apparent slip at the inner rotating wall and the presence of flow instabilities [46]. As this is a 1D measurement averaged over a 10 mm slice in the vorticial direction, the three dimensional flow due to axial velocity contributes to fluctuations in the measured velocity [46].

In the initial few seconds, corresponding to the large stress overshoot in the bulk mechanical response (Figure 2b), the velocity profile is linear (Figure 4b). The shear bands then begin to form, with the high shear band growing and the interface between the bands migrating further into the fluid gap until it reaches its steady state position. The steady state position can be roughly predicted with the lever rule as long as wall slip is not present.

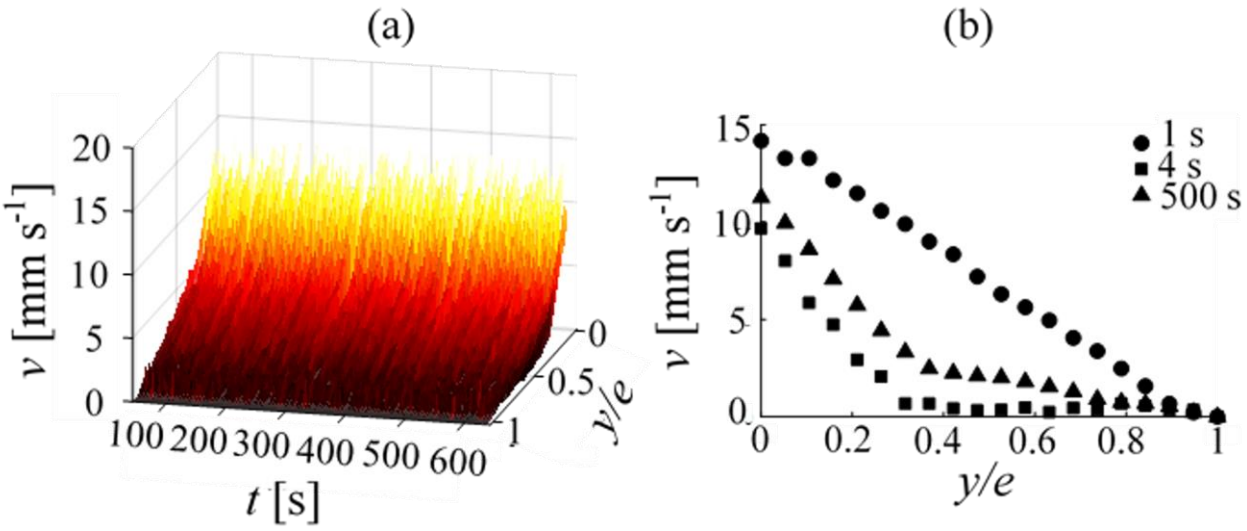

Figure 4: (a) 1D velocity profiles across the normalized fluid gap *y/e* as a function of time following *shear startup* at a shear rate of 12 s^{-1}, where *e* refers to the fluid gap width of 1 mm. The velocity fluctuates with time and exhibits apparent slip at the inner rotating wall. (b) 1D velocity profiles across the normalized fluid gap *y/e* at 1s, 4 s and 500 s after *shear startup*. The velocity at 1 s, prior to shear banding during the initial stress overshoot, exhibits a linear profile. By 4 s, shear bands have begun to form and the interface position is in the process of migrating from the inner rotating wall to its steady state position, shown for the profile at 500 s.

Here we identify timescales of the fluctuations in velocity and of the transient response. Even though we are limited by a 1D measurement, we attempt to extract information about the evolution of the flow from transient to steady state as well as about the instabilities that give rise to 3D flow by using a Reynolds decomposition approach [61], where we split the measured values into an average and the deviation from the average, *i.e*. the fluctuation. Since it is difficult to obtain velocity information with both high temporal and spatial resolution due to inherent limitations in the measurement methods, we choose to quantify and characterize the nature of both average quantities and the fluctuations in order to reveal insight into the flow behavior.

WLM solutions are known to exhibit memory. In other words, the fluid response depends on the shear history of a given sample[62] and this will impact the transient response in particular [63]. To fully characterize the impact of shear history on the transient and steady state flow behavior, a protocol used by Lopez-Barron *et al.* [55] in a previous study utilizing pre-shear is compared to one for samples without any shear history.

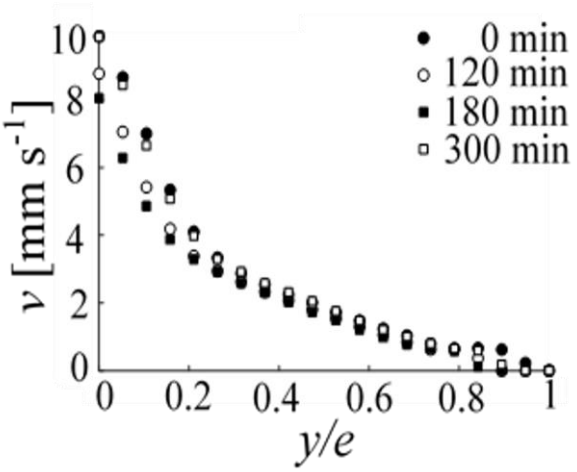

Figure 5: Velocity vs normalized fluid gap *y/e*. The 1D velocity profiles are time averaged over the last 2.12 min of the 10.6 min *shear startup* experiment to ensure the flow is at steady state and to average over fluctuations in the velocity. Profiles are shown for wait times t_w between experiments of 0 min (no shear history; filled circles), 120 min (open circles), 180 min (filled squares) and 300 min (open squares). After 300 min, the velocity profile overlays that for the sample without shear history, indicating a return to an equilibrium state.

To ensure that no shear history was present, shear startup experiments were performed with increasing wait time t_w between the experiments. The sample was assumed to be free of memory when no differences in the shear banded flow were observed as compared to the results from a fresh sample that had been at rest following sample loading into the Couette shear cell for > 12 hrs. Figure 5 shows 1D velocity profiles as a function of wait time across the fluid gap,

time averaged over the last 2.12 min of the 10.6 min shear startup experiment to ensure the flow was at steady state and to average over fluctuations in the velocity, as a function of wait time t_w. After 300 min wait time, the velocity profiles overlap within experimental error, indicating that the sample had returned fully to its equilibrium state at t_w=0.

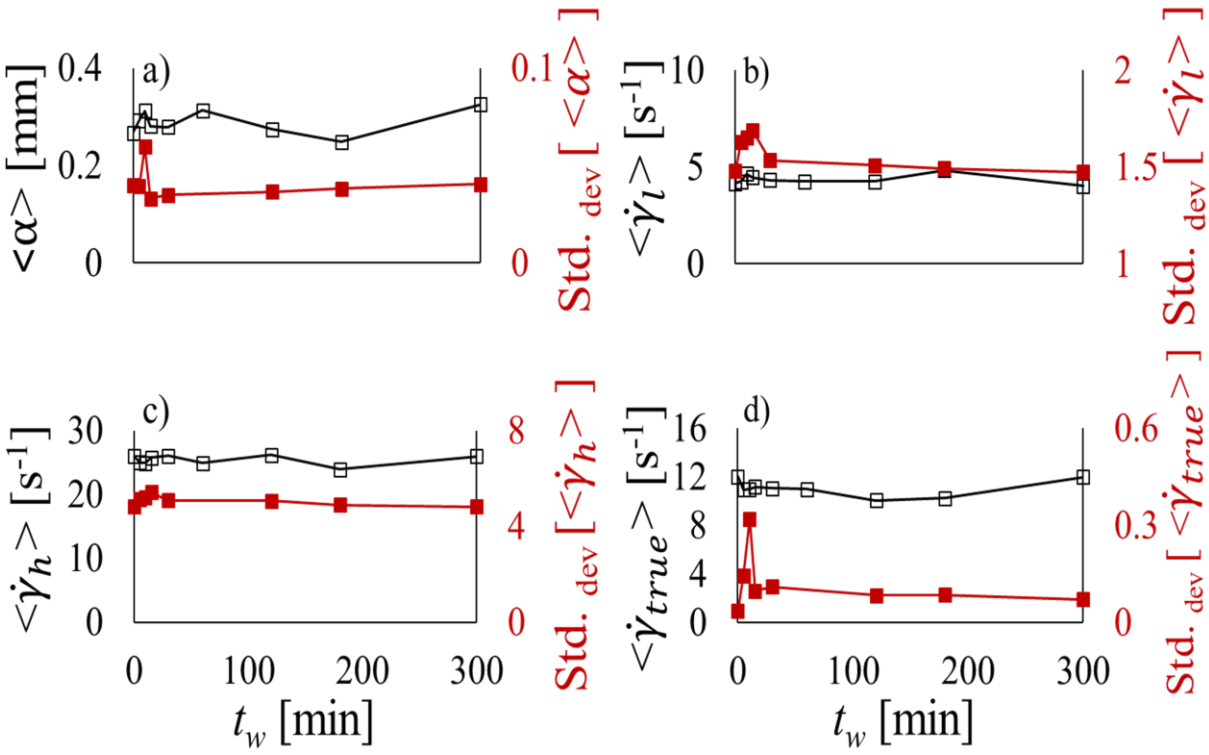

Figure 6: Shear banding characteristics (open symbols) and the standard deviation (closed symbols) as a function of wait time t_w. Lines are to guide the eye. (a) the interface position α (b) the shear rate in the low shear band $\dot{\gamma}_l$, (c) the shear rate in the high shear band $\dot{\gamma}_h$ and (d) the true shear rate $\dot{\gamma}_{true}$, which is a measure of apparent wall slip. The standard deviation becomes constant after 30 min.

To further evaluate how long a sample must be at rest to be rid of shear history, the velocity profiles were analyzed to quantify the characteristics of the shear banded flow. The shear rate in the high and low band, the interface position and the amount of apparent wall slip were

monitored as a function of t_w. The regions of high and low shear in the 1D velocity profiles were fitted linearly with the slopes of the lines being the values of the shear rate $\dot{\gamma}_h$ and $\dot{\gamma}_l$ for the high and low shear band respectively. The intersect of the lines was considered the interface position α and to evaluate the apparent wall slip, following Fardin *et al.* [57], a "true" shear rate $\dot{\gamma}_{true}$ was calculated as $\dot{\gamma}_{true} = |v(0)\text{-}v(e)|/e$ where e is the gap width. The shear banding characteristics obtained from the time averaged velocity profiles (as shown in Figure 5) are plotted in Figure 6 as a function of t_w. The values change the most significantly in the first 30 min. Also plotted in Figure 6 is the standard deviation from the average taken over the final 2.12 min of the experiment. After 30 min wait times, the standard deviation stays constant, another indication that shear history is having minimal impact on the characteristics of the flow.

While the individual velocity profiles we obtained didn't overlap exactly until t_w = 300 min, the primary characteristics of the flow (α, $\dot{\gamma}_h$, $\dot{\gamma}_l$, and $\dot{\gamma}_{true}$) stay the same after a t_w = 30 min, indicating the sample has returned to an equilibrium state (*i.e.* is no longer dependent on shear history) within 30 min. Experimental noise and sample to sample variation could account for small changes to the individual velocity profiles, so using the characteristics features of the flow seems a practical method to evaluate the impact of shear history. In the following results, a wait time of 300 min was used, but future studies could be made more time efficient by using a 30 min wait time.

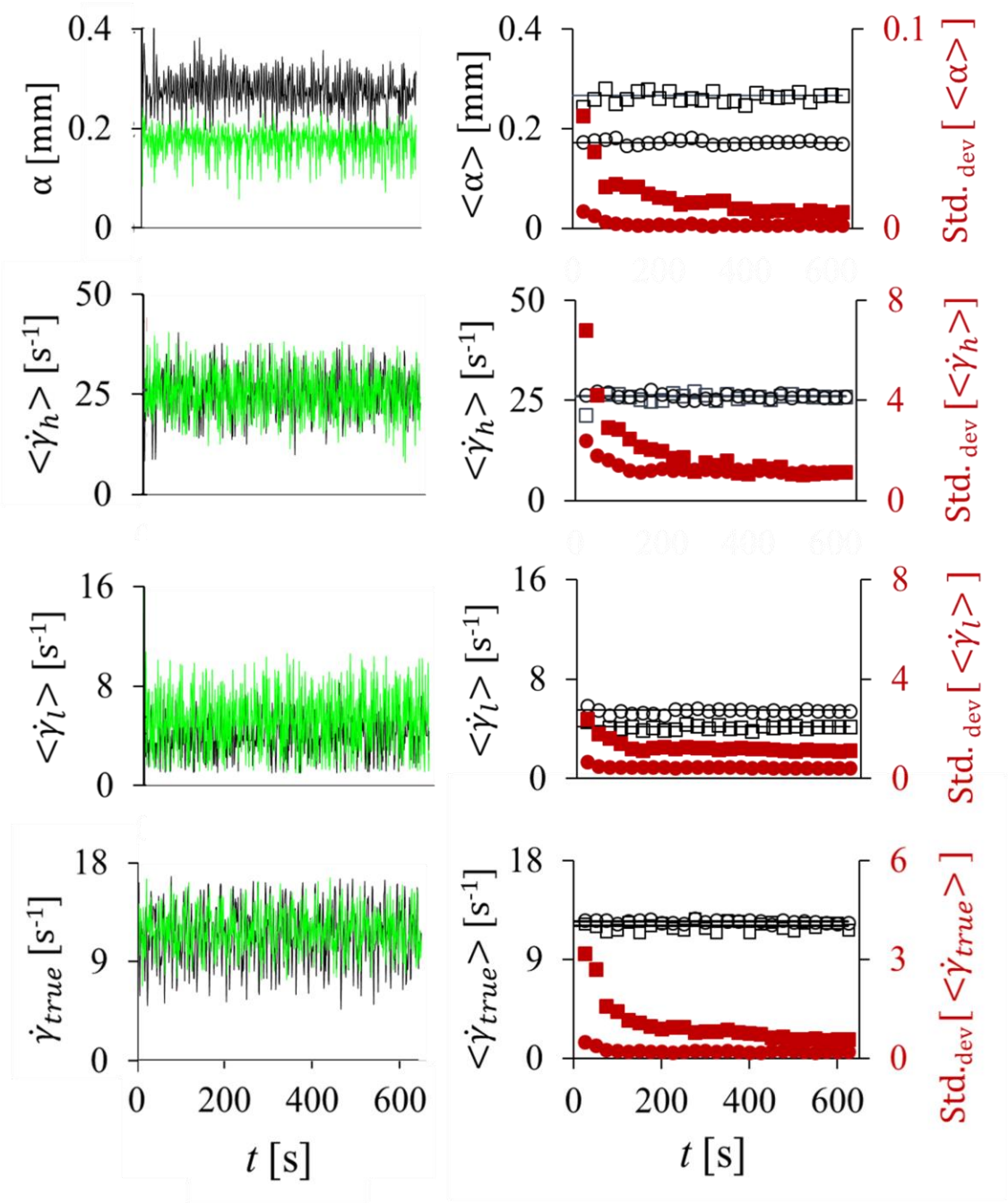

Figure 7: Left panels: top to bottom is the interface position α (a), the shear rate in the high shear band $\dot{\gamma}_h$ (c), the shear rate in the low shear band $\dot{\gamma}_l$ (e) and the true shear rate $\dot{\gamma}_{true}$ (g) obtained from 1D velocity profiles acquired every 1 s as a function of time following *shear startup* to 12 s^{-1}. The black line is protocol 1 (no shear history) and the green line is protocol 2 (with shear history). There are large fluctuations with time. Right panels: top to bottom is α (b), $\dot{\gamma}_h$ (d), $\dot{\gamma}_l$ (f), and $\dot{\gamma}_{true}$(h) averaged over 25 s, a timescale larger than that for the fluctuations. Protocol 1 are open black squares and protocol 2 are open black circles. Solid lines represent the

average values for the entire experiment (Protocol 1: $\dot{\gamma}_h$= 26 s^{-1}, $\dot{\gamma}_l$ =4.2 s^{-1}, α =0.27 and $\dot{\gamma}_{true}$ = 12 s^{-1}; Protocol 2: $\dot{\gamma}_h$= 26 s^{-1}, $\dot{\gamma}_l$ =5.5 s^{-1}, α =0.17 and $\dot{\gamma}_{true}$ = 12.5 s^{-1}). Closed red symbols are the standard deviations within each 25 s period. For protocol 1, the standard deviation decreases rapidly in early times (t < 75 s), then at a slower rate (until t ~200-400 s) and finally is minimized (t > 400 s). For protocol 2, the standard deviation rapidly decreases to reach its minimal value by t = 100 s.

The left panels of Figure 7 show the primary characteristics of the flow (α, $\dot{\gamma}_h$, $\dot{\gamma}_l$, and $\dot{\gamma}_{true}$) obtained from 1D velocity profiles acquired every 1 s following abrupt shear startup to 12 s^{-1} (Figure 4) for shear startup protocols without pre-shear (protocol 1) and with pre-shear (protocol 2). The velocity, and therefore corresponding shear banding characteristics, show large fluctuations with time due to apparent slip and hydrodynamic instabilities. Taking a Reynolds decomposition approach [61], where variables are decomposed into a time-averaged quantity and a fluctuation about the time average, the velocity profiles were averaged over 25 s and the shear banding characteristics for these profiles are plotted in the right panels of Figure 7. The closed symbols are the coarse-grained time averaged values of the shear banding characteristics, while the solid lines are the average over the entire experiment. This approach was taken in order to extract any timescales in the system for characterizing the evolution from transient to steady state that are obscured by the fluctuations. As with any coarse graining approach, the averaging time must be carefully selected to be longer than the fluctuation timescale τ_f, but shorter than any other timescale that would yield information. Also shown (red closed symbols) is the standard deviation of the 25 s time averaged values from the overall mean. The standard deviation more clearly reveals the changes in the shear banding characteristics with time.

As noted previously, shear bands begin to form after the first 2 seconds (Figure 4b), corresponding to the initial large stress overshoot (Figure 2b). The interface position then

migrates to its steady state position within the fluid gap. Previous work has similarly shown linear velocity profiles during the stress overshoot [14, 43, 64] and identified a long lived "metastable" state several hundred seconds long, where the interface position migrates to its steady state position and flow instabilities develop prior to settling into a steady state [45]. We define the timescale to reach this steady state as τ_{ss}. During the metastable regime, several features of the stress have been observed [65, 66], including a stress undershoot [67] as observed for the system for a shear startup at 12 s^{-1} (Figure 2b).

The metastable regime could be broken down into several parts, each with different features in the stress and the flow behavior. Shear bands form and the interface position migrates to its steady state mean value (the solid line) within ~25 s. The standard deviation, i.e. the fluctuation or oscillation about the mean value, is initially at its highest value and decreases rapidly for a timescale we will designate as τ_{trans} ~=75-100 s. Beyond ~75-100 s, the standard deviation shows a more gradual change until ~200-250 s, where it finally plateaus to a minimum value. The more gradual change in deviation from the mean would correspond to the metastable state where the stress undershoot occurs, which has been deemed a mechanical signature of the onset and development of flow instabilities [58]. The minimization of the standard deviation indicates that the overall flow behavior, despite the presence of 3D flow from instabilities and the resulting velocity fluctuations in a 1D measurement, is no longer changing with time and we have reached a steady state. Therefore, the steady state timescale τ_{ss}~= 200-250 s. This behavior is reflected in $\dot{\gamma}_h$, $\dot{\gamma}_l$, and $\dot{\gamma}_{true}$ as well as α. It can be seen most clearly by looking at the standard deviation of the time averaged values (right panels, Figure 7).

It is expected that the transient and steady state timescales would depend on multiple factors, such as the geometry of the shear cell, the applied shear rate, and shear history to name a few. They should also depend on the properties of the sample, such as the relaxation time τ_r, the time it takes for a single chain to relax back to its equilibrium state after being out of equilibrium, which is a function of surfactant and counter-ion concentration as well as temperature.

Comparing protocol 1 (no shear history) with protocol 2 (with pre-shear), we see that the standard deviation of α, $\dot{\gamma}_h$, $\dot{\gamma}_l$, and $\dot{\gamma}_{true}$ is minimized within the first 50-75 s for protocol 2. It appears as though the transient timescale is now equal to the steady state timescale. With pre-shear, the microstructure of the sample is presumably disturbed, which may have allowed the hydrodynamic instabilities to develop more rapidly, bypassing a "metastable" state as observed in previous studies [46, 58, 67].

In addition, several of the shear banding characteristics are changed. The average interface position goes from 0.27 in protocol 1 to 0.17 (nearer to the inner rotating wall of the Couette) in protocol 2 where pre-shear occurred. The average value of the low shear rate $\dot{\gamma}_l$ increased from 4.2 s^{-1} in protocol 1 to 5.5 s^{-1} in protocol 2. The high shear rate $\dot{\gamma}_h$ and amount of apparent wall slip, as indicated by the value of $\dot{\gamma}_{true}$, however, were roughly the same (26 s^{-1} and 12 s^{-1} respectively). Significant wall slip is not observed in either protocol. It appears there is a compensation mechanism, in which when the interface position is located farther in the fluid gap (protocol 1 without pre-shear), the value for the low shear rate is smaller.

To extract information about the 3D flow instabilities during the various regimes observed in the stress response and shear banded flow behavior, we further analyze the fluctuations. The

fluctuations are not random but reflect the coherent 3D nature of the flow. Previously, the Fourier transform of Rheo-NMR velocimetry data [68] and velocity autocorrelation functions [41] were used to analyze velocity fluctuations in wormlike micelle systems . The autocorrelation function can provide a better understanding of nature of the fluctuations by cleaning up a noisy signal and illuminating the underlying regular frequencies that are present. Here, we Fourier Transform time autocorrelation functions of the four characteristics of shear banding to obtain power spectra, which is a standard analysis and has the advantage over direct Fourier transform of reducing noise in the resulting spectra. The time domain data was divided into 64 s time intervals following shear startup and was used to calculate time autocorrelation functions, which were then Fourier transformed to obtain the spectra in Figures 8 and 9 (α and $\dot{\gamma}_h$ in Figure 8 and $\dot{\gamma}_l$ and $\dot{\gamma}_{true}$ in Figure 9). We clearly observe different frequencies depending upon the particular characteristic of shear banding and between the two flow protocols.

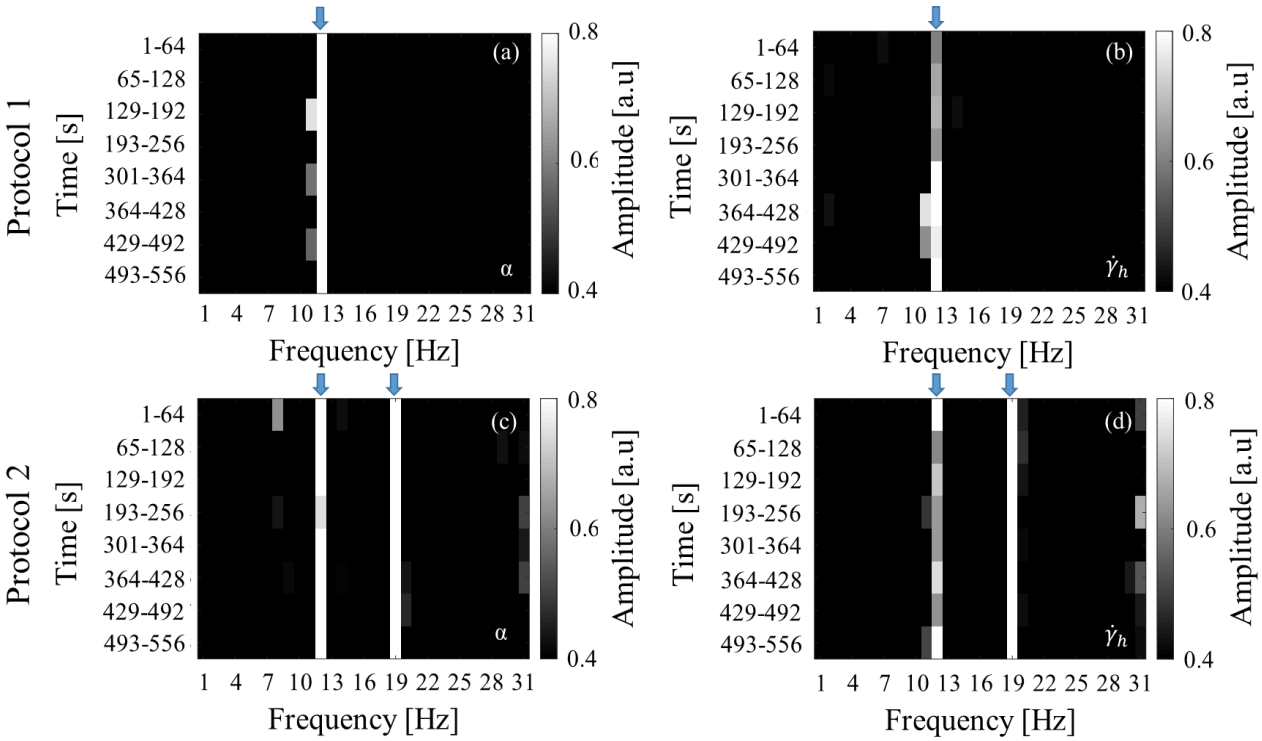

Figure 8: Frequency images from the Fourier transform of the time correlation functions. The colorbars correspond to amplitude (intensity normalized by the maximum intensity) in arbitrary units (a.u.). (a, c) interface position for protocol 1 (a) and protocol 2 (c). The dominant frequencies in the spectra are shown with blue arrows. In protocol 1, there is one frequency at 12 Hz that occurs for all times following *shear startup* to 12 s^{-1}. For protocol 2, there are two frequencies at 12 and 19 Hz. (b, d) high shear rate for protocol 1 (b) and protocol 2 (d). The same frequencies for protocol 1 (12 Hz) and protocol 2 (12 and 19 Hz) are observed in the spectra for the high shear rate.

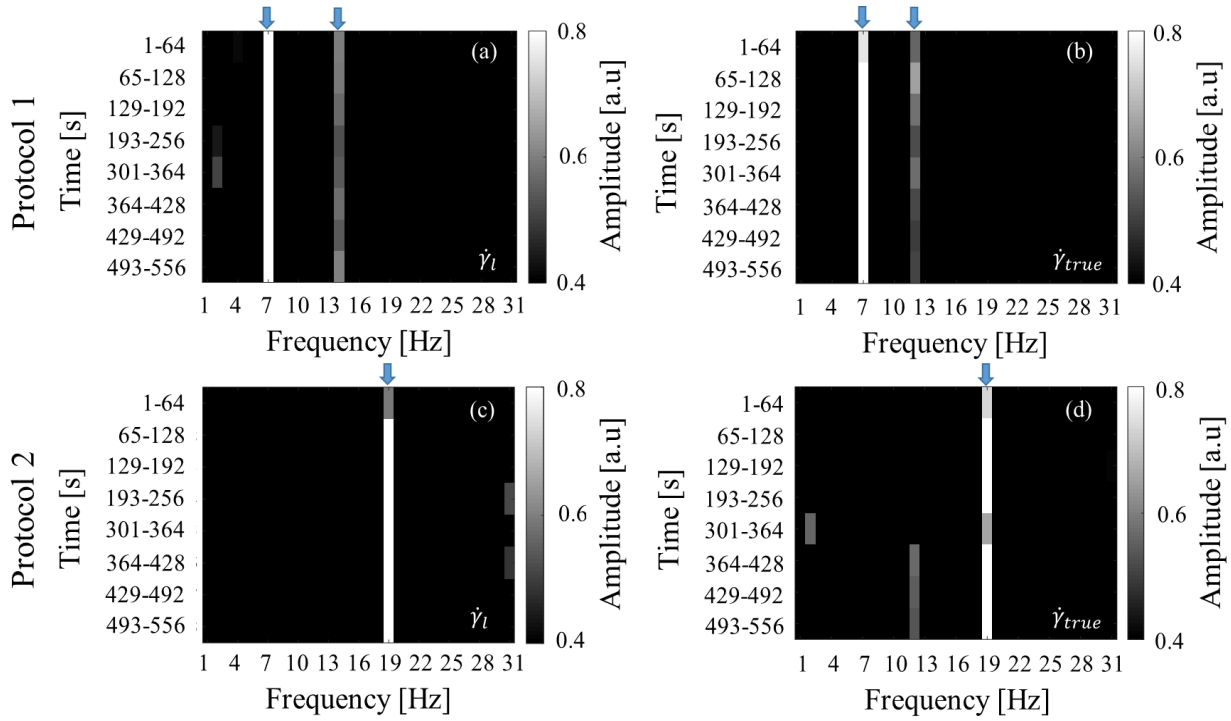

Figure 9: Frequency images from the Fourier transform of the time autocorrelation functions. The colorbars correspond to amplitude (intensity normalized by the maximum intensity) in arbitrary units (a.u.). (a, c) low shear rate for protocol 1 (a) and protocol 2 (c). The dominant frequencies in the spectra are shown with blue arrows. In protocol 1, there are frequencies at 7 and 14 Hz that occur for all times following *shear startup* to 12 s^{-1}. For protocol 2, there is a single dominant frequency at 19 Hz. (b, d) the true shear rate for protocol 1 (b) and protocol 2 (d). Similar frequencies are observed for protocol 1 (7 and 12 Hz) and protocol 2 (19 Hz).

For protocol 1, there is nearly a universal frequency of 0.19 Hz present at all times following shear startup and in all characteristics of shear banding (in the low shear rate there is a small shift to 0.22 Hz). However, a second high intensity frequency of 0.11 Hz is present in the low and true shear rates. There appears to be correlation between the interface and high shear rate fluctuations and the low shear rate and true shear rate fluctuations. The appearance of a strong lower second frequency in low shear rate and true shear rate indicates a coupling between slip and low shear rate. For protocol 2, there is a universal frequency of 0.3 Hz present at all

times and in all of the characteristics of shear banding. A second frequency of 0.19 Hz of roughly similar intensity occurs in the interface position and high shear rate, indicating a coupling between these two values.

In general, we see correlations between fluctuations of the high shear rate and interface position, as well as between fluctuations of low shear rate and apparent wall slip (seen through the true shear rate). Comparing the two protocols, we see a shift in the frequency universal to all shear banding characteristics. With Protocol 2 that involved a short wait time and pre-shear, the universal frequency is higher (0.3 Hz) than with Protocol 1 where a long wait time and no pre-shear was employed (0.19 Hz). A second, high intensity frequency presents itself in the low shear rate and true shear rate for protocol 1 (0.11 Hz). In protocol 2, a second equal intensity frequency appears in the high shear rate and interface position at a higher value (0.19 Hz). Interestingly, the frequency values do not shift depending on the regime (time after shear startup). Data for a range of applied shear rates is needed to correlate these frequencies to the specific nature of the hydrodynamic instabilities and the resulting secondary flows and research is currently ongoing in this direction.

Conclusions

Shear banding following shear startup was studied in a solution of wormlike micelles (WLMs) by measuring 1D velocity profiles across the 1 mm fluid gap of a Rheo-NMR concentric cylinder Couette cell using Rheo-NMR velocimetry. Fits to the velocity profiles were used to evaluate the shear banding characteristics, including the shear rates in the low and high shear band, the interface position and the true shear rate. Measurements were made for two flow protocols, one with and one without pre-shear. Due to the presence of flow instabilities, large

temporal fluctuations were observed in the flow characteristics obtained from a 1D measurement. Extending the spatial dimension to 2D would sacrifice temporal resolution, therefore, we instead separated the averaged quantities from the fluctuations about the average and analyzed them separately. The timescales for the flow to transition from a transient response to steady state were identified and quantified from analysis of the average values. The fluctuations were quantified through Fourier Transform of the time correlation functions of the data to obtain spectra of fluctuation frequencies. Pre-shear resulted in different magnitudes of the timescales and a shift in the frequencies of the fluctuation of all shear banding characteristics. Further experiments are needed to elucidate the connection between these frequencies and the nature of the hydrodynamic instabilities.

Acknowledgements

JRB acknowledges the NSF (1543875) for funding. RA acknowledges the Higher Committee for Education Development in Iraq (HREC) for fellowship funding. JRB, SLC and JDS acknowledge the M. J. Murdoch charitable trust for equipment funding.

References

1. Cates, M. and S. Candau, *Statics and dynamics of worm-like surfactant micelles.* Journal of Physics: Condensed Matter, 1990. **2**(33): p. 6869.

2. Rehage, H. and H. Hoffmann, *Viscoelastic surfactant solutions: model systems for rheological research.* Molecular Physics, 1991. **74**(5): p. 933-973.

3. Cates, M., *Nonlinear viscoelasticity of wormlike micelles (and other reversibly breakable polymers).* Journal of Physical Chemistry, 1990. **94**(1): p. 371-375.

4. Rehage, H. and H. Hoffmann, *Rheological properties of viscoelastic surfactant systems.* The Journal of Physical Chemistry, 1988. **92**(16): p. 4712-4719.

5. Cates, M.E., *Reptation of living polymers: dynamics of entangled polymers in the presence of reversible chain-scission reactions.* Macromolecules, 1987. **20**(9): p. 2289-2296.

6. Spenley, Cates, and McLeish, *Nonlinear rheology of wormlike micelles.* Physical review letters, 1993. **71**(6): p. 939.

7. Cates, M.E. and M.R. Evans, *Soft and fragile matter: nonequilibrium dynamics, metastability and flow (PBK)*. 2000: CRC Press.

8. Candau, S. and R. Oda, *Linear viscoelasticity of salt-free wormlike micellar solutions.* Colloids and Surfaces A: Physicochemical and Engineering Aspects, 2001. **183**: p. 5-14.

9. Yang, J., *Viscoelastic wormlike micelles and their applications.* Current opinion in colloid & interface science, 2002. **7**(5-6): p. 276-281.

10. Lerouge, S. and J.-F. Berret, *Shear-induced transitions and instabilities in surfactant wormlike micelles*, in *Polymer Characterization*. 2009, Springer. p. 1-71.

11. Olmsted, P.D., *Perspectives on shear banding in complex fluids.* Rheologica Acta, 2008. **47**(3): p. 283-300.

12. Fardin, M.-A. and S. Lerouge, *Flows of living polymer fluids.* Soft Matter, 2014. **10**(44): p. 8789-8799.

13. Berret, J.-F., D. Roux, and P. Lindner, *Structure and rheology of concentrated wormlike micelles [4] at the shear-induced isotropic-to-nematic transition.* The European Physical Journal B-Condensed Matter and Complex Systems, 1998. **5**(1): p. 67-77.

14. Hu, Y.T. and A. Lips, *Kinetics and mechanism of shear banding in an entangled micellar solution.* Journal of Rheology, 2005. **49**(5): p. 1001-1027.

15. Berret, J.-F., D.C. Roux, and G. Porte, *Isotropic-to-nematic transition in wormlike micelles under shear.* Journal de Physique II, 1994. **4**(8): p. 1261-1279.

16. Callaghan, P., et al., *A Study of the "Spurt Effect" in Wormlike Micelles Using Nuclear Magnetic Resonance Microscopy.* Journal de Physique II, 1996. **6**(3): p. 375-393.

17. Lerouge, S., J.P. Decruppe, and P. Olmsted, *Birefringence banding in a micellar solution or the complexity of heterogeneous flows.* Langmuir, 2004. **20**(26): p. 11355-11365.

18. Manneville, S., *Recent experimental probes of shear banding.* Rheologica Acta, 2008. **47**(3): p. 301-318.

19. Boukany, P.E. and S.Q. Wang, *Exploring the transition from wall slip to bulk shearing banding in well-entangled DNA solutions.* Soft Matter, 2009. **5**(4): p. 780-789.

20. Tapadia, P. and S.-Q. Wang, *Yieldlike constitutive transition in shear flow of entangled polymeric fluids.* Physical review letters, 2003. **91**(19): p. 198301.

21. Sprakel, J., et al., *Shear banding and rheochaos in associative polymer networks.* Soft Matter, 2008. **4**(8): p. 1696-1705.

22. Krishan, K. and M. Dennin, *Viscous shear banding in foam.* Physical Review E, 2008. **78**(5): p. 051504.

23. Ovarlez, G., K. Krishan, and S. Cohen-Addad, *Investigation of shear banding in three-dimensional foams.* EPL (Europhysics Letters), 2010. **91**(6): p. 68005.

24. Paredes, J., N. Shahidzadeh-Bonn, and D. Bonn, *Shear banding in thixotropic and normal emulsions.* Journal of Physics: Condensed Matter, 2011. **23**(28): p. 284116.

25. Coussot, P., et al., *Coexistence of liquid and solid phases in flowing soft-glassy materials.* Physical review letters, 2002. **88**(21): p. 218301.

26. Gibaud, T., C. Barentin, and S. Manneville, *Influence of boundary conditions on yielding in a soft glassy material.* Physical Review Letters, 2008. **101**(25): p. 258302.

27. Losert, W., et al., *Particle dynamics in sheared granular matter.* Physical Review Letters, 2000. **85**(7): p. 1428-1431.

28. Mueth, D.M., et al., *Signatures of granular microstructure in dense shear flows.* Nature, 2000. **406**(6794): p. 385.

29. Larson, R.G., *The Structure and Rheology of Complex Fluids*. 1999, New York: Oxford University Press.

30. Berret, J.-F., *Rheology of wormlike micelles: equilibrium properties and shear banding transitions*, in *Molecular gels*. 2006, Springer. p. 667-720.

31. Berret, J.-F.c., G. Porte, and J.-P. Decruppe, *Inhomogeneous shear flows of wormlike micelles: mA master dynamic phase diagram.* Physical Review E, 1997. **55**(2): p. 1668.

32. Britton, M.M. and P.T. Callaghan, *Two-phase shear band structures at uniform stress.* Physical Review Letters, 1997. **78**: p. 4930-4933.

33. Lopez-Gonzalez, M.R., et al., *Shear Banding Fluctuations and Nematic Order in Wormlike Micelles.* Physical Review Letters, 2004. **93**: p. 268-302.

34. Douglass, B.S., et al., *Rheo-NMR of wormlike micelles formed from nonionic pluronic surfactants.* Macromolecules, 2008. **41**(3): p. 804-814.

35. Miller, E. and J.P. Rothstein, *Transient evolution of shear-banding wormlike micellar solutions.* Journal of Non-Newtonian Fluid Mechanics, 2007. **143**(1): p. 22-37.

36. Bécu, L., S. Manneville, and A. Colin, *Spatiotemporal dynamics of wormlike micelles under shear.* Physical review letters, 2004. **93**(1): p. 018301.

37. Becu, L., et al., *Evidence for three-dimensional unstable flows in shear-banding wormlike micelles.* Physical Review E, 2007. **76**(1).

38. Fischer, E. and P.T. Callaghan, *Is a birefringence band a shear band?* Europhysics Letters, 2000. **50**(6): p. 803-809.

39. Britton, M. and P. Callaghan, *Shear banding instability in wormlike micellar solutions.* The European Physical Journal B-Condensed Matter and Complex Systems, 1999. **7**(2): p. 237-249.

40. Salmon, J.B., et al., *Velocity profiles in shear-banding wormlike micelles.* Physical Review Letters, 2003. **90**(22).

41. Lopez-Gonzalez, M.R., W.M. Holmes, and P.T. Callaghan, *Rheo-NMR phenomena of wormlike micelles.* Soft Matter, 2006. **2**: p. 855-869.

42. Manneville, S., L. Bécu, and A. Colin, *High-frequency ultrasonic speckle velocimetry in sheared complex fluids.* The European Physical Journal-Applied Physics, 2004. **28**(3): p. 361-373.

43. Lettinga, M.P. and S. Manneville, *Competition between Shear Banding and Wall Slip in Wormlike Micelles.* Physical Review Letters, 2009. **103**(24).

44. Feindel, K.W. and P.T. Callaghan, *Anomalous shear banding: multidimensional dynamics under fluctuating slip conditions.* Rheologica Acta, 2010. **49**(10): p. 1003-1013.

45. Fardin, M.A., et al., *Shear-banding in surfactant wormlike micelles: elastic instabilities and wall slip.* Soft Matter, 2012. **8**(8): p. 2535-2553.

46. Fardin, M.-A., et al., *Shear-banding in wormlike micelles: Beware of elastic instabilities.* Journal of Rheology, 2016. **60**(5): p. 917-926.

47. Mohammadigoushki, H. and S.J. Muller, *Inertio-elastic instability in Taylor-Couette flow of a model wormlike micellar system.* Journal of Rheology, 2017. **61**(4): p. 683-696.

48. Fardin, M.A., et al., *Taylor-like Vortices in Shear-Banding Flow of Giant Micelles.* Physical Review Letters, 2009. **103**(2): p. 4.

49. Fardin, M.A., et al., *Interplay between elastic instabilities and shear-banding: three categories of Taylor-Couette flows and beyond.* Soft Matter, 2012. **8**(39): p. 10072-10089.

50. Hu, Y.T., C. Palla, and A. Lips, *Comparison between shear banding and shear thinning in entangled micellar solutions.* Journal of Rheology, 2008. **52**(2): p. 379-400.

51. Moorcroft, R.L. and S.M. Fielding, *Shear banding in time-dependent flows of polymers and wormlike micelles.* Journal of Rheology, 2014. **58**(1): p. 103-147.

52. Pipe, C., et al., *Wormlike micellar solutions: II. Comparison between experimental data and scission model predictions.* Journal of Rheology, 2010. **54**(4): p. 881-913.

53. Brown, E., W. Burghardt, and D. Venerus, *Tests of the Lodge− Meissner Relation in Anomalous Nonlinear Step Strain of an Entangled Wormlike Micelle Solution.* Langmuir, 1997. **13**(14): p. 3902-3904.

54. Vasquez, P.A., G.H. McKinley, and L.P. Cook, *A network scission model for wormlike micellar solutions: I. Model formulation and viscometric flow predictions.* Journal of non-newtonian fluid mechanics, 2007. **144**(2-3): p. 122-139.

55. Lopez-Barron, C.R., et al., *Microstructural evolution of a model, shear-banding micellar solution during shear startup and cessation.* Physical Review E, 2014. **89**(4).

56. Helgeson, M.E., et al., *Rheology and spatially resolved structure of cetyltrimethylammonium bromide wormlike micelles through the shear banding transition.* Journal of Rheology, 2009. **53**(3): p. 727-756.

57. Fardin, M.-A. and S. Lerouge, *Instabilities in wormlike micelle systems.* The European Physical Journal E, 2012. **35**(9): p. 1-29.

58. Lerouge, S., et al., *Interface dynamics in shear-banding flow of giant micelles.* Soft Matter, 2008. **4**(9): p. 1808-1819.

59. Callaghan, P.T., *Translational Dynamics and Magnetic Resonance: Principles of Pulsed Gradient Spin Echo NMR*. 2011, New York: Oxford University Press.

60. Brox, T.I., et al., *Observations of the influence of Taylor-Couette geometry on the onset of shear-banding in surfactant wormlike micelles.* Journal of Rheology, 2016. **60**(5): p. 973-982.

61. Glasgow, L.A., *Transport phenomena: an introduction to advanced topics*. 2010: John Wiley & Sons.

62. Oelschlaeger, C., et al., *Structural, kinetics, and rheological properties of low ionic strength dilute solutions of a dimeric (gemini) surfactant.* Langmuir, 2002. **18**(20): p. 7265-7271.

63. Berret, J.F., et al., *Shear-thickening transition in surfactant solutions: New experimental features from rheology and flow birefringence.* European Physical Journal E, 2000. **2**(4): p. 343-350.

64. Gallot, T., et al., *Ultrafast ultrasonic imaging coupled to rheometry: Principle and illustration.* Review of Scientific Instruments, 2013. **84**(4).

65. Berret, J.-F., *Transient rheology of wormlike micelles.* Langmuir, 1997. **13**(8): p. 2227-2234.

66. Lerouge, S., J.P. Decruppe, and J.F. Berret, *Correlations between rheological and optical properties of a micellar solution under shear banding flow.* Langmuir, 2000. **16**(16): p. 6464-6474.

67. Lerouge, S., M. Argentina, and J.P. Decruppe, *Interface instability in shear-banding flow.* Physical Review Letters, 2006. **96**(8): p. 4.

68. Brown, J.R. and P.T. Callaghan, *Changing micellar order, lever rule behavior and spatio-temporal dynamics in shear-banding at the onset of the stress plateau.* Soft Matter, 2011. **7**(21): p. 10472-10482.

CHAPTER FIVE

RHEO-NMR VELOCIMETRY OF LARGE AMPLITUDE OSCILLATORY SHEAR

Contribution of Authors and Co-Authors

Manuscript in Chapter 5

Author: Jayesha S Jayaratne

Contributions: Wrote manuscript. Helped in designing and conceiving the experiment. Prepared samples, collected, analyzed and interpreted Rheo-NMR data.

Co-Author: Rehab N. Al-Kaby

Contributions: Provided training on rheo-NMR equipment. Will provide feedback on manuscript.

Co-Author: Josephine Maley

Contributions: Collected (strain sweeps and frequency sweeps) and analyzed rheology data.

Co-Author: Timothy I. Brox

Contributions: Designed the Rheo-NMR rheometer used. Provided training on rheo-NMR equipment. Will provide feedback and comments on the manuscript.

Co-Author: Petrik Galvosas

Contributions: Provided training on experimental methodology. Will provide feedback on the manuscript.

Co-Author: Sarah L. Codd

Contributions: Helped conceive and design NMR methods for the study. Helped with data analysis methods. Will provide feedback and comments on the manuscript.

Co-Author: Joseph D. Seymour

Contributions: Edited manuscript with significant contributions to the data discussion section. Provided training on experimental methodology. Helped perceive experimental and implementation concepts. Helped interpret data. Secured funding.

Manuscript Information

Jayesha S. Jayaratne, Rehab N. Al-Kaby, Josephine Maley, Timothy I. Brox, Petrik Galvosas, Sarah L. Codd, Joseph D. Seymour

Journal of Rheology

Status of Manuscript:
__X_ Prepared for submission to a peer-reviewed journal
___ Officially submitted to a peer-reviewed journal
___ Accepted by a peer-reviewed journal
___ Published in a peer-reviewed journal

RHEO-NMR VELOCIMETRY OF LARGE AMPLITUDE OSCILLATORY SHEAR

Abstract

Complex fluids display flow heterogeneities and a rich variety of nonlinearities under large imposed shears. Large amplitude oscillatory shear (LAOS) has been an appropriate way of characterizing the nonlinearities posed by fluids in rheology. In this study we introduce means of classifying LAOS using rheo-nuclear magnetic resonance (Rheo-NMR). Rheo-NMR is frequently used to study velocity responses of complex fluids to steady shear deformations due to the technique's ability to image local velocities across a fluid gap with the added benefit of studying opaque fluids noninvasively. The field however had fallen short of the ability to study oscillatory responses of these fluids owing to hardware limitations that prevailed. As of recent years updated Rheo-NMR equipment makes venturing into LAOS in the field of Rheo-NMR possible. Being the first time LAOS is being studied under Rheo-NMR, non-linearities are studied using spatial velocity profiles, time dependent local velocity profiles and Lissajous curves. Ultimately this study aims to show the possibility of expanding Rheo-NMR to predict flow behavior under LAOS and build a conversation to develop analysis methods for this novel data in the future.

Introduction

Yield stress fluids and shear thinning fluids are encountered everywhere in life. Emulsions, dense suspensions, foams, and polymeric gels are yield stress fluids seen commonly in industries related to consumer products, pharmaceuticals, foods and civil engineering. These materials flow only once a stress larger than a fluid specific critical stress has been overcome, a

feature related to their ‘soft jammed’ structures[1, 2]. Once the critical stress is surpassed and these materials are under flow they often exhibit shear thinning behavior [3-6]. Viscometric flow assumptions allow for the these materials to be modeled by the Herschel-Bulkley (HB) equation $\tau(\dot{\gamma}) = \tau_y + K\dot{\gamma}^n$, where τ_y is the material’s yield stress, *K*, the material’s consistency index, $\dot{\gamma}$, the shear rate and *n*, the power-law index of the material[7-10] . This model combines the Bingham plastic model that describes ideal yield stress materials, with the Ostwald de Waele power law model to express the complex behavior of yield stress fluids we studied here [9, 11-16]. Shear thinning fluids are well modeled by a simple power law model, $\tau(\dot{\gamma}) = K\dot{\gamma}^n$, with the value of the power-law index being less than unity [16]. Many polymer melts and particle suspensions (e.g. bentonite-in-water) exhibit thixotropy or time dependent shear thinning category [2, 3, 17-19] .

Dynamic oscillatory tests are widely used in characterizing a spectrum of a material’s responses going from a liquid to a solid or linear to non-linear allowing the conceptualization of its viscoelastic properties[20]. Material response varies based on the degree of strain. Low applied strain amplitudes generate linear responses or small amplitude oscillatory shear (SAOS) and provide the relationships between the microstructure and the rheological properties of complex fluids as long as the total applied sinusoidal deformation is small such that the applied frequency (first harmonic) is what is detected [21-25]. Despite the wealth of information generated by SAOS, small deformations tested are not common in processing and use applications. Large amplitude oscillatory shear (LAOS) is present in most industrial processes involving complex fluid based products utilizing high shears over short time scales during which a steady state is not achieved [20]. As the degree of deformation is increased and the material

transitions to the nonlinear viscoelastic region (non-LVR) , the material's structure may change bringing in higher order harmonics (mainly 3^{rd} and other odd harmonics) that influence the applied first order harmonic hence giving the nonlinear response[20, 23, 25, 26]. While utilitarian in approaching realistic processing conditions in rheology LAOS measured nonlinear stress responses distinguish among complex fluids with similar micro- and nano- molecular structures, which under small deformations are not captured [20, 21, 27, 28]. LAOS experiments also allow for the nonlinear responses to be a function of both strain amplitude and frequency [23].

Measurement of flow fields during these material deformations provide additional insight into the bulk stress, strain and strain rate responses e.g. when shear banding is present [10]. Optical methods, such as Doppler velocimetry, particle image velocimetry, ultrasound velocimetry, and rheo-light scattering techniques, provide flow visualization but can be limited by sample density heterogeneity, geometry limitations, transparency constraints and often add particulates which interact with the material [29]. Rheo-NMR velocimetry has the advantage that it does not require doping samples with tracers, hence is considered a non-invasive technique and has the capacity to study three-dimensional velocity fields using a range of geometries [29-31]. Steady shear Rheo-NMR has been a well-established technique used for over 30 years to provide complimenting data to steady shear rheology. Rheo-NMR is progressively integrating further with the rheometer, where both bulk and microstructural information can be simultaneously obtained [32-34]. A further stride in that direction is demonstrated here using equipment designed to create large amplitude oscillatory shear in the NMR magnet.

Using classical signal input-response analysis in LAOS rheology, the projection of the oscillatory stress response against the applied strain (γ) gives rise to an 'elastic Lissajous-Bowditch curve', where details of the elastic moduli are seen [27, 28, 35, 36]. Oscillatory stress response plotted against the input strain rate ($\dot{\gamma}$) gives a 'viscous Lissajous-Bowditch curve', where instantaneous viscosities are seen [37-43]. A linear viscous fluid shows a linear viscous Lissajous curve, while an ellipse is seen for a viscoelastic material in the linear viscoelastic regime which then begins to depict nonlinearities as one moves to the nonlinear regime [35, 36, 38].

This work investigates the flow of a range of fluids exhibiting Newtonian, shear thinning and yield stress behavior under LAOS within a NMR magnet employing a prototype rheometer driveshaft and motor. While previous studies related to shear induced multilamellar vesicles under LAOS have been conducted using 1D NMR spectra post oscillatory flow cessation with a similar prototype driveshaft, the current study is the first to have delved into 1D velocity profiles of fluids during the LAOS deformation process [44, 45]. Given the novelty of the data acquired several potential analysis approaches are demonstrated. The local velocity responses to input sinusoidal strain are measured in time, indicating nonlinearities in comparison to simple small-molecule fluids subject to the same strain. Lissajous figures are plotted for each fluid versus the Newtonian velocity behavior as the input. The evolution of complex material flow behavior from shear thinning plug flow, shear banding type flow and no flow that coexist under the same applied shear rate, and transience related memory effects (lead and lag) of xanthan gum solution, yoghurt, ketchup and Carbopol solution will be explored in this paper by means of LAOS Rheo-NMR data.

Materials and Methods

Materials

Two of the complex fluids used in this study were consumer products directly purchased from stores, Heinz ketchup and Siggi's non-fat yogurt. Additionally, a 0.2wt.% Carbopol solution was made using Carbomer 940 (Making Cosmetics) which was neutralized to a pH 7 using triethanalamine (TEA), following methods suggested by Di Guiseppe *et al.* [46]. Since this Carbopol solution was highly water based, 0.2% (v/v) $GdCl_3$ was used to dope the solution, reducing its magnetic relaxation time. These chosen complex fluids, ketchup, drinking yogurt and 0.2wt.% Carbopol were used in this study to represent fluids modeled by the HB model.

A 0.6% (w/v) xanthan gum solution was chosen to explore the LAOS behavior shown by fluids modeled by the power law model. This solution was prepared by mixing powdered xanthan gum of molecular weight 2,000,000 (MP Biomedicals) in DI water. Work by Rofe *et al.* explored a lower concentration of this solution (0.2% (w/v)) at shear rates of $5s^{-1}$ and $10s^{-1}$, but the xanthan gum (UNAM) they used was of a higher molecular weight compared to samples from other suppliers [47]. In contrary, the 0.2% (w/v) xanthan gum solution (MP Biomedicals) we prepared showed Newtonian velocity profiles at the applied shear rate amplitudes used for this study. Defined nonlinear velocity profiles were observed only at a xanthan gum concentration of 0.6% (w/v), for the in house prepared solution, leading to its selection for this study.

Deionized water doped in 0.2% (v/v) $GdCl_3$ and a 1,000 cSt (1 Pa.s) silicone oil sample (Consolidated Chemicals & Solvents LLC) were used as Newtonian references. While certain molecular weights of silicone oils at higher shear rates show shear thinning behavior, for the

used low shear rates in this study, the used silicone oil showed Newtonian behavior [48]. All samples were tested at room temperature, 21℃, and care was taken to ensure that no bubbles were trapped in the samples.

Rheometry

A strain-controlled AR-G2 Rheometer by TA instruments was employed in collecting strain sweeps to ensure that the non-Newtonian samples tested on the NMR rheometer were in fact in the nonlinear region at the selected strain amplitudes. A cone and plate steel geometry of diameter 60mm and cone angle 2° was used for this purpose. Strain sweeps with varying percent strains from 0.1% to 100% at individual fixed frequencies of 0.1, 4, and 100 $rads^{-1}$ were run. The strain sweeps were used to determine the angle of rotation required to enter the non-linear regime for each sample. The highest strain at which the non-linear regime for each complex fluid was approached at was: 2% strain at an angular frequency of 0.1$rads^{-1}$ for drinking yogurt (corresponding to an angular amplitude of 0.04°), 0.79% strain at an angular frequency of 0.1$rads^{-1}$ for Heinz ketchup (corresponding to an angular amplitude of 0.0158°), and 1.99% strain at an angular frequency of 100 $rads^{-1}$ for 0.2wt.% Carbopol (corresponding to an angular amplitude of ~0.04°) and 0.7% strain at an angular frequency of 0.1$rads^{-1}$ for 0.6% (w/v) xanthan gum (corresponding to an angular amplitude of 0.014 °). The Rheo-NMR tests done with a Couette shear cell, at an angular frequency of 0.196 $rads^{-1}$ and strain amplitudes of 6.3 and 25.2 had angular amplitudes of 45° and 180° respecively while rotating a total of 90° and 360° back and forth. The samples were all well into the non-linear regime of the applied strains in the Couette shear cell as well.

Rheo-NMR LAOS

The NMR LAOS measurements were performed using an Avance 250 spectrometer by Bruker with a superconducting wide bore magnet of 5.8 T field strength and a resonance frequency of 250 MHz (for proton spectrometry). A Micro 2.5 imaging probe by Bruker with shielded gradient coils that bears a maximum gradient strength of 1.49 T/m was utilized to produce flow-gradients and slice selective gradients. Non-selective excitation was produced using a 25mm diameter radio frequency coil that acted as both a receiver and transmitter. The NMR method employed was a single pulse gradient spin echo (PGSE) pulse sequence [49] with a double slice selection: a 10mm slice in the vorticity direction that helped avoid edge effects, and a 1mm slice in the direction of flow that aided in the reduction of curvature effects on the velocity profiles, that resulted in 1D images just as those seen in studies by Al-Kaby *et al.* [50] the difference being that the acquisitions were timed using triggers here.

A magneto-safe portable rheometer, with an attached shear cell was inserted from the top of the magnet ensuring that the central region of the shear cell was centered within the RF coil such that edge effects of flow would not hinder flow visualization across the fluid gap. The shear cell is a geometry commonly referred to as the Taylor-Couette shear cell, that comprised of two cylinders: a rotating inner cylinder called the rotor of radius of 8mm (r_i) made of PEEK and an outer stationery cup called the stator of radius 9mm (r_o) made of borosilicate. The imaged 1D velocity profiles hence detailed the local velocities acquired across a 1mm fluid gap. The Couette cell dimensions were selected in accordance to experiments conducted by Brox *et al.* Since Rheo-NMR gives us access to local velocities, $v(r)$, inside the fluid gap, this information can be used in deriving the local shear rates. The local shear rate, $\dot{\gamma}_{(r)} = \nabla v_{(r)}$, for Newtonian fluids

expected to be constant with radial position, *r*, under the narrow gap limit of the Couette shear cell. A representation of the resulting local shear rate, $\dot{\gamma}_{(r)}$ can be calculated by directly using the annular velocity gradient, $\nabla v_{(r)}$, in Eqn. 1 [7, 29, 51, 52]:

$$\dot{\gamma}_{(r)} = r\,\frac{\partial\,(v_{(r)}/r)}{\partial r} = \frac{\partial v_{(r)}}{\partial r} - \frac{v_{(r)}}{r} \qquad \text{Eqn. 1}$$

Based on this equation, for a Newtonian fluid, the shear rate at the rotor ($\dot{\gamma}_{(r_i)}$) under the narrow gap assumption can then be shown using Eqn. 2 [7, 53, 54] :

$$\dot{\gamma}_{(r_i)} = \frac{v_{(r_i)}}{r_o - r_i} = \frac{v_{(r_i)}}{1} \qquad \text{Eqn. 2}$$

where r_i and r_o are the inner and outer cylinder radii.

The sample suspended in the Couette shear cell of the drive shaft was sheared using a strain controlled magneto safe Rheo-NMR rheometer. This Rheo-NMR rheometer is the first of its kind with the capability of inducing both steady state shear and oscillatory shear at frequencies between 0.001Hz and 9.99Hz that also has a built in trigger function. The motor was allowed to run for 256 oscillatory cycles for each of the strain amplitudes of $\gamma_o = 6.3$ and $\gamma_o = 25.2$, at a fixed angular frequency of 0.196 rad s^{-1}. Data was collected at the same 32 points of each cycle making use of the trigger function that was built in to the rheometer, that enabled the acquisition of data at the same calculated position vectors of every oscillatory cycle. Prior to the data acquisition from the 256 cycles, upon the command from the motor, the rotor was made to oscillate at the fixed angular frequency (0.196 $rads^{-1}$; a period of 32s) for 320 seconds. This angular frequency was so selected in order to be within the non-linear regime of the sample while avoiding mechanical issues arising at higher angular frequencies. To increase the signal to noise ratio velocity data acquired at each position vector was averaged 16 times giving a final

data set resulting in 1 D flow images of what seemed as 8 oscillatory cycles. All 1D flow images possess a 25.6 mm field of view in read direction with 512 pixels, resulting in a 50 μm/pixel high resolution. Data was analyzed using Prospa (Magritek, NZ) and MATLAB (MathWorks, Natick, MA) to derive spatially and temporally resolved velocity information using which Lissajous curves were also constructed.

Discussion

Steady State Velocity Profiles

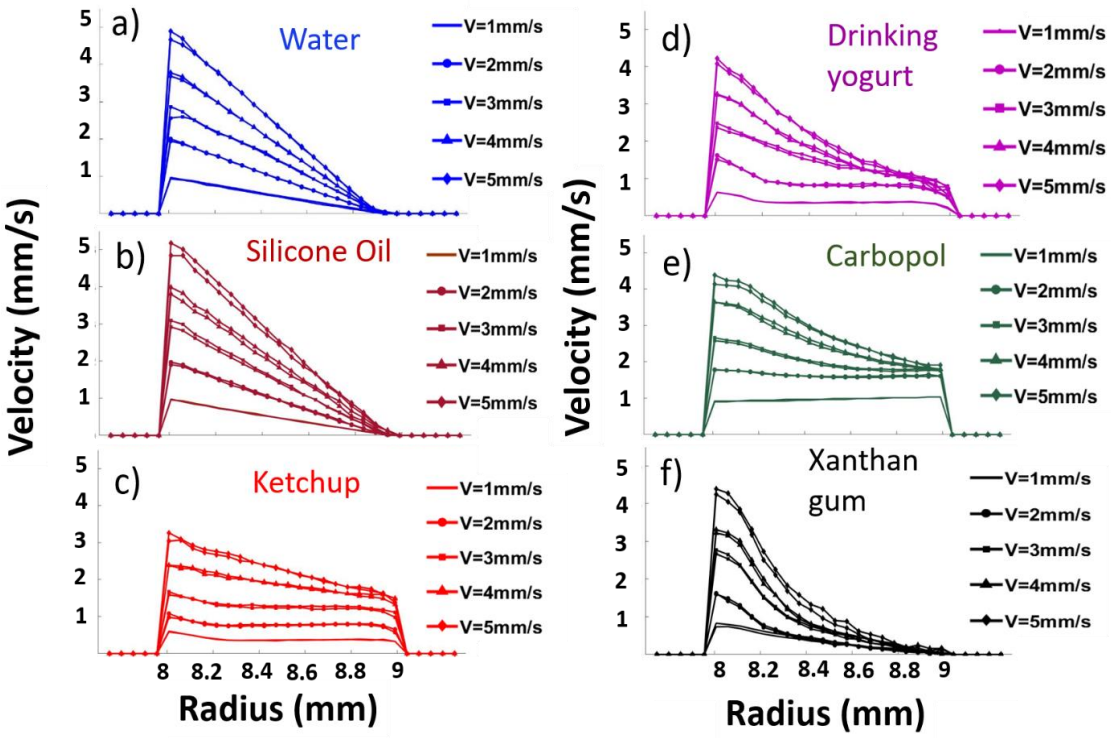

Figure 1: Steady state velocity profiles at applied shear rates of 1 s^{-1}(—), 2 s^{-1}(●), 3 s^{-1}(■), 4 s^{-1}(▲) , and 5 s^{-1}(♦) for a) water b) silicone oil c) ketchup d) drinking yogurt e) 0.2wt.% Carbopol and f) 0.6% (w/v) xanthan gum. Two velocity profiles are plotted per applied shear rate to depict inconsistencies encountered with noise.

Figure 1 shows results of steady state experiments, widely used in Rheo-NMR, that depict a nonlinear rheological flow (unidirectional rotation) that has reached steady state [55, 56]. Five different applied shear rates are shown (Figure 1 a)- f)) for each sample. The velocity profiles of two different steady state experiments for each shear rate are overlaid to depict variations encountered due to vibrations from the drive shaft, noise from NMR voltage, signal and other experimental limitations. Newtonian fluids, water and silicone oil (Figure 1 a) and b)), exhibit linear velocity profiles with the rotor (8mm) velocity equal to the applied shear rate (Eqn. 2) and no flow boundary condition of zero velocity at the stator wall (9mm).

The steady state data for the HB type fluids (Figure 1 c)-1 e)) at each applied shear rate show inhomogeneous velocity profiles across the fluid gap. Here, the fluid close to the rotor wall shows a yielded flow while fluid close to the stator flows as a plug, un-yielded [34, 55]. This behavior is described as shear banding of soft-jammed materials and is physically different to the shear banding phenomenon observed with micellar solutions [57, 58].

Each of the samples failed to acquire a zero velocity near the stator, at 9mm in Figures 1 c)- e), indicating wall slip at the stator [55]. This stator wall slip can be attributed to an ‘apparent slip layer’, a condition that arises due to the inability for the dispersed phase to physically occupy spaces adjacent to solid boundaries, which instead is occupied by a thin layer of low viscosity or Newtonian based fluid of thickness 0.1-10 μm along the glass stator wall [59-61]. At a spatial resolution of 50 $\mu m/pix$, in the experiments, this layer is averaged with and dominated by larger fluid mass, hence commensurate ^{1}H spins moving at a higher velocity in the material bulk. Here, the terminology ‘apparent slip’ is identified as a suspending fluid layer will be in

continuous contact with the solid boundaries, unlike for polymer melts where the fluid loses contact with the solid boundaries [61].

Rotor wall slip is also observed at all applied shear rates for steady state velocity profiles of yogurt and ketchup (Figure 1 c) and d)). This rotor wall slip is identified by the velocity achieved at the rotor being less than the expected velocity by fluid near the rotor which should numerically equal to the applied shear rates. Existence of rotor slip for Carbopol is also seen at all applied steady state shear rates except at 1 s^{-1}, where the fluid in the entire fluid gap seems to drag along with the rotor's velocity as a plug (Figure 1 e)). While no rotor wall slip is observed at a steady state applied shear rate of 1 s^{-1} for Carbopol, a higher velocity (of ~1.2 mm s^{-1}) is observed at the stator wall (Figure 1 e)). A similar phenomenon is also observed and discussed below for Carbopol oscillated at a strain amplitude of 6.3. This phenomenon likely arises from surface interactions between the Carbopol and borosilicate glass stator wall, an interaction that is absent at the rotor wall made of PEEK [62].

In contrast to the Newtonian and HB type fluids measured, the steady state velocity data for 0.6% (w/v) xanthan gum water solution, power law fluid, shows only rotor wall slip and no stator wall slip (Figure 1 f)). A uniform velocity distribution is observed at 1 mm s^{-1}. Curved nonlinear velocity profiles are generated at higher applied shear rates corresponding to 2 mm s^{-1} - 5 mm s^{-1}. Such curvature has been connected to a form of shear-banding where the interface of the shear 'bands' is considered to be broad for a polymer entanglement system like the xanthan gum solution [63]. The velocity profiles indicate strong shear thinning behavior [47, 64-67].

Oscillatory Spatial Velocity Profiles

Eight oscillatory cycles of a 32 s period were averaged over 256 rotor oscillatory cycles. Spatially resolved velocity profiles corresponding to half of a single oscillatory cycle are shown in Figure 2 a)- f) and 3 a)- f).

The corresponding figures to the right of the velocity profiles are the shear rate calculations of those velocity profiles from a finite difference method (Figure 2 g)- l) and 3 g)- l)). The irregularities toward the rotor and stator of the shear rate profiles are from the use of finite difference formulas applying the forward and backward differences at the boundaries. The shear rates between the gray dashed lines, of radius 8.2 mm -8.85 mm, (Fig 2 g)- l) and 3 g)- l)) can be considered to show the correct shear rates.

Spatial LAOS velocity profiles of the two Newtonian fluids, water and silicone oil, at both strain amplitudes (Figure 2 and 3 a) - b)) show homogeneous velocity distributions. Each profile of the half cycle showing the maximum velocity achieved near the rotor wall (numerically equal to the shear rate applied by the rotor) and a zero velocity achieved at the stator wall. This was consistent with the steady state velocity profiles for the two Newtonian fluids in Figure 1 a) and b). A narrow gap flow cell would have a constant shear rate across the gap for a Newtonian fluid. However, Figure 2 g) and Figure 3 g) for water under LAOS, slightly decreasing shear rates from rotor to stator are seen. The more viscous silicone oil shear rate distributions are more constant across the fluid gap (Figure 2 and 3 h)).

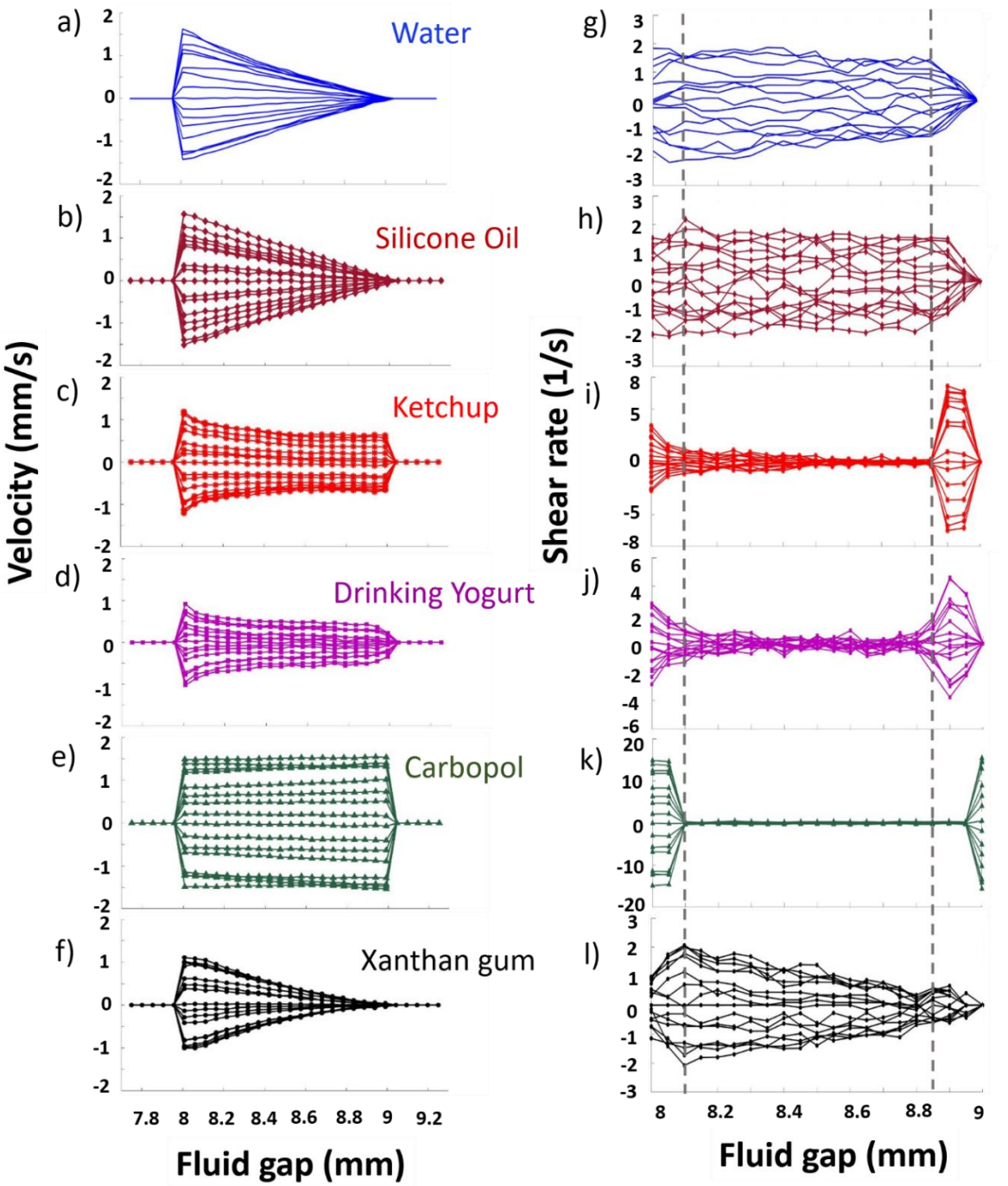

Figure 2: 1D LAOS velocity and shear rate profiles at a strain amplitude of 6.3. Spatially resolved 1D LAOS velocity profiles of a) water, b) silicone oil, c) ketchup, d) drinking yogurt, e) 0.2wt.% Carbopol and f) 0.6% (w/v) xanthan gum. Spatially resolved 1D LAOS shear rate profiles, plotted applying a finite difference methods to velocity data, of g) water, h) silicone oil, i) ketchup, j) drinking yogurt, k) 0.2wt.% Carbopol and l) 0.6% (w/v) xanthan gum.

The oscillatory spatial velocity profiles of ketchup at both strain amplitudes (Figure 2 and 3 c)) show rotor and stator wall slip, consistent with the steady state profiles (Figure 1 c)). The spatial velocity profiles at a 6.3 strain amplitude (Figure 2 c)) show heterogeneous flow with position. This was characterized by a partially yielded narrow region close to the rotor and a large region in plug flow toward the stator along with both a rotor and stator slip at each acquired velocity profile of the half cycle depicted. As the strain amplitude was increased to 25.2 (Figure 3 c)) stator slip was retained throughout the half cycle. There is a heterogeneous flow at the intermediate shears with a trend toward a more pronounced continuous flow corresponding to rotor slip decreasing at the higher velocity amplitudes of the half cycle. Ketchup is a particulate suspension of tomato concentrate suspended in a Newtonian system, causing rapid rotor motion to disrupt the fiber network and align it along the flow allowing for a shear thinning behavior [68, 69]. For the ketchup closer to the stator, the dispersion network is not disrupted showing a plug flow by the stator, while a thin Newtonian film along the stator wall causes stator slip.

Spatially resolved oscillatory velocity profiles of Siggi's non-fat drinking yogurt for the half cycle show both rotor and stator slip for a strain amplitude of 6.3 (Figure 2 d)) as did the steady state profiles (Figure 1 d)). The fluid region experiencing less stress than the yield stress ($\sigma < \sigma_y$), that shows plug flow near the stator, is larger than the plug flow region seen for ketchup (Figure 2 c)). This indicates drinking yogurt having a higher yield stress at a 6.3 strain amplitude. At the higher strain amplitude of 25.2 (Figure 3 d)) both rotor and stator slip reduce, with each of the profiles of the half cycle tending toward a more homogeneous shear thinning profile. Oscillatory velocity profiles in the half cycle shown of 0.2wt.% Carbopol at a strain amplitude of 6.3, show the material moving in plug flow with a stator wall slip (Fig. 2 g)) as was seen in the

steady state profiles at 1 mm s^{-1} and 2 mm s^{-1} (Figure 1 e)). The Carbopol has the highest yield stress than the rest of the fluids measured, essentially composed of swollen hydrophilic elastic gel particles in a Newtonian base. This forms a jammed structure spanning the fluid gap that moves as a solid body [70, 71]. Interestingly, this plug flow behavior is only seen from rotor velocities of 0 to +/- 0.5 mm s^{-1} beyond which the fluid layer closest to the stator wall begins to acquire higher velocities than that of the fluid layer closest to the rotor, a phenomenon seen in the 1 mm s^{-1} steady state velocity profile (Fig. 1 e)). In other words, as the rotor moves from +0.5 mm s^{-1} toward a maximum velocity of ~+1.5 mm s^{-1} the stator wall acquires a velocity higher than that shown at the rotor. A partial explanation for this is the negative charged polymer particles show a repulsive interaction with the borosilicate glass stator, while at the rotor the interaction is neutral [62]. At the point in the oscillatory cycle where the rotor transitions from going to a higher velocity to a lower velocity (Figure 2 g)), between rotor velocities of +/-1.18 and +/- 1.5 mm s^{-1}, the velocity of the gel at the stator fluctuates +1.53 mm s^{-1} to +1.3 mm s^{-1} and back to +1.5 mm s^{-1}, indicating a transient response relative to the velocity change of the rotor. Following this transience, as the rotor approaches a zero velocity, in its oscillatory motion, the gel at the stator wall maintains a higher velocity than the rotor velocity, again exhibiting a lag. This lag follows through once again till a velocity of $+/-0.5$ mm s^{-1} is reached, after which the gel continues in plug flow until it comes to rest at 0 mm s^{-1}. Here, the absence of a rotor slip indicates the absence of a depletion layer at the rotor, or the effect of it being negligible if present. At a strain amplitude of 25.2, Carbopol velocity profiles show a similar behavior to ketchup, with discontinuous velocity profiles at higher strains of the half cycle marked by a yielded region close to the rotor and a bulk flowing non-sheared region close to the stator (Fig. 3 e)).

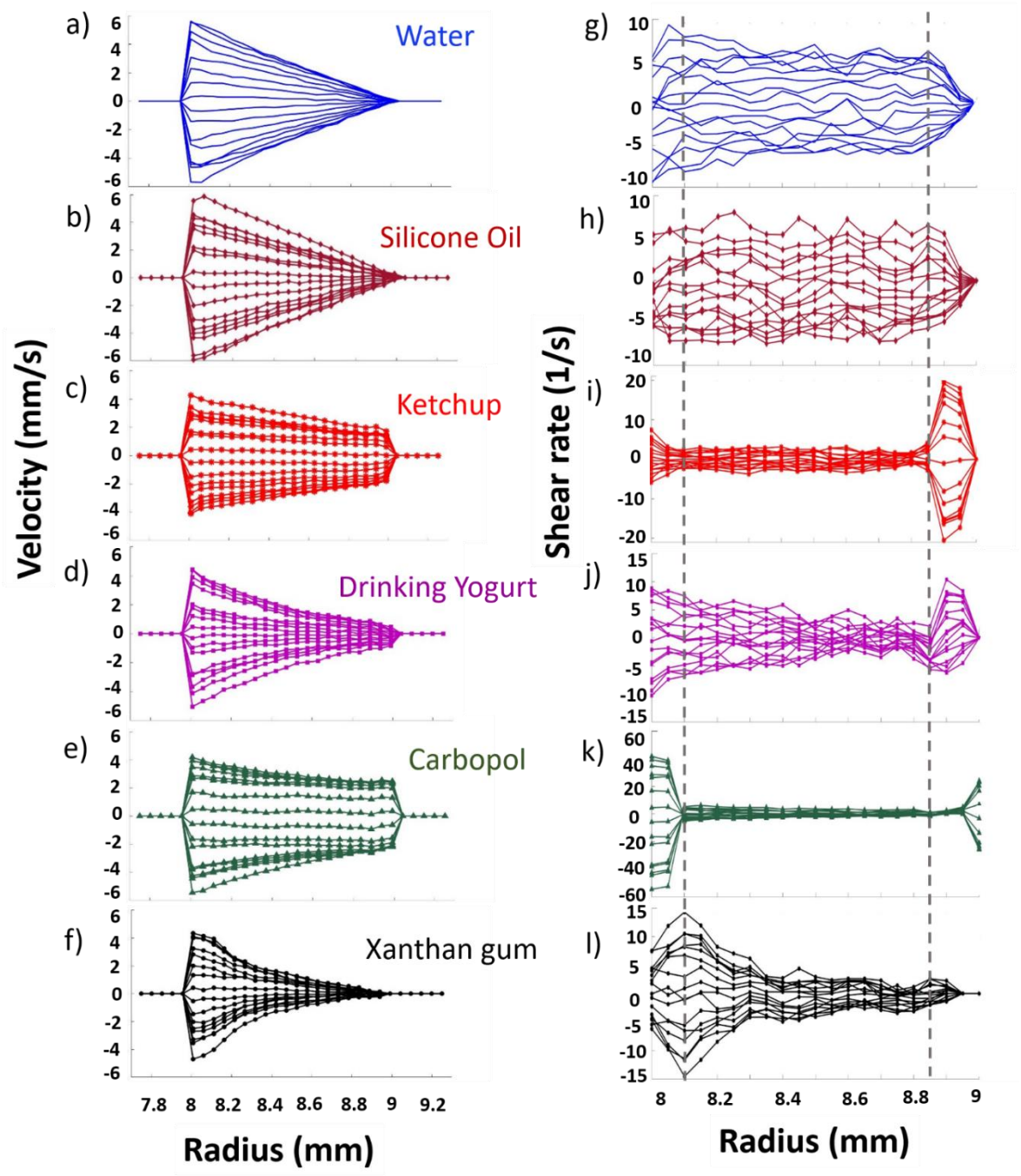

Figure 3: 1D LAOS velocity and shear rate profiles at a strain amplitude of 25.2. Spatially resolved 1D LAOS velocity profiles of a) water, b) silicone oil, c) ketchup, d) drinking yogurt, e) 0.2wt.% Carbopol and f) 0.6% (w/v) xanthan gum. Spatially resolved 1D LAOS shear rate profiles, plotted applying a central finite difference method to velocity data, of g) water, h) silicone oil, i) ketchup, j) drinking yogurt, k) 0.2wt.% Carbopol and l) 0.6% (w/v) xanthan gum.

This is consistent with a shear disruption of the gel particle network in the Carbopol analogous to the fiber network of ketchup. The fluid behavior at the stationary wall experiencing plug flow also shows prominent lag as was seen for 6.3 strain amplitude as the rotor's velocity decreases from 5 mm s^{-1} to 0.7 mm s^{-1}.

0.6% (w/v) xanthan gum solution subject to a strain amplitude of 6.3 showed the maintenance of a homogeneous flow by each velocity profile of the oscillatory cycle with no stator slip (Figure 2 f)). The forward motion of the rotor toward the maximum positive velocity amplitude, from 0 mm s^{-1} to +1 mm s^{-1}, generated linear velocity profiles that transitions into shear thinning behavior as the rotor velocity increases from 1 mm s^{-1} to +1.3 mm s^{-1}. This is followed by a more linear velocity profile as the rotor reads a velocity of 1.5 mm s^{-1}. As the strain was further increased, with decreasing rotor velocity from +1.5 mm s^{-1} to 0 mm s^{-1} (to the rotor's turn around point at a strain 6.3) pronounced shear-thinning velocity profiles show power law flow. The same repeated trend is present in velocity profiles following the flow reversal from 0 mm s^{-1} to -1.5 mm s^{-1}. As the strain amplitude applied is increased to 25.2 (Figure 3 f)) a shear thinning profile with mild curvature is observed at 1.5 mm s^{-1} just as for the 6.3 strain amplitude. As the strain is further increased, a significant shear thinning develops at velocities: +2 mm s^{-1} to +5 mm s^{-1} and +5 mm s^{-1} to -2 mm s^{-1}), consistent with the steady state flow data in Figure 1 f).

Time Dependent Velocity Profiles

Figure 4 presents the local velocity oscillation with time at three positions across the fluid gap for each sample at each tested strain amplitude. The selected spatial positions are 1) two pixels (50 μm/pixel) from the rotor wall or at 8.1 mm from the central axis of the rotor, 2) at the middle of the fluid gap, 8.45 mm from the central axis of the rotor and 3) a pixel before the stator

wall or 8.95 mm from the central axis of the rotor accounting for the nonzero velocity observed for the Newtonian fluids at the stator. The positions closest to the walls were chosen 50 -100 μm away in order to avoid partial volume artifacts encountered at the pixels closest to the walls. This common artifact is a result of averaged velocity signal in a pixel partially being from the fluid in the cylindrical streamline of a Couette cell, with the other percentage of signal being from the wall material (no signal from the solid wall) both being mapped on to a Cartesian grid [72]. For clarity, only one cycle of the eight cycles is presented for each fluid sample at each strain amplitude (Figure 4 a)- j)).

Under LAOS the Newtonian fluids exhibit linear velocity distributions with no indication of wall slip seen in the half a cycles shown in Figure 2 a), b) and Figure 3 a) and b). This linear spatial velocity is consistent with the time dependent velocity in Figure 4 a) and f) where each gap position's velocity oscillation is perfectly sinusoidal.

The rotor and stator slip observed in the oscillatory spatial velocity profiles at both strain amplitudes (Figure 2 and 3 c)) appear in the time dependent velocity profiles as well (Figure 4 b) and g)). The wall slip close to the rotor marked by the velocity amplitude of ketchup being significantly less than that of the Newtonian fluid's velocity response. The stator wall slip on the other hand is indicated by the higher velocity amplitude achieved by ketchup than the near zero value achieved by water (Figure 4 b) and g)). In addition, these time dependent velocity profiles of ketchup at both strain amplitudes show a slightly distorted sinusoidal waveform particularly at the rotor wall, indicating a non-linear response (Figure 4 (b) and (d)).

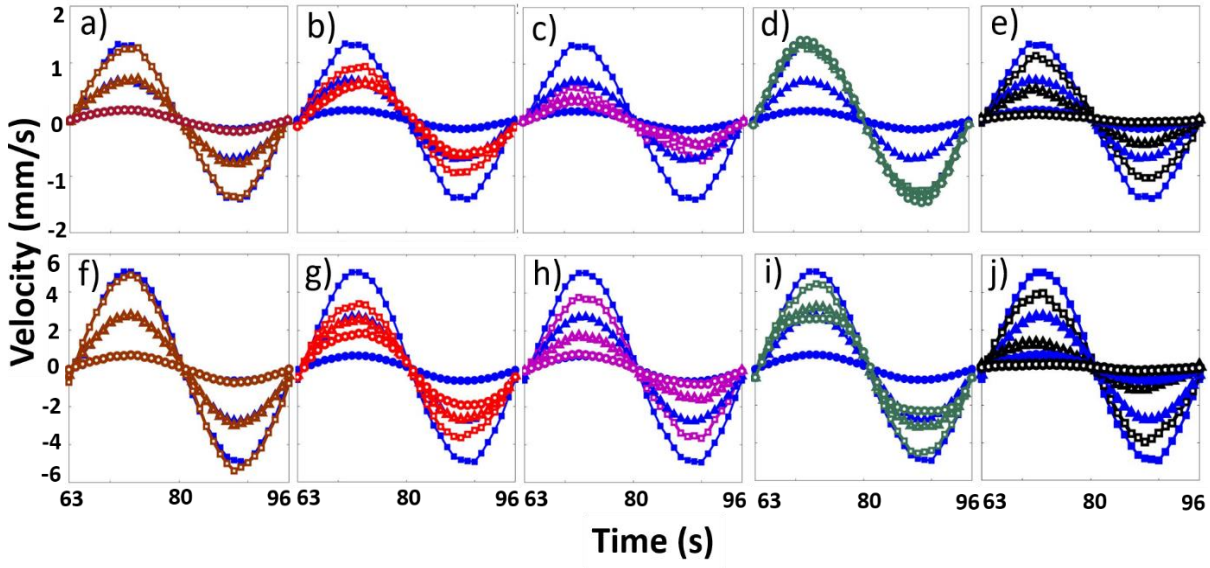

Figure 4: Time dependent velocity profiles.
Single oscillatory time dependent velocities cycles at three fluid gap positions, the rotor wall (■), mid gap (▲) and stator wall (●) for a period of 32 s at a)- e) an applied strain amplitude of 6.3 and f) –j) an applied strain amplitude of 25.2 for silicone oil (▬), ketchup (▬), drinking yogurt (▬), 0.2wt.% Carbopol (▬) and 0.6% (w/v) xanthan gum (▬) all compared to water (▬).

The time dependent velocity profiles for drinking yogurt at the lower applied strain amplitude of 6.3, clearly displays a nonlinear response as a triangular oscillatory pattern at all three positions across the gap (Figure 4 c)). Rotor and stator wall slip seen is also characterized similarly as for ketchup in Figure 4 b) and g)). From the spatially characterized LAOS velocity profiles in Figure 3 d) at a 25.2 strain amplitude, the presence of rotor slip and a slight presence of stator slip is observed. The temporally resolved velocity profiles at the stator for yogurt, clearly shows how negligible the stator slip is with the time dependent velocity profile of yogurt , as seen in Figure 4 h), aligning with that of water at the stator. This observation is also contradictory to the steady state data observed for drinking yogurt in Figure 1 d) at applied shear

rate of 5 s^{-1}, where stator slip is significantly seen. Demonstrating that the oscillatory flow alters the yogurt's flow response and microstructure at the stator. The time dependent velocity at the higher 25.2 strain, at all three positions across the gap for yogurt show a more sinusoidal behavior. Different from the triangular response seen at the lower strain amplitude, signifies a more linear behavior. The transition from a strain amplitude of 6.3 to 25.2 suggests that the yogurt's weak, 3D viscoelastic gel network of casein chains and aggregates, and polysaccharides [73] shows a microstructural rearrangement at higher strains. The stator slip for yogurt, controlled by the yogurt gel matrix, transmits stress toward the stator wall at the higher strain owing to the microstructural rearrangement due to LAOS motion at the stator, reducing stator slip to near negligible. Unlike for ketchup whose dispersion network allowed for a thin Newtonian fluid layer to generate a stator slip even at the higher strain amplitude (Figure 3 c)).

For Carbopol at a strain amplitude of 6.3 (Figure 4 d)) the absence of rotor slip along with the entire fluid across the fluid gap moving as a solid body as discussed with Figure 2 g) presents itself with each of the time dependent velocities imaged at the rotor, mid gap and stator overlaying along the time dependent velocity curve for water at the rotor. When closely analyzed, however, the time dependent velocity curve for Carbopol at the stator shows a stator velocity amplitude higher than that of the rotor velocity amplitude. Regardless, these time dependent velocities in Figure 4 d) exhibit sinusoidal behavior with negligible phase shift relative to the Newtonian reference, water. At a strain amplitude of 25.2, the 'lag' phenomenon of Carbopol at the stator wall, described with its spatially resolved LAOS velocity profiles in Figure 3 e)) above reflects as a square wave in the time dependent velocity profile of the stator in Figure 4 i). The time dependent velocity profiles at the rotor and mid gap however, are sinusoidal (Fig. 4 i)). This indicates that the

jammed structure of the gel experiences no to little shear at the stator wall. Thus the jammed structure at the stator does not rearrange in response to the decrease in velocity and once more exhibits a lag in approaching lower velocities.

For spatially resolved LAOS velocity at a 6.3 strain, as xanthan gum solution underwent an incrementing strain (Figure 2 f)) the velocity profiles generated at each second of the cycle approaching the maximum velocity (half strain amplitude) in the positive direction, showed transitions from linear to shear thinning to near linear, discussed previously. Followed by the velocity profiles showing a pronounced power law behavior with further increased strain in the positive direction. This flow response generates in the time dependent velocity of xanthan gum as a triangular oscillatory wave pattern observed at the mid gap (Figure 4 e)). It is reflected at the mid gap as the change in curvature of the velocity profiles from such strain induced transitional flow behaviors impacts the fluid layers at the middle of the fluid gap. The time dependent velocity profile at the stator is sinusoidal, but of lower velocity than its Newtonian reference temporal velocity due to rotor slip (Figure 4 e)). The high molecular weight xanthan gum polysaccharide has a polymer entanglement microstructure resulting shear thinning behavior. Time dependent velocity at the rotor and mid gap for xanthan gum at the 25.2 strain amplitude, are sinusoidal with a phase shift to the left relative to the Newtonian water (Figure 4 j)). At increasing rotor shear rate the amount of fluid across the gap showing strong shear thinning behavior increases (Figure 3 f) giving a larger low viscosity spatial region close to the rotor. The phase shift seen in both the rotor wall and mid gap time dependent velocities is due to the fluid in the gap that undergoes significant polysaccharide disentanglement with strong commensurate

shear thinning spatial expansion across the gap as the rotor reaches a maximum velocity amplitude, then failing to entangle in the time the rotor takes to decrease its velocity.

Lissajous Figures

Analysis of the data in the context of LAOS methodology presents two primary approaches [26, 27, 38]. Fourier transform analysis of the time dependent velocity data showed the presence of both odd harmonics up to 5^{th} order and even harmonics; however their intensities with respect to the fundamental frequency was insignificant and the analysis was inconclusive. Lissajous figures on the other hand exhibited quantitative variations with fluid response. Lissajous figures plot an output wave function against an input wave function. The acquired time dependent velocity at the rotor, mid gap and stator gap spatial positions for each fluid were plotted against the Newtonian velocity of water as an input. The velocity Lissajous figures generated show the deviation of a complex fluid's velocity to that of the ideal Newtonian fluid's linear behavior.

To determine the utility of the analysis approach, Lissajous figures using the sinusoidal behavior of the temporal velocity curves for water (blue curves Figure 4) at each position across the gap was analyzed as the input wave function (abscissa). The time dependent velocity of each of the other fluids at each select position across the fluid gap was used as the response wave function (ordinate). The plot of the two is as shown in Figure 5 for the Newtonian silicone oil and non-Newtonian ketchup.

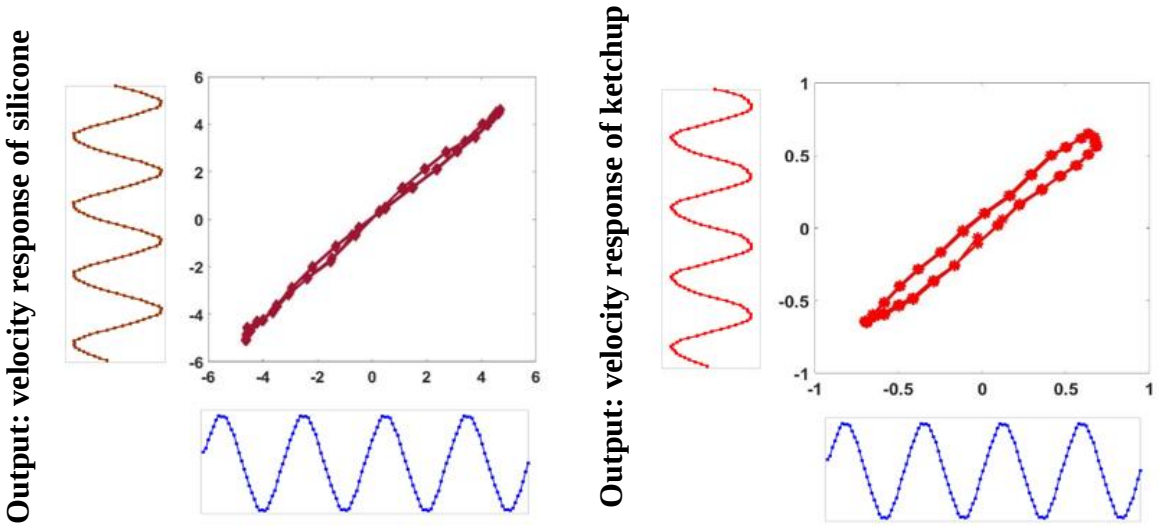

Figure 5: Construction of time dependent velocity Lissajous figures to quantify data changes. a) Testing a pure Newtonian response, the temporal velocity wave function of 1,000 cSt Silicone oil is plotted against the temporal velocity wave function of water b) For complex fluids, each of the fluid's time dependent velocities (in the example shown, of ketchup) were plotted against the sinusoidal temporal velocity wave function of water.

Lissajous figures for the non-Newtonian fluids at strain of 6.3 and 25.2 in Figure 6 and Figure 7 correspond to the same three positions across the fluid gap as described for Figure 4: rotor wall = 8.1 mm, mid gap= 8.45 mm and stator wall = 8.95 mm. The velocity Lissajous figures indicate Newtonian behavior as a straight line at a 45° angle or a slope of 1 for equal axes scaling for each position across the gap for both the strain amplitudes. This signifies both Newtonian fluids' time dependent velocities are in phase over the entire oscillatory period at each spatial position.

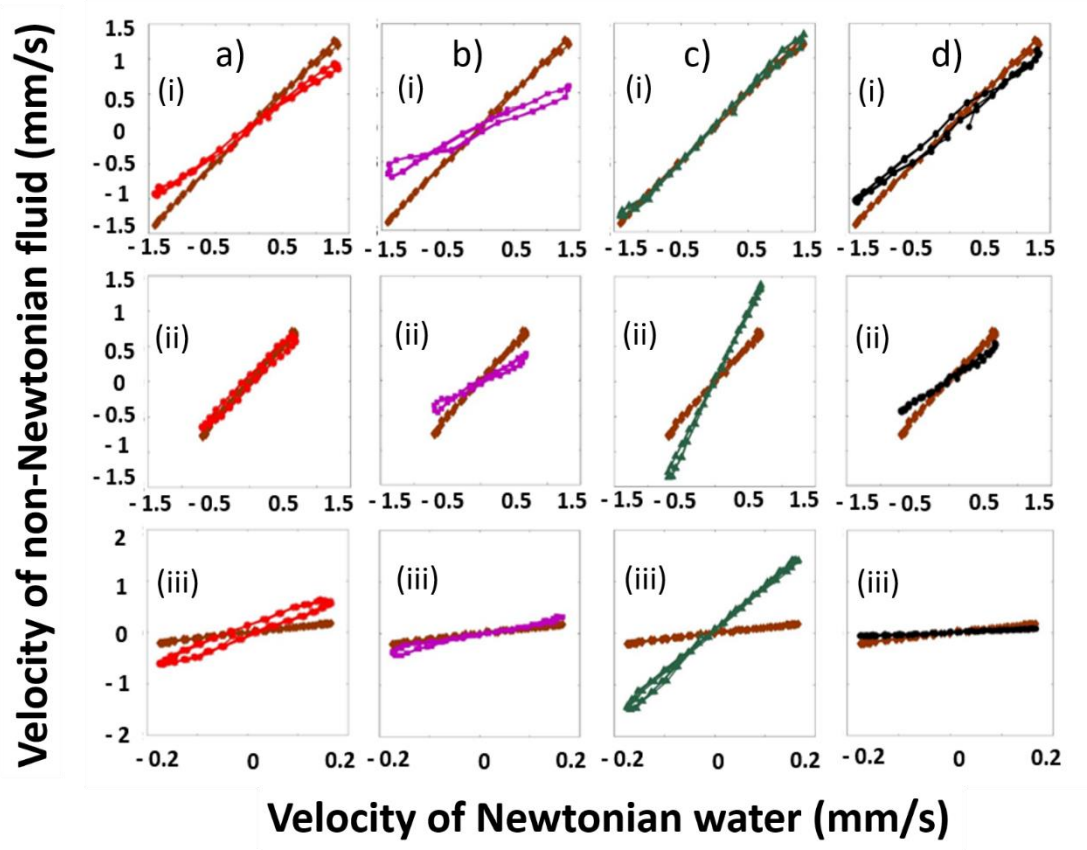

Figure 6 : Lissajous figures for non-Newtonian samples, using time dependent velocity of water, at a strain amplitude of 6.3. The Lissajous curve made with silicone oil (▬) are plotted for comparison as the Newtonian reference.

a) Lissajous figure for ketchup at the (i) rotor, (ii) mid gap and (iii) stator
b) Lissajous figure for non-fat drinking yogurt at the (i) rotor, (ii) mid gap and (iii) stator
c) Lissajous figure for 0.2wt.% Carbopol at the (i) rotor, (ii) mid gap and (iii) stator
d) Lissajous figure for 0.6% (w/v) xanthan gum at the (i) rotor, (ii) mid gap and (iii) stator

In Lissajous rheometry, the stress response to an applied sinusoidal strain rate or strain is plotted. Here, the LAOS regime is distinguished from the SAOS regime using Lissajous figures by observing symmetry. Fluids tend to maintain symmetry about the origin in both regimes,

however, lose their reflective (mirror) symmetry in the LAOS regime [74], a feature also observed in our velocity Lissajous figures.

Moving across the gap from rotor (i) to stator (ii) for all samples in Figure 6, ketchup (Figure 6 a) (i)-(iii)) to proceeds from a linear, non-Newtonian, response to an elliptical non-Newtonian response at the stator. A transition at the mid gap shows the onset of the ellipse aligned with the Newtonian curve at a 45° angle. At a strain amplitude of 25.2, ketchup (Figure 7 a) (i) – (iii)) a similar trend is seen across the analyzed gap positions with respect to the deviation from the Newtonian curve (45° angle), however the curves are linear with a slight "S" shape observed near the stator indicating a nonlinear behavior and wall slip at that location. The deviations of the curves from Newtonian response at the rotor and stator quantify wall slip at those positions. The smaller velocity amplitudes in the response ordinate (y-axis), for the rotor at strain amplitudes of 6.3 and 25.2, than for silicone oil indicates the rotor slip for ketchup, also present in the drinking yogurt at the rotor at both strain amplitudes (Figure 6 and 7 b) (i)). The velocity amplitudes at the stator (y-axis coordinates) for ketchup are higher than that of the Newtonian fluid due to stator slip. A characteristic that we can draw out from these Lissajous figures lies in the wall slip features described. Wall slip occurring at a boundary where the fluid is yielded due to flow will have a Lissajous curve of gradient less than unity, showing the curve tilting down and away from the Newtonian reference Lissajous curve, seen for ketchup at the rotor wall (Figure 6 and 7 a) (i)) . Conversely, wall slip occurring at a boundary where the fluid is un-yielded, and in plug flow, will present a Lissajous curve of gradient greater than unity, showing the fluid's curve tilting upward and away from the Newtonian reference curve of a gradient of 1 seen for ketchup at the stator wall (Figure 6 and 7 a) (iii)).

Drinking yogurt at 6.3 strain amplitude exhibits rotor slip as stated above, but also exhibits an elliptical twisted curve only at the negative velocities (Figure 6 b) (i)). This indicates the flow behavior is more sinusoidal with a phase difference in the positive velocities (forward rotation of rotor), however on the backward rotation sees an additional harmonic to the phase component which generates the twisted ellipse in the negative velocity. The rotor slip seen is characterized by a gradient less than unity indicates that yogurt is yielded near the rotor. Proceeding to the stator (Figure 6 b) (iii)), the forward flow becomes linear while the negative velocity (during the backward motion) bears just a simple ellipse. This indicates that flow in the positive velocity (forward) direction becomes a sinusoidal wave that is in phase with the sinusoidal waveform of water, while the negative velocity direction just shows a difference in phase to that of water's sinusoidal curve, but also shows no added harmonics (loss of the twist in the ellipse). This is a clear indication that drinking yogurt shows different forward and backward velocity patterns that are repeated throughout all 256 oscillatory cycles that have been averaged into eight cycles and can be seen as a potential signature of fluid thixotropy. At the higher applied strain amplitude of 25.2 at the rotor, the yogurt curve becomes more linear (Figure 7 b) (i)). A gradient less than unity showing a deviation from the Newtonian reference Lissajous curve exists, but the gradient is higher than that was seen for yogurt at a 6.3 strain. This can be attributed to a rotor slip that occurs in the presence of a more yielded fluid, than at 6.3 strain (Figure 7 b) (i)).

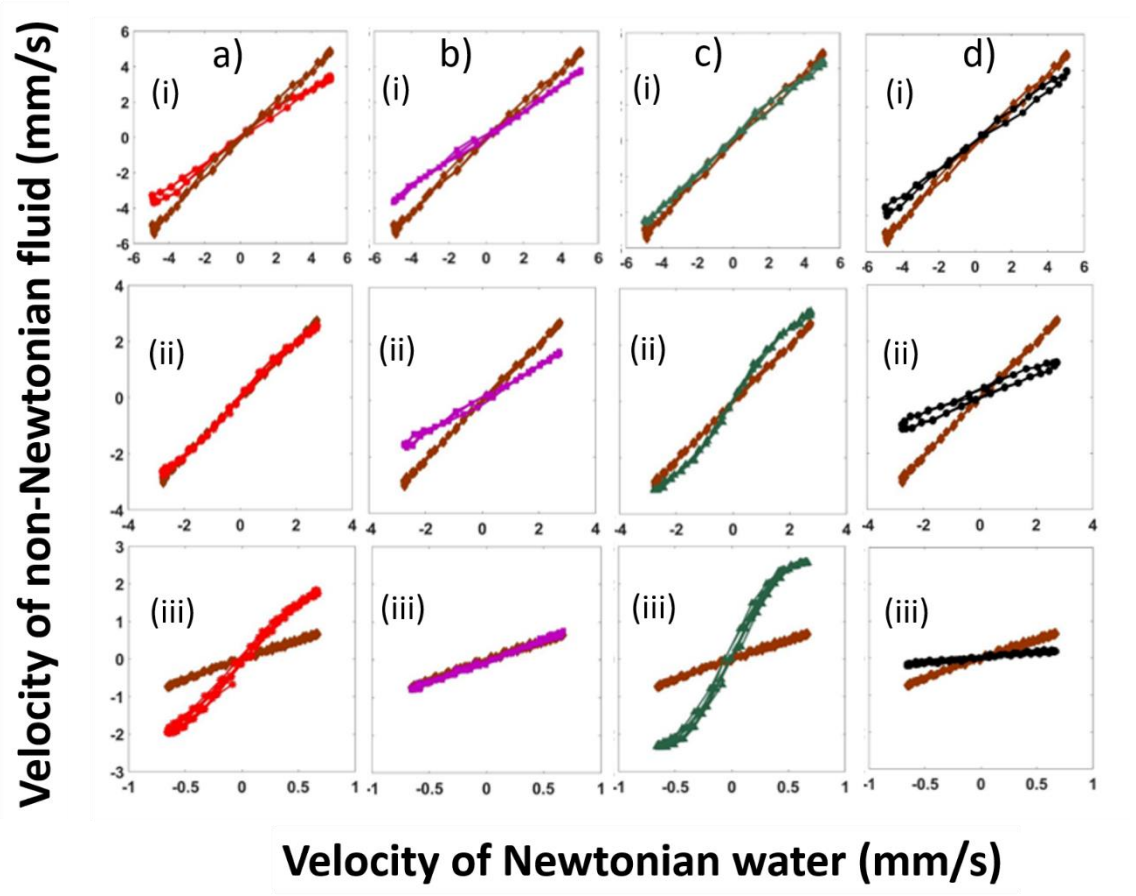

Figure 7 : Lissajous figures for non-Newtonian samples, using time dependent velocity of water, at a strain amplitude of 25.2. The Lissajous curve made with silicone oil (▬) are plotted for comparison as the Newtonian reference.

a) Lissajous figure for ketchup at the (i) rotor, (ii) mid gap and (iii) stator
b) Lissajous figure for non-fat drinking yogurt at the (i) rotor, (ii) mid gap and (iii) stator
c) Lissajous figure for 0.2wt.% Carbopol at the (i) rotor, (ii) mid gap and (iii) stator
d) Lissajous figure for 0.6% (w/v) xanthan gum at the (i) rotor, (ii) mid gap and (iii) stator

The 0.2wt.% Carbopol at 6.3 strain amplitude shows a plug flow response with the higher velocity amplitude at the stator than at the rotor as was previously discussed. The Lissajous figure confirms this (Figure 6 (c) (ii) and (iii)) where a linear Newtonian behavior in phase with that of the Newtonian behavior at the rotor is achieved. The steep gradient of the Carbopol

velocity Lissajous curve at the rotor compared to that of the Newtonian reference velocity Lissajous curve points once more to stator slip that occurring due to plug flow (Figure 6 c) (iii)). At the stator wall of the higher strain amplitude, 25.2, Carbopol again shows the steep gradient related to stator slip in the presence of plug flow (Figure 7 c) (iii)). The "S" shape that this curve takes, however, is the projection of the square wave form discussed with time dependent velocities of Carbopol (Figure 4 i)), where this feature was attributed to the 'lag' phenomenon of velocity at the stator where nonlinear surface interaction effects played a major role.
xanthan gum at each position across the fluid gap and for both strain amplitudes exhibits velocity Lissajous curves of gradient less than that of the Newtonian fluid, confirming that the curve's gradient is related to the extent of shearing of the sample (Figure 6 and 7 (d) (i)-(iii)). This indicates that the hydrated polymer chains of xanthan gum disentangle and align with the flow even at the stator [75].

Conclusions

1D spatially resolved velocity profiles of Herschel-Bulkley (HB) and a shear thinning fluid subject to LAOS motion in a cylindrical Couette cell with a 1mm fluid gap were studied employing Rheo-NMR velocimetry. Analysis methods of time dependent velocity data at three positions across the gap was undertaken using velocity Lissajous curves to elucidate complex fluid velocity variations relative to Newtonian reference under large transient motions.

Oscillatory spatial velocity profiles showed linear behavior for Newtonian fluids (DI water and 1,000 cSt silicone oil), and nonlinear spatial distributions for HB and power law fluids (Heinz ketchup, Siggi's non-fat drinking yogurt, 0.2wt.% Carbopol and 0.6% (w/v) xanthan gum) that

varied with the oscillatory flow cycles. Time dependent velocities at three different positions across the fluid gap at the two strain amplitudes were extracted from the data and were shown to provide novel data of the flow of fluids as a function of the time it was acquired in the oscillatory cycle. The velocity Lissajous figures were shown to identify the deviations each fluid showed from Newtonian fluids, with distinct signatures of slip evident.

References

1. Bonn, D., et al., *Yield stress materials in soft condensed matter.* Reviews of Modern Physics, 2017. **89**(3): p. 035005.

2. Larson, R.G., *The structure and rheology of complex fluids (Topics in chemical engineering).* 1999, New York: Oxford University Press.

3. Mewis, J. and A.J.B. Spaull, *Rheology of concentrated dispersions.* Advances in colloid and interface science, 1976. **6**(3): p. 173-200.

4. Bird, R.B., G.C. Dai G.C and B.J. Yarusso, *The rheology and flow of viscoplastic materials.* J. Fluid Mech.Journal of Fluid Mechanics, 1983. **135**: p. 1-70.

5. Rodts, S., J. Baudez, and P. Coussot, *From "discrete" to "continuum" flow in foams.* Europhys. Lett., 2005. **69**(4): p. 636-642.

6. Coussot, P., et al., *Coexistence of liquid and solid phases in flowing soft-glassy materials.* Physical review letters, 2002. **88**(21): p. 218301.

7. Macosko, C.W., *Rheology : principles, measurements, and applications*. 1994, New York: New York : Wiley-VCH.

8. Ovarlez, G., et al., *On the existence of a simple yield stress fluid behavior.* Journal of Non-Newtonian Fluid Mechanics, 2012. **193**(C).

9. Coussot, P., *Yield stress fluid flows: A review of experimental data.* J NON-NEWTON FLUID, 2014. **211**: p. 31-49.

10. Alexandrou, A.N., N. Constantinou, and G. Georgiou, *Shear rejuvenation, aging and shear banding in yield stress fluids.* J NON-NEWTON FLUID, 2009. **158**(1): p. 6-17.

11. Bonn, D., et al., *Yield stress materials in soft condensed matter.* Reviews of Modern Physics, 2017. **89**(3).

12. Dimitriou, C.J., R.H. Ewoldt, and G.H. McKinley, *Describing and prescribing the constitutive response of yield stress fluids using large amplitude oscillatory shear stress (LAOStress).* Journal of Rheology, 2013. **57**(1): p. 27-70.

13. Khalil, M. and B. Mohamed Jan, *Herschel-Bulkley rheological parameters of a novel environmentally friendly lightweight biopolymer drilling fluid from xanthan gum and starch.* Journal of Applied Polymer Science, 2012. **124**(1): p. 595-606.

14. Rao, M.A., *Rheology of Fluid, Semisolid, and Solid Foods: Principles and Applications*. 3rd ed. 2014 ed, ed. G.V. Barbosa-Cánovas. 2014, Boston, MA: Boston, MA: Springer US.

15. Al-Zahrani, S.M., *A generalized rheological model for shear thinning fluids.* Journal of Petroleum Science and Engineering, 1997. **17**(3): p. 211-215.

16. Chhabra, R.P., Richardson, J.F. , *Non-Newtonian Flow in the Process Industries: Fundamentals and Engineering Applications*. 1999: Butterworth-Heinemann. 436.

17. Chhabra, R.P., *Non-Newtonian Fluids: An Introduction*, in *Rheology of Complex Fluids*, J.M. Krishnan, A.P. Deshpande, and P.B.S. Kumar, Editors. 2010, Springer New York: New York, NY. p. 3-34.

18. Mewis, J. and N.J. Wagner, *Colloidal Suspension Rheology*. 2011, Cambridge: Cambridge: Cambridge University Press.

19. Coussot, P., *Rheophysics Matter in all its States*. 2014, Cham : Springer International Publishing : Imprint: Springer.

20. Nettesheim, F. and S.A. Rogers, *The unification of disparate rheological measures in oscillatory shearing.* PHYS FLUIDS, 2019. **31**(7): p. 73107.

21. Ptaszek, P., *Chapter 5 - Large Amplitude Oscillatory Shear (LAOS) Measurement and Fourier-Transform Rheology: Application to Food*, in *Advances in Food Rheology and Its Applications*, J. Ahmed, P. Ptaszek, and S. Basu, Editors. 2017, Woodhead Publishing. p. 87-123.

22. Barnes, H.A., Hutton, J.F., and Walters, K., *An Introduction to Rheology*. 1989: Elsevier :, Distributors for the U.S. and Canada, Elsevier Science Pub. Co. 201.

23. Hyun, K., et al., *A review of nonlinear oscillatory shear tests: Analysis and application of large amplitude oscillatory shear (LAOS).* Progress in Polymer Science, 2011. **36**(12): p. 1697-1753.

24. Dealy, J.M., *Melt Rheology and Its Role in Plastics Processing Theory and Applications*, K.F. Wissbrun, Editor. 1990, Boston, MA : Springer US.

25. Melito, H.S., C.R. Daubert, and E.A. Foegeding, *Validation of a large amplitude oscillatory shear protocol.* Journal of Food Engineering, 2012. **113**(1): p. 124-135.

26. Wilhelm, M., P. Reinheimer, and M. Ortseifer, *High sensitivity Fourier-transform rheology.* Rheol. Acta, 1999. **38**(4): p. 349-356.

27. Hyun, K., et al., *A review of nonlinear oscillatory shear tests: Analysis and application of large amplitude oscillatory shear (LAOS).* Progress in Polymer Science, 2011. **36**(12): p. 1697-1753.

28. Hyun, K., et al., *Large amplitude oscillatory shear as a way to classify the complex fluids.* J NON-NEWTON FLUID, 2002. **107**(1): p. 51-65.

29. Callaghan, P.T., *Rheo-NMR: nuclear magnetic resonance and the rheology of complex fluids.* REP PROG PHYS, 1999. **62**(4): p. 599-670.

30. Han, S.-l. and S. Stapf, *NMR imaging in chemical engineering*. 2006, Weinheim : [Chichester]: Weinheim : Wiley-VCH, Chichester : John Wiley, distributor.

31. Callaghan, P.T., *Rheo-NMR and velocity imaging.* Current Opinion in Colloid & Interface Science, 2006. **11**(1): p. 13-18.

32. Britton, M.M. and P.T. Callaghan, *Two-phase shear band structures at uniform stress.* PHYS REV LETT, 1997. **78**(26): p. 4930-4933.

33. Britton, M.M. and P.T. Callaghan, *Shear banding instability in wormlike micellar solutions.* Eur. Phys. J. B, 1999. **7**(2): p. 237-249.

34. Coussot, P., *Progress in rheology and hydrodynamics allowed by NMR or MRI techniques.* Experiments in Fluids, 2020. **61**(9): p. 207.

35. Dodge, J.S., *Oscillatory shear of nonlinear fluids* 1969, ProQuest Dissertations Publishing.

36. Pyshnograi, G.V., N.A. Cherpakova, and H.N.A. Al Joda, *Special Features of Nonlinear Behavior of a Polymer Solution on Large Periodic Deformations.* Journal of Engineering Physics and Thermophysics, 2020. **93**(3): p. 617-625.

37. Watanabe, H., Kuwahara, S. and Kotaka, T., *Rheology of Styrene-Butadiene-Styrene Triblock Copolymer in n-Tetradecane Systems* Journal of Rheology, 1984. **28**(4): p. 393.

38. Ewoldt, R.H., et al., *Large amplitude oscillatory shear of pseudoplastic and elastoviscoplastic materials.* Rheol Acta, 2010. **49**(2): p. 191-212.

39. Dealy, J.M. and K.F. Wissbrun, *Melt Rheology and Its Role in Plastics Processing: Theory and Applications*. 1990, Dordrecht: Dordrecht: Springer Netherlands.

40. Hyun, K., et al., *Large amplitude oscillatory shear behavior of PEO-PPO-PEO triblock copolymer solutions.* Rheol Acta, 2006. **45**(3): p. 239-249.

41. Ewoldt, R.H., A.E. Hosoi, and G.H. McKinley, *Nonlinear viscoelastic biomaterials: meaningful characterization and engineering inspiration.* Integr Comp Biol, 2009. **49**(1): p. 40-50.

42. Giacomin, A.J. and J.G. Oakley, *Obtaining Fourier series graphically from large amplitude oscillatory shear loops.* Rheologica acta, 1993. **32**(3): p. 328-332.

43. Ewoldt, R.H., et al., *Rheological fingerprinting of gastropod pedal mucus and synthetic complex fluids for biomimicking adhesive locomotion.* Soft Matter, 2007. **3**(5): p. 634-643.

44. Kuczera, S., et al., *Multilamellar Vesicle Formation Probed by Rheo-NMR and Rheo-SALS under Large Amplitude Oscillatory Shear.* LANGMUIR, 2018. **34**(28): p. 8314-8325.

45. Galvosas, P., T.I. Brox, and S. Kuczera, *Rheo-NMR in food science—Recent opportunities.* Magnetic Resonance in Chemistry, 2019. **57**(9): p. 757-765.

46. Di Giuseppe, E., et al., *Characterization of Carbopol hydrogel rheology for experimental tectonics and geodynamics.* Tectonophysics, 2015. **642**: p. 29-45.

47. Rofe, C.J., et al., *Nuclear magnetic resonance imaging of apparent slip effects in xanthan solutions.* Journal of Rheology, 1996. **40**(6): p. 1115-1128.

48. Johnson, G.C., *Flow Characteristics of Linear, End-Blocked Dimethylpolysiloxane Fluids.* Journal of Chemical & Engineering Data, 1961. **6**(2): p. 275-278.

49. Callaghan, P.T., *Translational Dynamics and Magnetic Resonance: Pronciples of Pulse Gradient Spin Echo NMR.* Oxford University Press, New York, 2011.

50. Al-kaby, R.N., et al., *Rheo-NMR of transient and steady state shear banding under shear startup.* Journal of Rheology, 2018. **62**(5): p. 1125-1134.

51. Webb, G.A., et al., *Magnetic resonance in food science: a view to the future*. Vol. 262. 2007, Cambridge: Cambridge: NBN International.

52. de Kort, D.W., T. Nikolaeva, and J.A. Dijksman, *Rheo-NMR: Applications to Food*, in *Modern Magnetic Resonance*, G.A. Webb, Editor. 2017, Springer International Publishing: Cham. p. 1-21.

53. Spandan, V., et al., *Drag reduction in numerical two-phase Taylor–Couette turbulence using an Euler–Lagrange approach.* J FLUID MECH, 2016. **798**: p. 411-435.

54. Brox, T.I., *New Methods for Studying Materials Under Shear with Nuclear Magnetic Resonance*, in *Physics*. 2016, Victoria University of Wellington.

55. Wassenius, H. and P.T. Callaghan, *NMR velocimetry studies of the steady-shear rheology of a concentrated hard-sphere colloidal system.* Eur. Phys. J. E, 2005. **18**(1): p. 69-84.

56. Ragouilliaux, A., et al., *Flow instability and shear localization in a drilling mud.* Rheol Acta, 2006. **46**(2): p. 261-271.

57. Coussot, P., et al., *Coexistence of liquid and solid phases in flowing soft-glassy materials.* PHYS REV LETT, 2002. **88**(21): p. 218301-2183014.

58. Ovarlez, G., et al., *Phenomenology and physical origin of shear localization and shear banding in complex fluids.* Rheol Acta, 2009. **48**(8): p. 831-844.

59. He, J., S.S. Lee, and D.M. Kalyon, *Shear viscosity and wall slip behavior of dense suspensions of polydisperse particles.* Journal of Rheology, 2019. **63**(1): p. 19-32.

60. Derakhshandeh, B., S.G. Hatzikiriakos, and C.P.J. Bennington, *Rheology of pulp suspensions using ultrasonic Doppler velocimetry.* Rheol Acta, 2010. **49**(11): p. 1127-1140.

61. Barnes, H.A., *A review of the slip (wall depletion) of polymer solutions, emulsions and particle suspensions in viscometers: its cause, character, and cure.* J NON-NEWTON FLUID, 1995. **56**(3): p. 221-251.

62. Sögaard, C., I. Simonsson, and Z. Abbas, *Development and Evaluation of Polyether Ether Ketone (PEEK) Capillary for Electrospray.* ACS OMEGA, 2019. **4**(1): p. 1151-1156.

63. Tang, H., et al., *Shear-banding in entangled xanthan solutions: tunable transition from sharp to broad shear-band interfaces.* Soft Matter, 2018. **14**(5): p. 826-836.

64. Milas, M., et al., *FLOW AND VISCOELASTIC PROPERTIES OF XANTHAN GUM SOLUTIONS.* Macromolecules, 1990. **23**(9): p. 2506-2511.

65. Pipe, C.J., T.S. Majmudar, and G.H. McKinley, *High shear rate viscometry.* Rheologica Acta, 2008. **47**(5-6): p. 621-642.

66. Carmona, J.A., et al., *Large amplitude oscillatory shear of xanthan gum solutions. Effect of sodium chloride (NaCl) concentration.* Journal of Food Engineering, 2014. **126**: p. 165-172.

67. Zhong, L., et al., *Rheological behavior of xanthan gum solution related to shear thinning fluid delivery for subsurface remediation.* Journal of Hazardous Materials, 2013. **244**: p. 160-170.

68. Tan, J. and W.L. Kerr, *Rheological properties and microstructure of tomato puree subject to continuous high pressure homogenization.* Journal of Food Engineering, 2015. **166**: p. 45-54.

69. Harper, J.C. and A.F. El Sahrigi, *Viscometric Behavior of Tomato Concentrates.* Journal of food science, 1965. **30**(3): p. 470-476.

70. Dinkgreve, M., et al., *Carbopol: From a simple to a thixotropic yield stress fluid.* Journal of Rheology, 2018. **62**(3): p. 773-780.

71. Piau, J.M., *Carbopol gels: Elastoviscoplastic and slippery glasses made of individual swollen sponges Meso- and macroscopic properties, constitutive equations and scaling laws.* Journal of Non-Newtonian Fluid Mechanics, 2007. **144**(1): p. 1-29.

72. Nevo, U., et al., *A system and mathematical framework to model shear flow effects in biomedical DW-imaging and spectroscopy.* Nmr in Biomedicine, 2010. **23**(7): p. 734-744.

73. Lobato-Calleros, C., et al., *Microstructural and Rheological Properties of Low-Fat Stirred Yoghurts Made with Skim Milk and Multiple Emulsions.* Journal of Texture Studies, 2009. **40**(6): p. 657-675.

74. Läuger, J. and H. Stettin, *Differences between stress and strain control in the non-linear behavior of complex fluids.* Rheol Acta, 2010. **49**(9): p. 909-930.

75. Khan, S.Y.Y., M.; Sardar, N. , *Studies on Rheological Behavior of Xanthan Gum Solutions in Presence of Additives.* Petroleum and Petrochemical Engineering Journal, 2018. **2**(5).

CHAPTER SIX

FRACTAL VANE GEOMETRY, A POTENTIAL MEANS TO REDUCE WALL SLIP: RHEO-NMR PERSPECTIVE

Contribution of Authors and Co-Authors

Manuscript in Chapter 6

Author: Jayesha S Jayaratne

Contributions: Wrote manuscript. Helped in designing experimental protocols and conceiving the experiment. Prepared samples, collected, analyzed and interpreted Rheo-NMR data collected and analyzed rheology data.

Co-Author: Crystal E. Owens

Contributions: Designed and fabricated the 12-arm fractal vane for the rheo-NMR rheometer used. Helped in designing experiment protocols. Discussed data and data interpretation. Will provide feedback and comments on the manuscript.

Co-Author: Gareth H. McKinley

Contributions: Discussed data, data interpretation and suggested experimental protocol improvements. Will provide feedback and comments on the manuscript.

Co-Author: Joseph D. Seymour

Contributions: Edited manuscript with significant contributions to the data discussion section. Helped in experiment protocol design and NMR technique setup. Discussed data, data interpretation and suggested experimental protocol improvements. Secured funding.

Manuscript Information

Jayesha S. Jayaratne, Crystal E. Owens, Gareth H. McKinley and Joseph D. Seymour

Status of Manuscript:
__X_ Prepared for submission to a peer-reviewed journal
___ Officially submitted to a peer-reviewed journal
___ Accepted by a peer-reviewed journal
___ Published in a peer-reviewed journal

FRACTAL VANE GEOMETRY, A POTENTIAL MEANS TO REDUCE WALL SLIP: RHEO-NMR PERSPECTIVE

Abstract

Rheo-NMR velocimetry measurements were used to test a novel 3D printed Rheo-NMR 12 arm fractal vane rotor. In the study of complex fluids, such as yield stress fluids and shear banding wormlike micelles, wall slip commonly occurs, making interpretation of rheological data difficult. Typically shear cell surfaces are physically roughened in order to negate wall lip. One common practice to roughen boundaries is using sandpaper, however, that can leave dust particles in samples and the application and removal process can be tedious. There is also difficulty in determining an appropriate roughness with this method. This study tests whether a fractal vane rotor can be used to reduce or entirely eliminate wall slip over the widely used geometry in rheo-NMR, the concentric cylinder. The type of fractal vane geometry used in this work was shown in previous studies to nullify slip and its design comes with an advantage of being easily fabricated via 3D printing for use in Rheo-NMR applications. 1D and 2D velocity maps were acquired through rheo-NMR velocimetry for a simple yield stress fluid (Carbopol) and, for calibration purposes, a high viscosity Newtonian fluid (silicone oil). Applied shear rates of 5 s^{-1} and 7 s^{-1} were selected for study, as slip was noted for the yield stress fluid at these shear rates. Results showed that the fractal vane shear cell was able to reduce stator slip, but not necessarily rotor slip, for the yield stress fluid at the shear rates imposed and that no secondary flows were present.

Introduction

Many industrial fluids and natural materials are yield stress fluids. Yield stress fluids readily flow once the applied stress is greater than a critical value, called the yield stress, and otherwise behave as viscoelastic solids [1-3]. While the existence of a true yield stress has been debated in the literature, yield stress is still considered a well-recognized rheological parameter [4, 5]. In addition to the yield stress behavior, these fluids can also show wall slip, time dependent thixotropic effects (ageing, shear rejuvenation), transition regimes of flow behavior and sedimentation [2, 6-8] . Under shear, yield stress fluids primarily exhibit two modes of flow: plug flow and fully sheared flow [9] [10].

Yield stress fluids are of interest as they account for many commercial products widely seen in industries like personal care products (toothpaste, hair gel etc.) and foods (mayonnaise, ice cream etc.). These yield stress fluids encompass a wide range of material types; including pastes, concentrated suspensions, emulsions, foams and composites [11].

In industry, the use of rheology in determining the yield stress of these viscoplastic complex fluids is a common practice. A typical geometry used in research and development laboratories is the concentric cylinder, or Taylor Couette, system [11]. Used extensively in the study of hydrodynamic instabilities, dating back to G.I. Taylor's experiments in 1923, flow in the concentric cylinder today can be considered the 'hydrogen atom of fluid dynamics' [12-14]. The concentric cylinder geometry has appeal as it is possible to carry out experiments in a closed system and the cylinder's rotation rate is controllable with high accuracy [15]. While the design and model of the concentric cylinder works well for Newtonian systems, measurements may not fully capture the material properties of complex fluids as ideal laminar Couette flow (no

secondary flows) is typically assumed, shear heating or imperfections in the measurement device are not accounted for and wall slip effects are neglected [1, 16]. For a yield stress fluid, the flow within a concentric cylinder cell will be plug flow in the regions of the fluid gap that experience a stress less than the yield stress (toward the stationary boundary) while a sheared layer could appear closer to the rotor wall [9]. A transition to a fully sheared regime may be observed at higher applied shear rates when the shear stress close to the stationary 'stator' wall becomes higher than the material's yield stress [9]. Another characteristic feature of a yield stress fluid is wall slip at solid and smooth boundaries, the concentric cylinder geometry being no exclusion to this [13, 17-21]. This wall slip or wall depletion effect happens when the dispersed phase of a two-phase (or multi-phase) material moves away from the solid boundaries of the geometry leaving a thin low viscosity depletion layer, with a thickness in the order of 0.1-10μm, that effectively flows with ease acting like a lubricant at the boundary [17]. Large particles in the disperse phase and geometry boundaries with like electrostatic charges, accompanied with an electrically conductive continuous phase, also cause wall slip [17]. This phenomenon complicates the determining of a reliable yield stress [22]. While roughening the rotor boundary or widening the fluid gap aids in reducing wall slip, they are not fool proof methods. In some instances the roughness maybe insufficient and widening the gap creates a non-homogeneous shear rate distribution [20, 23].

Another method employed to reduce slip, dating back to 1936, was the use of a glass vane geometry in place of a cylinder [24, 25]. A vane geometry typically consists of thin straight blades of equal length, termed "arms", arranged in a hexagonal or cruciform pattern around a central point. The fluid to be tested sits within a cylindrical "cup" and the vane is inserted and

acts as the rotor. The use of the vane geometry was further developed by Nguyen and Boger in the 1980s where they studied yield stress behavior in clays and found it to be the most suitable geometry [9, 25]. The use of the four vane and six vane geometry then became common practice as measurements of these geometries agreed well with those of the concentric cylinder [25-27]. The vane geometry also reduced time dependent or thixotropic effects shown by most yield stress fluids as the material structure was retained during sample loading, when the thin vane is inserted into the fluid [28-30]. The fluid between the blades was assumed to move as a solid body along with the vanes, creating a 'soft' boundary where slip would not be expected to occur. Any yielding behavior outside this soft boundary would then be a property of the fluid itself [26, 31]. However, secondary flows between vanes have been observed for low viscosity fluids and circular streamlines, indicative of an ideal axisymmetric stress field, are not obtained when measuring strongly shear-thinning fluids [32, 33].

A novel fractal vane rotor was designed with a Bethe lattice like fractal structure [32]. This structure provides a large contact surface area for the fluid while maintaining a sparse internal structure that reduces time thixotropic effects in the sample during sample loading. The fractal geometry was 3D printed, allowing for easy and cost-effective fabrication of an interchangeable rheological geometry that is also chemically compatible with a wide range of solvents. Owens *et al.* measured bulk torque for fractal vane geometries with varying contact edges and compared results to "reference" measurements made by cone-and-plate geometries with roughened surfaces [32]. This study also combined the results from analytically calculated 2D stress field contour plots for Newtonian fluids with a vane geometry (using the Wiener-Hopf method), and numerically calculated occluded area fraction (OAF) for the fractal vane geometry

[27, 32]. They found, from calculations done on bulk torque measurements, that a fractal vane geometry bearing 12 or 24 contact vane edges exhibited the least degree of slip while bearing a sufficiently homogeneous stress field and low OAF.

In this work, Rheo-NMR techniques were used to obtain 1D and 2D spatially resolved velocity measurements of the flow field within a 3D printed 12 arm fractal vane geometry designed to replace the rotor of a Rheo-NMR concentric cylinder shear cell. Rheo-NMR is a combination of rheometry and nuclear magnetic resonance (NMR) techniques that can be used to observe spatio-temporal velocity fields in fluids. Rheo-NMR has the advantages of being non-invasive, non-destructive and capable of measuring velocity in any direction, even for opaque materials [34-37].

Rheo-NMR is complimentary to traditional bulk rheology measurements, as spatially resolved measurements of the flow field allows for inspection of localized effects, such as the wall slip and flow heterogeneities often present in yield stress fluids [7, 18, 34, 38].
With Rheo-NMR velocimetry measurements, it was possible to directly detect whether the 12 arm fractal vane rotor was able to reduce wall slip and maintain axisymmetric flow in yield stress fluids. Carbopol, a model non-thixotropic yield stress fluid known to exhibit wall slip, and a high viscosity Newtonian silicone oil were the fluids chosen for this study [39].

Materials and Methods

Materials

0.6wt.% Ultrez10 Carbopol (Lubrizol) solution was used for all Rheo-NMR and rheology measurements. The solution was prepared by dissolving Carbopol powder in deionized water by stirring it at 50 rpm for an hour using a stir bar. The aqueous Carbopol solution was then

neutralized to a pH 7 using triethanalamine (TEA) and left to rest for 24 hours prior to loading the samples to the shear cell. The preparation method followed protocols by Dinkgreve *et al.* as close as possible to ensure the solution prepared was a simple yield stress fluid [39].

Air bubbles induced in the samples on loading the shear cells were removed by shearing the samples at 15 s^{-1} while being heated in a water bath at 45^{o}C. The Carbopol sample using the fractal vane shear cell required 4 days of continuous shearing for the degassing process. For the concentric cylinder Couette shear cell, the Carbopol sample required 24 hours of shearing for degassing. The sample was then left to rest for 24 hours prior to any Rheo-NMR measurements. A 1,000 cSt (1 Pa.s) silicone oil sample (Consolidated Chemicals & Solvents LLC) was also studied as a Newtonian reference. A bubble removal protocol was not required for this sample since bubbles did not remain trapped once the Newtonian fluid was loaded to the shear cells.

Rheo-NMR Equipment

A magneto safe, strain controlled Rheo-NMR rheometer, with the capability of inducing constant rotations between 0.001 Hz - 9.99 Hz was used for all measurements. The Rheo-NMR Couette cell was comprised of a glass stator and a polyether ether ketone (PEEK) smooth rotor. The outer and inner radii of the shear cell were R_o = 9 and R_i = 8 mm, respectively, resulting in a fluid gap of 1 mm and a radius ratio ($\kappa = R_i / R_o$) of 0.89. The 12-arm fractal vane rotor was 3D printed, also from PEEK, with the radius of the knife edge of the fractal vane, $R_v = 8$ mm, keeping to the same radius as the Rheo-NMR concentric cylinder rotor. The Rheo-NMR rheometer was built such that the rotor could be interchanged, while keeping the glass stator the same.

Methods

All Rheo-NMR velocity measurements were performed using a Bruker AVANCE 300 spectrometer equipped with a Micro-2.5 gradient system (maximum Gradient: 1.5 T/m 60A) and a 25 mm diameter ^{1}H radiofrequency coil, along with Bruker Paravision 5.1 and Topspin 3.5 software. Data was anlayzed using Prospa (Magritek, NZ) and MATLAB (MathWorks, Natick, MA).

1D and 2D Rheo-NMR velocity measurements were acquired at two applied shear rates, 5 and 7 s^{-1}. A standard PGSE flow encoding imaging sequence [40] was used to acquire 2D velocity images. 2D axial velocity images were acquired with a field of view of 23 mm x 23 mm and matrix size 512 x 512, resulting in a voxel resolution of 45 μm x 45 μm over a 1 mm slice. The imaging slice was located at half the fill height of the fluid (~5.5 cm), i.e. the longitudinal center of the shear cell, so as to avoid end effects. All 2D velocity images had four averages and two q-steps each of duration, δ =1 ms, with an observation time, Δ, of 8 ms, a repetition time of 1,500 ms and echo time of 12.3 ms. Separate images were obtained that measured velocity in all three orthogonal directions, v_x, v_y and v_z. Velocity images were also acquired without flow to allow for any necessary phase corrections to be made to the images acquired under flow.

In order to acquire all echoes at the same position vector of the fractal vane rotor and thus avoid ghosting artifacts, a trigger was added to the pulse sequence. Once the acquisition command was given, the spectrometer would wait for the trigger signal from the Rheo-NMR rheometer before data acquisition. The trigger signal would command a data acquisition from the spectrometer each time the rotor completed a full revolution and arrived at the same position.

However, this came at the expense of the total acquisition time. The acquisition times were 12 hours at a shear rate of 5 s^{-1} and 8 hours at a 7 s^{-1}.

To acquire 1D velocity profiles, pulsed gradient spin echo (PGSE) motion encoding was employed with double slice selection and frequency encoding [40-43]. 1D velocity images were acquired with a spatial resolution of 45 μm across the fluid gap (FOV= 23 mm with 512 points). The imaging region was a 10mm slice in the vorticity direction that was 1mm thick in the direction of flow. The 1mm thickness was chosen, as it was the optimal slice thickness to eliminate any curvature effects for a concentric cylinder Couette shear cell of $R_o = 9$ mm and $R_i = 8$ mm [44]. Velocity was measured in the direction of flow with displacement observation time Δ = 8 ms, magnetic field gradient pulse duration δ = 1 ms, 2 q-steps, and 32 averages. Since the experiments were triggered, the acquisition time for the 1D velocity profiles at 5 s^{-1} was 10 minutes and 46 s minutes while for 7 s^{-1} was 7 minutes 40 s. For the Couette shear cell, since the rotor was symmetric through all time points across a revolution, only a single 1D velocity image in the direction of the flow was obtained for both samples at both shear rates. The fractal vane however had multiple imaging regions, with 1D velocity profiles collected at three separate positions relative to the vane arms (Figure 2). In the data processing step, for both 1D and 2D images, a mask was applied to remove noise. This mask was constructed by ignoring the pixels that bore signal intensities less 25% of the average in the fluid's intensities in the magnitude image.

Discussion

The Couette shear cell was designed with a narrow gap. For a Newtonian fluid this meant that the fluid layers closest to the rotor wall would achieve a velocity equal to that of the shear

rate applied by the rotor, $v_{r_i} = \Omega r_i$, where Ω is the angular frequency of the rotor and r_i is the rotor radius [1, 7]. For the fluid layers closest to the stator, assuming a no slip boundary condition means the expected stator velocity would be zero. In the narrow gap limit, a constant shear rate and therefore linear velocity distribution would be expected. The 1D velocity profiles for Newtonian silicone oil in Figure 1 a) and 1 b) exhibit a nearly linear velocity distribution and slip is not observed at the walls, as expected. The 1D velocity profiles for the simple yield stress fluid (0.6wt.% Carbopol) show slip at both stator and rotor walls at both applied shear rates (Figure 1 c) and d)). At a shear rate of 5 s^{-1} (Figure 1 c)), the rotor velocity for Carbopol is 4.2 mm s^{-1} as opposed to the expected 5 mm s^{-1} and the stator velocity is 1.46 mm s^{-1} instead of the expected zero velocity. Similarly, at the 7 s^{-1} shear rate (Figure 1 d)), Carbopol shows a rotor velocity of 6.2 mm s^{-1} as opposed to the expected 7 mm s^{-1} with a stator velocity of 1.7 mm s^{-1}. It is in our interest to understand if this wall slip effect observed when using the Couette shear cell for simple yield stress fluids can be reduced or completely mitigated using the 12-arm fractal vane geometry.

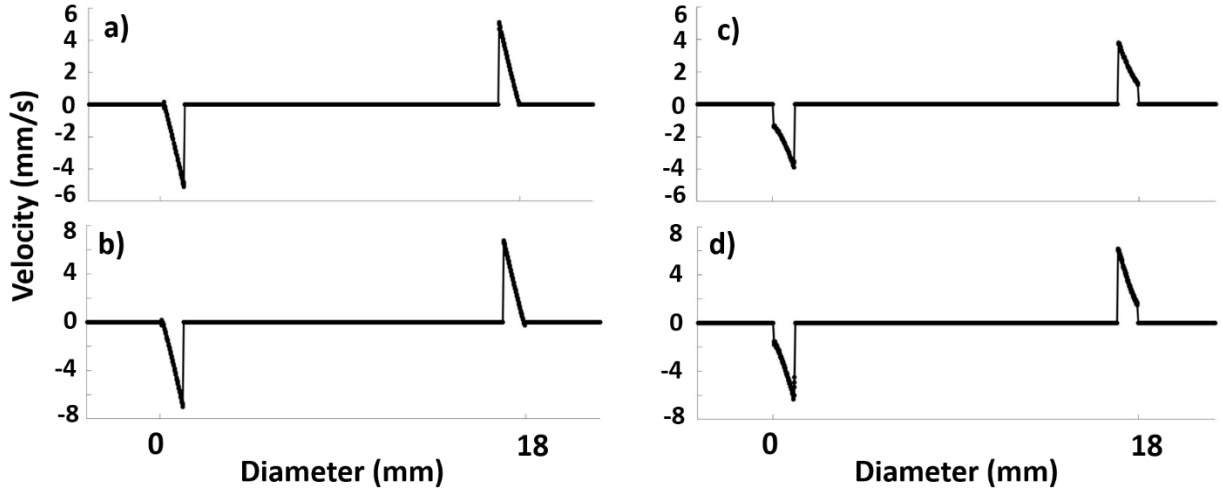

Figure 1: 1D NMR velocity profiles of 1,000 cSt silicone oil and 0.6wt% Carbopol at steady state in a Couette shear cell, sheared at shear rates of 5 s^{-1} and 7 s^{-1}. The outer stationary cup wall is found at 0mm and 18mm. a) Silicone oil sheared at a shear rate of 5 s^{-1} with no wall slip at either boundary. b) Silicone oil sheared at a shear rate of 7 s^{-1} with no wall slip at either boundary. c) Carbopol sheared at a shear rate of 5 s^{-1} exhibiting a Herschel-Bulkley type flow and both rotor and stator slip. d) Carbopol sheared at a shear rate of 7 s^{-1} exhibiting a Herschel-Bulkley type flow and both rotor and stator slip.

Figure 2 shows 2D cross-sectional images of the fractal vane geometry. The signal is derived from the fluid shown by the regions in green and grey in figure 2 a) and entire region in green of Figure 2 b). The black region within the fluid for both Figure 2 a) and b) is the solid fractal vane rotor made of PEEK where no signal is derived from. The regions in black surrounding the fluid are the glass stator and the empty space between the RF coil and the shear cell. The region considered to be the 1 mm "fluid gap" for the vane geometry is found between the perimeter outlined by the vane radius, R_v, and the outer stator (Figure 2a)). The fluid trapped in the fractal vane cavities is expected to behave as a solid body (grey region in Figure 2 a)) hence creating a "soft" cylindrical boundary [32].

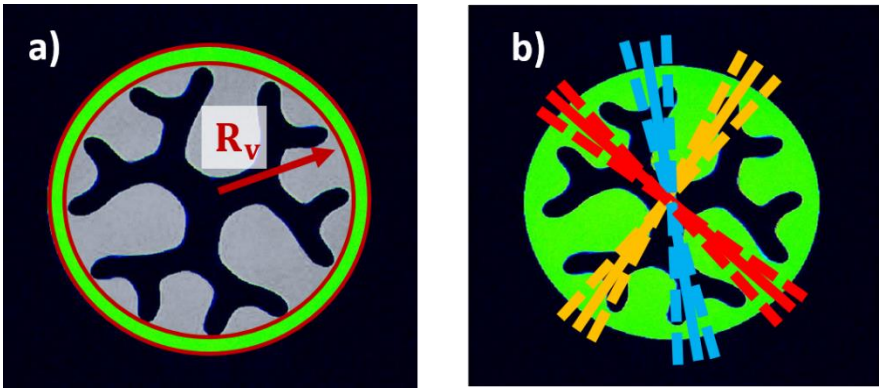

Figure 2: 2D image of the 12-arm fractal vane shear cell.
a) Region of interest where fluid velocity profiles are of interest is shown by the green region outlined in red. The gray region depicting the fluid trapped within the cavities of the fractal vane that behaves as a solid body during rotation of the fractal vane rotor.
b) Anticipated alignment (solid lines) vs approximate region (dashed lines) of the 1mm thick slices imaged in the 1D velocity profiles for the 12-arm fractal vane geometry.

The red, blue and yellow slices in Figure 2 b) correspond to the approximate alignment of the 1D velocity profiles and correspond to the red, blue and yellow boxes in Figures 3 and 4. We say ‘approximate’ as the exact placement of the slice depended on the orientation of the geometry when it was attached to the drive shaft which was difficult to precisely determine. In addition, as the 1D velocity profiles acquired are averaged across a 1mm slice thickness in the direction of flow, some pixels nearest the knife edge may be impacted by curvature. As a result, a few pixels closest to the fractal vane geometry may show differences between each expected orientation of acquisition.

The red slice in Figure 2 b) corresponds to a ‘soft’ rotor wall boundary, since the fluid in the “fluid gap” is directly in contact with the fluid moving as a solid body in the deep cavity. In the blue slice, the fluid in the ‘fluid gap’ is located at the vane edge responsible for pushing forward the fluid trapped in the deep cavity. Finally, the yellow slice indicates the imaged region

with the vane edge that is heading the spin of the rotor. In essence the fluid in the deep cavity gets pulled along by this vane edge.

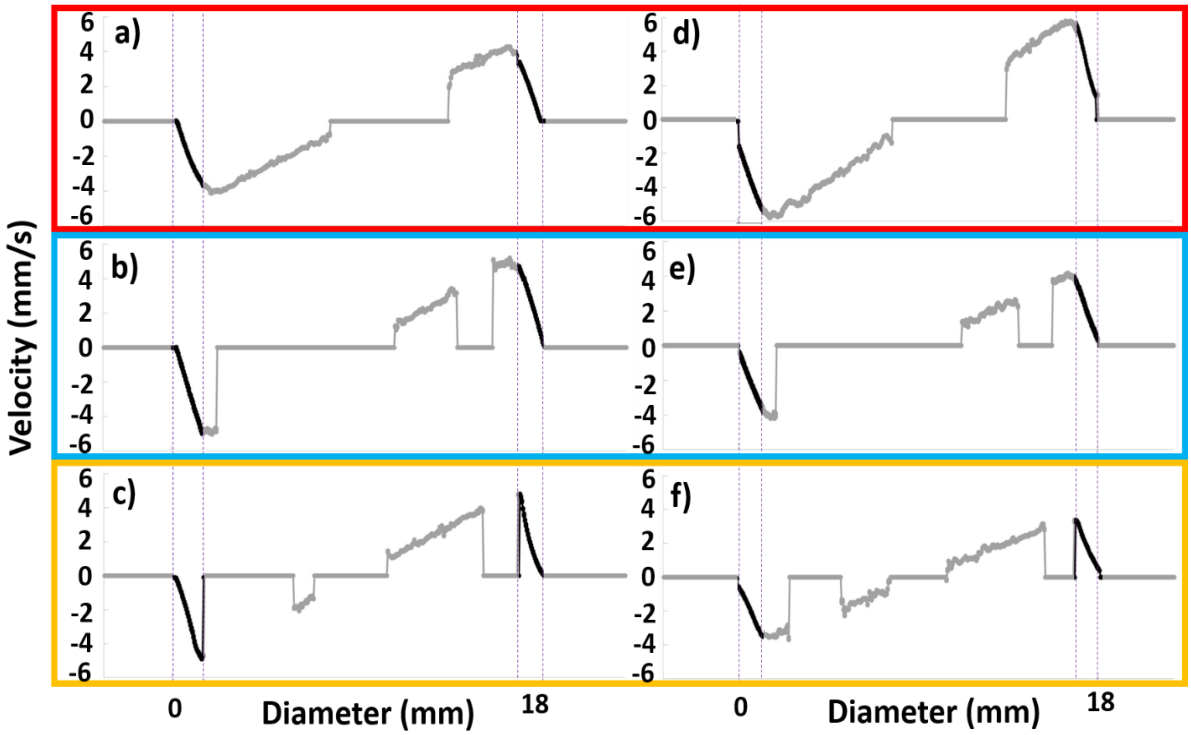

Figure 3: 1D NMR velocity profiles for the 12-arm fractal vane at an applied shear rate of 5 s^{-1} for a)-c) 1,000 cSt silicone oil and d)-f) 0.6wt% Carbopol. Each 1D velocity profile outlined with the color corresponding to the imaged regions in Figure 2 b). Velocity profile of the fluid gap in interest is outlined on black while all other regions in grey are expected to behave as a solid body. a) - c) for Newtonian silicone oil, no stator slip is seen (at 0mm or 18mm) with an expected zero velocity at the stator. Rotor slip perceived only in slices a) and c). d) - f) for the yield stress fluid, Carbopol, show stator slip (at 0mm nor 18mm) with the velocity at the stator wall being greater than zero.The highest stator slip detected, 1.45 mm s^{-1}, was in the fluid cavity region (d) where a peculiar velocity overshoot instead of a rotor slip is seen at R_v. Slices in e) and f) showing lesser stator slip, however, show higher rotor slip than Carbopol in the Couette cell.

1D images for 1,000 cSt silicone oil at a 5 s^{-1} shear rate, shown in Figure 3 a) - c), show zero velocity at the stator (at diameters of 0 mm and 18 mm), displaying a no-slip boundary

condition for all slices. The velocity at the 'soft' boundary (Figure 3 a); red slice) exhibited a velocity of 4.2 mm s^{-1}, lower than the expected 5 mm s^{-1} velocity of the rotor, R_v, a 'soft' boundary rotor slip. The Newtonian fluid reached the expected 5mm s^{-1} rotor velocity in the region where fluid is pushed by the vane edge (Figure 3 b); blue slice). For the region of fluid that gets pulled by the vane edge (Figure 3 c); yellow slice), the velocity nearest the rotor is 4.7 mm s^{-1}, again exhibiting slip.

1D velocity profiles for Carbopol at an applied shear rate of 5 s^{-1} (Figure 3 d) e) and f)) showed varied degrees of stator wall slip. Slices closer to the arms of the vane (Figure 3 e) and f); blue and yellow slices respectively), exhibited a decreased stator slip compared to that observed by Carbopol in the Couette shear cell (Figure 1 c)). The blue slice (Figure 3 e)) showed a stator velocity of 0.44 mm s^{-1} while the yellow slice (Figure 3 f)) exhibited a stator velocity of 0.41 mm s^{-1}. The stator velocity in the Couette cell was 1.46 mm s^{-1}. The stator velocity for the region in line with the deep fluid cavity (Figure 3 a); red slice) was approximately equal to the 1.45 mm s^{-1} stator velocity seen with the Couette cell for Carbopol (Figure 1 c)). Therefore, stator slip was not reduced for the 'soft' boundary.

Rotor slip was also observed for both the velocity profiles at the vane edge pushing the fluid cavity (Figure 3 e); blue slice) and the pulling the fluid cavity (Figure 3 f); yellow slice). The rotor velocities were 3.8 mm s^{-1} and 3.3 mm s^{-1} for the blue and yellow slices, respectively, as opposed to the 4.2 mm s^{-1} rotor velocity seen for Carbopol in the Couette cell. In essence, the 'partially soft' rotor boundary seems to have increased the slip detected at the rotor wall as opposed to the 'hard' rotor wall boundary of the Couette shear cell. The 'soft' rotor boundary (Figure d); red slice) showed a velocity of ~ 5.4 mm s^{-1}, higher than the expected applied

velocity of 5 mm/s at R_v. To eliminate any possible transient startup effects of Carbopol that may have contributed to this velocity overshoot, the experiment was repeated after a pre-shear of 5 s^{-1} for one hour. However, the same effect was observed.

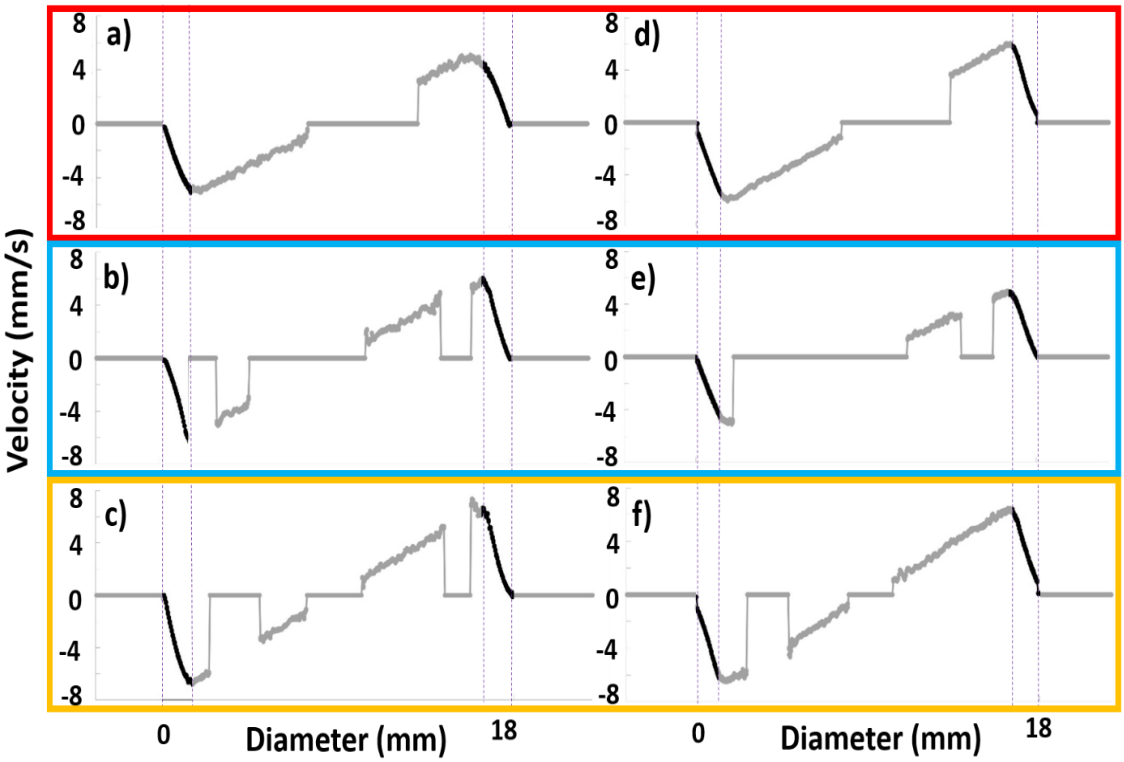

Figure 4: 1D NMR velocity profiles for the 12-arm fractal vane at an applied shear rate of 7 s^{-1} for a)-c) 1,000 cSt silicone oil and d)-f) 0.6wt% Carbopol. Each 1D velocity profile outlined with the color corresponding to the imaged regions in Figure 2 b). Velocity profile of the fluid gap in interest is outlined on black while all other regions in grey are expected to behave as a solid body.
a)- c) for the Newtonian silicone oil, no stator slip is seen (at 0mm or 18mm) with an expected zero velocity at the stator wall. Rotor slip perceived only in slices a) and b).
d) - f) for the yield stress fluid, Carbopol. Stator slip (at 0mm nor 18mm) only observed in d) and f) with the velocity at the stator wall being greater than zero, no flow boundary condition achieved at stator in slice e). All three slices d) - f) depicted different valued rotor slips (at R_v).

Figure 4 shows 1D velocity profiles at an applied shear rate of 7 s^{-1} for the fractal vane. Silicone oil again did not display any stator slip, however, similarly to the silicone oil at a 5 s^{-1}

shear rate, rotor slip was observed at the ‘soft’ boundary (Figure 4 a); red slice). The rotor velocity was 4.96 mm s^{-1}, lower than the 7 mm s^{-1} expected rotor velocity. The fluid at the vane edge pushing the fluid in the cavity (Figure 4 b); blue slice) also exhibited slip with a velocity of 5.95 mm s^{-1}. The fluid at the vane edge that pulls the fluid in the fluid cavity (Figure 4 c); yellow slice) registered the expected 7 mm s^{-1} rotor velocity, indicating an absence of slip.

Carbopol sheared at 7 s^{-1} (Figure 4 d)- f)) showed decreased stator slip compared to the Couette cell. Stator slip was not observed for the region where the vane edge was pushing the fluid of the fluid cavity (Figure 4 e); blue slice) and stator slip velocities of 0.75 mm s^{-1} and 0.95 mm s^{-1} were observed for the region with the ‘soft’ rotor boundary (Figure 4 d); red slice) and the region where the vane edge was pulling the fluid in the cavity (Figure 4 c); yellow slice), respectively. The stator velocity in the Couette cell was 1.7 mm s^{-1}.

Rotor slip was not reduced, and in fact increased, for Carbopol at the 7 s^{-1} applied shear rate. In the Couette cell, Carbopol showed a rotor velocity of 6.2 mm s^{-1}, as opposed to the expected 7 mm s^{-1}. In the fractal vane geometry, the imaged region at the ‘soft’ rotor boundary (Figure 4 d); red slice) exhibited a velocity of 5.6 mm s^{-1}, the region where the vane edge was pushing the fluid contained in the cavity had a rotor velocity (Figure 4 e); blue slice) that was 4.5 mm s^{-1} and the vane edge pulling the fluid cavity had a rotor velocity (Figure 4 f); yellow slice) of 5.7 mm s^{-1}.

The ideal qualities of the replacement of the Couette shear cell with the fractal vane shear cell would be: reduction of wall slip effects when studying yield stress fluids, the absence of secondary flows between arms that interfere with a homogenous shear stress existing at the fluid layers close to the vanes and the absence of significant dipole stress concentration at the vane

edges that will help in creating a smooth circular streamline flow at radii greater than the fractal vane arm radius [32]. 1D velocity images confirmed that the fractal vane geometry was able to reduce stator slip for both applied shear rates but not rotor slip. In order to determine whether secondary flows or dipole stress concentrations at the vane edges were present, qualitative, 2D velocity images of all three orthogonal velocity components, v_x, v_y and v_z were acquired.

Figure 5 a) and e) show the existence of flow in the x component, v_x, for both the Couette shear cell and the fractal vane shear cell at a 5 s^{-1} applied shear rate. The y velocity component acquired, v_y, is shown in Figure 5 b) and f) with velocity ranging from negative to positive ~5 mm s^{-1} corresponding to the intensity of blue to yellow. Figure 5 c) and g) depict the z velocity component. Any positive or negative velocities in the z direction, would signify the presence of secondary flows. For both the Couette cell (Figure 5 c)) and fractal vane shear cell (Figure 5 g)) however, this v_z component shows 0 mm s^{-1} velocity indicating that no secondary flows were occurring in silicone oil at 5 s^{-1} in either of the shear cells. The magnitudes of the v_x and v_y velocity components (Figure 5 a) and b)) were calculated, leading to speed maps (Figure 5 d) and h)). These speed maps provide a useful qualitative visual of the velocity distribution throughout the fluid gap and compliment the 1D velocity profiles. The speed map for silicone oil in the Couette shear cell in Figure 5 d) depicts a smooth, radial velocity distribution gradually declining from 5 mm s^{-1} at the rotor to 0 mm s^{-1} at the stator. The speed map in Figure 5 h) for the silicone oil sheared using the fractal vane rotor does not show a smooth transition, particularly close to the soft rotor boundary.

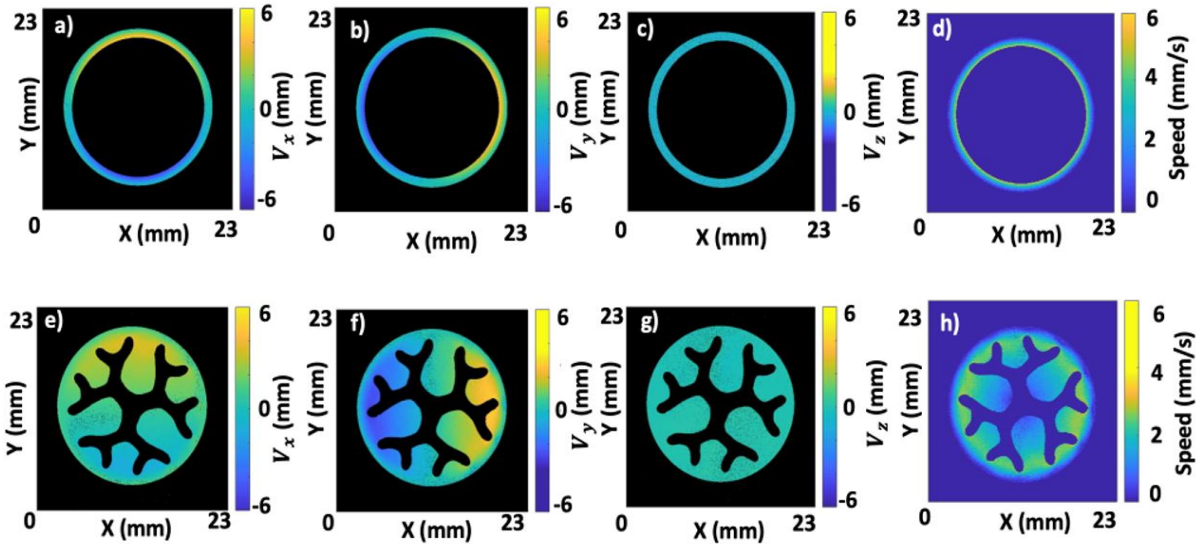

Figure 5: 2D NMR velocity maps (qualitative data deduction) for 1,000 cSt silicone oil under a shear rate of 5 s^{-1}.
a) Velocity component of v_x, b) v_y , c) v_z, and d) the speed map for the Couette shear cell depicting a radially symmetric velocity distribution gradually declining from 5mm s^{-1} at the rotor to a zero velocity at the stator (quantitatively deduced from Figure 1 a)). e) Velocity component of v_x, f) v_y , g) v_z, and h) the speed map for the 12-arm fractal vane shear cell depicting a velocity profile influenced by dipolar concentrations at the vane tips (quantitative deduction from Figure 3 d)-f)).
The v_z component of velocity for both geometries are null indicative of the absence of secondary flows for this silicone oil concentration.

The dark areass at the stator in the regions across the fluid gap from the vane edges are however imaging artifacts rather than reflective of the flow behavior. The imaging artifact is called flow mis-registration and gets encoded along the phase direction for each of the velocity components. These are also seen in the flow images of v_x and v_y components (Figure 5 e) and f)) but are exacerbated in the speed map (Figure 5 h)) on account of how the speed maps were constructed employing both velocity components. Given that a very small observation time, Δ=

8ms, was used, this artifact is difficult to eliminate without sacrificing voxel resolution. This artifact will be a common occurrence in all fractal vane images to follow (Figures 5-8 h)).

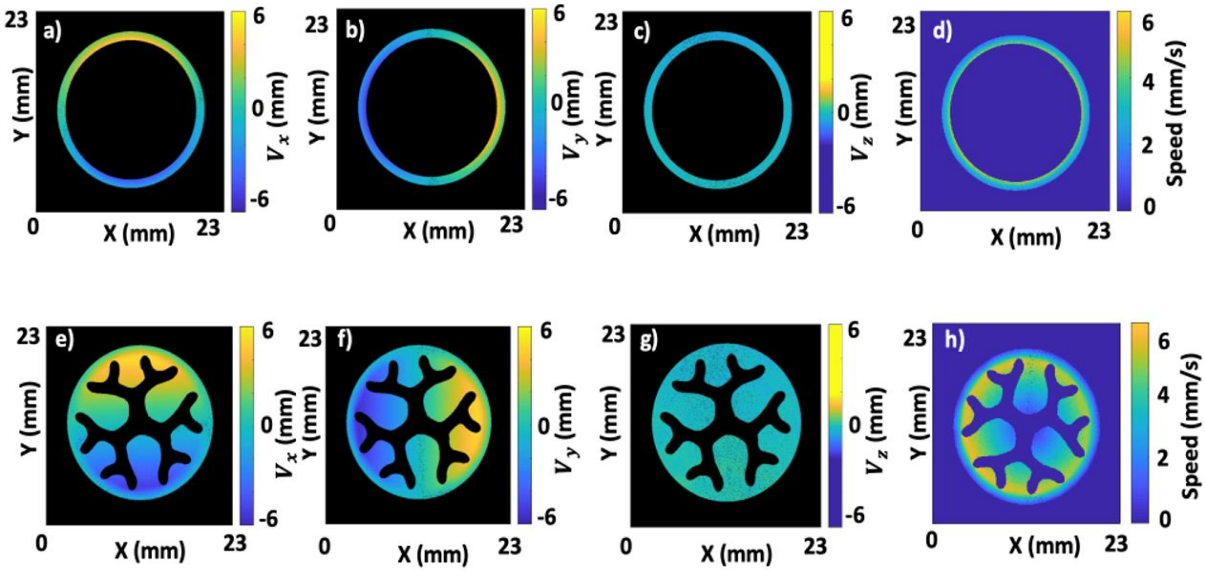

Figure 6: 2D NMR velocity maps (qualitative data deduction) for 0.6wt.% Carbopol under a shear rate of 5 s^{-1}.
a) Velocity component of v_x, b) v_y , c) v_z, and d) the speed map for the Couette shear cell depicting a radially symmetric velocity distribution gradually declining from 4.2 mm s^{-1} at the rotor to 1.46 mm s^{-1} velocity at the stator (quantitatively deduced from Figure 1 c)). e) Velocity component of v_x, f) v_y , g) v_z, and h) the speed map for the 12-arm fractal vane shear cell depicting a velocity profile influenced by dipolar concentrations at the vane tips.

Figure 6 a) and e) show the presence of flow in the x component, v_x, for the Couette shear cell and the fractal vane respectively for the 0.6wt.% Carbopol solution. The presence of flow in the y component, v_y, is shown in Figure 6 b) and f). Unidirectional flow is once again observed for both the Couette shear cell and the fractal vane shear cell at a 5 s^{-1} applied shear rate for Carbopol. Null velocity was observed in v_z components for both shear cells (Figure 6 c) and g)), implying the absence of secondary flow at a 5 s^{-1} applied shear rate for the Carbopol

solution. The speed map for the Couette shear cell in Figure 6 d) depicts a smooth, radial velocity distribution gradually declining from the maximum intensity at the rotor wall in yellow to a minimum intensity at the stator wall in blue. For the 12-arm fractal vane shear cell with Carbopol however, the speed map in Figure 6 h) depicts a velocity profile with higher intensities close to the vane edges that decrease between the arms. This is consistent with the analytical stress field contour plot plotted by Owens *et al.*, where they observe a sharp increase of stress by the vanes as a result of the stress dipole with decreasing stress between the arms for N=12 vane fractal vane geometry [32].

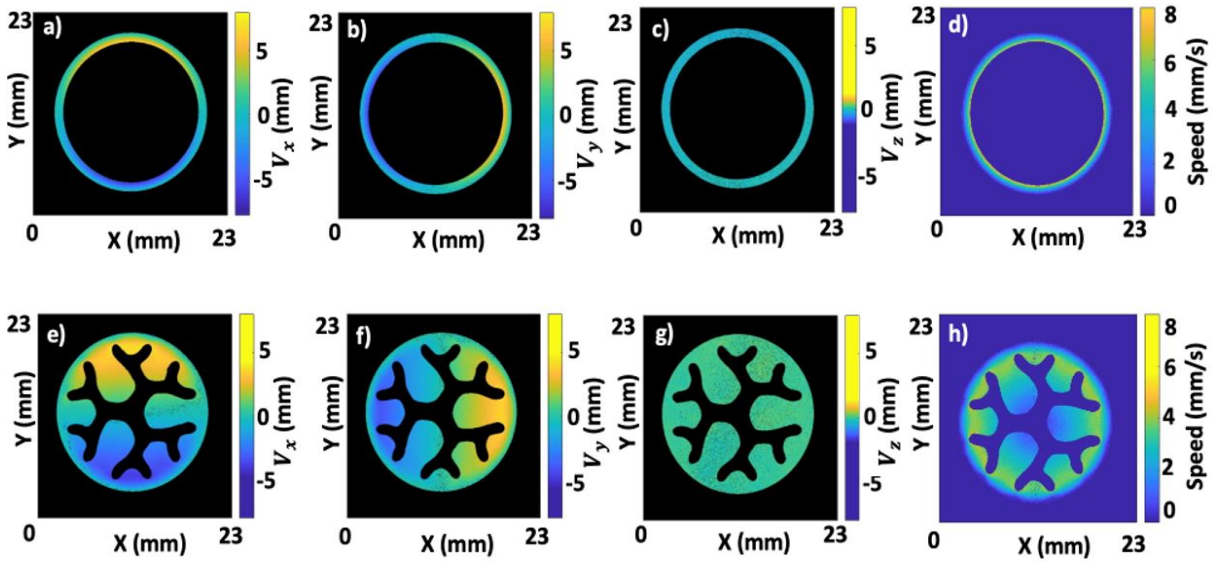

Figure 7: 2D NMR velocity maps (qualitative data deduction) for 1,000 cSt silicone oil under a shear rate of 7 s^{-1}.
a) Velocity component of v_x, b) v_y , c) v_z, and d) the speed map for the Couette shear cell depicting a radially symmetric velocity distribution gradually declining from 7mm s^{-1} at the rotor to a zero velocity at the stator (quantitatively deduced from Figure 1 b)). e) Velocity component of v_x, f) v_y , g) v_z, and h) the speed map for the 12-arm fractal vane shear cell, depicting a velocity profile influenced by dipolar concentrations at the vane tips (quantitative deduction from Figure 4 a)-c)).

The signal intensity from positive to negative ~ 7mm s^{-1} velocity in Figure 7 a) and e) depict the presence of flow in v_x, while Figure 7 b) and f) depict the presence of flow in v_y for silicone oil in both the Couette shear cell and the fractal vane shear cell, respectively. In the respective speed map for this Newtonian fluid (Figure 7 h)), the signal intensity closest to the knife edge is higher than in the region with the fluid cavity. The velocity component in the vorticity direction (v_z) is zero (Figure 7 g)), suggesting this effect is not a result of secondary flow, but due to a non-axisymmetric distribution of velocity across the radial, r, and θ directions of the fluid gap. This also suggests that the stress distribution of this fractal vane geometry is not axisymmetric as would be for the narrow gap Couette shear cell [1]. The Couette shear cell's stress distribution varies only as a function of radial position, r, while the fractal vane shear cell, may show a stress variation in the θ direction additionally [1, 32].

Figure 8 a) and e) and Figure 8 b) and f) show unidirectional v_x and v_y flow in the Couette shear cell and fractal vane shear cell for Carbopol. The speed map showed an axisymmetric velocity distribution for the Couette shear cell for Carbopol at a 7 s^{-1} shear rate as well (Figure 8 d)). The speed map for the fractal vane shear cell at 7 s^{-1} for the Carbopol solution (Figure 8 h)) showed influences from dipolar concentrations at the vane tips resulting in the non-axisymmetric velocity distribution. Once more the null v_z velocity component (Figure 8 g)) confirmed that the non-axisymmetric velocity distribution in the fractal vane shear cell was not due to secondary flows.

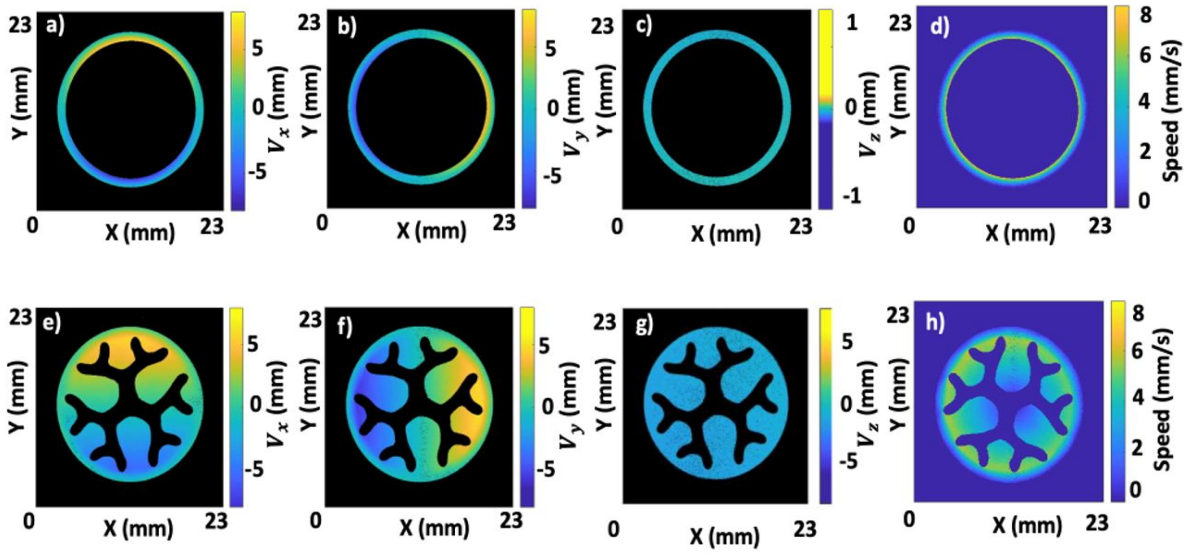

Figure 8: 2D NMR velocity maps (qualitative data deduction) for 0.6wt.% Carbopol at a shear rate of 7 s^{-1}.
a) Velocity component of v_x, b) v_y , c) v_z, and d) the speed map for the Couette shear cell depicting a radially symmetric velocity distribution gradually declining from 6.2 mm s^{-1} at the rotor to 1.7 mm s^{-1} velocity at the stator (quantitatively deduced from Figure 1 d)). e) Velocity component of v_x, f) v_y , g) v_z, and h) the speed map for the 12-arm fractal vane shear cell depicting a velocity profile influenced by dipolar concentrations at the vane tips (can be quantitatively deduced from Figure 4 d)-f)).

Conclusions

This work used 1D and 2D Rheo-NMR velocity images to study the flow behavior of a Newtonian fluid and a model yield stress fluid in a 3D printed Rheo-NMR 12-arm fractal vane geometry as compared to a standard Rheo-NMR concentric cylinder Couette geometry. Specifically, we were interested in whether the fractal vane geometry reduced wall slip effects for yield stress fluids, and if so, whether this was done in the absence of secondary flows. It was also in our interest to observe if the stress field was axisymmetric, indicating that the fractal vane serves as a concentric cylinder geometry with a ‘soft’ boundary. The Newtonian response

showed no wall slip for the concentric cylinder geometry at either applied shear rates in both 1D and 2D imaging. In the case of the fractal vane however, while stator slip was absent, signs of potential rotor slip was observed at both 5 $s^{-1}$and 7 s^{-1} for select slice orientations (slices crossing through the vane edge and the slices across the fluid filled cavities of the geometry). The slip effect become more prominent as the shear rate was increased. The 2D speed maps for silicone oil sheared with the fractal vane further provided evidence of this occurrence. While the 2D speed map at 5 s^{-1} for silicone oil with the fractal vane visually presented an axisymmetric velocity field, the speed map for 7 s^{-1} shows a prominent presence of a non-axisymmetric flow. The rotor slip observed in the 1D velocity profiles hence may be attributed to a potential stress depression resulting a non-axisymmetric flow.

For the 0.6wt.% Carbopol solution, a yield stress fluid, the 1D velocity profiles determined that the fractal vane geometry was able to reduce stator slip as compared to the concentric cylinder geometry, but rotor slip was increased. The 2D speed maps for the yield stress fluid also showed more non-axisymmetric velocity fields compared to those of the Newtonian fluid. 2D velocity maps of both fluids with the 12-arm fractal vane at both shear rates conclude the absence of secondary flows between the vanes with 2D velocity maps in v_z being null.

In summary the use of the fractal vane to study yield stress fluids may be beneficial if the correct slice orientation that is unaffected by the non-symmetric velocity field is chosen. This process however is a time consuming and tedious so it would make more sense to make the overall velocity field around the 12-arm fractal vane geometry more symmetric by either widening the fluid gap or by increasing the number vanes (N=24).

References

1. Macosko, C.W., *Rheology : principles, measurements, and applications*. 1994, New York: New York : Wiley-VCH.

2. Coussot, P., et al., *Macroscopic vs. local rheology of yield stress fluids.* Journal of Non-Newtonian Fluid Mechanics, 2009. **158**(1): p. 85-90.

3. Coussot, P., et al., *Coexistence of liquid and solid phases in flowing soft-glassy materials.* PHYS REV LETT, 2002. **88**(21): p. 218301-2183014.

4. Barnes, H.A. and K. Walters, *The yield stress myth?* Rheologica acta, 1985. **24**(4): p. 323-326.

5. Bird, R.B., G.C. Dai, and B.J. Yarusso, *The Rheology and Flow of Viscoplastic Materials.* Reviews in Chemical Engineering, 1983. **1**(1): p. 1-70.

6. Alexandrou, A.N., N. Constantinou, and G. Georgiou, *Shear rejuvenation, aging and shear banding in yield stress fluids.* Journal of Non-Newtonian Fluid Mechanics, 2009. **158**(1): p. 6-17.

7. Callaghan, P.T., *Rheo-NMR: nuclear magnetic resonance and the rheology of complex fluids.* Reports on Progress in Physics, 1999. **62**(4): p. 599-670.

8. Toorman, E.A., *An analytical solution for the velocity and shear rate distribution of non-ideal Bingham fluids in concentric cylinder viscometers.* Rheologica acta, 1994. **33**(3): p. 193-202.

9. Nguyen, Q.D. and D.V. Boger, *Characterization of yield stress fluids with concentric cylinder viscometers.* Rheologica acta, 1987. **26**(6): p. 508-515.

10. Toorman, E.A., *Controlled rate concentric cylinder rheometry of estuarine mud suspensions.* MAST G8M Coastal Morphodynamics Research Project Report (HYD148), 1995.

11. Nguyen, Q.D. and D.V. Boger, *Measuring the Flow Properties of Yield Stress Fluids.* Annual Review of Fluid Mechanics, 1992. **24**(1): p. 47-88.

12. Taylor, G.I., *Stability of a viscous liquid contained between two rotating cylinders.* Philosophical Transactions of the Royal Society of London A, 1923. **223**.

13. Swinney, H.L. and J.P. Gollub, *Hydrodynamic Instabilities and the Transition to Turbulence*. 1985, Berlin, Heidelberg : Springer Berlin Heidelberg : Imprint: Springer.

14. Fardin, M.A., Perge, C. and Taberlet, N., *"The hydrogen atom of fluid dynamics"--introduction to the Taylor-Couette flow for soft matter scientists.* Soft Matter, 2014. **10**(20).

15. Di Prima, R.C. and H.L. Swinney, *Instabilities and transition in flow between concentric rotating cylinders*, in *Hydrodynamic Instabilities and the Transition to Turbulence*, H.L. Swinney and J.P. Gollub, Editors. 1985, Springer Berlin Heidelberg: Berlin, Heidelberg. p. 139-180.

16. Brox, T.I., Douglass, B., Galvosasa, P. and Brown, J.R., *Observations of the influence of Taylor-Couette geometry on the onset of shear-banding in surfactant wormlike micelles.* Journal of Rheology 2016. **60**(973).

17. Barnes, H.A., *A review of the slip (wall depletion) of polymer solutions, emulsions and particle suspensions in viscometers: its cause, character, and cure.* Journal of Non-Newtonian Fluid Mechanics, 1995. **56**(3): p. 221-251.

18. Larson, R.G., *The structure and rheology of complex fluids*. 1999, New York: New York: Oxford University Press.

19. Pérez-González, J., et al., *Rheo-PIV of a yield-stress fluid in a capillary with slip at the wall.* Rheol Acta, 2012. **51**(11): p. 937-946.

20. Ewoldt, R.H., M.T. Johnston, and L.M. Caretta, *Experimental Challenges of Shear Rheology: How to Avoid Bad Data*. 2014, New York, NY: Springer New York: New York, NY. p. 207-241.

21. Wassenius, H. and P.T. Callaghan, *NMR velocimetry studies of the steady-shear rheology of a concentrated hard-sphere colloidal system.* Eur. Phys. J. E, 2005. **18**(1): p. 69-84.

22. Kaylon, D.M., *Apparent slip and viscoplasticity of concentrated suspensions.* Journal of Rheology, 2005. **49**(621).

23. Magnin, A. and J.M. Piau, *Cone-and-plate rheometry of yield stress fluids. Study of an aqueous gel.* Journal of Non-Newtonian Fluid Mechanics, 1990. **36**(1): p. 85-108.

24. Russell, J.L., *Studies on thixotropic gelation - II—The coagulation of clay suspensions.* Proceedings of the Royal Society of London Series a-Mathematical Physical and Engineering Sciences, 1936. **154**(883): p. 550-560.

25. Barnes, H.A. and Q.D. Nguyen, *Rotating vane rheometry — a review.* Journal of Non-Newtonian Fluid Mechanics, 2001. **98**(1): p. 1-14.

26. Alderman, N.J., G.H. Meeten, and J.D. Sherwood, *Vane rheometry of bentonite gels.* Journal of Non-Newtonian Fluid Mechanics, 1991. **39**(3): p. 291-310.

27. Atkinson, C. and J.D. Sherwood, *The Torque on a Rotating n-Bladed Vane in a Newtonian Fluid or Linear Elastic Medium.* P ROY SOC LOND A MAT, 1992. **438**(1902): p. 183-196.

28. Briggs, J.L., J.F. Steffe, and Z. Ustunol, *Vane Method to Evaluate the Yield Stress of Frozen Ice Cream.* Journal of Dairy Science, 1996. **79**(4): p. 527-531.

29. Liddel, P.V. and D.V. Boger, *Yield stress measurements with the vane.* Journal of Non-Newtonian Fluid Mechanics, 1996. **63**(2): p. 235-261.

30. Barnes, H.A. and J.O. Carnali, *The vane-in-cup as a novel rheometer geometry for shear thinning and thixotropic materials.* Journal of Rheology, 1990. **34**(841).

31. Nguyen, Q.D. and D.V. Boger, *Yield Stress Measurement for Concentrated Suspensions.* Journal of Rheology 1983. **27**(321).

32. Owens, C.E., A.J. Hart, and G.H. McKinley, *Improved rheometry of yield stress fluids using bespoke fractal 3D printed vanes.* Journal of Rheology, 2020. **64**(3): p. 643-662.

33. Atkinson, C. and J.D. Sherwood, *The Torque on a Rotating n-Bladed Vane in a Newtonian Fluid or Linear Elastic Medium.* Proceedings of the Royal Society of London Series a-Mathematical Physical and Engineering Sciences, 1992. **438**(1902): p. 183-196.

34. Callaghan, P.T., *Principles of nuclear magnetic resonance microscopy*. 1993, Oxford: Oxford : Clarendon Press.

35. Jarny, S., et al., *Rheological behavior of cement pastes from MRI velocimetry.* Cement and Concrete Research, 2005. **35**(10): p. 1873-1881.

36. Caprihan, A. and E. Fukushima, *Flow measurements by NMR.* Physics Reports, 1990. **198**(4): p. 195-235.

37. Fukushima, E., *Nuclear magnetic resonance as a tool to study flow.* Annual Review of Fluid Mechanics 1999. **31**(1): p. 95-123.

38. Coussot, P., *Rheometry of Pastes, Suspensions, and Granular Materials: Applications in Industry and Environment*. 2005, New York: Wiley.

39. Dinkgreve, M., et al., *Carbopol: From a simple to a thixotropic yield stress fluid.* Journal of Rheology, 2018. **62**(3): p. 773-780.

40. Callaghan, P.T., *Translational Dynamics & Magnetic Resonance: Principles of Pulsed Gradient Spin Echo NMR*. 2011, New York: Oxford University Press.

41. Al-kaby, R.N., et al., *Rheo-NMR of transient and steady state shear banding under shear startup.* Journal of Rheology, 2018. **62**(5): p. 1125-1134.

42. Al-kaby, R.N., et al., *Characterization of velocity fluctuations and the transition from transient to steady state shear banding with and without pre-shear in a wormlike micelle solution under shear startup by Rheo-NMR.* Applied Rheology, 2020. **30**(1): p. 1-13.

43. Brox, T., et al., *Observations of the influence of Taylor-Couette geometry on the onset of shear-banding in surfactant wormlike micelles.* Journal of Rheology, 2016. **60**(5): p. 973-982.

44. Kuczera, S. and P. Galvosas, *Advances and artefact suppression in RARE-velocimetry for flow with curved streamlines.* Journal of Magnetic Resonance, 2015. **259**: p. 135-145.

CHAPTER SEVEN

STEADY STATE AND TRANSIENT RHEO-NMR VELOCIMETRY ON MIXED SURFACTANT-EMULSION SOLUTIONS

Contribution of Authors and Co-Authors

Manuscript in Chapter 7

Author: Jayesha S. Jayaratne

Contributions: Wrote manuscript. Helped in designing and conceiving the experiment. Collected, analyzed and interpreted Rheo-NMR data.

Co-Author: William Hartt

Contributions: Secured funding through P&G. Discussed data and analysis methods.

Co-Author: Marco Caggioni

Contributions: Provided analyzed rheology data. Discussed data and helped in experimental design. Will provide feedback and comments on the manuscript.

Co-Author: Joseph D. Seymour

Contributions: Edited manuscript. Provided training on experimental methodology. Helped perceive experimental and implementation concepts. Helped interpret data. Secured funding.

Manuscript Information

Jayesha S. Jayaratne, Marco Caggioni, William Hartt, Joseph D. Seymour

Journal of Rheology

Status of Manuscript:
__X_ Prepared for submission to a peer-reviewed journal
___ Officially submitted to a peer-reviewed journal
___ Accepted by a peer-reviewed journal
___ Published in a peer-reviewed journal

STEADY STATE AND TRANSIENT RHEO-NMR VELOCIMETRY ON MIXED SURFACTANT-EMULSION SOLUTIONS

Abstract

The work here reports on the local flow behavior of four different concentrations of an oil-in-water emulsion by means of Rheo-NMR velocimetry. A concentric cylinder Couette shear cell with rotating inner cylinder (rotor), a stationary outer cylinder (stator) and a 1mm fluid gap was used. Data was acquired at a range of shear rates surrounding the critical shear rate calculated from the three component model of each emulsion concentration. The data acquired comprised 1D startup velocity profiles and 1D steady state velocity profiles with up ramp and down ramp profiles compared. Startup velocity profiles showed that a steady state flow was achieved by all emulsion concentrations at each applied shear rate by 10 minutes of shearing. Startup experiments also allowed to characterize the variances that were shown by the Rheo-NMR rheometer at each imposed shear rate for each sample viscosity (which was concentration dependent). At high emulsion concentrations, steady state velocity data showed spatial inhomogeneity's of the flow below a critical shear rate while they depicted a homogeneous flow at applied shear rates higher than the critical shear rate. Also ramp up and down steady state velocity profiles, at each applied shear rate for each of the concentrations, overlaying suggested the absence of shear dependent flow behavior.

Introduction

Complex fluids seen in industrial applications are often yield stress fluids [1, 2]. Yield stress fluids flow once a critical stress, the yield stress, has been overcome. Below the yield

stress, they behave as solids [2-5]. Emulsions, dense suspensions, foams, and polymeric gels can exhibit yield stress behavior and these fluids are ubiquitous in consumer products, pharmaceuticals, foods and civil engineering. Emulsions are frequently used in personal care product and cosmetic industries to ensure a pleasant texture and an even smear-ability, which depends upon the yield stress properties [6][7][8-10]. For example, the yield stress property of lotion is what allows for an even and thick layer of lotion to occur during application while the internal micro-structure of the emulsion provides a desired smooth texture [6]. Emulsions are made of two immiscible fluids, where the droplets of one fluid are dispersed in a continuous phase containing a surface-active agent [6, 11]. Industrially, emulsions are appealing as they have tunable rheological properties dependent on their composition and flow histories [7].

Flow curves of yield stress fluids are often modeled using the Herschel-Bulkley (HB) model. The critical shear rate where yielding occurs can be calculated as , $\dot{\gamma}_{c,HB} = (\sigma_y/K)^{-n}$, where σ_y, is the yield stress, K is the consistency index and n, is the power law index [5, 12]. While the HB model accurately describes the flow behavior of yield stress fluids, it is limited by the fact that *K* and *n* do not have a clear physical meaning, as they are simply fit parameters. The three component (TC) model, introduced by Caggioni *et al.*, combines the Bingham model and the mode coupling model to bring in physical meaning to the model [13]. The TC model relates how stress dissipation in sheared yield stress materials occurs due to elastic, plastic and viscous dissipations respectively, as shown in Eqn. 1 [13].

$$\sigma = \sigma_y + \sigma_y \cdot \left(\frac{\dot{\gamma}}{\dot{\gamma}_{c,TC}}\right)^{\frac{1}{2}} + \eta_{BG} \cdot \dot{\gamma} \qquad \text{Eqn. 1}$$

where $\dot{\gamma}_{c,TC}$ is the critical shear rate and η_{BG} is the Bingham viscosity (a viscosity related to the continuous phase for the case of emulsions).

Yield stress fluids under shear often exhibit inhomogeneous flow patterns and wall slip [8, 14, 15, 16]. Due to shear rate heterogeneities, the fluid in some locations may be above the critical shear rate and will flow, while at other locations it is un-yielded and stationary or flowing as a plug with wall slip at the boundaries [17]. In rheological studies, the presence of flow heterogeneities and wall slip are undesirable, as it is then difficult to assign the bulk rheological response to a particular material property. In the packing of personal care products however, these features of the flow are useful. Toothpaste for instance will flow from the tube without attaching to the walls as a result of wall slip.

In this work, Rheo-NMR, a non-invasive and non-destructive technique that allows for the spatio-temporal observation of velocity was used to investigate flow heterogeneities and the influence of shear history on yield stress oil-in-water emulsions [18].

Materials and Methods

Materials

Oil-in-water emulsions consisting of a continuous aqueous phase and a dispersed oil phase at four different classified concentrations were provided by Proctor & Gamble. The continuous aqueous phase contained linear alkylbenzene sulfonate (LAS), a surfactant with hydrophilic sulfonate and hydrophilic alkylbenzene groups (P&G Chemicals). The dispersed phase was a hydrogenated castor oil (HCO), a mineral oil (Paragon Scientific) [13].

For confidentiality of the sample concentrations, each of the concentrations was named sample 1, 2, 3 and 4. Sample 1 had the highest concentrations of both LAS and HCO with a 4:1

LAS/HCO ratio was the most viscous of the samples. Sample 2 had a 3.85:1 LAS/HCO ratio. Sample 3, was the lowest concentration of all the samples also with a 3.85:1 LAS/HCO ratio. Sample 4 had an LAS concentration equal to that of sample 2 but a low HCO concentration equal to that of sample 3. The LAS/HCO ratio for sample 4 was 38.5:1. A 1,000cSt Silicone oil sample (Consolidated Chemicals & Solvents LLC) was also used as an ideal Newtonian fluid in order to establish baseline measurements accounting for flow cell geometry and rotational drive affects. All experiments were run at a room temperature of 21.1°C.

Rheo-NMR Methods

All NMR velocity measurements were performed using a Bruker AVANCE 300 spectrometer equipped with a Micro-2.5 gradient system (maximum Gradient: 1.5 T/m 60A) and a 25 mm diameter ^{1}H radiofrequency coil, along with Bruker Paravision 5.1 and Topspin 3.5 software. Data was anlayzed using Prospa (Magritek, NZ) and MATLAB (MathWorks, Natick, MA). A magneto safe, strain controlled Rheo-NMR rheometer, with the capability of inducing constant rotations between 0.001Hz - 9.99Hz and a concentric cylinder shear cell was used for all Rheo-NMR experiments. The shear cell had an inner rotating rotor of radius 8 mm and an outer stationery stator of radius 9 mm, resulting in a fluid gap of 1 mm and a radius ratio ($\kappa = R_i / R_o$) of 0.89.

1D velocity images were acquired employing a pulsed gradient spin echo (PGSE) pulse sequence with a double slice selection (Figure 1). The two slices were a 1mm thick slice in the direction of flow and 10mm thick in the vorticity direction. The PGSE pulse sequence used two gradient steps, each comprising two flow encoding gradients equal in duration (δ) but opposite in their magnitude (+/- g) between which a short observation time, Δ, was employed for the spin

displacements due to flow to occur. The flow encoding maximum gradient, which sets the velocity encoding range, along with δ and Δ were employed a wide range of value based on the imposed velocity at the rotor wall. Imaging gradients giving a field of view of 30 mm with 512 read points were used for a 58.6 μm resolution. The steady state experiments used 8 repetitions of the 2 gradient flow encoding, the resulting velocity data being an average of the 16 scans acquired over a period of 1 minute and 9 seconds. The transient start-up experiments used 2 scans per flow encoding gradient step, minimizing the data acquisition time to 8.16 seconds at the cost of low signal to noise ratio.

At each shear rate, Rheo-NMR velocity profiles were acquired with flow and without flow in order to correct for background magnetization phase shifts due to applied magnetic field gradients. The data presented in this study are the result of the phase difference of the two profiles- an analysis technique used to compensate effects from imaging pulses and any gradient imperfections.

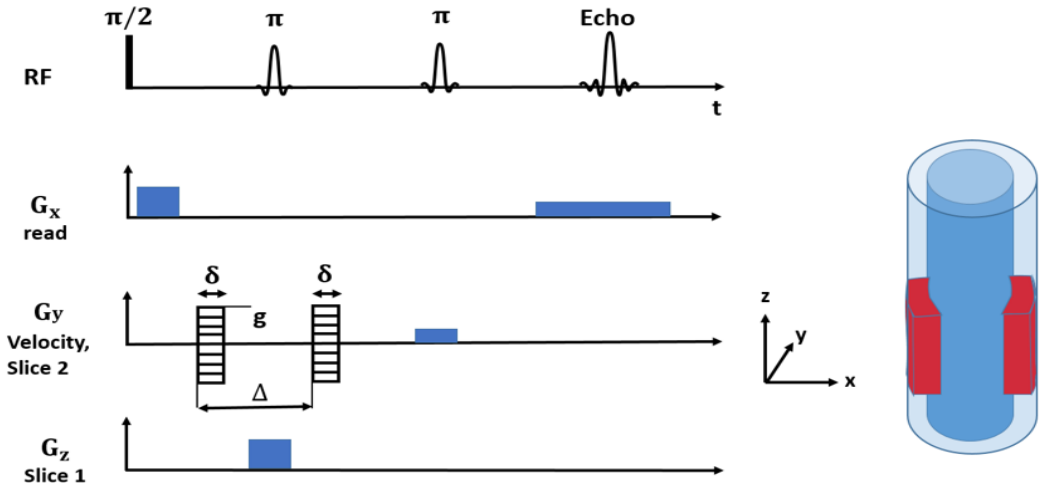

Figure 1: PGSE flow encoding pulse sequence used (simplified) and the region of the Couette shear cell imaged.

Experimental Methods

Transient and steady state 1D velocity profiles were acquired during a shear rate ramp. Shear rates were incremented from low to high (ramp up), then high to low (ramp down) over a shear rate range around the critical shear rate ($\dot{\gamma}_{crit}$) for each fluid. For each shear rate increment, 1D velocity profiles of 8.16 s duration were collected for 10 minutes in order to capture the transient response. After 10 minutes, the flow was assumed to be at steady state and a 1D velocity profile with a 1 minute 9 second acquisition time (and therefore higher signal to noise) was acquired. No equilibration time was allocated following an increment in shear rate besides human response time (on clicking a button, roughly 30 seconds). The applied shear rates were chosen to select a range of shear rates that were both far from and near the critical shear rate ($\dot{\gamma}_{critical}$) for each emulsion composition. The critical shear rates for each sample, provided by P&G, were found using bulk rheological measurements conducted using a concentric cylinder geometry (Appendix A). The critical shear rate values were calculated from rheograms using the three component (TC) model [13].

Sample 1 had a critical shear rate of $\dot{\gamma}_{critical}$ = 2.84 s^{-1} and the shear rates applied during the ramps up and down were 0.5, 1, 2, 2.5, 3, 4 and 5 s^{-1} . Sample 2 had a critical shear rate of $\dot{\gamma}_{critical}$ = 9.98 s^{-1} and the shear rates applied during the ramps up and down were 7, 9, 10, and 12 s^{-1}. Sample 3 had a critical shear rate of $\dot{\gamma}_{critical}$ = 0.7 s^{-1} and range of applied shear rates of 0.4, 0.6, 0.7, 0.8 and 1 s^{-1}. Sample 4 had a critical shear rate, $\dot{\gamma}_{critical}$ = 0.6 s^{-1} and shear rates were applied at 0.2, 0.4, 0.5, 0.6 and 0.7 and 1 s^{-1} during the ramps up and down.

Discussion

Select data is presented in the main body of this paper represents applied shear rates with interesting features. Rheo-NMR velocimetry data for further applied shear rates of each emulsion concentration can be found in the appendices with Appendix A showing the applied shear rates along with their bulk flow behavior deduced from rheograms provided by P&G.

The concentric cylinder geometry used in this project, with its 1mm gap, is expected to generate linear velocity 1D velocity profiles for Newtonian fluids based on the narrow gap assumption [19]. Newtonian Silicone oil shown in blue in all the acquired steady state velocity profiles of Figures 2 and 3 shows the expected linear behavior. Here, a no slip boundary condition allows the fluid at the stator wall to achieve a zero velocity, and close to the rotor wall, to achieve a velocity numerically equal to that of the shear rate applied by the rotor. Deviations from Newtonian behavior exhibited by the emulsion samples can be attributed to flow inhomogeneities and the fluid's micelle structure interactions upon shear, e.g. elastic effects, yield stress and/or shear thinning.

Figure 2 shows the steady state velocity profiles observed for samples 1 and 2 on ramp up and down over a range of shear rates compared to steady state behavior of the Newtonian fluid. For velocity profiles of all shear rates examined refer to figures in Appendix B.

Sample 1, with the highest concentration of oil droplets and surfactant concentration in the aqueous continuous phase, exhibits the most non-Newtonian behavior of all the samples. Sample 1 exhibits rotor and stator slip-characteristic features of a yield stress fluid (Figure 2 a) i) and ii)) which decreases as the critical shear rate of 2.84 /s is surpassed (Figure 2 a) iii) and iv)) [20]. At $\dot{\gamma} < \dot{\gamma}_{crit}$ steady state profiles (Figure 2 a) i) and ii)) show a yielded and a narrow non-

yielded region as well as stator wall slip. The non-yielded region is identified by a velocity plateau ~160 μm into the gap from the stator while the yielded region throughout the rest of the gap shows shear thinning behavior [21, 22]. The extent of the sheared region of the material increases till the critical shear rate (2.84 s^{-1}) is surpassed, the non-yielded region at an applied shear rate of 2.5 s^{-1} decreasing to < 100μm of the gap (Figure 2 a) ii)). More homogeneous shear thinning velocity profiles are observed beyond the critical shear rate which are similar to that of the start-up velocity profiles (Figure D 1 - D 4).

Sample 2 is interesting in that it shows shear thinning behavior, and therefore is yielded throughout the fluid gap, at all shear rates with rotor wall slip, but not significant stator slip. (Figure 2 b) i), ii), iii) and iv)). However the startup velocity profiles (Figure D 5 and D 6) suggest the presence of a ~50μm scale non-sheared unstable region near the stator at an applied shear rate of 7/s. For both sample 1 and sample 2, the 1D velocity profiles acquired during the ramp up and the ramp down at each of the applied shear rate overlay (Figure 2 a) and b) i), ii), iii) and iv)), suggest the absence of significant shear history effects in the two emulsion concentrations.

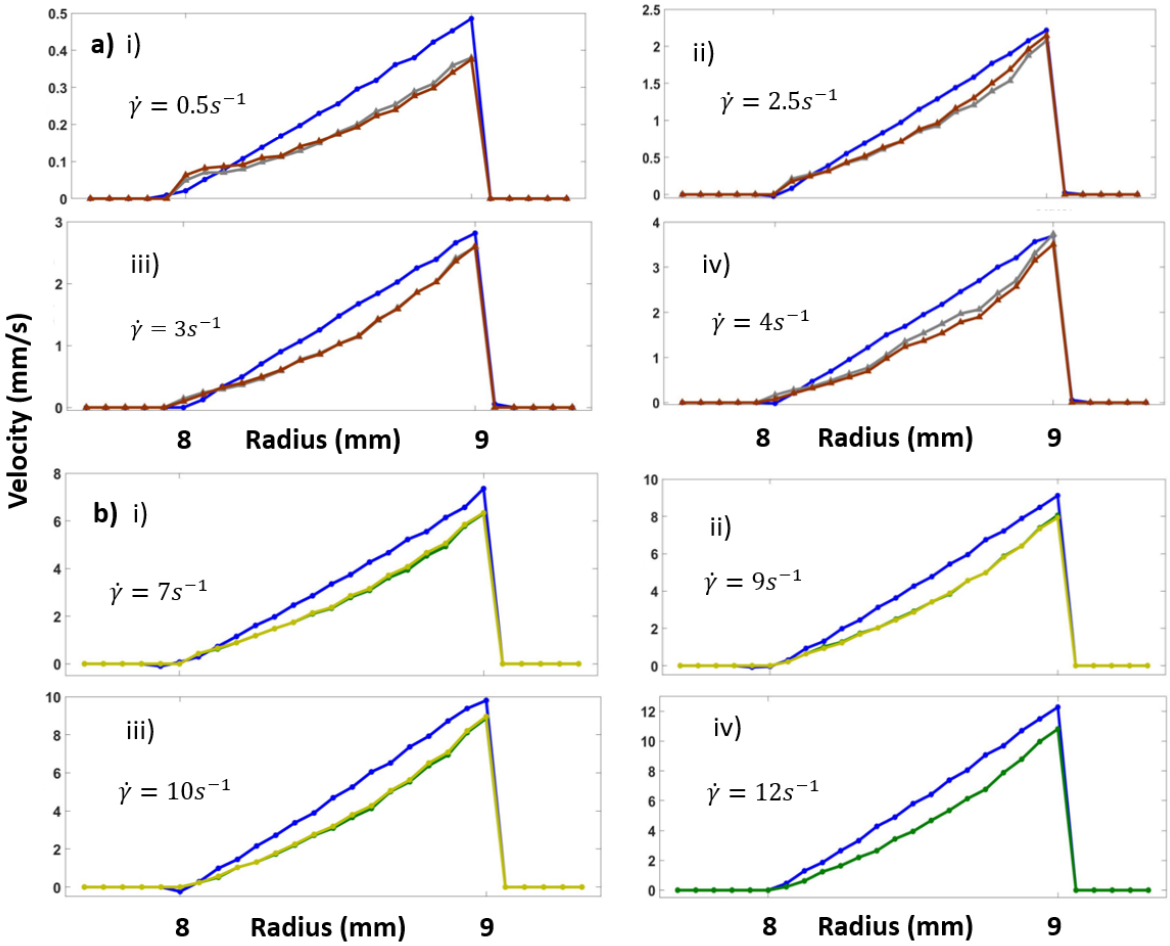

Figure 2: Steady state left hand fluid gap velocity profiles for a) sample 1 and b) Sample 2. a) i) and ii) shear rates less than the critical shear rate, a) iii) and iv) shear rates higher than the critical shear rate of 2.84 s^{-1} for sample 1. b) i) and ii) shear rates less than the critical shear rate, b) iii) and iv) shear rates higher than the critical shear rate of 9.98 s^{-1} for sample 2.
- 1,000 cSt Silicone oil, - sample 1 ramp up, - sample 1 ramp down, - sample 2 ramp up, - sample 2 ramp down

Figure 3 shows 1D velocity profiles for samples 3 and 4. The profiles show homogeneous linear profiles, as seen for the Newtonian fluid, potentially because the HCO concentration in these samples is low compared to samples 1 and 2. Samples 3 and sample 4 also

showed a lack of shear history as the velocity profiles for the up ramp and down ramp at each applied shear rate overlay on top of each other (Figure 3 a) and b) i), ii), iii) and iv)).

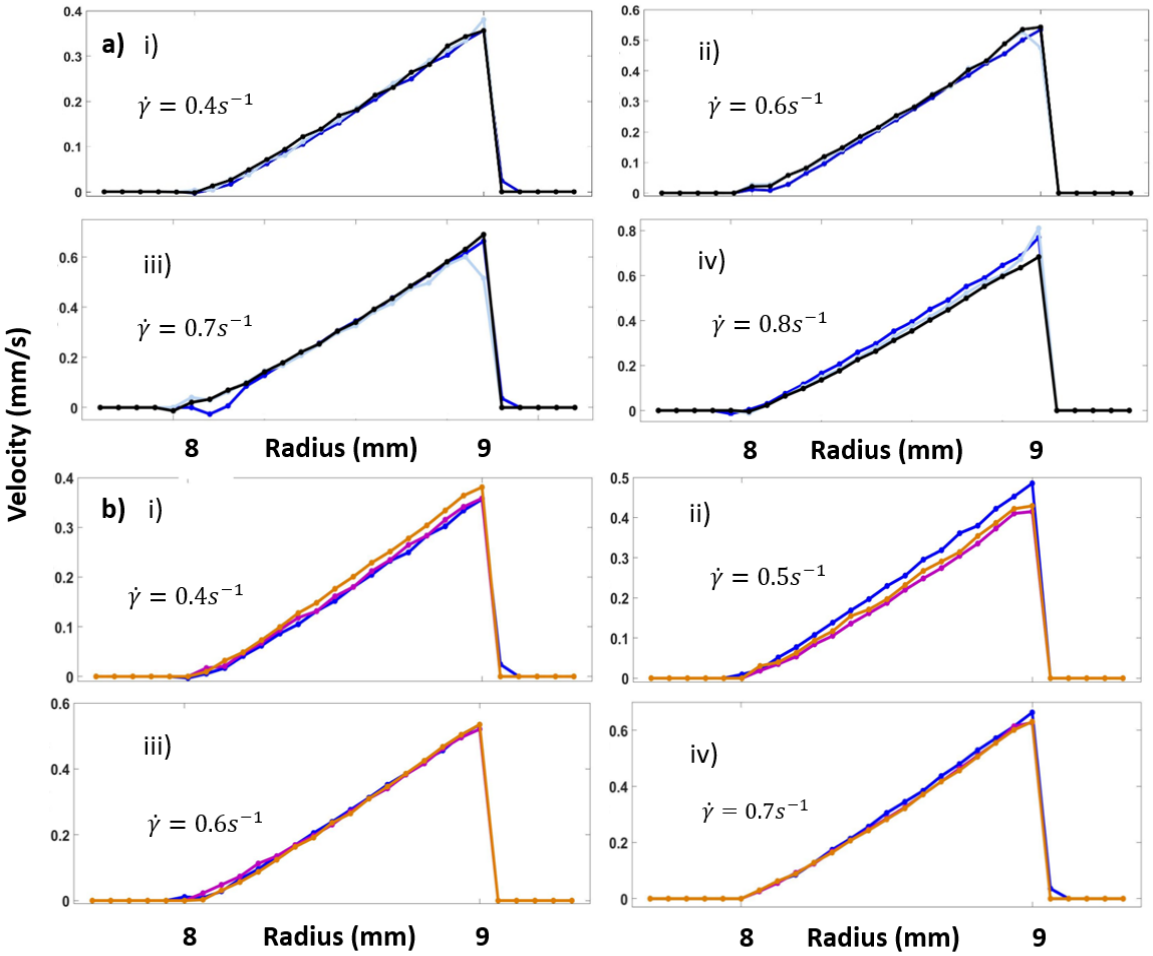

Figure 3: Steady state left hand fluid gap velocity profiles for a) sample 3 and b) Sample 4. a) i) and ii) shear rates less than the critical shear rate, a) iii) and iv) shear rates higher than the critical shear rate of 0.7 s^{-1} for sample 3. b) i) and ii) shear rates less than the critical shear rate, b) iii) and iv) shear rates higher than the critical shear rate of 0.6 s^{-1} for sample 4.
– 1,000 cSt Silicone oil, - sample 3 ramp up, - sample 3 ramp down, - sample 4 ramp up, - sample 4 ramp down

In order to analyze how the velocity evolved with time following an increment in shear rate, Figure 4 and 5 show the velocity of samples 1 and 3 respectively at three locations across

the fluid gap plotted against time. These velocities were selected from the 1D velocity profiles acquired every 8.16 seconds over 10 minutes immediately following an increment in shear rate (shown in Figures D 1 – D 11). Locations were selected near the rotor at radius r = 8.23 mm, at the mid-point of the fluid gap (r =8.53 mm) and near the stator (r =8.82mm). Velocity was not analyzed for the pixels nearest the rotor and stator in order to avoid any possible partial volume artifacts arising at the boundaries.

Figure 4 a) shows that for sample 1 at an applied shear rate of 0.5/s, which is below the critical shear rate of 2.84 s^{-1}, the velocity near the rotor and at the midpoint of the fluid gap increase over the first 250 seconds, i.e. is transient, before reaching a plateau. Within the plateau, the flow can be assumed to be at steady state, while the transient velocity is indicative of microstructural evolution that occurs within the emulsions following an increment in shear rate. When the applied shear rates were higher than the critical shear rate ($\dot{\gamma}_{applied} \geq \dot{\gamma}_{critical}$), the velocity has reached the plateau within the first 8.16 second acquisition, indicating that steady state was achieved already within this time period (Figure 4 b) - d)). The velocities for all shear rates and locations within the gap fluctuate with time about the average plateau value.

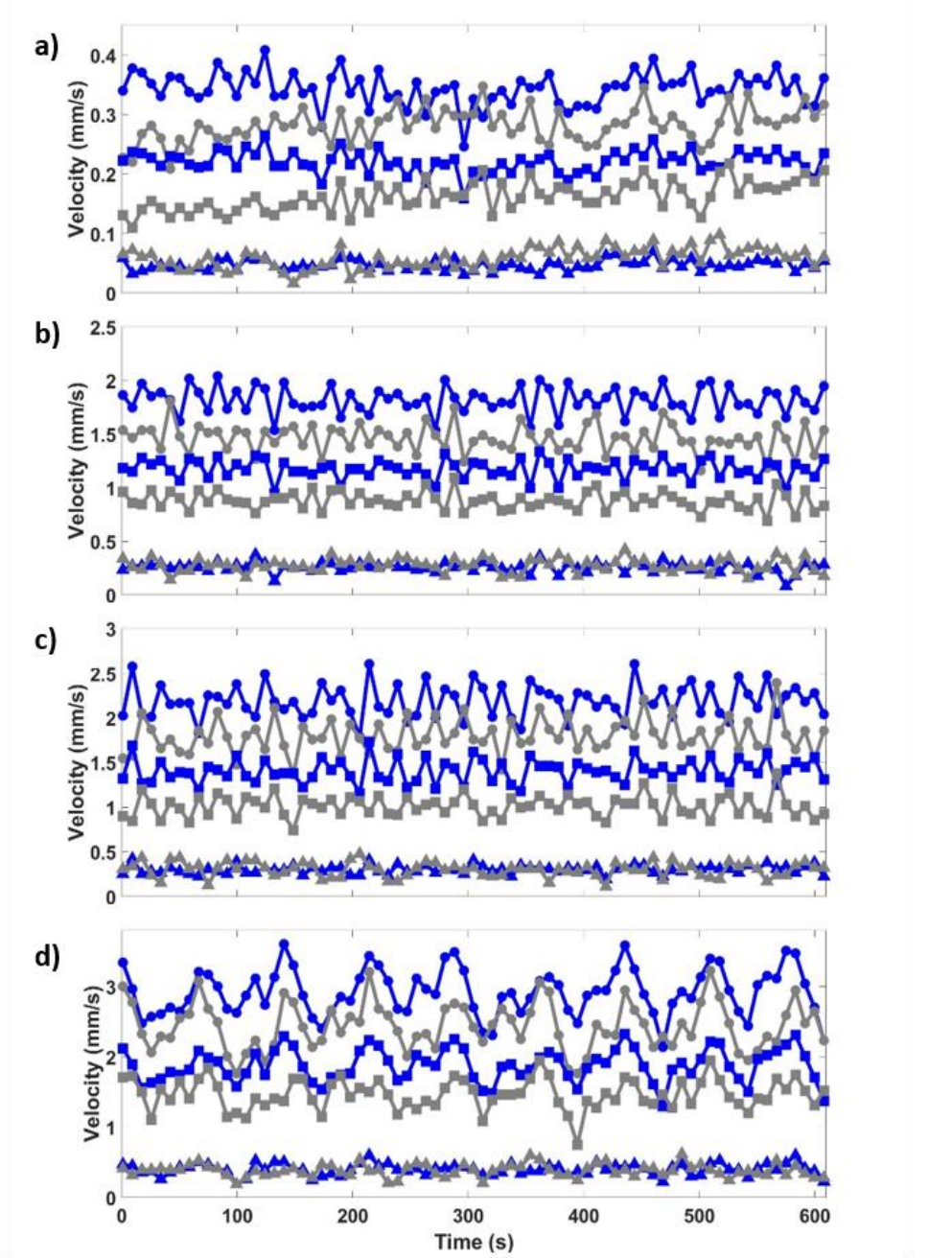

Figure 4: Velocity change with time on a ramp up flow as sample 1 reached steady state near the rotor (circle), mid gap (square) and stator (triangle) for sample 1. a) Applied shear rate of 0.5 s^{-1} b) applied shear rate of 2.5 s^{-1} c) applied shear rate of 3 s^{-1} and d) applied shear rate of 4 s^{-1}. Critical shear rate 2.84 s^{-1}.

– 1,000 cSt Silicone oil, - sample 1 ramp up

Figure 5 a)-c) and e) shows that for sample 3 at shear rates equal to or less than the critical shear rate, a steady state velocity is observed within the first 8.16 second acquisition with fluctuations in velocity about the mean. For an applied shear rate of 0.8 s^{-1} however, the velocity at the rotor oscillates between 0.4 s^{-1} - 0.9 s^{-1} with a repeated ~50 second period (Figure 5 d)). The same periodic trend was observed at 0.8/s during the down ramp (Figure C 3). The transient velocity profiles examined over time from the start of the rotation with a ramp up of shear rates for all other samples and shear rates showed roughly steady state velocities at each position analyzed across the fluid gap (Appendix C) with only a small variance (Table E 1).

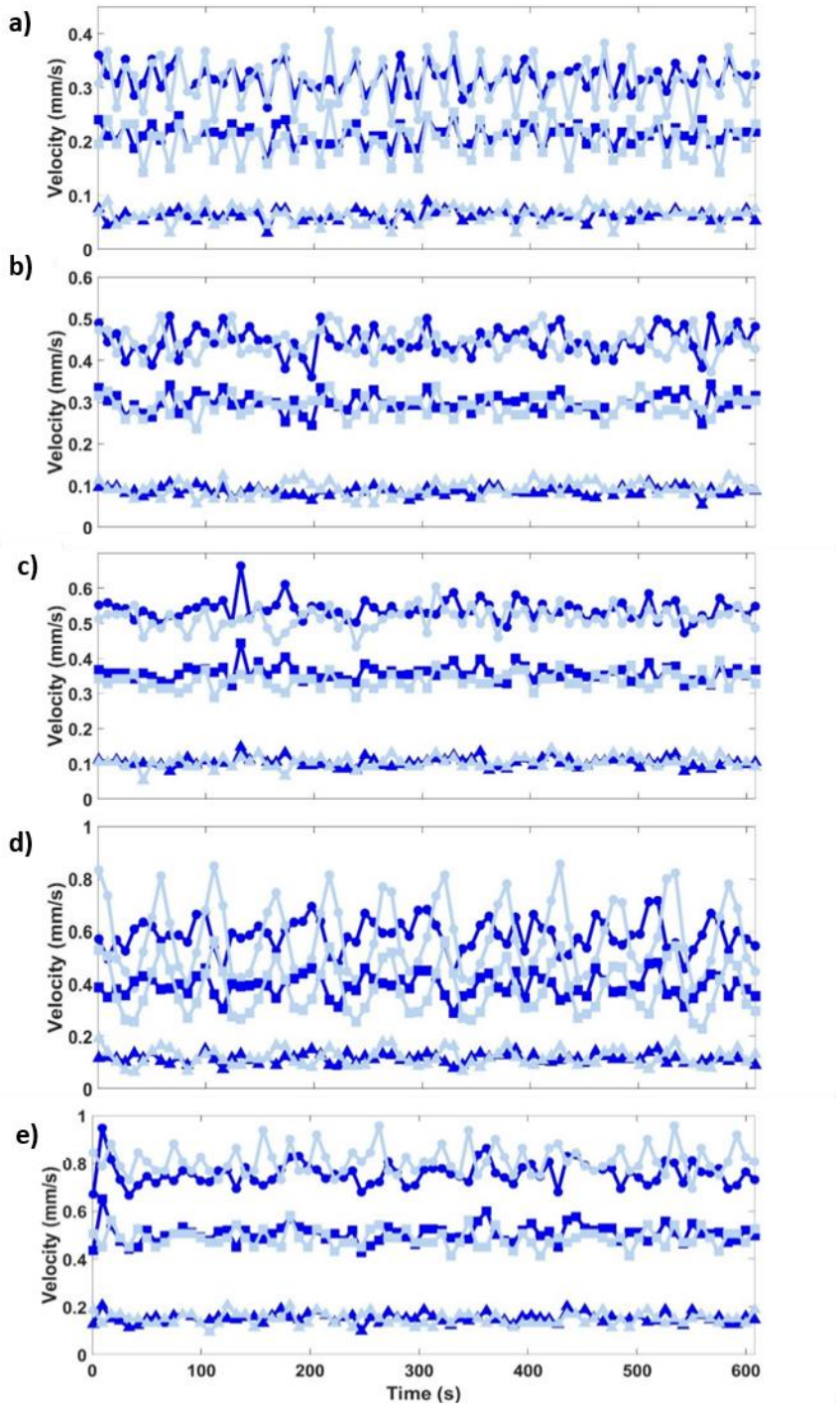

Figure 5: Velocity change with time on a ramp up flow as sample 3 reached steady state near the rotor (circle), mid gap (square) and stator (triangle) for sample 3. a) Applied shear rate of 0.4 s^{-1} b) applied shear rate of 0.6 s^{-1} c) applied shear rate of 0.7 s^{-1} d) applied shear rate of 0.8 s^{-1} and e) applied shear rate of 1 s^{-1}. Critical shear rate 0.7 s^{-1}. – 1,000 cSt Silicone oil, - sample 3 ramp up

In order to examine the nature of the fluctuations and oscillations in velocity with time, the standard deviation of the data shown in Figures 4 and 5 were calculated and are shown in Figure 6. The variance of the velocity data with time is proportional to the intensity of the velocity time correlation fluctuation intensity,$< V_\theta'^2 >_0$, where $< V_\theta(t) \cdot V_\theta(t + \Delta t) > = < V_\theta'^2 > f(\Delta t)$. All the fluctuations exhibit deviations less than 0.5 indicating a reasonably high average velocity confidence.

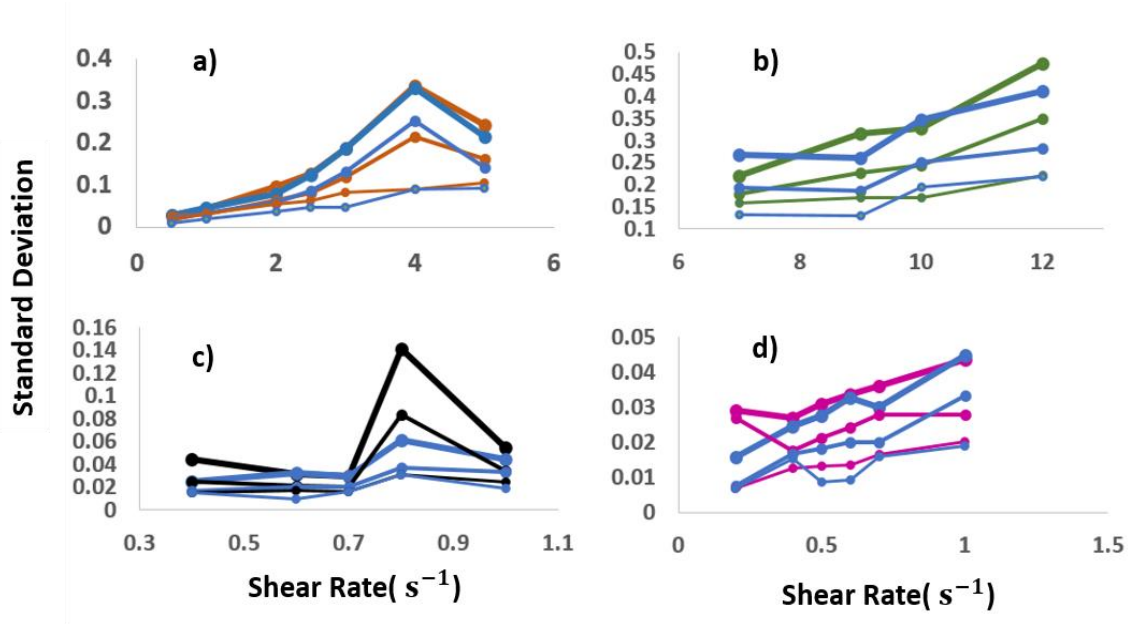

Figure 6: Standard deviations of velocities over time at the rotor, mid gap and stator for a) sample 1, b) sample 2, c) sample 3 and d) sample 4.

There is an increase in standard deviation with an increase in rotor rotation rate. This fairly linear increase, seen with the increase of applied shear rates, is consistent with an increase in vibrations due to the stepper motor function. This indicates that the fluctuations in velocity with time are due to motor vibrations being transmitted into the fluid. A noise spike, seen as an increase in the standard deviation for both the Newtonian silicone oil and the emulsion sample, is observed at 4 s^{-1} in Figure 6 a) and at 0.8 s^{-1} in Figure 6 c). At these particular rotation rates, it is possible the stepper motor vibration is larger. Sample 3 also shows a larger standard deviation relative to the silicone oil at an applied shear rate of 0.8 s^{-1}, indicative of an amplification of the fluctuation due to motor noise in the non-Newtonian emulsion of low viscosity compared to the Newtonian silicone oil.

Conclusions

The study was successful in acquiring 1D startup and steady state Rheo-NMR velocimetry data for four different concentrations of an oil-in-water emulsion. For the emulsions with a higher linear alkylbenzene sulfonate (LAS) and hydrogenated castor oil (HCO) concentration, steady state data concluded the existence of non-linear local velocities. Sample 1, the highest concentration sample, exhibited yield stress behavior at applied shear rates below its critical shear rate and power law shear-thinning behavior applied shear rates above the critical shear rate. Sample 2, with a lower concentration, maintained shear thinning behavior throughout the range of applied shear rates. Samples 3 and 4, the two samples with lowest LAS and HCO concentrations, depicted Newtonian-like spatially linear velocity behaviors. A likely reason for this would be the structural breakdown of the samples on sample loading. Ramp up and ramp

down steady state velocity profiles conducted for all the samples overlaid on each other eliminating any influence from flow history.

REFERENCES CITED

1. Bonn, D., et al., *Yield stress materials in soft condensed matter.* REV MOD PHYS, 2017. **89**(3): p. 035005.

2. Coussot, P., *Yield stress fluid flows: A review of experimental data.* J NON-NEWTON FLUID, 2014. **211**: p. 31-49.

3. Coussot, P., et al., *Coexistence of liquid and solid phases in flowing soft-glassy materials.* PHYS REV LETT, 2002. **88**(21): p. 218301-2183014.

4. Coussot, P., et al., *Macroscopic vs. local rheology of yield stress fluids.* Journal of Non-Newtonian Fluid Mechanics, 2009. **158**(1): p. 85-90.

5. Macosko, C.W., *Rheology : principles, measurements, and applications*. 1994, New York: New York : Wiley-VCH.

6. Brummer, R., *Rheology Essentials of Cosmetic and Food Emulsions*. 1. Aufl. ed. 2005, Berlin, Heidelberg: Berlin, Heidelberg: Springer-Verlag.

7. Kim, H.S. and T.G. Mason, *Advances and challenges in the rheology of concentrated emulsions and nanoemulsions.* ADV COLLOID INTERFAC, 2017. **247**: p. 397-412.

8. Bocquet, L., A. Colin, and A. Ajdari, *Kinetic Theory of Plastic Flow in Soft Glassy Materials.* PHYS REV LETT, 2009. **103**(3): p. 036001-036001.

9. Brennan, J.G., *Food texture and viscosity: Concept and measurement: By M. C. Bourne, Academic Press, New York, 1982. Price: £23.80*. 1984, Elsevier Ltd. p. 80-81.

10. Schramm, L.L., *Emulsions, foams, suspensions, and aerosols: microscience and applications, second edition*. 2nd ed. ed. 2014: Wiley.

11. Leal-Calderon, F., V. Schmitt, and J. Bibette, *Emulsion Science: Basic Principles*. 2007, New York, NY: New York, NY: Springer New York. 227.

12. Herschel, W.H. and R. Bulkley, *Measurement of consistency as applied to rubber-benzene solutions.* Proceedings - American Society for Testing and Materials, 1926. **26**(2): p. 621-633.

13. M. Caggioni, V.T., and P. T. Spicer, *Variations of the Herschel–Bulkley exponent reflecting contributions of the viscous continuous phase to the shear rate-dependent stress of soft glassy materials.* Journal of Rheology, 2020. **64**(2): p. 413-422.

14. Besseling, R., et al., *Shear Banding and Flow-Concentration Coupling in Colloidal Glasses.* PHYS REV LETT, 2010. **105**(26): p. 268301-268301.

15. Dauchot, O., G. Marty, and G. Biroli, *Dynamical heterogeneity close to the jamming transition in a sheared granular material.* PHYS REV LETT, 2005. **95**(26): p. 265701.1-265701.4.

16. Larson, R.G., *The structure and rheology of complex fluids*. 1999, New York: New York: Oxford University Press.

17. Maillard, M., et al., *Blade-coating of yield stress fluids.* J NON-NEWTON FLUID, 2016. **237**: p. 16-25.

18. Callaghan, P.T., *Rheo-NMR: nuclear magnetic resonance and the rheology of complex fluids.* Reports on Progress in Physics, 1999. **62**(4): p. 599-670.

19. Kuczera, S. and P. Galvosas, *Advances and artefact suppression in RARE-velocimetry for flow with curved streamlines.* Journal of Magnetic Resonance, 2015. **259**: p. 135-145.

20. Coussot, P., *Slow flows of yield stress fluids: yielding liquids or flowing solids?* Rheol Acta, 2018. **57**(1): p. 1-14.

21. Huang, N., et al., *Flow of wet granular materials.* PHYS REV LETT, 2005. **94**(2): p. 028301.1-028301.4.

22. Chhabra, R.P., Richardson, J.F. , *Non-Newtonian Flow in the Process Industries: Fundamentals and Engineering Applications*. 1999: Butterworth-Heinemann. 436.

23. Escudier, M.P., I.W. Gouldson, and D.M. Jones, *Circular Couette Flow and Taylor Vortices in Shear-Thinning Liquids*. Berlin, Heidelberg: Springer Berlin Heidelberg: Berlin, Heidelberg. p. 16-33.

APPENDICES

APPENDIX A

RHEOGRAMS WITH APPLIED SHEAR RATES IN RHEO-NMR

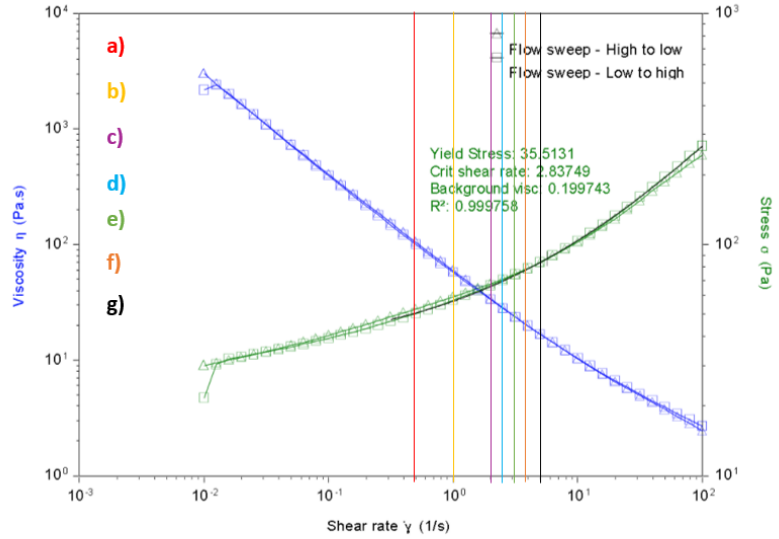

Figure A 1: Ramp up and ramp down flow curves with shear rates applied in rheo NMR experiments marked for sample 1. Applied shears: a) 0.5/s, b) 1/s, c) 2/s, d) 2.5/s, e) 3/s, f) 4/s and g) 5/s. The rheogram was sent in by and is the property of P&G.

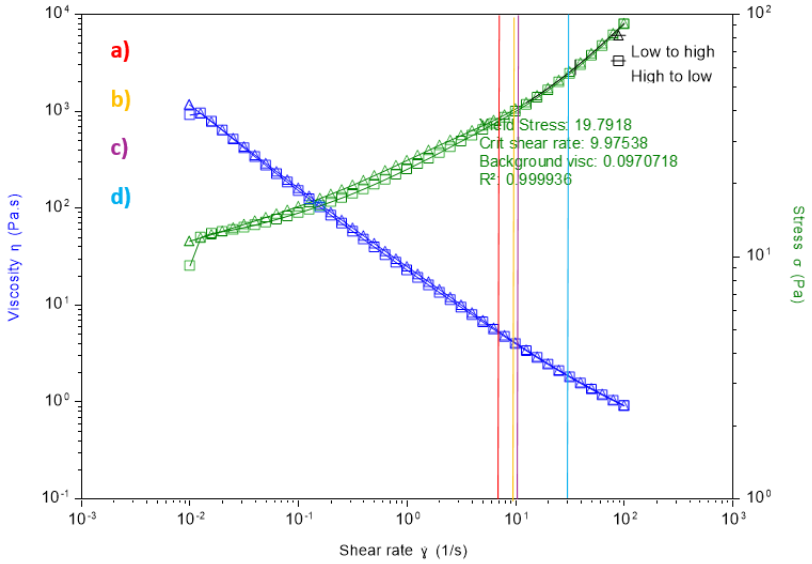

Figure A 2: Ramp up and ramp down flow curves with shear rates applied in rheo NMR experiments marked for sample 2. Applied shears: a) 7/s, b) 9/s, c) 10/s and d) 12/s. The rheogram was sent in by and is the property of P&G.

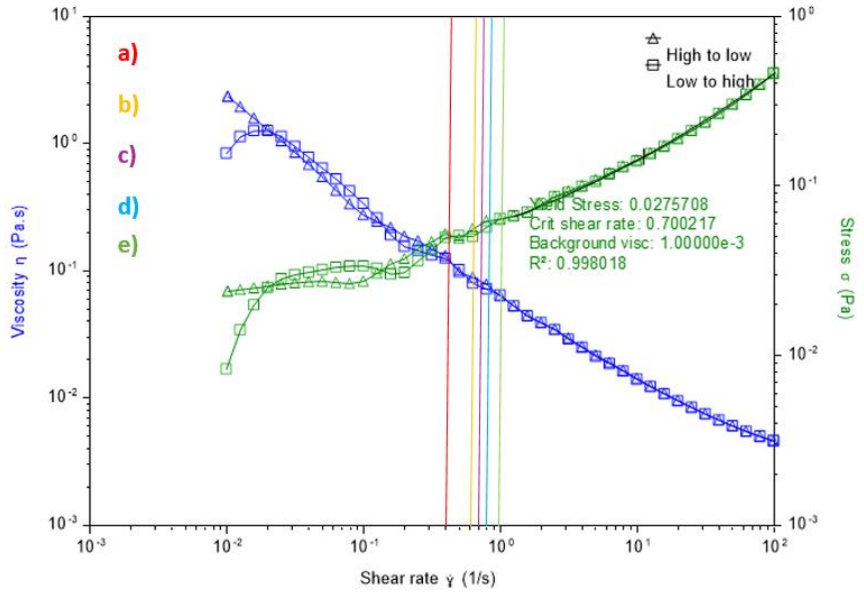

Figure A 3: Ramp up and ramp down flow curves with shear rates applied in rheo-NMR experiments marked for sample 3. Applied shears: a) 0.4/s, b) 0.6/s, c) 0.7/s, d) 0.8/s and e) 1/s. The rheogram was sent in by and is the property of P&G.

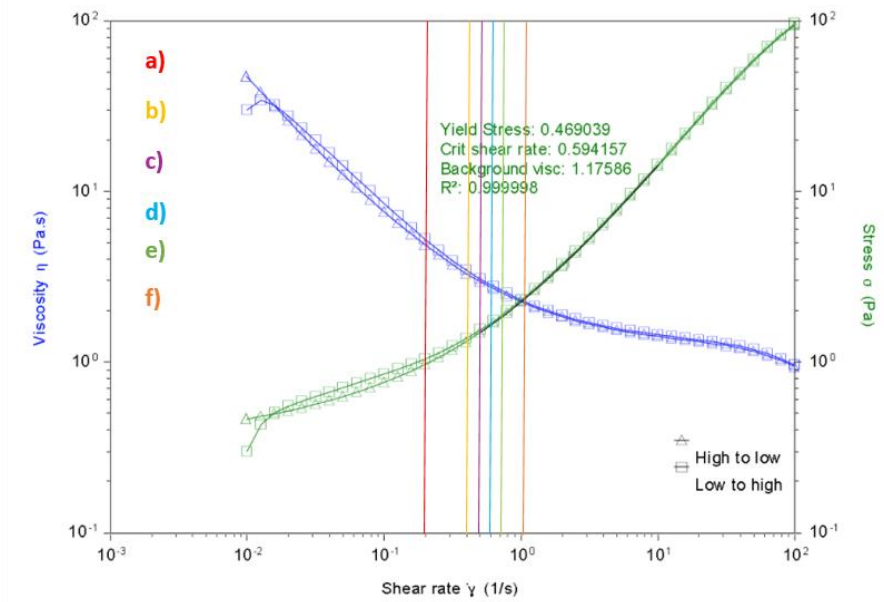

Figure A 4: Ramp up and ramp down flow curves with shear rates applied in rheo-NMR experiments marked for sample 4. a) 0.2/s, b) 0.4/s, c) 0.5/s, d) 0.6/s, e) 0.7/s and f) 1/s. The rheogram was sent in by and is the property of P&G.

APPENDIX B

STEADY STATE VELOCITY PROFILES

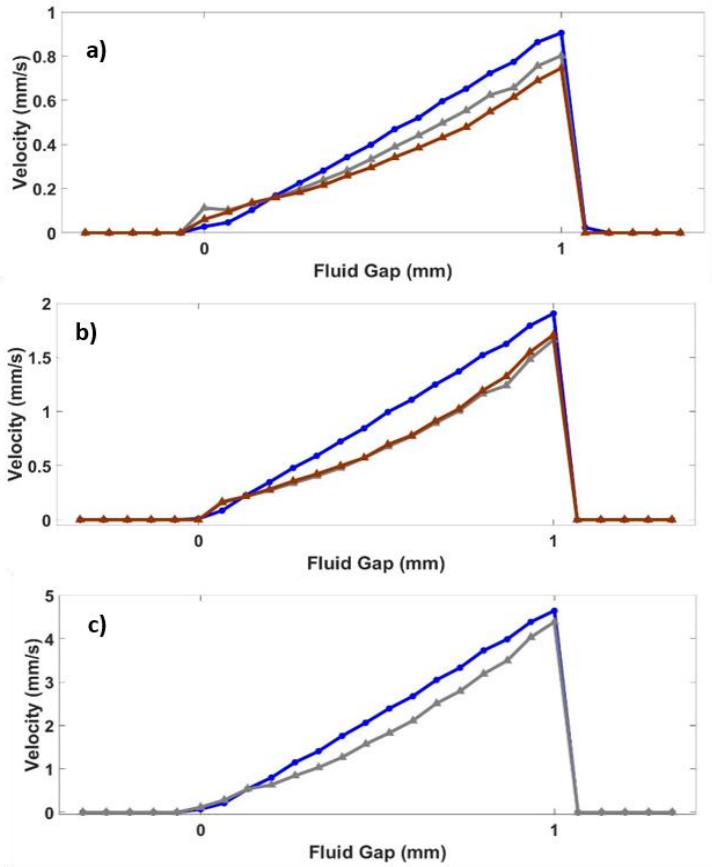

Figure B 1: Steady state left hand fluid gap velocity profiles for sample 1 at applied shear rates of a) 1/s b) 2/s and c) 5/s.
– 1,000 cSt Silicone oil, - sample 1 ramp up, - sample 1 ramp down

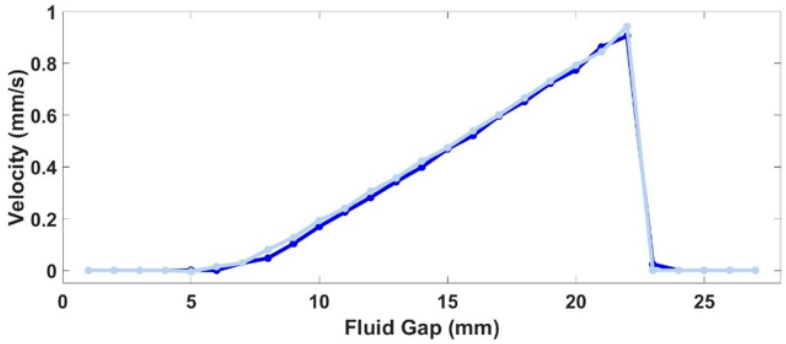

Figure B 2: Steady state left hand fluid gap velocity profiles for sample 3 at an applied shear rate of 1/s.
– 1,000 cSt Silicone oil, - sample 3 ramp up

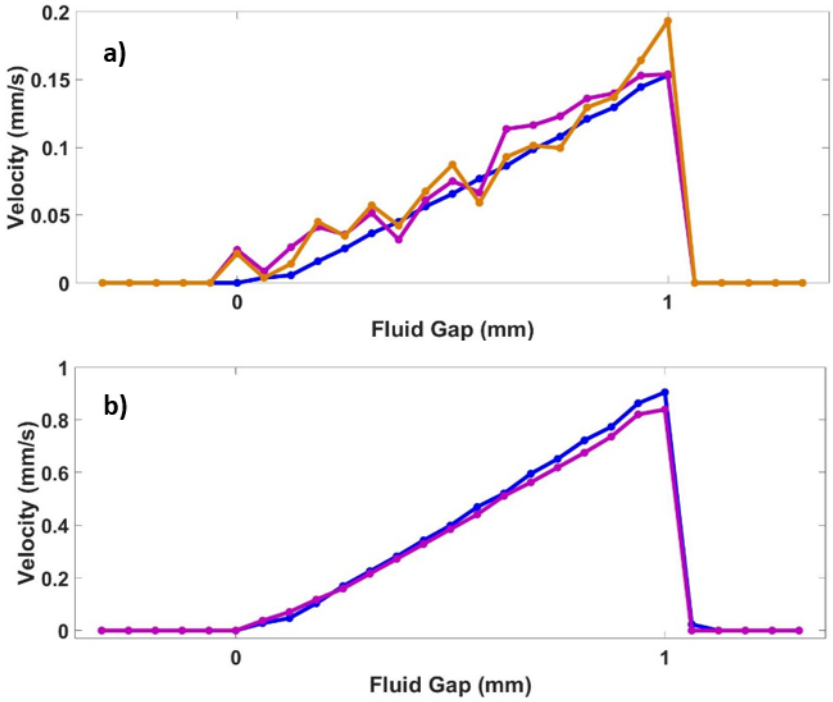

Figure B 3: Steady state left hand fluid gap velocity profiles for sample 4 at applied shear rates of a) 0.2/s and c) 1/s.
– 1,000 cSt Silicone oil, - sample 4 ramp up, - sample 4 ramp down

APPENDIX C

VELOCITY TIME SERIES FROM STRAT-UP

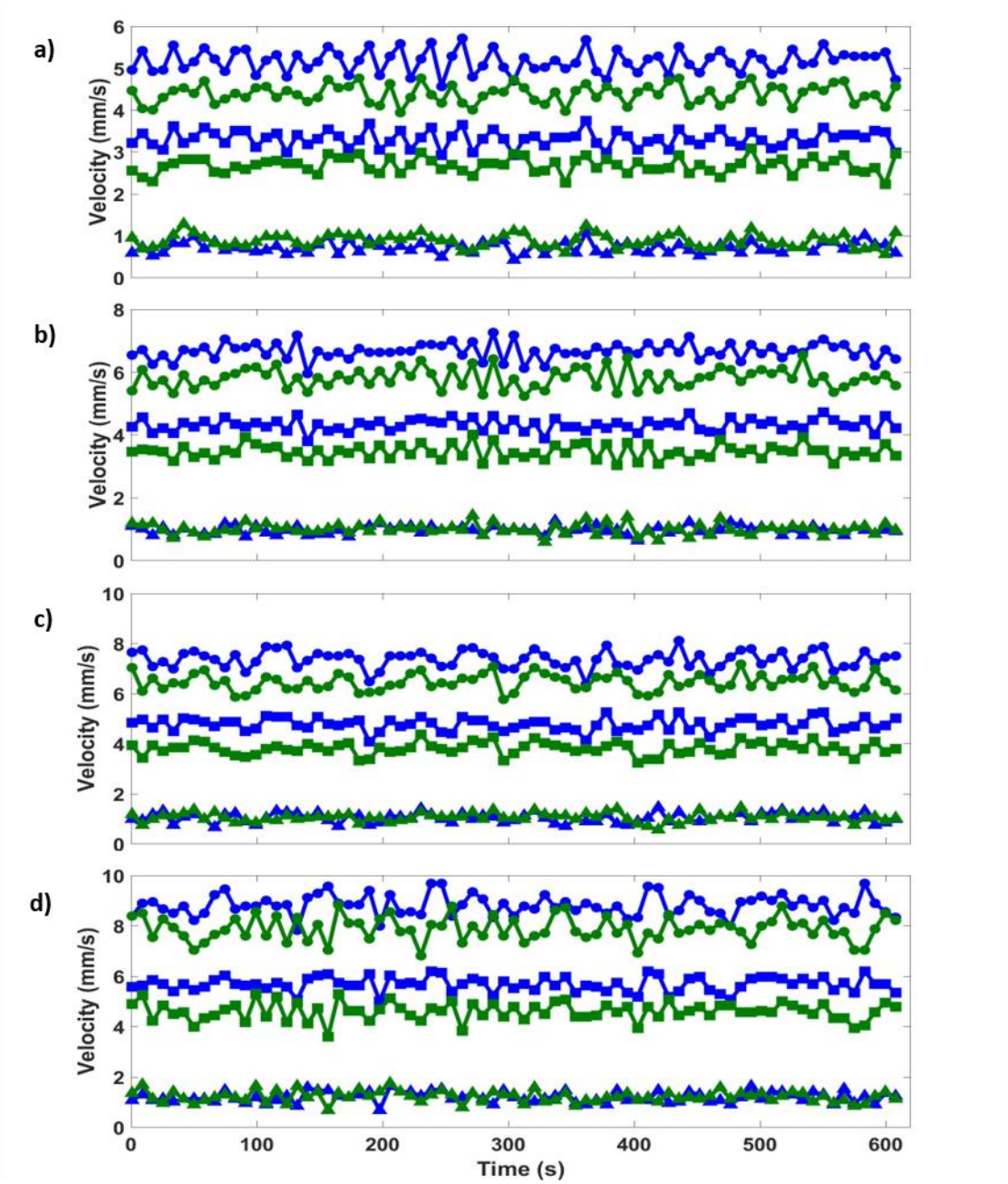

Figure C 1: Velocity change with time on a ramp up flow as the sample reached steady state at the rotor (circle), mid gap (square) and stator (triangle) for sample 2. a) Applied shear rate of 7/s b) applied shear rate of 9/s c) applied shear rate of 10/s and d) applied shear rate of 12/s. Critical shear rate 9.97538/s.
– 1,000 cSt Silicone oil, - sample 2 ramp up

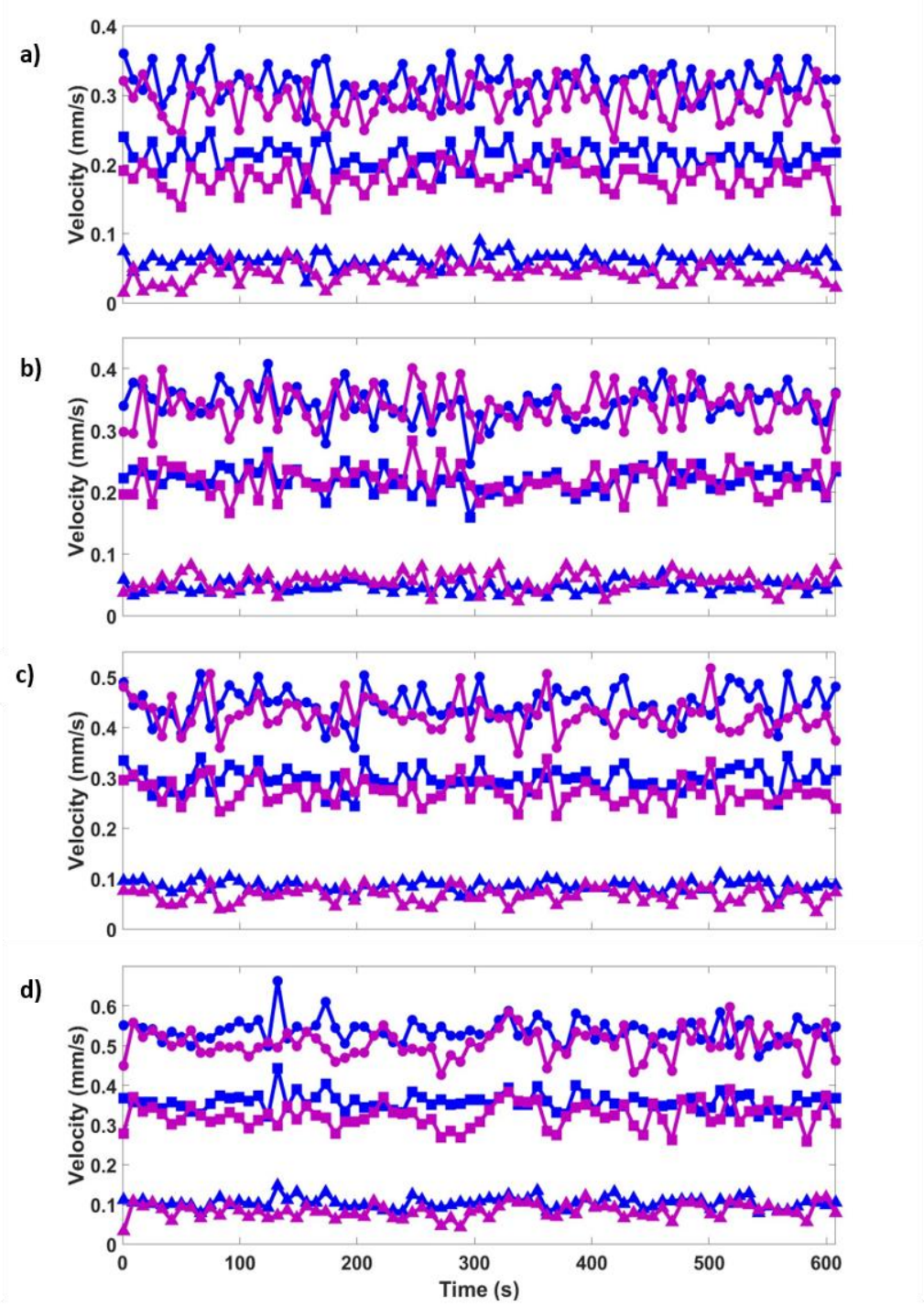

Figure C 2: Velocity change with time on a ramp up flow as the sample reached steady state at the rotor (circle), mid gap (square) and stator (triangle) for sample 4. a) Applied shear rate of 0.4/s b) applied shear rate of 0.5/s c) applied shear rate of 0.6/s and d) applied shear rate of 0.7/s. Critical shear rate 0.594157/s. **– 1,000 cSt Silicone oil, - sample 4 ramp up**

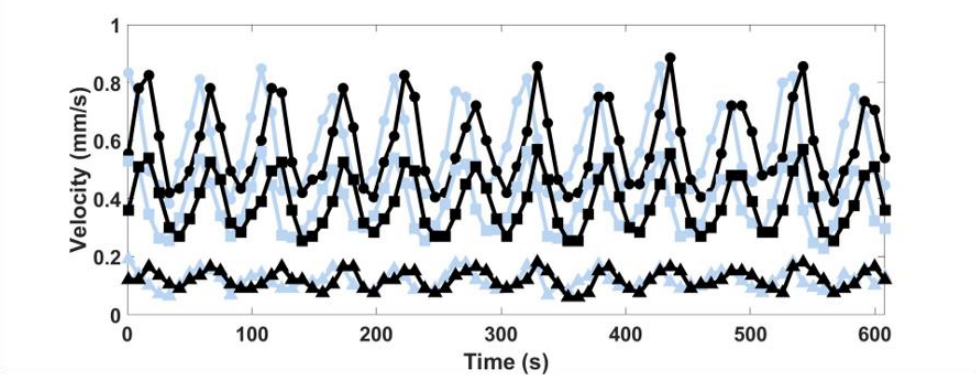

Figure C 3: Velocity change with time on a ramp up and ramp down flow as the sample reached steady state at the rotor (circle), mid gap (square) and stator (triangle) for sample 3 at a 0.8/s applied shear rate. Critical shear rate 0.700217/s.
– sample 3 ramp up, **- sample 3 ramp down**

APPENDIX D

TRANSIENT START-UP VELOCITY PROFILES

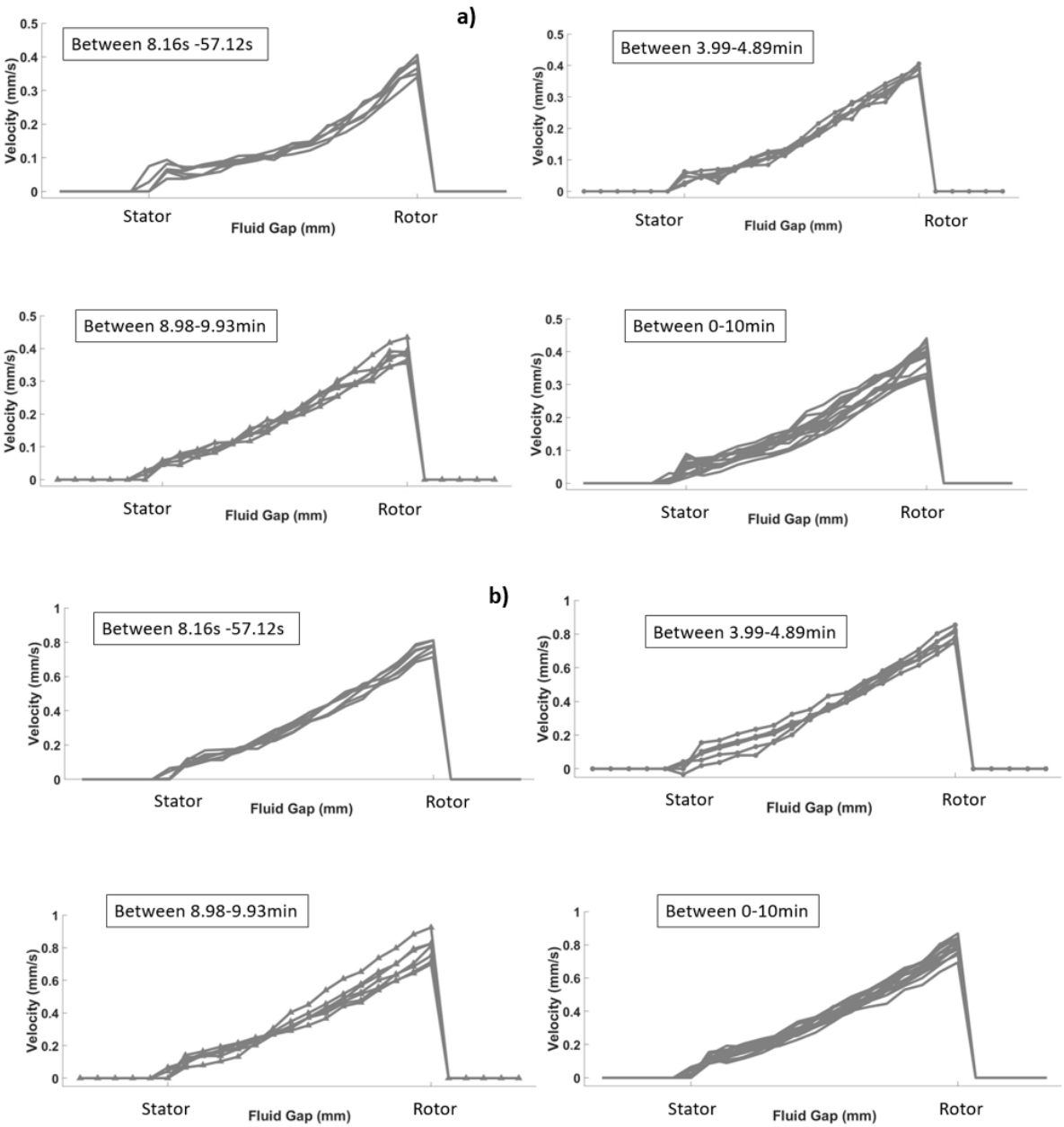

Figure D 1: Start up velocity profiles for sample 1 at applied shear rates of a) 0.5/s and b) 1/s. Critical shear rate (2.83749/s).

- sample 1 ramp up

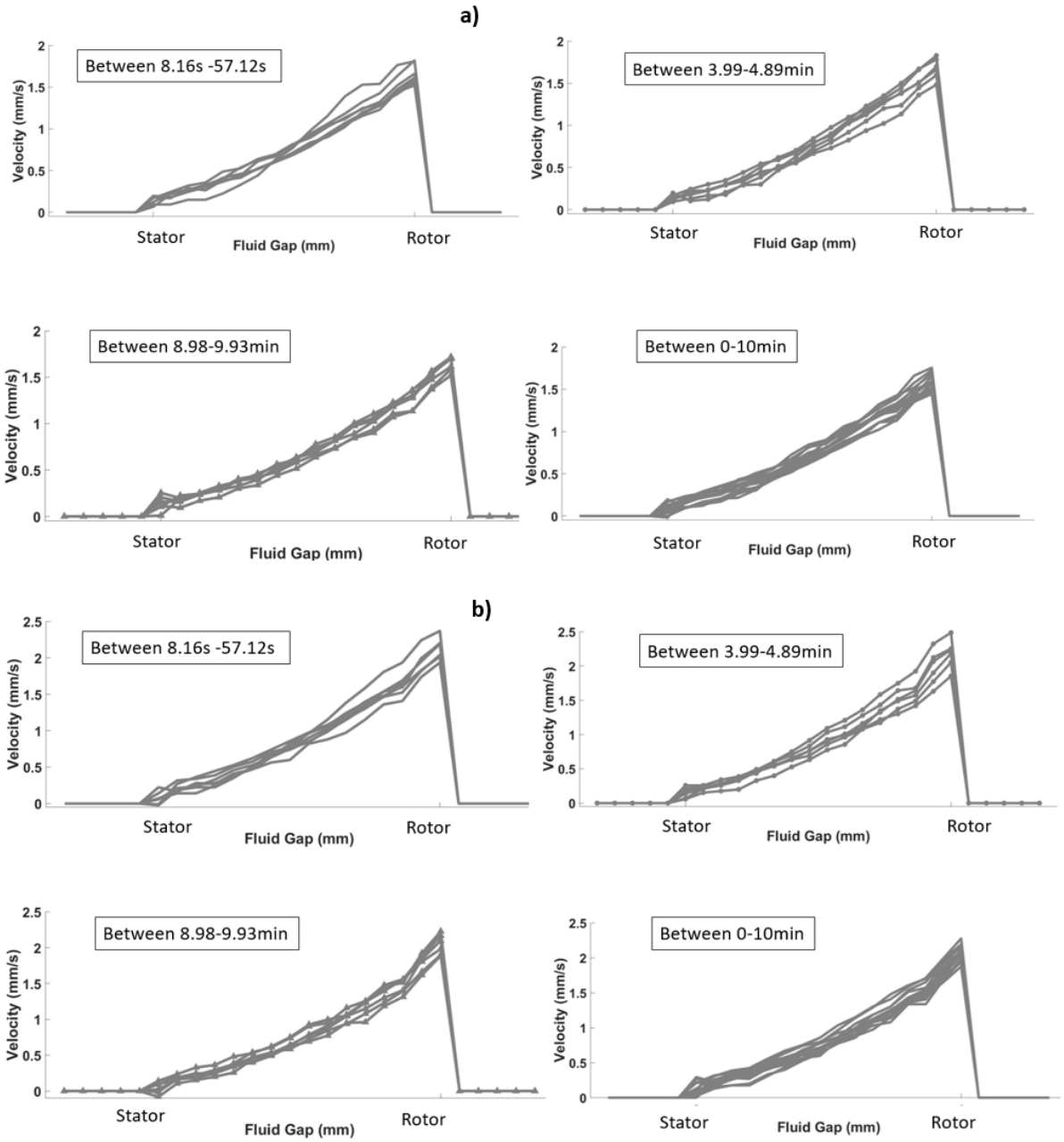

Figure D 2: Start up velocity profiles for sample 1 at applied shear rates of a) 2/s and b) 2.5/s. Critical shear rate (2.83749/s).

- sample 1 ramp up

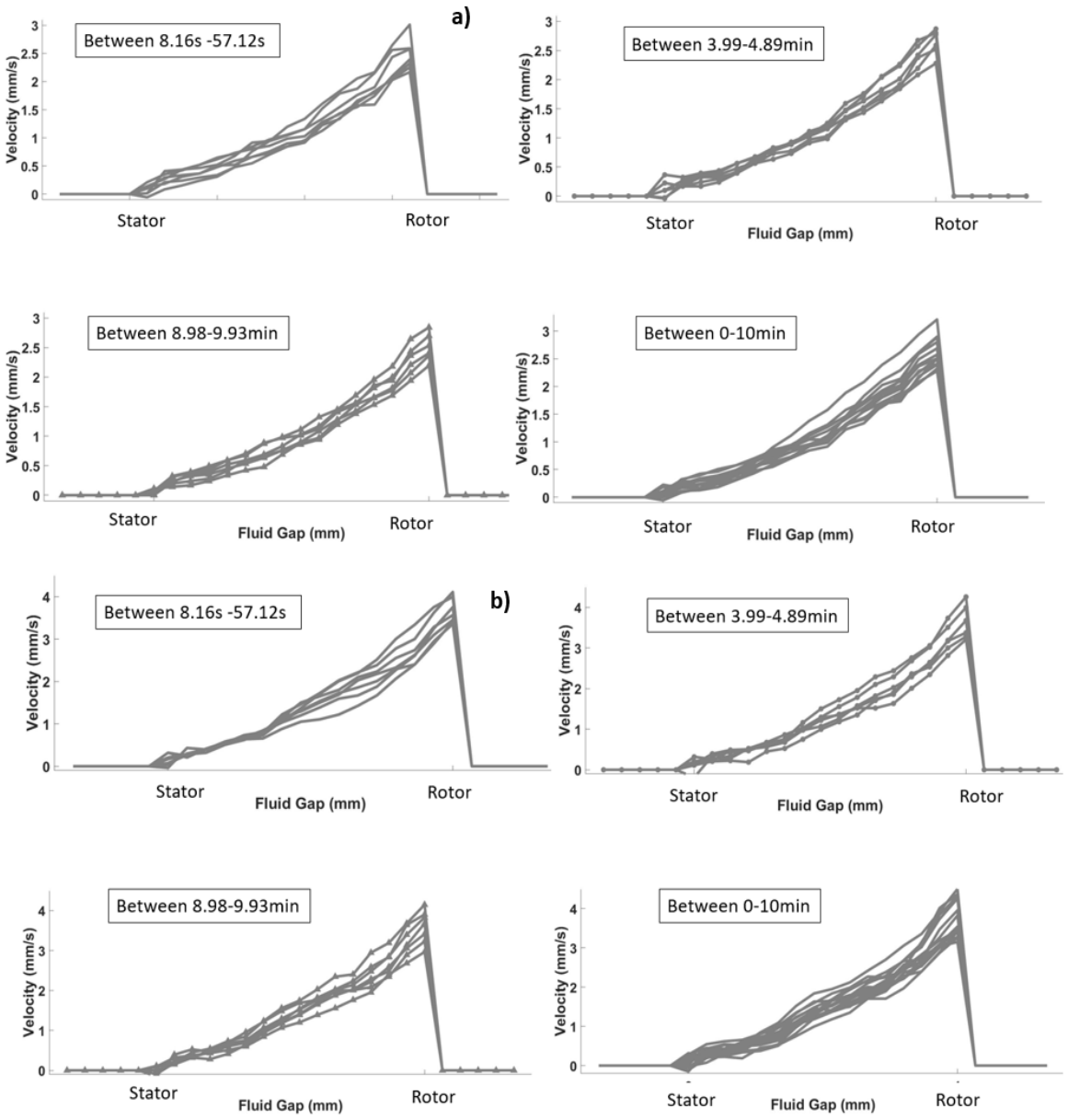

Figure D 3: Start up velocity profiles for sample 1 at applied shear rates of e) 3/s and f) 4/s. Critical shear rate (2.83749/s).

- sample 1 ramp up

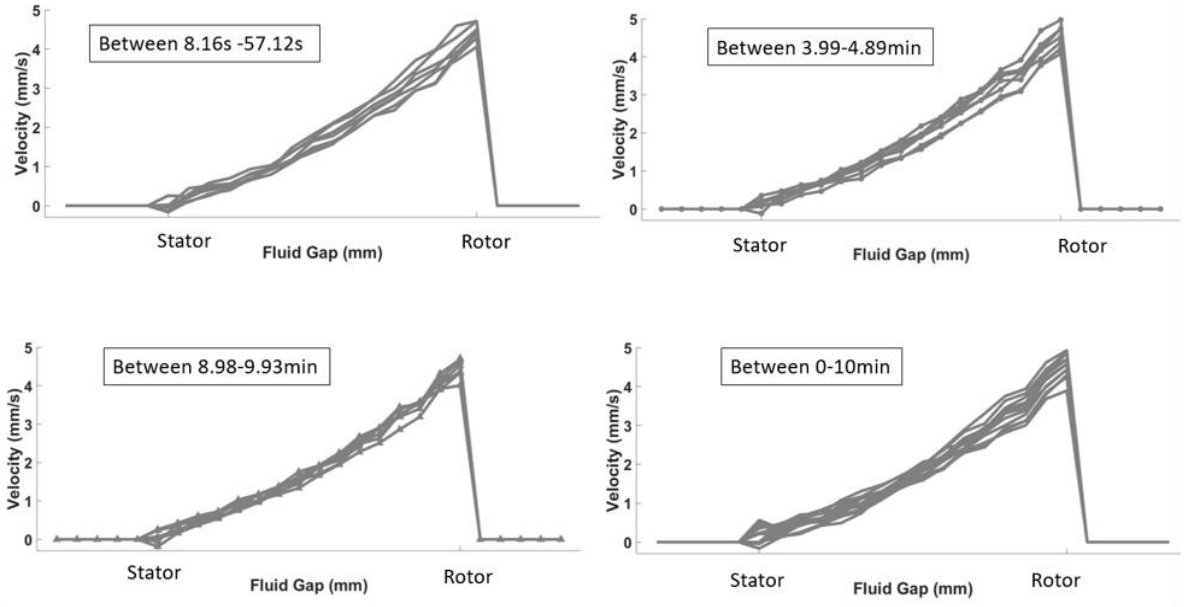

Figure D 4: Start up velocity profiles for sample 1 at an applied shear rate of 5/s. Critical shear rate (2.83749/s).
- sample 1 ramp up

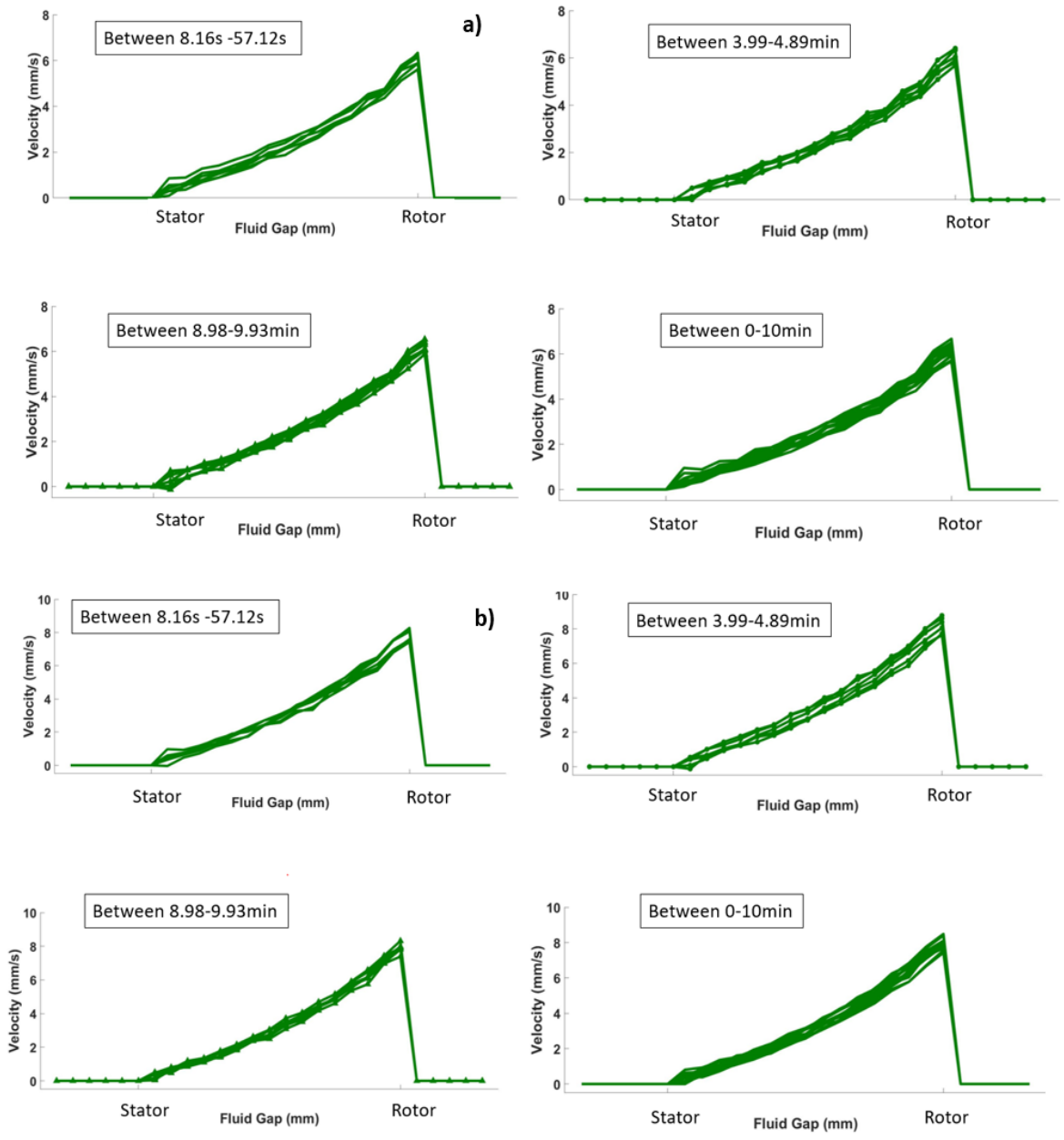

Figure D 5: Start up velocity profiles for sample 2 at applied shear rates of a) 7/s and b) 9/s. Critical shear rate (9.97538 /s).

- sample 2 ramp up

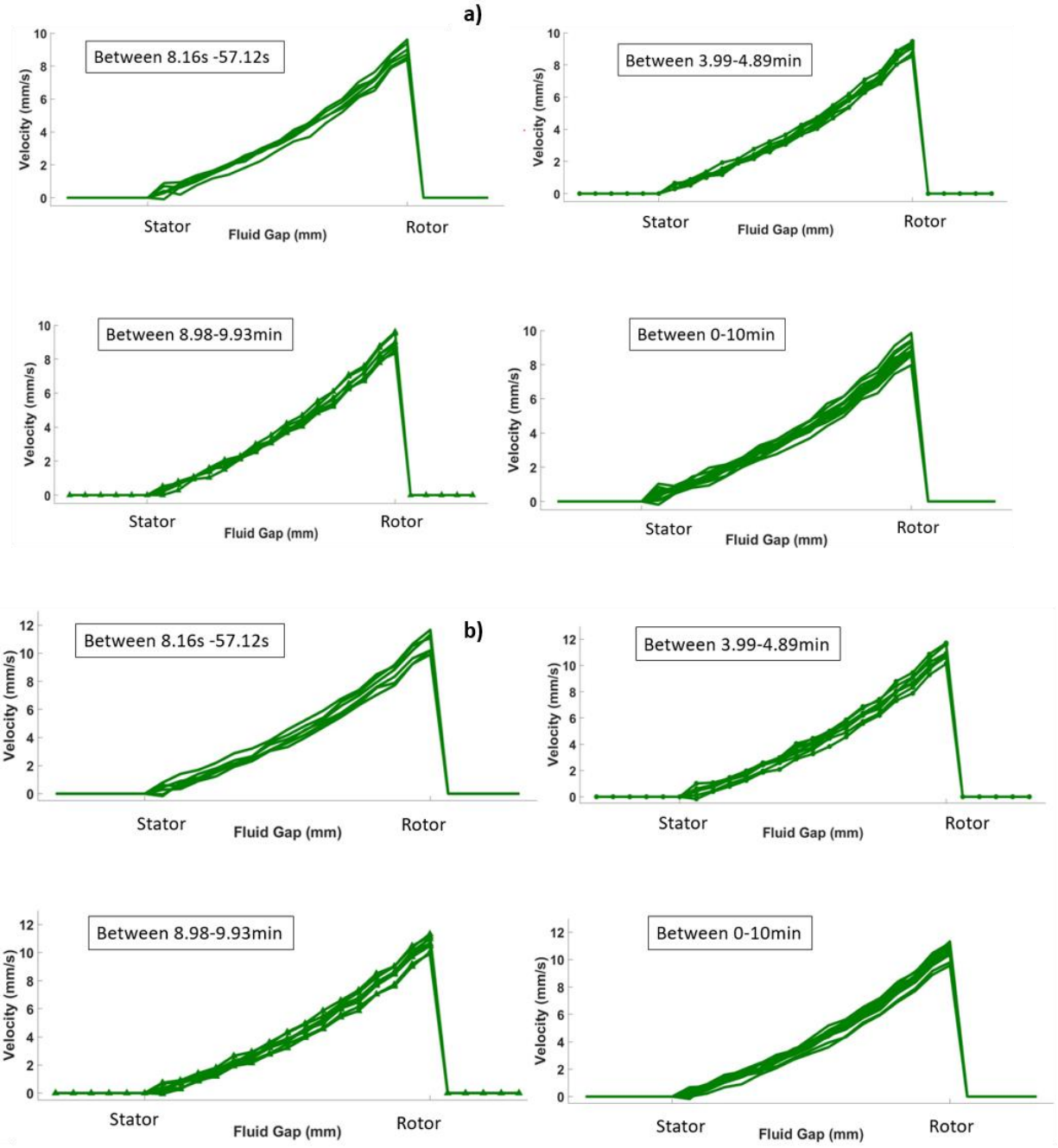

Figure D 6: Start up velocity profiles for sample 2 at applied shear rates of a) 10/s and b) 12/s. Critical shear rate (9.97538 /s).

- sample 2 ramp up

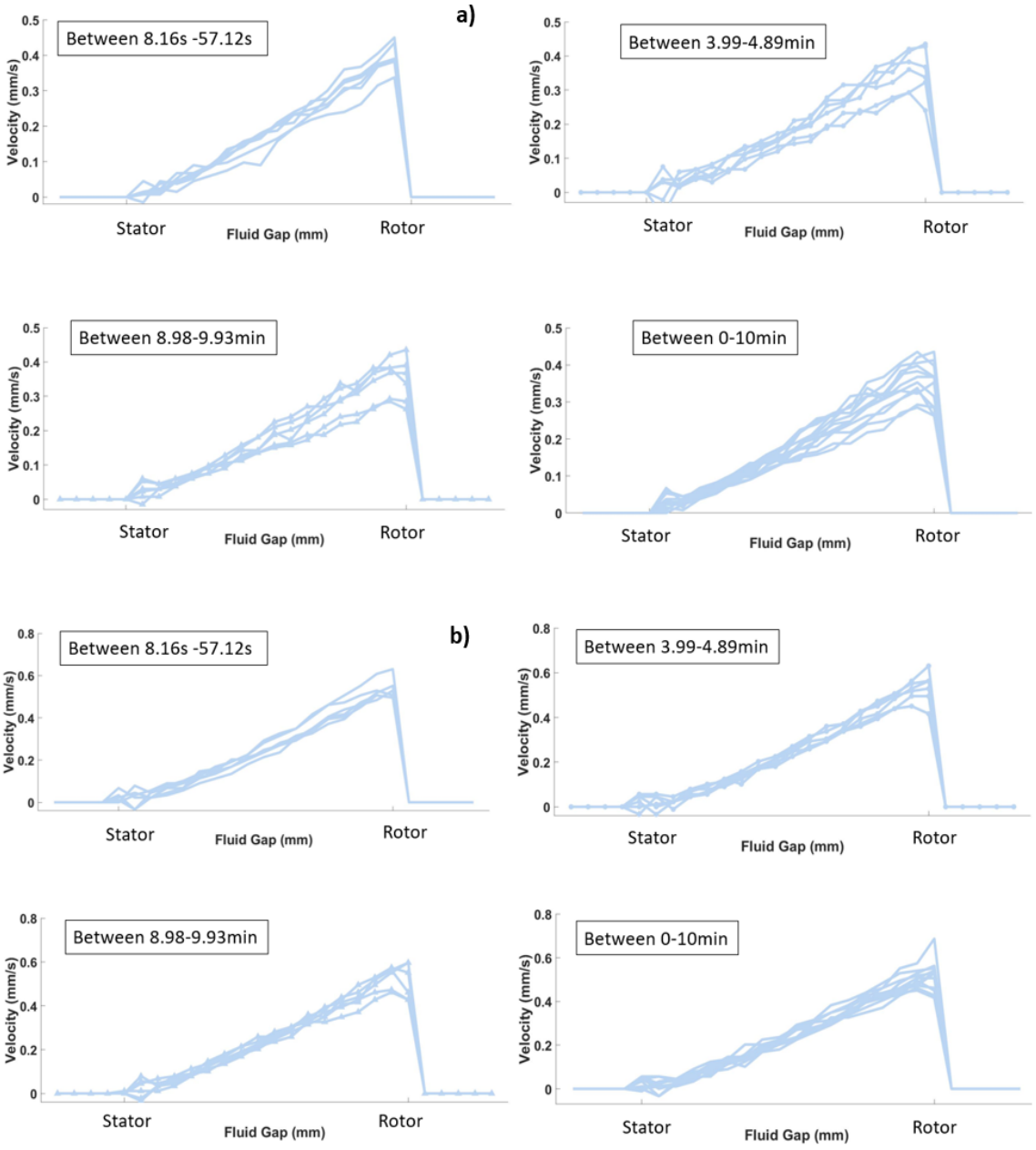

Figure D 7: Start up velocity profiles for sample 3 at applied shear rates of a) 0.4/s and b) 0.6 /s. Critical shear rate (0.700217 /s).

- sample 3 ramp up

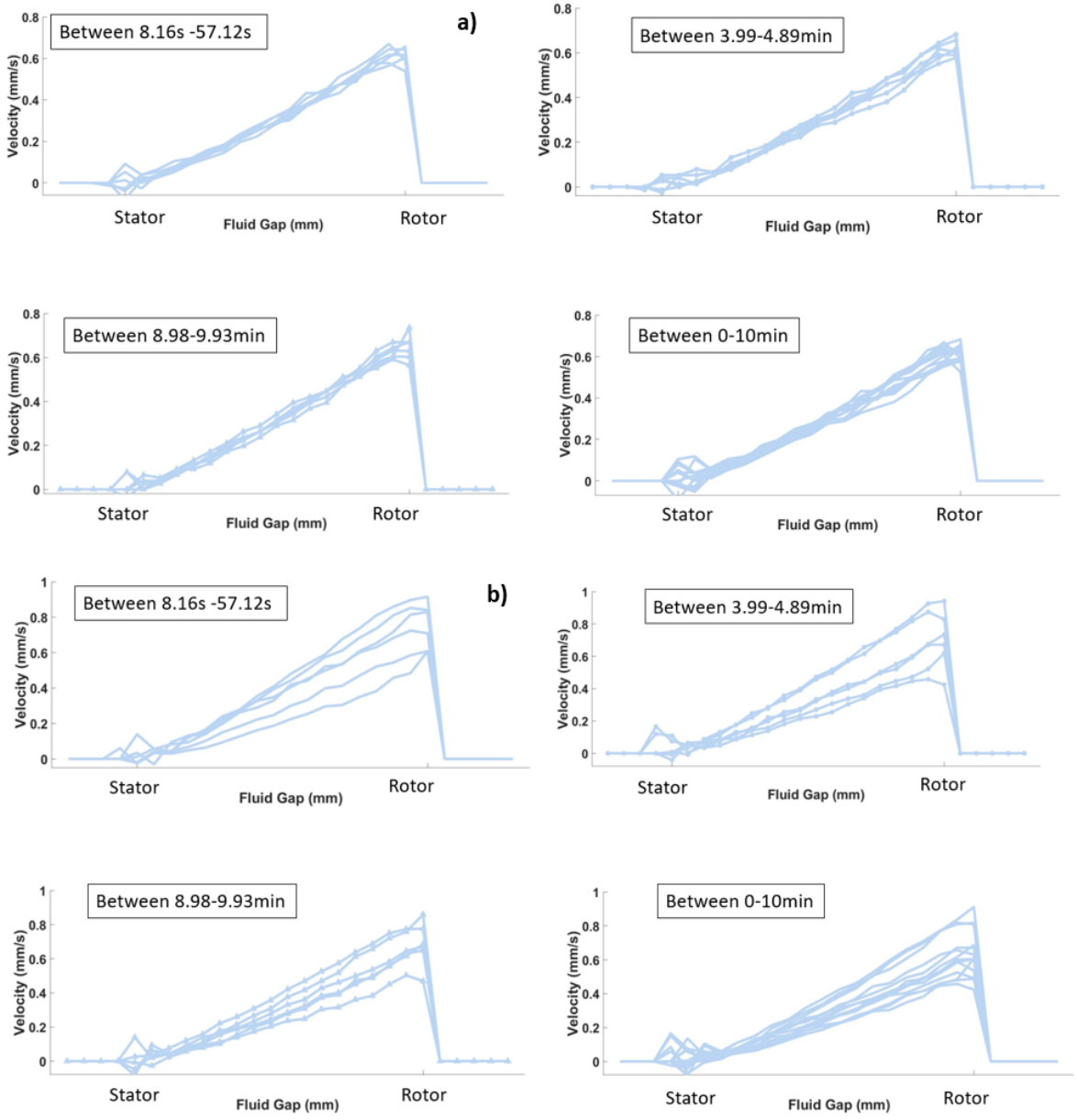

Figure D 8: Start up velocity profiles for sample 3 at applied shear rates of a) 0.7/s and b) 0.8 /s. Critical shear rate (0.700217 /s).

- sample 3 ramp up

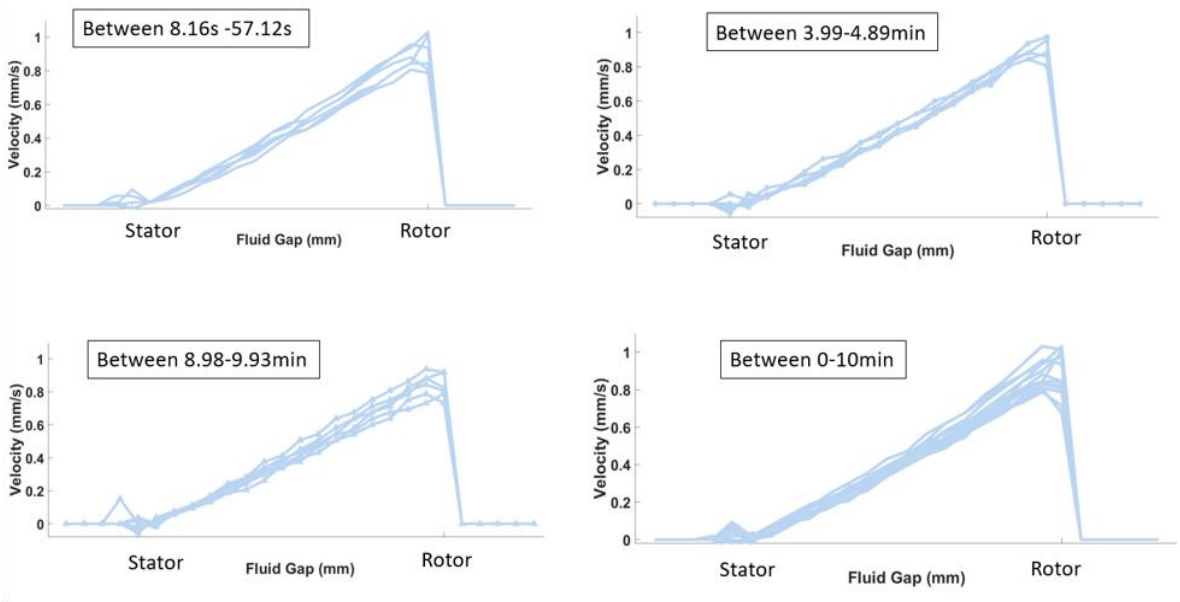

Figure D 9: Start up velocity profiles for sample 3 at an applied shear rate of 1 /s. Critical shear rate (0.700217 /s).
- sample 3 ramp up

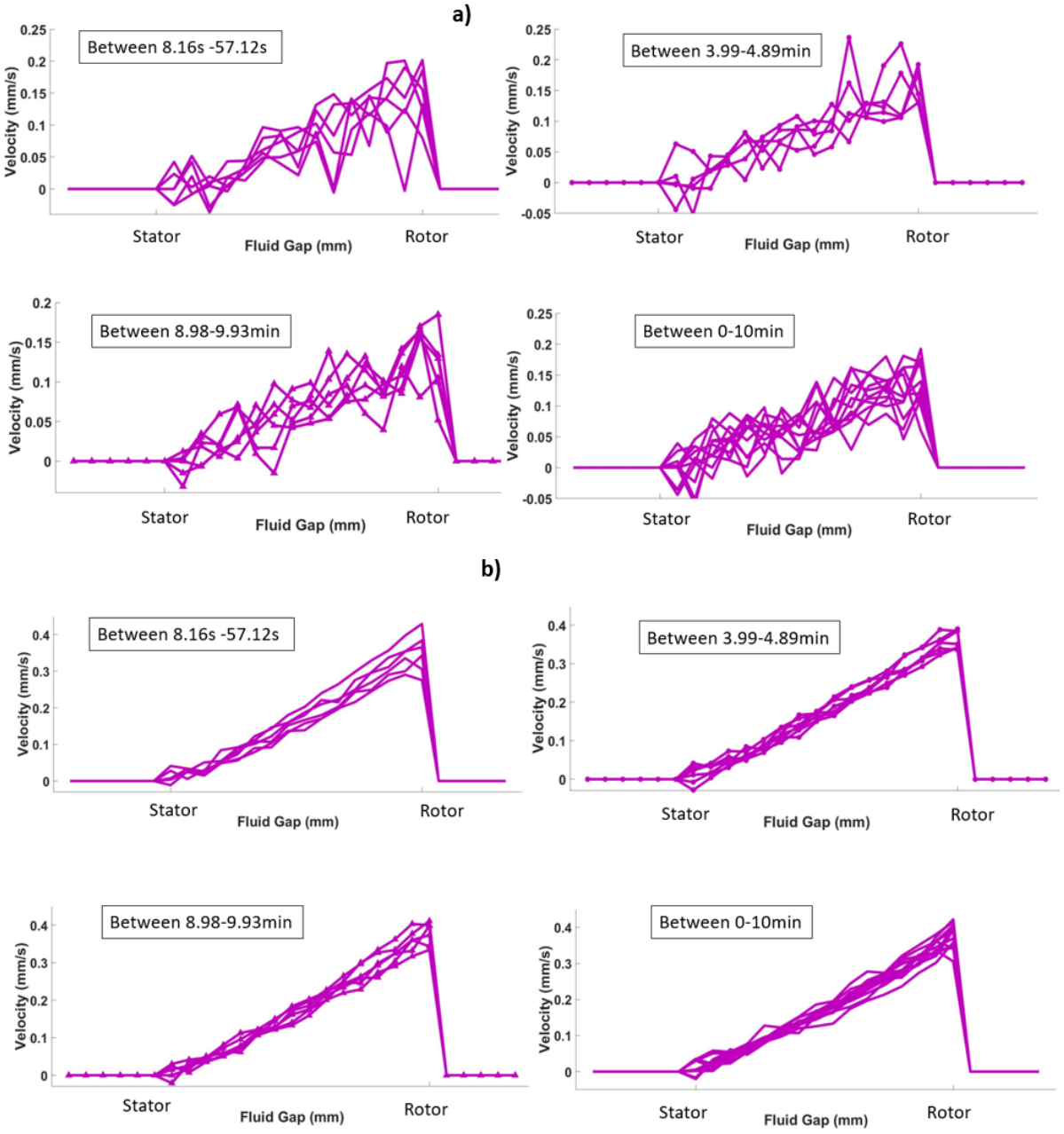

Figure D 10: Start up velocity profiles for sample 4 at applied shear rates of a) 0.2/s and b) 0.4 /s. Critical shear rate (0.594157 /s).

- sample 4 ramp up

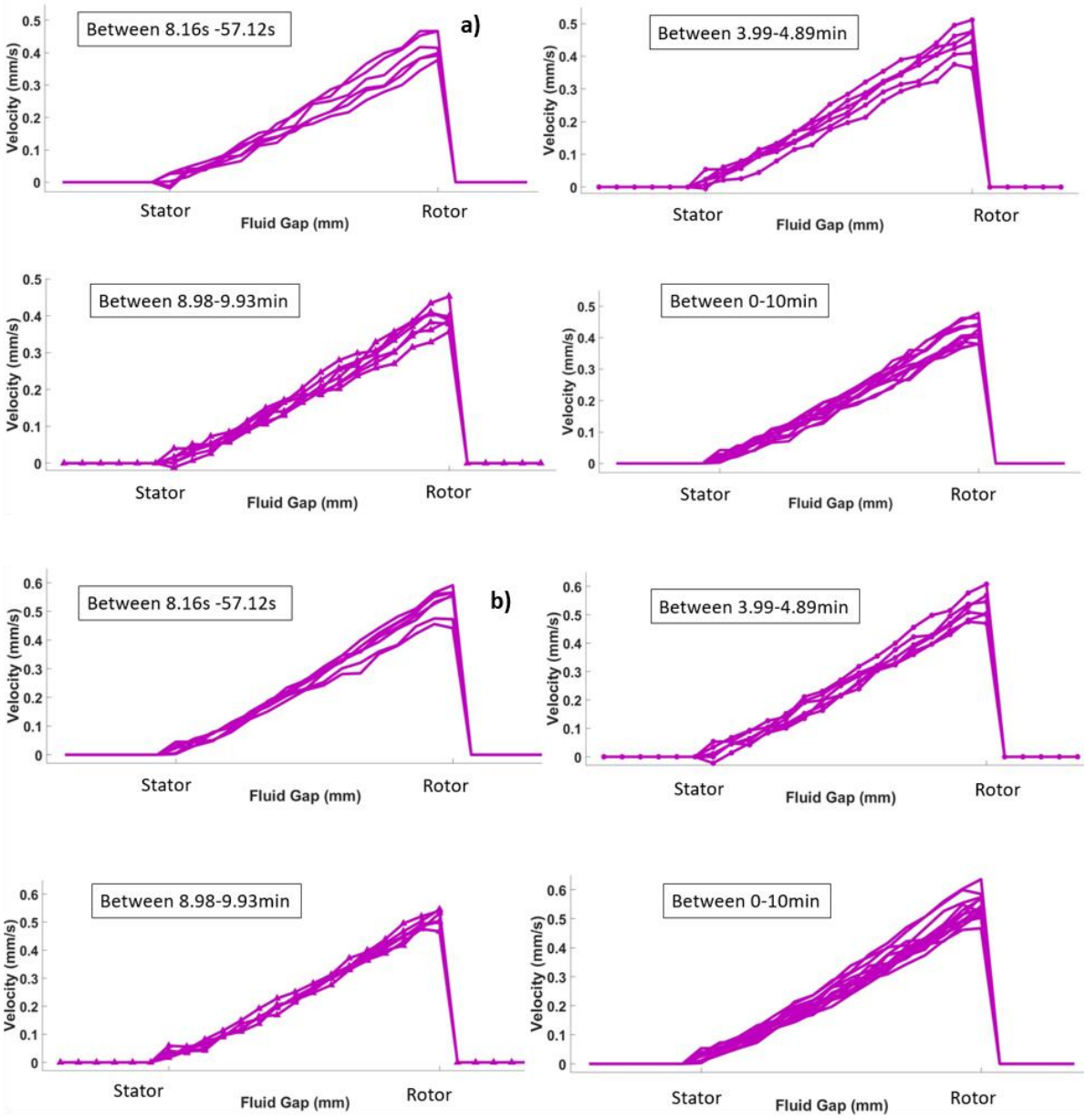

Figure D 11: Start up velocity profiles for sample 4 at applied shear rates of a) 0.5/s and b) 0.6 /s. Critical shear rate (0.594157 /s).

- sample 4 ramp up

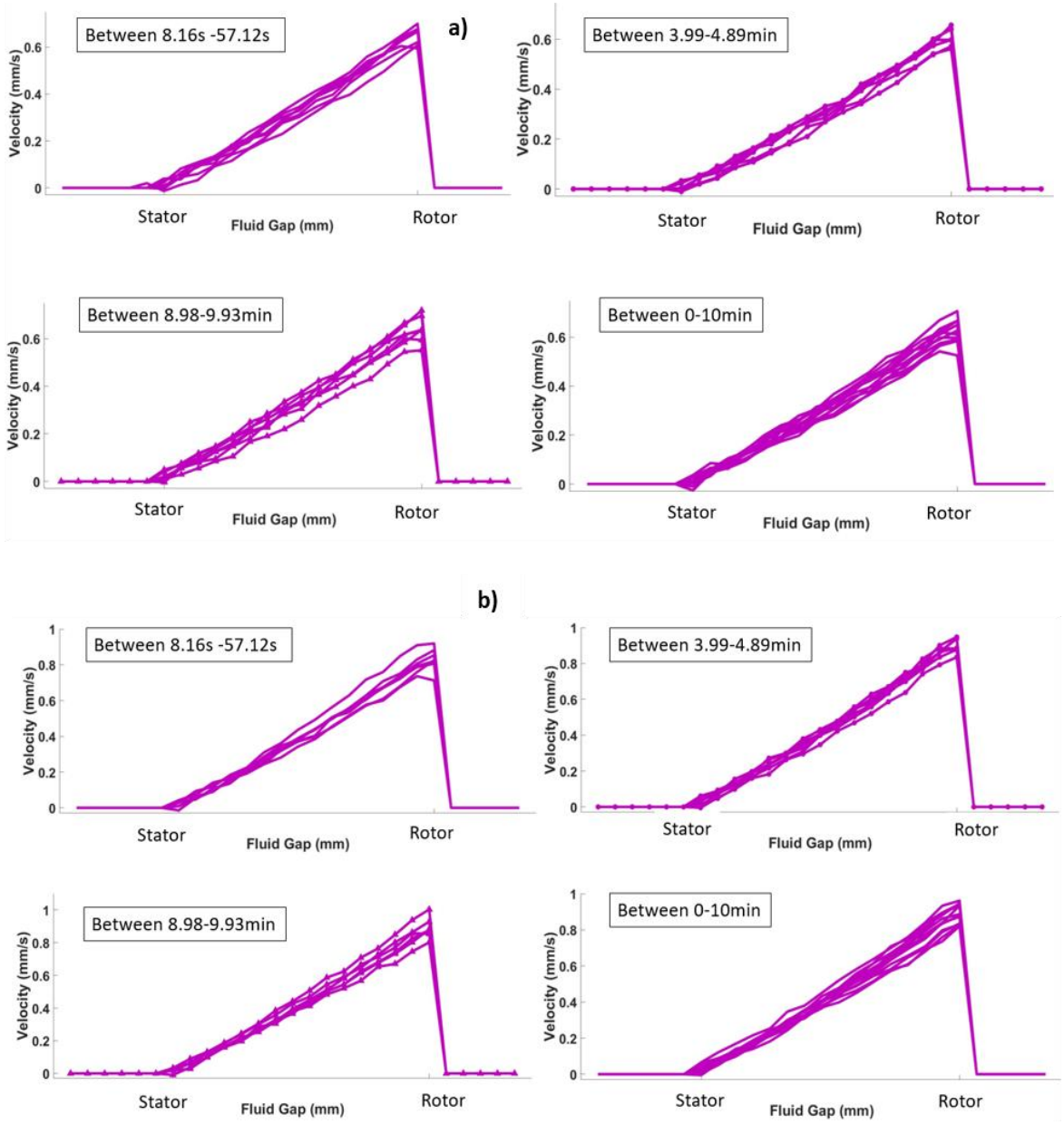

Figure D 12: Start up velocity profiles for sample 4 at applied shear rates of a) 0.7/s and b) 1/s. Critical shear rate (0.594157/s).

- sample 4 ramp up

APPENDIX E

STANDARD DEVIATIONS FOR EACH SAMPLE

Sample	Applied shear rate	Standard dev. At Rotor (8.23 mm)	Standard dev. at mid gap (8.53 mm)	Standard dev. at Rotor (8.82 mm)
Sample #1	0.5	0.0276	0.0243	0.0173
	1	0.0436	0.03	0.0311
	2	0.0969	0.0640	0.0557
	2.5	0.1265	0.0806	0.0632
	3	0.1871	0.1183	0.0825
	4	0.3376	0.2145	0.0894
	5	0.2429	0.1612	0.1049
Sample #2	7	0.2205	0.1780	0.1581
	9	0.3162	0.2258	0.1703
	10	0.3286	0.2429	0.1703
	12	0.4733	0.3492	0.22
Sample #3	0.4	0.0447	0.0253	0.0152
	0.6	0.031	0.0214	0.0170
	0.7	0.03	0.02	0.0158
	0.8	0.1414	0.0837	0.0313
	1	0.0548	0.0346	0.0245
Sample #4	0.2	0.029	0.027	0.0069
	0.4	0.027	0.0177	0.0126
	0.5	0.0308	0.0212	0.0132

	0.6	0.0335	0.0241	0.0136
	0.7	0.0361	0.0279	0.0164
	1	0.0436	0.0297	0.02
Silicone oil	0.2	0.0158	0.0075	0.0069
	0.4	0.0245	0.0166	0.0152
	0.5	0.0276	0.0182	0.00880
	0.6	0.0326	0.02	0.0092
	0.7	0.03	0.02	0.0158
	0.8	0.0608	0.0374	0.0313
	1	0.0447	0.0332	0.019
	2	0.0794	0.0574	0.0360
	2.5	0.1245	0.0866	0.0469
	3	0.1871	0.1304	0.0480
	4	0.3317	0.253	0.0894
	5	0.2145	0.1414	0.0917
	7	0.2678	0.1926	0.1327
	9	0.2608	0.1871	0.1304
	10	0.3464	0.251	0.1949
	12	0.4123	0.2811	0.2191

Table E 1: Standard deviations of velocities over time at the rotor, mid gap and stator.

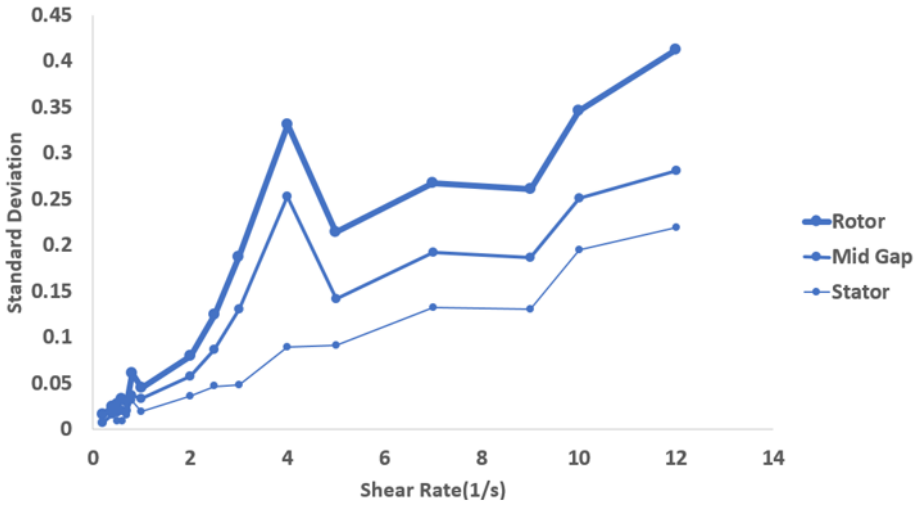

Figure E 1: Standard deviations of silicone oil at all tested shear rates supporting data from Table E 1.

CHAPTER EIGHT

CONCLUSIONS

The work encompassed this dissertation extends the use of rheo-NMR as a tool for the spatio-temporal study of flow properties of complex fluids. In particular, we cover ways that this technique can be used in studying transient flow behaviors, and steady state flow behavior of fluids and be used in providing spatial information that is lacking in standard rheometry due to the use of bulk flow measures under the viscometric assumption. New, advanced rheo-NMR rheometer functions and a novel fractal vane geometry were explored. Changing the mechanical deformation by subjecting materials to large amplitude oscillatory shear (LAOS) periodic motions, in place of a unidirectional steady flow, was shown to provide unique velocity distribution signatures for flow of fluids classified using different rheological models. The flow impact on the fluid flow when the standard concentric cylinder geometry was replaced by a fractal vane was also measured. With the ability to non-invasively investigate material properties through velocity measurements, rheo-NMR further demonstrated to provide novel data for studying complex fluids.

Rheo-NMR measurements used a magneto safe portable rheometer to create shear deformations on fluid samples within a concentric cylinder shear cell in the narrow gap flow limit. Rheo-NMR used magnetic resonance imaging (MRI) pulsed gradient stimulated echo (PGSE) flow encoding to track the motion of spins in the fluid by means of residual phase shifts in magnetization. Resulting 1D velocity profiles and 2D velocity maps quantitatively and qualitatively allowed us to study the local velocity behavior of complex fluids exhibiting a range of flow behaviors like shear banding, shear thinning, yield stress and a combination of the two.

The technique was also able to overcome the experimental challenge of providing high resolutions sufficient to characterize local velocity responses of these fluids, under the wide range of applied deformations, within the 1mm fluid gap that held the sample.

The study observing transient shear banding of worm like micelle solutions, (6 wt. % CPCL/NaSal solution) at shear rates exhibiting shear banding using 1D velocity profiles acquired every 1s showed temporal fluctuations of the material in reaching steady state [1]. The resulting time to steady state was determined and the fluctuations were quantified by taking the Fourier transform of the time correlation functions, providing the velocity frequency. Two separate protocols used in rheometry were analyzed: one with preshear and one without. Each protocol exhibited different frequency shifts indicating the significance of pre-shear protocols when studying shear banding materials.

Rheo-NMR was also employed using large amplitude oscillatory shear (LAOS) deformations to characterize the velocity behavior of two predominant fluid behaviors in industry and biology: shear thinning and yield stress. A variety of fluids modeled as Herschel-Bulkley fluids in rheology (0.2 wt.% carbomer 940 carbopol, ketchup and drinking yogurt) along with a fluid known to show power law shear thinning model fluid behavior (0.6% (w/v) xanthan gum) were subjected to LAOS deformations for strain amplitudes of 6.3 and 25.2 at a fixed frequency of 0.196 rad/s (of period T=32s). Strain amplitudes were chosen based on strain sweeps acquired on an ARES G2 rheometer (TA Instruments, New Castle, DE) and finding the strains in the non-linear viscoelastic region. NMR 1D velocity profiles of 32 velocity steps per periodic cycle were acquired with 32 averages (16 scans per q-step for a 2-qstep sequence) for higher signal to noise in data. Each of the resulting 1D velocity profiles taking over ~2 hours for

its acquisition. Each LAOS velocity profile for each fluid was compared to the LAOS velocity response of Newtonian fluids (water and silicone oil).

The complex fluid LAOS velocity distributions deviated from linear at different times within the cycle. Yield stress fluids show velocity profiles going from plug flow to partially yielded to fully yielded with a shear thinning behavior. The novelty of this data requires new analysis approaches to fully utilize it to rheological fluid responses. One analysis method introduced to study the differences between fluids is Lissajous-Bowditch approach using the Newtonian fluid velocity response as the input and the non-Newtonian fluid velocity response as the output wave function, hence measuring the deviation from the ideal velocity distribution. The data also provides time dependent velocity fluctuations at each position across the fluid gap.

A characteristic feature of yield stress fluids is apparent wall slip [2] [3]. A rheometer with a concentric cylinder geometry, as is often used in industrial R&D settings, also depicts this wall slip so vane geometries have been developed [4]. A modified vane geometry, based on fractals (bearing either 12 or 24 arms) was proposed as an ideal, easy to fabricate by 3D printing and interchangeable geometry in reducing slip effects encountered with the concentric cylinder cell [5]. Rheo-NMR is able to provide spatial velocity resolution to studying new rheology advancements such as this. A 0.6wt.% Carbopol simple yield stress solution (Ultrez 10 from Lubrizol) was used to study wall slip effects while a viscous 1,000cSt Newtonian silicone oil was used to measure the fluid mechanics to determine whether secondary flows are generated by the complicated geometry. 1D velocity profiles that analyzed the unidirectional flow velocity, $V_\theta(r)$, of carbopol showed reduction of wall slip. However the flow behavior in certain regions of fluid exhibited secondary flows even for the silicone oil. Using 2D velocity maps, we were able to

qualitatively show that this was due to the presence of a non-axisymmetric velocity field concluded as null images were obtained for the radial and vorticity velocity components ($V_r = V_z = 0$).

Rheo-NMR was also applied to study an oil-in-water emulsion. The critical shear rates of different concentrations of the solution found based on a three component model applied in interpreting the rheograms. The velocity distributions in the four different concentration of hydrogenated castor oil dispersed in aqueous linear alkyl benzene surfactant solution were resolved both temporally and spatially using 1D velocity profiles. Steady state velocity profiles indicated that at low hydrogenated castor oil concentration the samples showed more Newtonian like behaviors, while at higher surfactant and oil concentrations a Herschel Bulkley model behavior was observed. The connection between the TC model and the velocity data was discussed [6].

Rheo-NMR provides unique data on velocity distributions in complex fluids to study localized flow behavior. Advancements in the rheo-NMR hardware is applied to extend its application to rheology in general [7]. Rheo-NMR applications in industry have significant potential and are currently underutilized.

Future Work

Oscillatory responses under short acquisition times for each 1D velocity profile in a single cycle can be made shorter and repeated multiple times, without applying a pre-oscillatory shear, to observe potential oscillatory startup effects. The questions being: 1) would a fluid exhibiting shear induced networks, for example poly vinyl alcohol/sodium borate solution, lose its strain hardening characteristic if LAOS is repeated over a long period of time? This question maybe

applicable to weak strain overshoot materials like xanthan gum too, 2) What is an optimal approach to measure thixotropy, where from hysteresis tests we know a loop is formed to quantify thixotropy? Can this effect be observed in the back and forth motion, perhaps the distortion of each periodic cycle changing over time for a thixotropic fluid?

It would be beneficial to vary the fluid gap by change the narrow gap to wide gap limit and radius of curvature. Further vane measurements using large cups to avoid wall effects and increasing the number of arms of the fractal vane to determine if the velocity field can be made more axisymmetric are suggested. This will explore the possibility of using the fractal vane geometry as a compliment to the concentric cylinder geometry in rheo-NMR experiments done on yield stress fluids. While wall slip hinders industrial processes (interfering with a homogeneous mixing process or requiring higher pressures and use of energy in transporting fluids within pipes) it is a highly desired attribute in product packaging (for example, wall slip contributes to get toothpaste out of the tube). Fabricating rheo-NMR geometries similar to that of industrial mixers and exploring their velocity fields is an important extension of this project. Further studies of surface interfacial effects by coating the concentric cylinders with chemicals like LiquiGlide and using surface materials of varying controlled charge can also be a project to encompass the study of wall slip.

Last and perhaps the most important future study would be including NMR relaxometry and diffusometry methods to spatially localized regions of different material responses (shear banding of wormlike micelles or yielded vs yielded regions of yield stress fluids) should be developed. This will allow for the microscale structure and dynamics to be measured and integrated into fluid response modeling.

References

1. Al-kaby, R.N., et al., *Rheo-NMR of transient and steady state shear banding under shear startup.* Journal of Rheology, 2018. **62**(5): p. 1125-1134.

2. Barnes, H.A., *A Review of the Slip (Wall Depletion) of Polymer-Solutions, Emulsions and Particle Suspensions in Viscometers - Its Cause, Character, and Cure.* Journal of Non-Newtonian Fluid Mechanics, 1995. **56**(3): p. 221-251.

3. Wassenius, H. and P.T. Callaghan, *NMR velocimetry studies of the steady-shear rheology of a concentrated hard-sphere colloidal system.* European Physical Journal E, 2005. **18**(1): p. 69-84.

4. Nguyen, Q.D.a.D.V.B., *Characterization of yield stress fluids with concentric cylinder viscometers.* Rheologica acta, 1987. **24**(1): p. 508-515.

5. Owens, C.E., A.J. Hart, and G.H. McKinley, *Improved rheometry of yield stress fluids using bespoke fractal 3D printed vanes.* Journal of Rheology, 2020. **64**(3): p. 643-662.

6. Spicer, M.C.V.T.a.P.T., *Variations of the Herschel–Bulkley exponent reflecting contributions of the viscous continuous phase to the shear rate-dependent stress of soft glassy materials.* Journal of Rheology, 2020.

7. Brox, T.I., *New Methods for Studying Materials Under Shear with Nuclear Magnetic Resonance*. 2016, Victoria University of Wellington, NZ.

REFERENCES CITED

1. Macosko, C.W., *Rheology : principles, measurements, and applications*. 1994, New York: New York : Wiley-VCH.

2. Callaghan, P.T., *Rheo-NMR: nuclear magnetic resonance and the rheology of complex fluids.* Reports on Progress in Physics, 1999. **62**(4): p. 599-670.

3. Chiara, F.F., et al., *Role of Rheology in Achieving Successful Concrete Performance.* Concrete International, 2017. **39**(6): p. 43.

4. Jarny, S., et al., *Rheological behavior of cement pastes from MRI velocimetry.* CEMENT CONCRETE RES, 2005. **35**(10): p. 1873-1881.

5. Hyun, K., et al., *A review of nonlinear oscillatory shear tests: Analysis and application of large amplitude oscillatory shear (LAOS).* Progress in Polymer Science, 2011. **36**(12): p. 1697-1753.

6. Coussot, P., *Rheometry of Pastes, Suspensions, and Granular Materials: Applications in Industry and Environment*. 2005, New York: Wiley.

7. Fukushima, E., *NUCLEAR MAGNETIC RESONANCE AS A TOOL TO STUDY FLOW.* ANNU REV FLUID MECH, 1999. **31**(1): p. 95-123.

8. Callaghan, P.T., *Principles of nuclear magnetic resonance microscopy*. 1993, Oxford: Oxford : Clarendon Press.

9. Brox, T.I., *New Methods for Studying Materials Under Shear with Nuclear Magnetic Resonance*, in *Physics*. 2016, Victoria University of Wellington.

10. Nguyen, Q.D. and D.V. Boger, *Characterization of yield stress fluids with concentric cylinder viscometers.* Rheologica acta, 1987. **26**(6): p. 508-515.

11. Barnes, H.A. and Q.D. Nguyen, *Rotating vane rheometry — a review.* Journal of Non-Newtonian Fluid Mechanics, 2001. **98**(1): p. 1-14.

12. Wassenius, H. and P.T. Callaghan, *NMR velocimetry studies of the steady-shear rheology of a concentrated hard-sphere colloidal system.* Eur. Phys. J. E, 2005. **18**(1): p. 69-84.

13. Owens, C.E., A.J. Hart, and G.H. McKinley, *Improved rheometry of yield stress fluids using bespoke fractal 3D printed vanes.* Journal of Rheology, 2020. **64**(3): p. 643-662.

14. Al-kaby, R.N., et al., *Rheo-NMR of transient and steady state shear banding under shear startup.* Journal of Rheology, 2018. **62**(5): p. 1125-1134.

15. M. Caggioni, V.T., and P. T. Spicer, *Variations of the Herschel–Bulkley exponent reflecting contributions of the viscous continuous phase to the shear rate-dependent stress of soft glassy materials.* Journal of Rheology, 2020. **64**(2): p. 413-422.

16. Callaghan, P.T., *Translational Dynamics & Magnetic Resonance: Principles of Pulsed Gradient Spin Echo NMR*. 2011, New York: Oxford University Press.

17. Han, S.-l. and S. Stapf, *NMR imaging in chemical engineering*. 2006, Weinheim : [Chichester]: Weinheim : Wiley-VCH, Chichester : John Wiley, distributor.

18. Levitt, M.H., *Spin Dynamics*. 2013: Wiley.

19. Purcell, E.M., H.C. Torrey, and R.V. Pound, *Resonance Absorption by Nuclear Magnetic Moments in a Solid.* Physical review, 1946. **69**(1-2): p. 37-38.

20. Bloch, F., *NUCLEAR INDUCTION.* Physical Review, 1946. **70**(7-8): p. 460-474.

21. Günther, H., *NMR spectroscopy : basic principles, concepts and applications in chemistry*. 2013, Weinheim an der Bergstrasse, Germany : Wiley-VCH.

22. Slichter, C.P., P. Fulde, and K. von Klitzing, *Principles of Magnetic Resonance*. Third Enlarged and Updated Edition. ed. Vol. 1. 1996, Berlin, Heidelberg: Berlin, Heidelberg: Springer Berlin / Heidelberg.

23. Vogt, S.J., *Nuclear magnetic resonance studies of biological and biogeochemical processes*, in *Engineering*. 2013, Montana State University.

24. Keeler, J., *Understanding NMR spectroscopy*. 2011: John Wiley & Sons.

25. Simkins, J.W., *Spatiotemporal mapping of oxygen in model porous media biofilms*, in *Chemical Engineering*. 2019, Montana State University.

26. Thrane, L.W., *Nuclear magnetic resonance studies to characterize phase transitions in porous systems*, in *Engineering*. 2018, Montana State University.

27. Weishaupt, D., *How does MRI work? An Introduction to the Physics and Function of Magnetic Resonance Imaging*, V.D. Koechli, B. Marincek, and V.D. Köchli, Editors. 2006, Berlin, Heidelberg : Springer Berlin Heidelberg : Imprint: Springer: Berlin: New York.

28. Bernstein, M.A., K.F. King, and X.J. Zhou, *Handbook of MRI Pulse Sequences*. 2004, San Diego: San Diego: Elsevier Science & Technology.

29. Chhabra, R.P., Richardson, J.F. , *Non-Newtonian Flow in the Process Industries: Fundamentals and Engineering Applications*. 1999: Butterworth-Heinemann. 436.

30. Coussot, P., *Rheometry of Pastes, Suspensions, and Granular Materials: Applications in Industry and Environment.* JCT coatingstech, 2005. **4**(1): p. 306.

31. Janmey, P.A. and M. Schliwa, *Rheology.* CURR BIOL, 2008. **18**(15): p. R639-R641.

32. Astarita, G., G. Marrucci, and L. Nicolais, *Rheology: Principles*. 2013, New York, NY: New York, NY: Springer.

33. Poole, R.J., *The Deborah and Weissenberg numbers.* The British Society of Rheology, 2012. **2**(53): p. 32-39.

34. Barnes, H.A., Hutton, J.F., and Walters, K., *An Introduction to Rheology*. 1989: Elsevier :, Distributors for the U.S. and Canada, Elsevier Science Pub. Co. 201.

35. Astarita, G., *Rheology Volume 1: Principles*, G. Marrucci and L. Nicolais, Editors. 1980, New York, NY : Springer US : Imprint: Springer.

36. Franck, A., *Viscoelastic and dynamic mechanical testing* AN004-TA Instruments.

37. Spagnolie, S.E., *Complex Fluids in Biological Systems Experiment, Theory, and Computation*. 2015, New York, NY : Springer New York : Imprint: Springer.

38. Morozov, A. and S.E. Spagnolie, *Introduction to Complex Fluids*, in *Complex Fluids in Biological Systems: Experiment, Theory, and Computation*, S.E. Spagnolie, Editor. 2015, Springer New York: New York, NY. p. 3-52.

39. Dreisbach, D., *Statistical Theory of Liquids (Fisher, I. Z.).* J. Chem. Educ, 1966. **43**(10): p. A912.

40. Marx, N., et al., *Shear Thinning and Hydrodynamic Friction of Viscosity Modifier-Containing Oils. Part I: Shear Thinning Behaviour.* Tribol Lett, 2018. **66**(3): p. 1-14.

41. Guvendiren, M., Lu, H.D. and Burdick, J.A., *Shear-thinning hydrogels for biomedical applications.* Soft Matter, 2012. **8**.

42. Barnes, H.A. and K. Walters, *The yield stress myth?* Rheologica acta, 1985. **24**(4): p. 323-326.

43. Coussot, P., *Yield stress fluid flows: A review of experimental data.* J NON-NEWTON FLUID, 2014. **211**: p. 31-49.

44. Alexandrou, A.N., N. Constantinou, and G. Georgiou, *Shear rejuvenation, aging and shear banding in yield stress fluids.* J NON-NEWTON FLUID, 2009. **158**(1): p. 6-17.

45. Larson, R.G., *The structure and rheology of complex fluids*. 1999, New York: New York: Oxford University Press.

46. Nelson, A.Z., *Rheology and Design of Yield-Stress Fluids*. 2018, ProQuest Dissertations Publishing.

47. R. Varges, P., et al., *Rheological Characterization of Carbopol® Dispersions in Water and in Water/Glycerol Solutions.* Fluids (Basel), 2019. **4**(1): p. 3.

48. Piau, J.M., *Carbopol gels: Elastoviscoplastic and slippery glasses made of individual swollen sponges Meso- and macroscopic properties, constitutive equations and scaling laws.* J NON-NEWTON FLUID, 2007. **144**(1): p. 1-29.

49. Malvern Instruments Limited, S.p., *Understanding Yield Stress Measurements.* White paper, 2012.

50. Franck, A., *Understanding Rheology of Structured Fluids.* AAN016-TA Instruments.

51. Barry, B.W., Meyer, M.C., *The rheological properties of carbopol gels I. Continuous shear and creep properties of carbopol gels.* Int. J. Pharm. **2**(1): p. 1-25.

52. Ptaszek, P., *Chapter 5 - Large Amplitude Oscillatory Shear (LAOS) Measurement and Fourier-Transform Rheology: Application to Food*, in *Advances in Food Rheology and Its Applications*, J. Ahmed, P. Ptaszek, and S. Basu, Editors. 2017, Woodhead Publishing. p. 87-123.

53. Ferry, J.D.a.H.S.M., *Viscoelastic Properties of Polymers.* Journal of The Electrochemical Society, 1961. **108**(7).

54. Hyun, K., et al., *Large amplitude oscillatory shear as a way to classify the complex fluids.* J NON-NEWTON FLUID, 2002. **107**(1): p. 51-65.

55. Nettesheim, F. and S.A. Rogers, *The unification of disparate rheological measures in oscillatory shearing.* PHYS FLUIDS, 2019. **31**(7): p. 73107.

56. Dodge, J.S., *OSCILLATORY SHEAR OF NONLINEAR FLUIDS*. 1969, ProQuest Dissertations Publishing.

57. Nam, J.G., et al., *Prediction of normal stresses under large amplitude oscillatory shear flow*. J NON-NEWTON FLUID, 2008. **150**(1): p. 1-10.

58. Carotenuto, C., M. Grosso, and P.L. Maffettone, *Fourier Transform Rheology of Dilute Immiscible Polymer Blends: A Novel Procedure To Probe Blend Morphology.* MACROMOLECULES, 2008. **41**(12): p. 4492-4500.

59. Mas, R. and A. Magnin, *Experimental validation of steady shear and dynamic viscosity relation for yield stress fluids.* Rheol Acta, 1997. **36**(1): p. 49-55.

60. Ewoldt, R.H., et al., *Large amplitude oscillatory shear of pseudoplastic and elastoviscoplastic materials.* Rheol Acta, 2010. **49**(2): p. 191-212.

61. Bird, R.B., *Transport phenomena*. 2nd ed.. ed, ed. W.E. Stewart and E.N. Lightfoot. 2002, New York: New York : J. Wiley.

62. Kuczera, S. and P. Galvosas, *Advances and artefact suppression in RARE-velocimetry for flow with curved streamlines.* J MAGN RESON, 2015. **259**: p. 135-145.

63. Brox, T., et al., *Observations of the influence of Taylor-Couette geometry on the onset of shear-banding in surfactant wormlike micelles.* Journal of Rheology, 2016. **60**(5): p. 973-982.

64. Mooney, M. and R.H. Ewart, *The Conicylindrical Viscometer*. Physics (New York. 1931), 1934. **5**(11): p. 350-354.

65. Adams, N. and A.S. Lodge, *Rheological Properties of Concentrated Polymer Solutions II. A Cone-And-Plate and Parallel-Plate Pressure Distribution Apparatus for Determining Normal Stress Differences in Steady Shear Flow.* Phil. Trans. R. Soc. Lond. A, 1964. **256**(1068): p. 149-184.

66. Products, M.C. *NEMA 23 High Torque Stepper Motors Hybrid Stepper Motor*. 2021; Available from: https://www.motioncontrolproducts.com/electric-motors/stepper-motors/hybrid-stepper-motors/nema-23-high-torque-stepper-motors/.

67. Cates, M. and S. Candau, *Statics and dynamics of worm-like surfactant micelles.* Journal of Physics: Condensed Matter, 1990. **2**(33): p. 6869.

68. Rehage, H. and H. Hoffmann, *Viscoelastic surfactant solutions: model systems for rheological research.* Molecular Physics, 1991. **74**(5): p. 933-973.

69. Cates, M., *Nonlinear viscoelasticity of wormlike micelles (and other reversibly breakable polymers).* Journal of Physical Chemistry, 1990. **94**(1): p. 371-375.

70. Rehage, H. and H. Hoffmann, *Rheological properties of viscoelastic surfactant systems.* The Journal of Physical Chemistry, 1988. **92**(16): p. 4712-4719.

71. Cates, M.E., *Reptation of living polymers: dynamics of entangled polymers in the presence of reversible chain-scission reactions.* Macromolecules, 1987. **20**(9): p. 2289-2296.

72. Spenley, Cates, and McLeish, *Nonlinear rheology of wormlike micelles.* Physical review letters, 1993. **71**(6): p. 939.

73. Cates, M.E. and M.R. Evans, *Soft and fragile matter: nonequilibrium dynamics, metastability and flow (PBK)*. 2000: CRC Press.

74. Candau, S. and R. Oda, *Linear viscoelasticity of salt-free wormlike micellar solutions.* Colloids and Surfaces A: Physicochemical and Engineering Aspects, 2001. **183**: p. 5-14.

75. Yang, J., *Viscoelastic wormlike micelles and their applications.* Current opinion in colloid & interface science, 2002. **7**(5-6): p. 276-281.

76. Lerouge, S. and J.-F. Berret, *Shear-induced transitions and instabilities in surfactant wormlike micelles*, in *Polymer Characterization*. 2009, Springer. p. 1-71.

77. Olmsted, P.D., *Perspectives on shear banding in complex fluids.* Rheologica Acta, 2008. **47**(3): p. 283-300.

78. Fardin, M.-A. and S. Lerouge, *Flows of living polymer fluids.* Soft Matter, 2014. **10**(44): p. 8789-8799.

79. Berret, J.-F., D. Roux, and P. Lindner, *Structure and rheology of concentrated wormlike micelles [4] at the shear-induced isotropic-to-nematic transition.* The European Physical Journal B-Condensed Matter and Complex Systems, 1998. **5**(1): p. 67-77.

80. Hu, Y.T. and A. Lips, *Kinetics and mechanism of shear banding in an entangled micellar solution.* Journal of Rheology, 2005. **49**(5): p. 1001-1027.

81. Berret, J.-F., D.C. Roux, and G. Porte, *Isotropic-to-nematic transition in wormlike micelles under shear.* Journal de Physique II, 1994. **4**(8): p. 1261-1279.

82. Callaghan, P., et al., *A Study of the "Spurt Effect" in Wormlike Micelles Using Nuclear Magnetic Resonance Microscopy.* Journal de Physique II, 1996. **6**(3): p. 375-393.

83. Lerouge, S., J.P. Decruppe, and P. Olmsted, *Birefringence banding in a micellar solution or the complexity of heterogeneous flows.* Langmuir, 2004. **20**(26): p. 11355-11365.

84. Manneville, S., *Recent experimental probes of shear banding.* Rheologica Acta, 2008. **47**(3): p. 301-318.

85. Boukany, P.E. and S.Q. Wang, *Exploring the transition from wall slip to bulk shearing banding in well-entangled DNA solutions.* Soft Matter, 2009. **5**(4): p. 780-789.

86. Tapadia, P. and S.-Q. Wang, *Yieldlike constitutive transition in shear flow of entangled polymeric fluids.* Physical review letters, 2003. **91**(19): p. 198301.

87. Sprakel, J., et al., *Shear banding and rheochaos in associative polymer networks.* Soft Matter, 2008. **4**(8): p. 1696-1705.

88. Krishan, K. and M. Dennin, *Viscous shear banding in foam.* Physical Review E, 2008. **78**(5): p. 051504.

89. Ovarlez, G., K. Krishan, and S. Cohen-Addad, *Investigation of shear banding in three-dimensional foams.* EPL (Europhysics Letters), 2010. **91**(6): p. 68005.

90. Paredes, J., N. Shahidzadeh-Bonn, and D. Bonn, *Shear banding in thixotropic and normal emulsions.* Journal of Physics: Condensed Matter, 2011. **23**(28): p. 284116.

91. Coussot, P., et al., *Coexistence of liquid and solid phases in flowing soft-glassy materials.* Physical review letters, 2002. **88**(21): p. 218301.

92. Gibaud, T., C. Barentin, and S. Manneville, *Influence of boundary conditions on yielding in a soft glassy material.* Physical Review Letters, 2008. **101**(25): p. 258302.

93. Losert, W., et al., *Particle dynamics in sheared granular matter.* Physical Review Letters, 2000. **85**(7): p. 1428-1431.

94. Mueth, D.M., et al., *Signatures of granular microstructure in dense shear flows.* Nature, 2000. **406**(6794): p. 385.

95. Berret, J.-F., *Rheology of wormlike micelles: equilibrium properties and shear banding transitions,* in *Molecular gels*. 2006, Springer. p. 667-720.

96. Berret, J.-F.c., G. Porte, and J.-P. Decruppe, *Inhomogeneous shear flows of wormlike micelles: mA master dynamic phase diagram.* Physical Review E, 1997. **55**(2): p. 1668.

97. Britton, M.M. and P.T. Callaghan, *Two-phase shear band structures at uniform stress.* Physical Review Letters, 1997. **78**: p. 4930-4933.

98. Lopez-Gonzalez, M.R., et al., *Shear Banding Fluctuations and Nematic Order in Wormlike Micelles.* Physical Review Letters, 2004. **93**: p. 268-302.

99. Douglass, B.S., et al., *Rheo-NMR of wormlike micelles formed from nonionic pluronic surfactants.* Macromolecules, 2008. **41**(3): p. 804-814.

100. Miller, E. and J.P. Rothstein, *Transient evolution of shear-banding wormlike micellar solutions.* Journal of Non-Newtonian Fluid Mechanics, 2007. **143**(1): p. 22-37.

101. Bécu, L., S. Manneville, and A. Colin, *Spatiotemporal dynamics of wormlike micelles under shear.* Physical review letters, 2004. **93**(1): p. 018301.

102. Becu, L., et al., *Evidence for three-dimensional unstable flows in shear-banding wormlike micelles.* Physical Review E, 2007. **76**(1).

103. Fischer, E. and P.T. Callaghan, *Is a birefringence band a shear band?* Europhysics Letters, 2000. **50**(6): p. 803-809.

104. Britton, M. and P. Callaghan, *Shear banding instability in wormlike micellar solutions.* The European Physical Journal B-Condensed Matter and Complex Systems, 1999. **7**(2): p. 237-249.

105. Salmon, J.B., et al., *Velocity profiles in shear-banding wormlike micelles.* Physical Review Letters, 2003. **90**(22).

106. Lopez-Gonzalez, M.R., W.M. Holmes, and P.T. Callaghan, *Rheo-NMR phenomena of wormlike micelles.* Soft Matter, 2006. **2**: p. 855-869.

107. Manneville, S., L. Bécu, and A. Colin, *High-frequency ultrasonic speckle velocimetry in sheared complex fluids.* The European Physical Journal-Applied Physics, 2004. **28**(3): p. 361-373.

108. Lettinga, M.P. and S. Manneville, *Competition between Shear Banding and Wall Slip in Wormlike Micelles.* Physical Review Letters, 2009. **103**(24).

109. Feindel, K.W. and P.T. Callaghan, *Anomalous shear banding: multidimensional dynamics under fluctuating slip conditions.* Rheologica Acta, 2010. **49**(10): p. 1003-1013.

110. Fardin, M.A., et al., *Shear-banding in surfactant wormlike micelles: elastic instabilities and wall slip.* Soft Matter, 2012. **8**(8): p. 2535-2553.

111. Fardin, M.-A., et al., *Shear-banding in wormlike micelles: Beware of elastic instabilities.* Journal of Rheology, 2016. **60**(5): p. 917-926.

112. Mohammadigoushki, H. and S.J. Muller, *Inertio-elastic instability in Taylor-Couette flow of a model wormlike micellar system.* Journal of Rheology, 2017. **61**(4): p. 683-696.

113. Fardin, M.A., et al., *Taylor-like Vortices in Shear-Banding Flow of Giant Micelles.* Physical Review Letters, 2009. **103**(2): p. 4.

114. Fardin, M.A., et al., *Interplay between elastic instabilities and shear-banding: three categories of Taylor-Couette flows and beyond.* Soft Matter, 2012. **8**(39): p. 10072-10089.

115. Hu, Y.T., C. Palla, and A. Lips, *Comparison between shear banding and shear thinning in entangled micellar solutions.* Journal of Rheology, 2008. **52**(2): p. 379-400.

116. Moorcroft, R.L. and S.M. Fielding, *Shear banding in time-dependent flows of polymers and wormlike micelles.* Journal of Rheology, 2014. **58**(1): p. 103-147.

117. Pipe, C., et al., *Wormlike micellar solutions: II. Comparison between experimental data and scission model predictions.* Journal of Rheology, 2010. **54**(4): p. 881-913.

118. Brown, E., W. Burghardt, and D. Venerus, *Tests of the Lodge− Meissner Relation in Anomalous Nonlinear Step Strain of an Entangled Wormlike Micelle Solution.* Langmuir, 1997. **13**(14): p. 3902-3904.

119. Vasquez, P.A., G.H. McKinley, and L.P. Cook, *A network scission model for wormlike micellar solutions: I. Model formulation and viscometric flow predictions.* Journal of non-newtonian fluid mechanics, 2007. **144**(2-3): p. 122-139.

120. Lopez-Barron, C.R., et al., *Microstructural evolution of a model, shear-banding micellar solution during shear startup and cessation.* Physical Review E, 2014. **89**(4).

121. Helgeson, M.E., et al., *Rheology and spatially resolved structure of cetyltrimethylammonium bromide wormlike micelles through the shear banding transition.* Journal of Rheology, 2009. **53**(3): p. 727-756.

122. Fardin, M.-A. and S. Lerouge, *Instabilities in wormlike micelle systems.* The European Physical Journal E, 2012. **35**(9): p. 1-29.

123. Lerouge, S., et al., *Interface dynamics in shear-banding flow of giant micelles.* Soft Matter, 2008. **4**(9): p. 1808-1819.

124. Callaghan, P.T., *Translational Dynamics and Magnetic Resonance: Principles of Pulsed Gradient Spin Echo NMR*. 2011, New York: Oxford University Press.

125. Brox, T.I., et al., *Observations of the influence of Taylor-Couette geometry on the onset of shear-banding in surfactant wormlike micelles.* Journal of Rheology, 2016. **60**(5): p. 973-982.

126. Glasgow, L.A., *Transport phenomena: an introduction to advanced topics*. 2010: John Wiley & Sons.

127. Oelschlaeger, C., et al., *Structural, kinetics, and rheological properties of low ionic strength dilute solutions of a dimeric (gemini) surfactant.* Langmuir, 2002. **18**(20): p. 7265-7271.

128. Berret, J.F., et al., *Shear-thickening transition in surfactant solutions: New experimental features from rheology and flow birefringence.* European Physical Journal E, 2000. **2**(4): p. 343-350.

129. Gallot, T., et al., *Ultrafast ultrasonic imaging coupled to rheometry: Principle and illustration.* Review of Scientific Instruments, 2013. **84**(4).

130. Berret, J.-F., *Transient rheology of wormlike micelles.* Langmuir, 1997. **13**(8): p. 2227-2234.

131. Lerouge, S., J.P. Decruppe, and J.F. Berret, *Correlations between rheological and optical properties of a micellar solution under shear banding flow.* Langmuir, 2000. **16**(16): p. 6464-6474.

132. Lerouge, S., M. Argentina, and J.P. Decruppe, *Interface instability in shear-banding flow.* Physical Review Letters, 2006. **96**(8): p. 4.

133. Brown, J.R. and P.T. Callaghan, *Changing micellar order, lever rule behavior and spatio-temporal dynamics in shear-banding at the onset of the stress plateau.* Soft Matter, 2011. **7**(21): p. 10472-10482.

134. Bonn, D., et al., *Yield stress materials in soft condensed matter.* Reviews of Modern Physics, 2017. **89**(3): p. 035005.

135. Larson, R.G., *The structure and rheology of complex fluids (Topics in chemical engineering).* 1999, New York: Oxford University Press.

136. Mewis, J. and A.J.B. Spaull, *Rheology of concentrated dispersions.* Advances in colloid and interface science, 1976. **6**(3): p. 173-200.

137. Bird, R.B., G.C. Dai G.C and B.J. Yarusso, *The rheology and flow of viscoplastic materials.* J. Fluid Mech.Journal of Fluid Mechanics, 1983. **135**: p. 1-70.

138. Rodts, S., J. Baudez, and P. Coussot, *From "discrete" to "continuum" flow in foams.* Europhys. Lett., 2005. **69**(4): p. 636-642.

139. Coussot, P., et al., *Coexistence of liquid and solid phases in flowing soft-glassy materials.* Physical review letters, 2002. **88**(21): p. 218301.

140. Ovarlez, G., et al., *On the existence of a simple yield stress fluid behavior.* Journal of Non-Newtonian Fluid Mechanics, 2012. **193**(C).

141. Bonn, D., et al., *Yield stress materials in soft condensed matter.* Reviews of Modern Physics, 2017. **89**(3).

142. Dimitriou, C.J., R.H. Ewoldt, and G.H. McKinley, *Describing and prescribing the constitutive response of yield stress fluids using large amplitude oscillatory shear stress (LAOStress).* Journal of Rheology, 2013. **57**(1): p. 27-70.

143. Khalil, M. and B. Mohamed Jan, *Herschel-Bulkley rheological parameters of a novel environmentally friendly lightweight biopolymer drilling fluid from xanthan gum and starch.* Journal of Applied Polymer Science, 2012. **124**(1): p. 595-606.

144. Rao, M.A., *Rheology of Fluid, Semisolid, and Solid Foods: Principles and Applications*. 3rd ed. 2014 ed, ed. G.V. Barbosa-Cánovas. 2014, Boston, MA: Boston, MA: Springer US.

145. Al-Zahrani, S.M., *A generalized rheological model for shear thinning fluids.* Journal of Petroleum Science and Engineering, 1997. **17**(3): p. 211-215.

146. Chhabra, R.P., *Non-Newtonian Fluids: An Introduction*, in *Rheology of Complex Fluids*, J.M. Krishnan, A.P. Deshpande, and P.B.S. Kumar, Editors. 2010, Springer New York: New York, NY. p. 3-34.

147. Mewis, J. and N.J. Wagner, *Colloidal Suspension Rheology*. 2011, Cambridge: Cambridge: Cambridge University Press.

148. Coussot, P., *Rheophysics Matter in all its States*. 2014, Cham : Springer International Publishing : Imprint: Springer.

149. Dealy, J.M. and K.F. Wissbrun, *Melt Rheology and Its Role in Plastics Processing: Theory and Applications*. 1990, Dordrecht: Dordrecht: Springer Netherlands.

150. Melito, H.S., C.R. Daubert, and E.A. Foegeding, *Validation of a large amplitude oscillatory shear protocol.* J FOOD ENG, 2012. **113**(1): p. 124-135.

151. Wilhelm, M., P. Reinheimer, and M. Ortseifer, *High sensitivity Fourier-transform rheology.* Rheol. Acta, 1999. **38**(4): p. 349-356.

152. Callaghan, P.T., *Rheo-NMR: nuclear magnetic resonance and the rheology of complex fluids.* REP PROG PHYS, 1999. **62**(4): p. 599-670.

153. Callaghan, P.T., *Rheo-NMR and velocity imaging.* Current Opinion in Colloid & Interface Science, 2006. **11**(1): p. 13-18.

154. Britton, M.M. and P.T. Callaghan, *Two-phase shear band structures at uniform stress.* PHYS REV LETT, 1997. **78**(26): p. 4930-4933.

155. Britton, M.M. and P.T. Callaghan, *Shear banding instability in wormlike micellar solutions.* Eur. Phys. J. B, 1999. **7**(2): p. 237-249.

156. Coussot, P., *Progress in rheology and hydrodynamics allowed by NMR or MRI techniques.* Experiments in Fluids, 2020. **61**(9): p. 207.

157. Dodge, J.S., *Oscillatory shear of nonlinear fluids* 1969, ProQuest Dissertations Publishing.

158. Pyshnograi, G.V., N.A. Cherpakova, and H.N.A. Al Joda, *Special Features of Nonlinear Behavior of a Polymer Solution on Large Periodic Deformations.* Journal of Engineering Physics and Thermophysics, 2020. **93**(3): p. 617-625.

159. Watanabe, H., Kuwahara, S. and Kotaka, T., *Rheology of Styrene-Butadiene-Styrene Triblock Copolymer in n-Tetradecane Systems* Journal of Rheology, 1984. **28**(4): p. 393.

160. Hyun, K., et al., *Large amplitude oscillatory shear behavior of PEO-PPO-PEO triblock copolymer solutions.* Rheol Acta, 2006. **45**(3): p. 239-249.

161. Ewoldt, R.H., A.E. Hosoi, and G.H. McKinley, *Nonlinear viscoelastic biomaterials: meaningful characterization and engineering inspiration.* Integr Comp Biol, 2009. **49**(1): p. 40-50.

162. Giacomin, A.J. and J.G. Oakley, *Obtaining Fourier series graphically from large amplitude oscillatory shear loops.* Rheologica acta, 1993. **32**(3): p. 328-332.

163. Ewoldt, R.H., et al., *Rheological fingerprinting of gastropod pedal mucus and synthetic complex fluids for biomimicking adhesive locomotion.* Soft Matter, 2007. **3**(5): p. 634-643.

164. Kuczera, S., et al., *Multilamellar Vesicle Formation Probed by Rheo-NMR and Rheo-SALS under Large Amplitude Oscillatory Shear.* LANGMUIR, 2018. **34**(28): p. 8314-8325.

165. Galvosas, P., T.I. Brox, and S. Kuczera, *Rheo-NMR in food science—Recent opportunities.* Magnetic Resonance in Chemistry, 2019. **57**(9): p. 757-765.

166. Di Giuseppe, E., et al., *Characterization of Carbopol® hydrogel rheology for experimental tectonics and geodynamics.* Tectonophysics, 2015. **642**: p. 29-45.

167. Rofe, C.J., et al., *Nuclear magnetic resonance imaging of apparent slip effects in xanthan solutions.* Journal of Rheology, 1996. **40**(6): p. 1115-1128.

168. Johnson, G.C., *Flow Characteristics of Linear, End-Blocked Dimethylpolysiloxane Fluids.* Journal of Chemical & Engineering Data, 1961. **6**(2): p. 275-278.

169. Callaghan, P.T., *Translational Dynamics and Magnetic Resonance: Pronciples of Pulse Gradient Spin Echo NMR.* Oxford University Press, New York, 2011.

170. Al-kaby, R.N., et al., *Rheo-NMR of transient and steady state shear banding under shear startup.* Journal of Rheology, 2018. **62**(5): p. 1125-1134.

171. Webb, G.A., et al., *Magnetic resonance in food science: a view to the future*. Vol. 262. 2007, Cambridge: Cambridge: NBN International.

172. Spandan, V., et al., *Drag reduction in numerical two-phase Taylor–Couette turbulence using an Euler–Lagrange approach.* J FLUID MECH, 2016. **798**: p. 411-435.

173. Ragouilliaux, A., et al., *Flow instability and shear localization in a drilling mud.* Rheol Acta, 2006. **46**(2): p. 261-271.

174. Zhang, X., et al., *Wall Slip of Soft-Jammed Systems: A Generic Simple Shear Process.* Physical Review Letters, 2017. **119**(20).

175. Barnes, H.A., *A Review of the Slip (Wall Depletion) of Polymer-Solutions, Emulsions and Particle Suspensions in Viscometers - Its Cause, Character, and Cure.* Journal of Non-Newtonian Fluid Mechanics, 1995. **56**(3): p. 221-251.

176. He, J., S.S. Lee, and D.M. Kalyon, *Shear viscosity and wall slip behavior of dense suspensions of polydisperse particles.* Journal of Rheology, 2019. **63**(1): p. 19-32.

177. Derakhshandeh, B., S.G. Hatzikiriakos, and C.P.J. Bennington, *Rheology of pulp suspensions using ultrasonic Doppler velocimetry.* Rheol Acta, 2010. **49**(11): p. 1127-1140.

178. Tang, H., et al., *Shear-banding in entangled xanthan solutions: tunable transition from sharp to broad shear-band interfaces.* Soft Matter, 2018. **14**(5): p. 826-836.

179. Milas, M., et al., *Flow and viscoelastic properties of xanthan gum solutions.* Macromolecules, 1990. **23**(9): p. 2506-2511.

180. Pipe, C.J., T.S. Majmudar, and G.H. McKinley, *High shear rate viscometry.* Rheol Acta, 2008. **47**(5-6): p. 621-642.

181. Carmona, J.A., et al., *Large amplitude oscillatory shear of xanthan gum solutions. Effect of sodium chloride (NaCl) concentration.* J FOOD ENG, 2014. **126**: p. 165-172.

182. Zhong, L., et al., *Rheological behavior of xanthan gum solution related to shear thinning fluid delivery for subsurface remediation.* J HAZARD MATER, 2013. **244-245**: p. 160-170.

183. Nevo, U., et al., *A system and mathematical framework to model shear flow effects in biomedical DW-imaging and spectroscopy.* NMR in Biomedicine, 2010. **23**(7): p. 734-744.

184. Tan, J. and W.L. Kerr, *Rheological properties and microstructure of tomato puree subject to continuous high pressure homogenization.* Journal of Food Engineering, 2015. **166**: p. 45-54.

185. Lobato-Calleros, C., et al., *Microstructural and Rheological Properties of Low-Fat Stirred Yoghurts Made with Skim Milk and Multiple Emulsions.* Journal of Texture Studies, 2009. **40**(6): p. 657-675.

186. Piau, J.M., *Carbopol gels: Elastoviscoplastic and slippery glasses made of individual swollen sponges Meso- and macroscopic properties, constitutive equations and scaling laws.* Journal of Non-Newtonian Fluid Mechanics, 2007. **144**(1): p. 1-29.

187. Läuger, J. and H. Stettin, *Differences between stress and strain control in the non-linear behavior of complex fluids.* Rheol Acta, 2010. **49**(9): p. 909-930.

188. Khan, S.Y.Y., M.; Sardar, N. , *Studies on Rheological Behavior of Xanthan Gum Solutions in Presence of Additives.* Petroleum and Petrochemical Engineering Journal, 2018. **2**(5).

189. Coussot, P., et al., *Macroscopic vs. local rheology of yield stress fluids.* Journal of Non-Newtonian Fluid Mechanics, 2009. **158**(1): p. 85-90.

190. Coussot, P., et al., *Coexistence of liquid and solid phases in flowing soft-glassy materials.* PHYS REV LETT, 2002. **88**(21): p. 218301-2183014.

191. Bird, R.B., G.C. Dai, and B.J. Yarusso, *The Rheology and Flow of Viscoplastic Materials.* Reviews in Chemical Engineering, 1983. **1**(1): p. 1-70.

192. Alexandrou, A.N., N. Constantinou, and G. Georgiou, *Shear rejuvenation, aging and shear banding in yield stress fluids.* Journal of Non-Newtonian Fluid Mechanics, 2009. **158**(1): p. 6-17.

193. Toorman, E.A., *An analytical solution for the velocity and shear rate distribution of non-ideal Bingham fluids in concentric cylinder viscometers.* Rheologica acta, 1994. **33**(3): p. 193-202.

194. Toorman, E.A., *Controlled rate concentric cylinder rheometry of estuarine mud suspensions.* MAST G8M Coastal Morphodynamics Research Project Report (HYD148), 1995.

195. Nguyen, Q.D. and D.V. Boger, *Measuring the Flow Properties of Yield Stress Fluids.* Annual Review of Fluid Mechanics, 1992. **24**(1): p. 47-88.

196. Taylor, G.I., *Stability of a viscous liquid contained between two rotating cylinders.* Philosophical Transactions of the Royal Society of London A, 1923. **223**.

197. Swinney, H.L. and J.P. Gollub, *Hydrodynamic Instabilities and the Transition to Turbulence*. 1985, Berlin, Heidelberg : Springer Berlin Heidelberg : Imprint: Springer.

198. Fardin, M.A., Perge, C. and Taberlet, N., *"The hydrogen atom of fluid dynamics"--introduction to the Taylor-Couette flow for soft matter scientists.* Soft Matter, 2014. **10**(20).

199. Di Prima, R.C. and H.L. Swinney, *Instabilities and transition in flow between concentric rotating cylinders*, in *Hydrodynamic Instabilities and the Transition to Turbulence*, H.L. Swinney and J.P. Gollub, Editors. 1985, Springer Berlin Heidelberg: Berlin, Heidelberg. p. 139-180.

200. Brox, T.I., Douglass, B., Galvosasa, P. and Brown, J.R., *Observations of the influence of Taylor-Couette geometry on the onset of shear-banding in surfactant wormlike micelles.* Journal of Rheology 2016. **60**(973).

201. Barnes, H.A., *A review of the slip (wall depletion) of polymer solutions, emulsions and particle suspensions in viscometers: its cause, character, and cure.* Journal of Non-Newtonian Fluid Mechanics, 1995. **56**(3): p. 221-251.

202. Pérez-González, J., et al., *Rheo-PIV of a yield-stress fluid in a capillary with slip at the wall.* Rheol Acta, 2012. **51**(11): p. 937-946.

203. Ewoldt, R.H., M.T. Johnston, and L.M. Caretta, *Experimental Challenges of Shear Rheology: How to Avoid Bad Data*. 2014, New York, NY: Springer New York: New York, NY. p. 207-241.

204. Kaylon, D.M., *Apparent slip and viscoplasticity of concentrated suspensions.* Journal of Rheology, 2005. **49**(621).

205. Magnin, A. and J.M. Piau, *Cone-and-plate rheometry of yield stress fluids. Study of an aqueous gel.* Journal of Non-Newtonian Fluid Mechanics, 1990. **36**(1): p. 85-108.

206. Russell, J.L., *Studies on thixotropic gelation - II—The coagulation of clay suspensions.* Proceedings of the Royal Society of London Series a-Mathematical Physical and Engineering Sciences, 1936. **154**(883): p. 550-560.

207. Alderman, N.J., G.H. Meeten, and J.D. Sherwood, *Vane rheometry of bentonite gels.* Journal of Non-Newtonian Fluid Mechanics, 1991. **39**(3): p. 291-310.

208. Atkinson, C. and J.D. Sherwood, *The Torque on a Rotating n-Bladed Vane in a Newtonian Fluid or Linear Elastic Medium.* P ROY SOC LOND A MAT, 1992. **438**(1902): p. 183-196.

209. Briggs, J.L., J.F. Steffe, and Z. Ustunol, *Vane Method to Evaluate the Yield Stress of Frozen Ice Cream.* Journal of Dairy Science, 1996. **79**(4): p. 527-531.

210. Liddel, P.V. and D.V. Boger, *Yield stress measurements with the vane.* Journal of Non-Newtonian Fluid Mechanics, 1996. **63**(2): p. 235-261.

211. Barnes, H.A. and J.O. Carnali, *The vane-in-cup as a novel rheometer geometry for shear thinning and thixotropic materials.* Journal of Rheology, 1990. **34**(841).

212. Nguyen, Q.D. and D.V. Boger, *Yield Stress Measurement for Concentrated Suspensions.* Journal of Rheology 1983. **27**(321).

213. Atkinson, C. and J.D. Sherwood, *The Torque on a Rotating n-Bladed Vane in a Newtonian Fluid or Linear Elastic Medium.* Proceedings of the Royal Society of London Series a-Mathematical Physical and Engineering Sciences, 1992. **438**(1902): p. 183-196.

214. Jarny, S., et al., *Rheological behavior of cement pastes from MRI velocimetry.* Cement and Concrete Research, 2005. **35**(10): p. 1873-1881.

215. Caprihan, A. and E. Fukushima, *Flow measurements by NMR.* Physics Reports, 1990. **198**(4): p. 195-235.

216. Fukushima, E., *Nuclear magnetic resonance as a tool to study flow.* Annual Review of Fluid Mechanics 1999. **31**(1): p. 95-123.

217. Dinkgreve, M., et al., *Carbopol: From a simple to a thixotropic yield stress fluid.* Journal of Rheology, 2018. **62**(3): p. 773-780.

218. Al-kaby, R.N., et al., *Characterization of velocity fluctuations and the transition from transient to steady state shear banding with and without pre-shear in a wormlike micelle solution under shear startup by Rheo-NMR.* Applied Rheology, 2020. **30**(1): p. 1-13.

219. Kuczera, S. and P. Galvosas, *Advances and artefact suppression in RARE-velocimetry for flow with curved streamlines.* Journal of Magnetic Resonance, 2015. **259**: p. 135-145.

220. Brummer, R., *Rheology Essentials of Cosmetic and Food Emulsions*. 1. Aufl. ed. 2005, Berlin, Heidelberg: Berlin, Heidelberg: Springer-Verlag.

221. Kim, H.S. and T.G. Mason, *Advances and challenges in the rheology of concentrated emulsions and nanoemulsions.* ADV COLLOID INTERFAC, 2017. **247**: p. 397-412.

222. Bocquet, L., A. Colin, and A. Ajdari, *Kinetic Theory of Plastic Flow in Soft Glassy Materials.* PHYS REV LETT, 2009. **103**(3): p. 036001-036001.

223. Brennan, J.G., *Food texture and viscosity: Concept and measurement: By M. C. Bourne, Academic Press, New York, 1982. Price: £23.80*. 1984, Elsevier Ltd. p. 80-81.

224. Schramm, L.L., *Emulsions, foams, suspensions, and aerosols: microscience and applications, second edition*. 2nd ed. ed. 2014: Wiley.

225. Leal-Calderon, F., V. Schmitt, and J. Bibette, *Emulsion Science: Basic Principles*. 2007, New York, NY: New York, NY: Springer New York. 227.

226. Herschel, W.H. and R. Bulkley, *Measurement of consistency as applied to rubber-benzene solutions.* Proceedings - American Society for Testing and Materials, 1926. **26**(2): p. 621-633.

227. Besseling, R., et al., *Shear Banding and Flow-Concentration Coupling in Colloidal Glasses.* PHYS REV LETT, 2010. **105**(26): p. 268301-268301.

228. Dauchot, O., G. Marty, and G. Biroli, *Dynamical heterogeneity close to the jamming transition in a sheared granular material.* PHYS REV LETT, 2005. **95**(26): p. 265701.1-265701.4.

229. Maillard, M., et al., *Blade-coating of yield stress fluids.* J NON-NEWTON FLUID, 2016. **237**: p. 16-25.

230. Kuczera, S. and P. Galvosas, *Advances and artefact suppression in RARE-velocimetry for flow with curved streamlines.* Journal of Magnetic Resonance, 2015. **259**: p. 135-145.

231. Coussot, P., *Slow flows of yield stress fluids: yielding liquids or flowing solids?* Rheol Acta, 2018. **57**(1): p. 1-14.

232. Huang, N., et al., *Flow of wet granular materials.* PHYS REV LETT, 2005. **94**(2): p. 028301.1-028301.4.

233. Escudier, M.P., I.W. Gouldson, and D.M. Jones, *Circular Couette Flow and Taylor Vortices in Shear-Thinning Liquids*. Berlin, Heidelberg: Springer Berlin Heidelberg: Berlin, Heidelberg. p. 16-33.

234. Wassenius, H. and P.T. Callaghan, *NMR velocimetry studies of the steady-shear rheology of a concentrated hard-sphere colloidal system.* European Physical Journal E, 2005. **18**(1): p. 69-84.

235. Nguyen, Q.D.a.D.V.B., *Characterization of yield stress fluids with concentric cylinder viscometers.* Rheologica acta, 1987. **24**(1): p. 508-515.

236. Owens, C.E., A.J. Hart, and G.H. McKinley, *Improved rheometry of yield stress fluids using bespoke fractal 3D printed vanes.* Journal of Rheology, 2020. **64**(3): p. 643-662.

237. Spicer, M.C.V.T.a.P.T., *Variations of the Herschel–Bulkley exponent reflecting contributions of the viscous continuous phase to the shear rate-dependent stress of soft glassy materials.* Journal of Rheology, 2020.

238. Brox, T.I., *New Methods for Studying Materials Under Shear with Nuclear Magnetic Resonance*. 2016, Victoria University of Wellington, NZ.